THÈSE

En vue de l'obtention du

DOCTORAT DE L'UNIVERSITÉ DE TOULOUSE

Délivré par :

Institut National Polytechnique de Toulouse (INP Toulouse)

Discipline ou spécialité :

Energétique et Transferts

Présentée et soutenue par :

Mme LAETITIA MOTTET

le mardi 23 février 2016

Titre :

SIMULATIONS OF HEAT AND MASS TRANSFER WITHIN THE CAPILLARY EVAPORATOR OF A TWO-PHASE LOOP

Ecole doctorale :

Mécanique, Energétique, Génie civil, Procédés (MEGeP)

Unité de recherche :

Institut de Mécanique des Fluides de Toulouse (I.M.F.T.)

Directeur(s) de Thèse :

M. MARC PRAT

Rapporteurs :

M. JAY OCHTERBECK, UNiVERSITY OF CLEMSON

M. VINCENT PLATEL, UNIVERSITE DE PAU ET DES PAYS DE L ADOUR

Membre(s) du jury :

M. YVES BERTIN, ENSMA POITIERS, Président

M. MARC PRAT, INP TOULOUSE, Membre

M. MICHEL QUINTARD, INP TOULOUSE, Membre

Acknowledgements

Les travaux présentés dans ce manuscrit ont eu lieu au sein du Groupe d'Étude sur les Milieux Poreux (GEMP) à l'Institut de Mécanique des Fluides de Toulouse (IMFT) et ont été financés par le Centre National d'Étude Spatiale (CNES) et Airbus Defence and Space. C'est donc tout naturellement que je tiens à remercier ces trois organismes.

Merci à mon directeur de thèse, Marc Prat. Je le remercie de m'avoir fait confiance pour travailler sur ce sujet, pour son encadrement de qualité et pour avoir toujours été disponible. Outre ses connaissances scientifiques, c'est également son optimisme, son humour et son calme à toute épreuve qui m'ont permis de vivre ces trois années de thèse avec sérénité. Sincèrement, merci Marc.

Merci également à Amaury Larue de Tournemine et Typhaine Coquard pour leur collaboration avec l'IMFT qui a permis de financer mes travaux, et merci d'avoir accepté de faire partie de mon jury de thèse. Je les remercie également pour toutes les discussions que l'on a pu avoir, pour leurs conseils, leurs remarques et leur gentillesse.

Merci aux deux rapporteurs de ma thèse, Vincent Platel et Jay Ochterbeck, ainsi qu'à Yves Bertin pour avoir présidé mon jury. Merci à tous les trois pour vos suggestions qui ont permis d'améliorer la version finale de ce manuscrit.

Merci à Michel Quintard. Tout d'abord pour avoir été membre de mon jury, mais également pour tous les échanges, toujours très enrichissants, scientifiques ou non, que j'ai eu l'occasion d'avoir avec lui. Merci également de m'avoir donné la chance d'être initiée à la spéléologie.

Merci à tous les autres permanents du groupe GEMP. En particulier, merci à Sylvie Lorthois, Manuel Marcoux, Paul Duru, Pascal Swider, Gérald Debenest, Rachid Ababou, et Yohan Davit, avec lesquels j'ai souvent eu l'occasion d'échanger. Merci à Suzy Bernard avec qui toutes les démarches administratives semblent simples et rapides. Merci à Ruddy Soeparno : même si je n'ai pas eu le plaisir de travailler personnellement avec lui, il contribue indéniablement à mener à bien de nombreux projets de recherche à GEMP ainsi qu'au bon moral des troupes.

Merci à toutes les autres personnes travaillant à l'IMFT. Merci à Sandrine Chupin pour tous ces petits moments de discussion, pour sa bonne humeur et son professionnalisme. Merci au service informatique et au service Cosinus pour leur efficacité et leur sympathie. Merci également à Muriel Sabater de la reproduction. Et finalement, un grand merci à André Rouch pour sa jovialité, les moments de partage et pour son travail quotidien qui contribue à faire de l'IMFT un lieu où il est agréable de travailler.

Merci à Karine Deperrois pour avoir passé beaucoup de temps à corriger avec rigueur mon manuscrit de thèse. Au-delà de l'aspect professionnel, j'ai aussi découvert une femme pleine de qualités entourée d'un mari et d'un fils remarquables.

Je tiens à remercier plus particulièrement certaines personnes qui m'ont beaucoup aidée dès mon arrivée à l'IMFT. Merci à Cyprien Soulaine d'avoir été présent lors de mes premiers questionnements poreux.

Sans lui, mes premiers mois de thèse aurait été beaucoup plus fastidieux. Il a pris du temps pour m'expliquer avec pédagogie des notions scientifiques nouvelles pour moi et il a su me donner des conseils pour vite progresser. Un grand merci au duo Pierre Horgue et Romain Guibert qui a toujours fait preuve de patience (et il en fallait) et de bienveillance lors de mes (très) nombreuses sollicitations tout au long de mes 3 années de thèse. Vous avez toujours accepté de répondre à mes questions, de prendre un peu de votre temps pour discuter avec moi et vous avez largement contribué à l'avancement de mes travaux, et plus particulièrement au modèle continu. Merci également à Philippe Lefort qui m'a aidée pour la partie « programmation en Fortran ». Il a su me faire profiter de son expérience numérique et m'a ainsi permis de me lancer plus rapidement dans le code.

Merci à mes deux frères de thèse : Mauricio Dueñas-Velasco et Benjamin Straubhaar, arrivés seulement quelques heures avant moi à l'IMFT un certain lundi 1er Octobre 2012. Merci d'avoir été tour à tour mes collègues de bureau (pour ne pas faire de jaloux). Nous avons partagé le même encadrant, les mêmes galères administratives, les mêmes joies, les mêmes doutes liés à une thèse et le même tableau pour y inscrire nos listes de rêves. Merci à tous les deux d'avoir été là. Merci à Myriam Peyrounette, arrivée un peu plus tard (et pas assez tôt) à GEMP. Merci pour toutes ces nombreuses soirées passées (et à venir) avec toi, merci d'avoir toujours une oreille attentive pour écouter mes longs flots de parole et surtout merci pour l'authenticité de chaque moment passé en ta compagnie. Merci également à Frédéric Pierre et à Maha Touati pour qui j'ai une affection toute particulière et avec qui j'ai passé de formidables moments dans et à l'extérieur de notre bureau. Merci à Yohan Davit, déjà remercié en tant que permanent de GEMP, mais que je tiens ici à remercier en tant que personne. Merci pour ces soirées passées avec toi en dehors du labo, merci d'avoir corriger ma lettre de motivation et merci pour toutes ces discussions parfois campagnardes !

De façon générale, je remercie tous mes partenaires de tarot qui ont joyeusement rythmé tous mes midis pendant trois ans (personnes en partie sus-citées) : Amy, Ange, Antoine, Benjamin, Chen, Fred, Jacques, Jian Wei, Lingguo, Maha, Martin, Mauricio, Myriam, Ruddy, Sylvain, Vincent, Yohan… Merci également aux anciens doctorants, post-doctorants, stagiaires et visiteurs qui sont passés par GEMP et avec qui j'ai passé de très bons moments : Benoit, Fabien, Felix, Masahito, Paul, Tristan, Victoria …

Merci aux Tipsies : on n'oublie pas, on s'était dit rendez-vous dans 10 ans… Merci au SOSKT pour les moments d'anthologie passés avec vous chez Rogé, à la balnélol à Loudenvieille et lors des soirées labellisées SOSKT. Merci à tous les pseudo-nantais à qui les mots « aouw » et « carton » disent quelque chose de près ou de loin, et merci plus particulièrement au G2 (parce qu'il est toujours là). Merci à Pushka et Consult Your Doctor pour tous ces concerts endiablés ! Merci à mes nouveaux amis toulousains et aux personnes rencontrées au volley. Merci Jean-Ba pour tous ces repas dignes de Master Chef et pour toutes ces soirées où, avec Mélanie, vous nous avez humiliées à « quizz TV ». Merci à Mélanie, d'être à la fois mon amie et à la fois de ma famille (et en même temps non). Tout nous destinait à nous retrouver un jour. Chose faite !

Merci à toute ma grande et nombreuse famille : les Mottet, les Mathieu et les Conangle ; et merci à ma famille d'adoption : les Maillard. Je ne peux citer quelqu'un en particulier sans citer tout le monde, alors j'en resterai là pour éviter dix pages supplémentaires de remerciements. Je tiens tous à vous remercier pour être chacun ce qu'il est. Je remercie plus particulièrement Lentignac, les gens qui y habitent et le lieu

en lui-même qui est pour moi mon petit coin de paradis. Merci aussi à Papi Jacques et Mamie Rolande d'être, et d'avoir été, des grands-parents attentionnés et toujours justes.

Merci à Papa Rémy qui ne peut pas me renier tellement je lui ressemble. Merci à Maman Nathalie qui est la femme la plus forte et la plus belle que je connaisse. Merci à tous les deux d'avoir toujours assumé les dépenses liées à mes plutôt « longues » études alors que je n'étais que la 1ère roue de votre 4L.

Merci Lolo de me supporter depuis 23 ans. Merci d'avoir fait ma vaisselle quand j'étais en prépa à Périgueux et quand j'étais en pleine rédaction de thèse à Toulouse. Merci de m'appeler dix fois par jour pour me raconter tout et rien. Merci d'être autant toquée et d'admirer le linge étendu pendant dix minutes (pour être sûre qu'il soit bien étendu). Merci d'être toi : une vraie sœur que j'insupporte parfois et qui parfois m'insupporte, mais qui est toujours présente !

Merci à mes deux kikis sœurs : Léna et Lisa. Bientôt 12 ans… Le temps passe vite… Vous êtes pétillantes de vie et les deux rayons de soleil de la famille ! Merci également à MaPoule et Pinpin.

Merci à Chris d'être mon compagnon de route depuis déjà plusieurs années. Merci d'être si différent de moi tout en me complétant si bien. Merci de me faire encore rêver.

Résumé

Le contrôle thermique des composants électroniques embarqués dans les engins spatiaux est souvent assuré par des boucles fluides diphasiques à pompage capillaire (Loop Heat Pipe (LHP) ou Capillary Pumped Loop (CPL)). La présente étude est centrée sur les évaporateurs des LHP. Ils sont composés principalement d'un bâti métallique, d'une mèche poreuse et de cannelures. Le milieu poreux est initialement saturé en liquide. La charge thermique à évacuer est appliquée sur le bâti entraînant la vaporisation du liquide au sein de la mèche. La vapeur est ensuite récoltée au sein des cannelures pour être évacuée.

L'étude est effectuée sur une cellule unitaire de l'évaporateur. Dans le but d'étudier les transferts de masse et de chaleur, un modèle de réseau de pores 3D dit mixte a été développé. Les champs de pression et de température sont calculés à partir des équations macroscopiques tandis que la capillarité est gérée à l'aide d'une approche réseau de pore classique. L'un des avantages d'une telle formulation est de pouvoir accéder à la répartition des phases liquide et vapeur au sein de l'espace poral du milieu poreux. Il a ainsi été mis en évidence qu'une zone diphasique (zone où le liquide et la vapeur coexistent) se met en place pour une large gamme de flux lorsque la vapeur apparait dans la structure capillaire. Cette zone diphasique est localisée sous le bâti métallique et est corrélée avec les meilleures performances thermiques de l'évaporateur. Cette observation diffère fortement de l'hypothèse souvent considérée de la présence d'une zone sèche dans cette région.

Trois positions différentes de cannelures ont été étudiées. Il a ainsi pu être mis en évidence que la plus large gamme de flux, pour laquelle les performances de l'évaporateur sont les meilleures, est obtenue lorsque les cannelures sont usinées à la surface extérieure de la mèche. Toujours dans le but d'améliorer les performances thermiques de l'évaporateur, une étude paramétrique a été menée pour mettre en évidence les paramètres qui influencent positivement la conductance de l'évaporateur. Finalement, l'étude de l'influence d'une mèche biporeuse/bidispersée, c'est-à-dire d'un milieu poreux caractérisé par deux tailles de pores/liens différentes, a été menée. La distribution des phases liquide et vapeur au sein de la structure capillaire bidispersée est différente de celle d'un milieu mono-poreux du fait des chemins préférentiels créés par les larges pores. Par ailleurs, l'analyse thermique a montré qu'un tel milieu poreux permet de réduire considérablement la température du bâti ainsi que d'augmenter les performances thermiques de l'évaporateur.

Un deuxième modèle basé sur une approche continue a été développé. Cette méthode utilise l'algorithme IMPES (IMplicit Pressure Explicit Saturation) et est couplé à la résolution du champ de température avec changement de phase. Ce type de résolution permet d'accéder à un champ de saturation. Les résultats ainsi obtenus sont en bon accord avec ceux prédits par le modèle réseau de pores mixte. Le modèle continu, moins gourmand en temps de calcul, permet d'envisager des simulations sur une plus grande partie de l'évaporateur.

Mots-clés : loop heat pipe, évaporateur capillaire, modèle réseau de pores, modèle continu, écoulement diphasique, changement de phase, milieux biporeux.

Abstract

The thermal control of electronic devices embedded in spacecraft is often carried out by capillary two-phase loop systems (Loop Heat Pipe (LHP) or Capillary Pumped Loop (CPL)). This thesis focuses on the LHP evaporators. They mostly consist of a metallic casing, a porous wick and vapour grooves. The porous medium is initially saturated with liquid. The heat load is applied at the external surface of the casing inducing the vaporisation of the liquid within the wick. The vapour is then evacuated thanks to the vapour grooves.

A unit cell of the evaporator is studied and corresponds to our computational domain. A so-called 3D mixed pore network model has been developed in order to study the heat and mass transfers. Pressure and temperature fields are computed from macroscopic equations, while the capillarity is managed using the classical pore network approach. The main advantage of such formulation is to obtain the liquid-vapour phase distribution within the porous medium pore space. The work highlights that a two-phase zone (characterized by the coexistence of the liquid and the vapour) exists for a large range of fluxes when vaporisation takes place within the capillary structure. This two-phase zone is located right under the casing and is positively correlated with the best evaporator thermal performances. This result differs from the often made assumption of a dry region under the casing.

Three different groove locations are tested. This investigation highlights that evaporator thermal performances are the best over a large range of fluxes for grooves manufactured at the external surface of the wick. In complement, a parametric study is performed to highlight parameters which impact positively the evaporator thermal performances. Finally, a biporous/bidispersed wick, i.e. a wick with a bimodal pore/throat size distribution, is studied. The liquid-vapour phase distribution within the capillary structure is different from the one for a monoporous structure due to preferential vapour paths created by the large throats and pores-network. Moreover, the thermal analysis shows that such a porous medium permits to reduce considerably the evaporator wall temperature and to increase the evaporator thermal performances.

A second model is developed based on a continuum approach. This method uses the IMPES (IMplicit Pressure Explicit Saturation) algorithm coupled with the heat transfer with phase change. Results are in good agreement with those predicted by the mixed pore network model. The continuum model, requiring less computing time, should allow considering larger sub domains of the evaporator.

Keywords: loop heat pipe, capillary evaporator, pore network model, continuum model, two phase flow, phase change, bidispersed porous medium.

Contents

Acknowledgements i

Résumé v

Abstract vii

Contents ix

Nomenclature xiii

Introduction 1

Chapter I Context 5

I.1 Capillary two-phase loops 6
I.1.1 Components constituting LHP/CPL and fluid motion in the loop 6
I.1.2 Thermodynamic cycle 7
I.1.3 Operating conditions 11
I.1.4 Thermal performance indicators of a capillary two-phase loop 14
I.1.5 Operating limits 14
I.1.6 Working fluid selection 16
I.2 Capillary evaporator of LHP 17
I.2.1 Thermal performance indicators of a capillary evaporator 17
I.2.2 Classification of capillary evaporators 18
I.2.3 General description of a capillary evaporator 20
I.2.4 Flux balance and parasitic heat flux 22
I.2.5 Components constituting a capillary evaporator 23

Chapter II Literature review 37

II.1 Analytical studies 38
II.1.1 Analytical LHP studies 38
II.1.2 Analytical evaporator study 38
II.2 Modelling of the whole loop system 39
II.2.1 Steady-state modelling 39
II.2.2 Transient modelling 45
II.2.3 Summary of whole loop models 48
II.3 Visualisation experiment of the evaporation process 48
II.4 Modelling of the capillary evaporator 51
II.4.1 Without vapour within the wick 51
II.4.2 With vapour within the wick 56
II.4.3 With a two-phase zone within the wick 68
II.4.4 Summary of capillary evaporator models 70
II.5 Synthesis and conclusion of the chapter 71

Chapter III Pore network modelling 81

III.1 Pore network model 82
III.1.1 General description 82
III.1.2 Classical pore network model 83
III.1.3 Mixed pore network model 84
III.2 Mathematical model 85
III.2.1 Hypothesis and computational domain 85
III.2.2 Governing equations 86
III.2.3 Flow in the porous structure 86
III.2.4 Heat transfer 86
III.2.5 Boundary conditions 87
III.2.6 Loop model 90
III.2.7 Flux balance 93
III.3 Numerical method 94
III.3.1 Finite volume method 94
III.3.2 Programming language and linear solver 94
III.3.3 Method of solution and computational chart 94
III.3.4 Hoshen-Kopelman algorithm: cluster location 98
III.4 Model validation and effective thermal conductivity correlation 100
III.4.1 Input parameters 100
III.4.2 Model validation: overheating of the casing 102
III.4.3 Influence of the correlation for the effective thermal conductivity 102
III.4.4 Summary 108
III.5 Results and discussions 108
III.5.1 Input parameters 108
III.5.2 Liquid-vapour distribution within the wick 108
III.5.3 Vaporisation partition 111
III.5.4 Maximum temperature 111
III.5.5 Conductance 113
III.5.6 Conclusion 114
III.6 Synthesis and conclusion of the chapter 115

Chapter IV Sensitivity study (Monoporous wick) 117

IV.1 Study of grooves location 118
IV.1.1 Input properties 118
IV.1.2 Results and discussions 120
IV.1.3 Summary 128
IV.2 Parametric study 129
IV.2.1 Input properties 129
IV.2.2 Results and discussions 131
IV.2.3 Summary 146
IV.3 Synthesis and conclusions of the chapter 146

Chapter V Bimodal capillary structure 147

V.1 Method of manufacturing the bimodal wick structure 148
V.2 Literature review 149

V.2.1 Experimental literature review 149
V.2.2 Numerical literature review 149
V.3 Bidispersed structure two-scale pore network model 151
V.4 Mathematical model 152
V.4.1 Governing equations 152
V.4.2 Boundary conditions 153
V.5 Model validation 154
V.5.1 Input properties 154
V.5.2 Numerical results vs. experimental results 155
V.5.3 Evaporator heat transfer coefficient and vapour saturation 156
V.5.4 Evaporator wall temperature 159
V.5.5 Vaporisation partition 159
V.5.6 Summary 160
V.6 Monoporous vs. bidispersed wick 160
V.6.1 Input properties 160
V.6.2 Nucleation flux 162
V.6.3 Liquid-vapour phase distribution 162
V.6.4 Evaporator thermal performances 165
V.6.5 Evaporator wall temperature 165
V.6.6 Summary 166
V.7 Synthesis and conclusions of the chapter 167

Chapter VI Continuum modelling 169

VI.1 Motivations 170
VI.2 Problem formulation 170
VI.2.1 Assumptions 170
VI.2.2 Governing equations 170
VI.2.3 Boundary condition 174
VI.2.4 Initial condition 175
VI.3 Method of solution 175
VI.4 Results and discussions 177
VI.4.1 Input parameters 177
VI.4.2 Continuum model simulation (CMS) vs. pore network simulation (PNS) 179
VI.4.3 Influence of β 193
VI.5 Synthesis and conclusions of the chapter 197

Conclusions and prospects 199

Appendix A. Determination of properties for the monoporous pore network 203

Appendix B. Determination of properties for the bidispersed pore network 207

Appendix C. Computation of permeability 213

Appendix D. Computation of capillary-pressure and relative permeability curves 215

References 219

Nomenclature

A	Aspect ratio value	-
a	Step between two pores centre	m
b	Lattice spacing of the large network	m
c_p	Specific heat capacity	J/kg/K
E	Young modulus	MPa
D_H	Hydraulic diameter	m
d	Diameter	m
G	Factor depending of aspect ratio value	-
g_{ij}	Hydraulic conductance of throat	m^3
$\bar{g}$	Hydraulic conductance using in mixed model	m^3
H	Height of grooves	m
$h_{contact}$	Thermal contact conductance	$W/m^2/K$
h_{ev}	Evaporator heat transfer coefficient (i.e. evaporator conductance)	$W/m^2/K$
h_g	Convective heat transfer coefficient	$W/m^2/K$
h_{lv}	Latent heat of vaporisation	J/kg
K	Permeability	m^2
K_{IC}	Fracture toughness	$MPa/m^{1/2}$
k	Thermal conductivity	W/m/K
k^*	Effective thermal conductivity	W/m/K
k_{rl}	Liquid relative permeability	-
k_{rv}	Vapour relative permeability	-
$L_x, L_y, L_z,$ $L_{xv}, L_{yg}, L_{yw}, L_{yt}$	Dimensions of the geometry	m
l	Length	m
	Counter in Hoshen-Kopelman algorithm	-
M	Molar mass	g/mol
M_l	Relative mobility of the liquid	$m^2/Pa/s$
M_v	Relative mobility of the vapour	$m^2/Pa/s$
m, m_l, m_v	Van Genuchten parameters	-
$\dot{m}$	Mass flow rate	kg/s
	Mass rate of generation of vapour or liquid	$kg/m^3/s$
N	Total number of grooves, pores, throats or clusters	-
$\mathbf{n}$	Unit normal vector	-
n	Coefficient in Chaudary and Bhandari correlation	-
n_i, n_j, n_k	Number of pore, i.e. grid point, in the wick in the x, y and z direction	-
n, n_l, n_v	Van Genuchten parameters	-
P	Pressure	Pa
	Perimeter	m

Q	Flux	W
q	Heat flux	W/m²
q_{ev}	Interface mass flow rate	kg/m²/s
q_{ij}	Mass flow rate between two adjacent nodes i and j	kg/s
R	Gas constant	J/kg/K
$R_{LHP/CPL}$	Thermal loop resistance	K/W
R_{ev}	Thermal evaporator resistance	K/W
r	Radius	m
r_m	Meniscus curvature	m
r_n, r_b	Nucleation radius of the vapour bubble	m
S	Surface	m²
$S_{fin/wick}, A_t$	Area contact between the casing and the wick	m²
S_c	Input surface where the flux is applied	m²
S_l	Liquid saturation	-
S_{lc}	Fraction of pore occupied by liquid under the casing	-
S_{lr}	Liquid phase residual saturation	-
S_v	Vapour saturation	-
S_{vc}	Fraction of pore occupied by vapour under the casing	-
S_{vr}	Vapour phase residual saturation	-
T	Temperature	K
t	Time	s
$\mathbf{u}$	Velocity vector	m/s
u	Velocity	m/s
V	Volume	m³
W	Width of grooves	m
x, y, z	Axis coordinates	m

Greek symbols

$\alpha, \alpha_1, \alpha_2$	Relaxation parameters	-
α	Van Genuchten coefficient	Pa^{-1}
β	Parameter in the phase change model	s^{-1}
γ	Proportional factor between Reynolds number and fanning factor	-
γ_l, γ_v	Van Genuchten parameters	-
ε	Porosity	-
Θ	LHP slope	°
θ	Contact angle	°
μ	Dynamic viscosity	Pa s
ν	Kinematic viscosity	m²/s
ξ	Depth of the two-phase zone	-
ρ	Density	kg/m³
σ	Surface tension	Pa/m
σ_{ts}	Tensile strength	MPa

σ_y	Yield strength	MPa
Ψ	Geometrical factor	-
$\omega, \omega_1, \omega_2$	Convergence criteria	-

Subscripts

c	Casing or cluster
cc	Compensation chamber
cap	Capillary
$cell$	Cell of the calculation grid
$cond$	Condenser or conduction
$conv$	Convection
ev	Evaporator
$evap$	Evaporation
g	Groove
L	Large network
l	Liquid
ll	Liquid line
$loop$	Loop
max	Maximum
new	New value
$nucl$	Nucleation
p	Pore
PN	Pore network value
$\mathbb{R}$	Experimental value
S	Small network
sat	Saturation
sub	Subcooled
sup	Superheated
T, tot	Total
t	Throat
$\mathbb{t}$	Theoretical value
v	Vapour
vl	Vapour line
$void$	Void
w	Wick

Dimensionless number

Nu	Nusselt number
Pr	Prandtl number
Re	Reynolds number
Ca	Capillary number

Introduction

Thermal control and regulation

A space platform is made up of electronic devices which ensure the proper operation of the apparatus. For hardware qualification reasons, the range of temperatures where devices can work correctly is narrow. In consequence, the heat produced by these devices need to be evacuated. Moreover, technologies used in these types of apparatus are more and more sophisticated, implying an increase in the overheating of electronic circuits, which may damage them. In other words, the heat that needs to be dissipated grows with emergence of new technologies. The range of temperature that spacecraft can undergo inside space is wide: between -100°C in darkness and 180°C in the sun. To deal with these extremes temperatures, devices are firstly isolated from the outside but the perfect thermal control of them stays a crucial point. To meet this need and concerning the heat transport, several technologies, mainly based on a fluid loop system (single-phase or two-phase loop), have been developed for many years. Four major families can be distinguished (Figure 0.1a):

- Mechanical pumped two-phase loop
- Mechanical pumped single-phase loop
- Capillary two-phase loops: Capillary Pumped Loop (CPL) and Loop Heat Pipe (LHP)
- Heat pipe

Over the last decades, capillary two-phase loops and mechanical pumped two-phase loops seem to be the best candidates as an answer to the thermal regulation challenge. They are composed by a heat source (evaporator) in which the liquid evaporates and a heat sink (a condenser) in which the vapour condenses (Figure 0.1b). In the capillary two-phase loop family, two different technologies can be distinguished:

- The Capillary Pumped Loop (CPL) (Figure I.1)
- The Loop Heat Pipe (LHP) (Figure I.1).

The capillary pumped loop (CPL) was developed in the US in the early 1960s while the loop heat pipe (LHP) appeared in the early 1970s in Russia. First developed in relation with aerospace applications, these devices are also studied nowadays for rail-bound transport, automobile transport or aeronautics applications. These two technologies have gained interest due to their robustness, flexibility and efficiency. Indeed, they present many advantages compared to mechanical pumped loop. There is no mechanical component (pump, compressor…) inside the loop, meaning no maintenance, and it avoids the vibration due to a mechanical pump. Capillary pumped two-phase loop are passive and auto-regulated devices which need no exterior energy source contrary to mechanical pumped loop. The motion of the fluid along the loop is induced by capillary forces due to the presence of a porous material, called the wick, within the evaporator. Moreover, these devices use phase change properties to evacuate large amounts of heat over distances of a few meters.

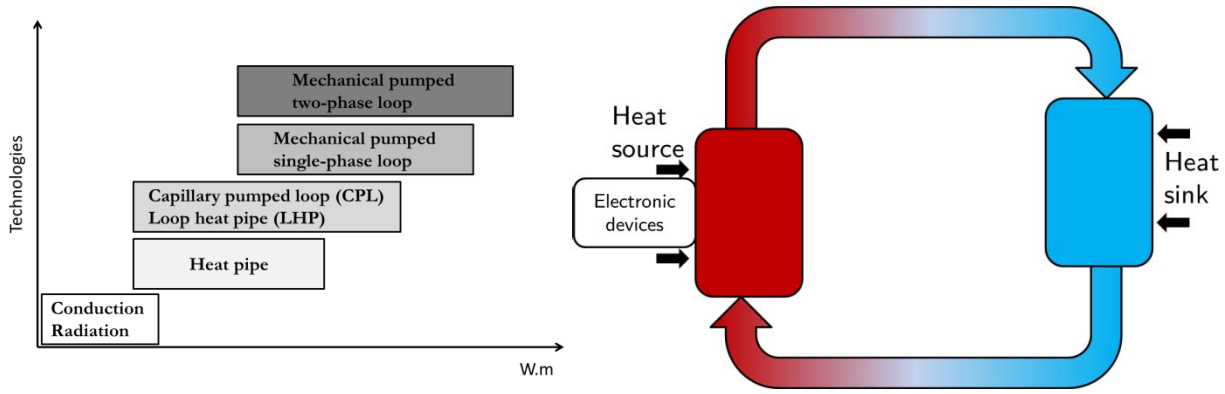

(a) (b)

Figure 0.1 – (a) Thermal control technologies [1]. (b) Sketch of the principle of the capillary pump loop.

Works at IMFT and collaborations with CNES and Airbus Defence and Space

For 20 years, the Group of Expertise on Porous Media (GEMP) at the Institut de Mécanique des Fluides de Toulouse (IMFT), in collaboration with CNES (French national center for space studies) and Airbus Defence and Space (ex Astrium since 2013), is involved in several research works in the aim to understand thermal and fluidic mechanisms which occur in the porous material of the evaporator. The main works are thesis of Christophe Figus (1996) [2], Typhaine Coquard (2006) [1] and Clément Louriou (2010) [3].

Christophe Figus (1996) [2] was the first to propose a pore network model to study heat and mass transfer with phase change in a 2D unit cell of a capillary evaporator under steady-state condition. This model was improved by Typhaine Coquard (2006) [1] and validated by a 2D experiment. An extensive parametric study has permitted to propose the use of a bilayer wick to enhance evaporator performance. Clément Louriou (2010) [3] studied experimentally and numerically the transient behaviour of the phase change in a 2D capillary evaporator unit cell.

Scope of the thesis

The present work follows on from the previous works conducted at IMFT for improving the understanding of physical mechanisms involved within capillary evaporators. The extensive investigations from the literature highlight the complexity of capillary two-phase loops and more especially of capillary evaporators. Indeed, several mechanisms are still not well understood. Moreover, the understanding of the liquid-vapour phase distribution within the wick is still a challenge and remains an issue to be addressed. The objective of the present thesis is to develop numerical models able to study the heat and mass transfers with phase change within the capillary evaporator, as well as to predict and analyse the liquid-vapour phase distribution within the capillary wick of the evaporators.

Outline of the thesis

Chapter I gives, in a first part, a general presentation of the two capillary two-phase loops: loop heat pipe (LHP) and capillary pumped loop (CPL), as well as their operating conditions. In a second part, a focus is made on capillary evaporators. Each component constituting capillary evaporators is discussed in detail.

Chapter II is an extensive literature review on analytical and numerical works. Two kinds of works are discussed: the ones which study the whole loop and the ones which study only the evaporator. For both works, transient and steady-state models are discussed.

Chapter III firstly presents a mixed pore network model to study, under steady-state operating condition, the heat and mass transfer in a three-dimensional evaporator unit cell. Then, a comparison between experimental results available in literature and numerical results using our model is performed. Finally, a detailed description of the liquid-vapour phase distribution within the wick and its impact on the evaporator thermal performance is conducted.

Chapter IV is a numerical sensitivity study. Firstly, the impact of grooves location on evaporator thermal performances is investigated. Three different geometries are studied. In a second part, a parametric study is proposed. Various wick materials, casing materials, throat mean diameters and porosities are tested and compared.

Chapter V is dedicated to the study of a bidispersed capillary structure and its influence on the liquid-vapour phase distribution and evaporator thermal performances. Numerical results from the mixed pore network model are compared to experimental results found in literature. Finally, two different grooves location are tested.

Chapter VI presents, in a first part, a continuum model based on macroscopic equations and the concept of saturation. In a second part, results obtained from this model are confronted to results obtained with the mixed pore network model. Finally, the influence of the phase change model used in the continuum approach on the saturation field is discussed.

Chapter I Context

Chapter I Context 5
I.1 Capillary two-phase loops 6
I.2 Capillary evaporator of LHP 17

This chapter is dedicated to a presentation of capillary two-phase loop systems used in the thermal control of electronic devices. Two technologies, almost equivalent, are described: the loop heat pipe (LHP) and the capillary pumped loop (CPL). These loop systems are both composed by: an evaporator, a liquid line, a condenser, a vapour line and a compensation chamber. The evaporator is the key element of the system since this is the place of the vaporisation process. A detailed description of the evaporator is presented.

Readers can refer to the following reviews published since 1999 about operating characteristics, working mechanisms, the analytical and numerical existing models as well as the experimental studies concerning closed two-phase loops (essentially the LHP).

- Ku (1999) [4] presented an extensive analysis of LHP operating characteristics.
- Maydanik (2005) [5] published a review on loop heat pipes with various designs and applications.
- Launay et al. (2007) [6] proposed a literature review based on a parametric analysis of loop heat pipe.
- Launay et al. (2011) [7] presented a review on the state-of-art on experimental studies on loop heat pipes from articles published between 1998 and 2010.
- Ambirajan et al. (2012) [8] proposed a review on loop heat pipes and discussed of the choice of the working fluid using the merit number technic.
- Maydanik et al. (2014) [9] published a review about loop heat pipes with flat evaporators.
- Siedel et al. (2015) [10] proposed a review on steady-state modelling of loop heat pipes published between 1999 and 2014.

I.1 Capillary two-phase loops

I.1.1 Components constituting LHP/CPL and fluid motion in the loop

Capillary two-phase loops, represented in Figure I.1, are composed by an evaporator, a compensation chamber (also called reservoir) and a condenser connected to each other by two transport lines (a liquid and a vapour line). The evaporator component will be discussed in more details in section I.2 as the present work focuses on it. The next paragraphs explain the fluid motion inside each component of the loop following the numeration written in Figure I.1.

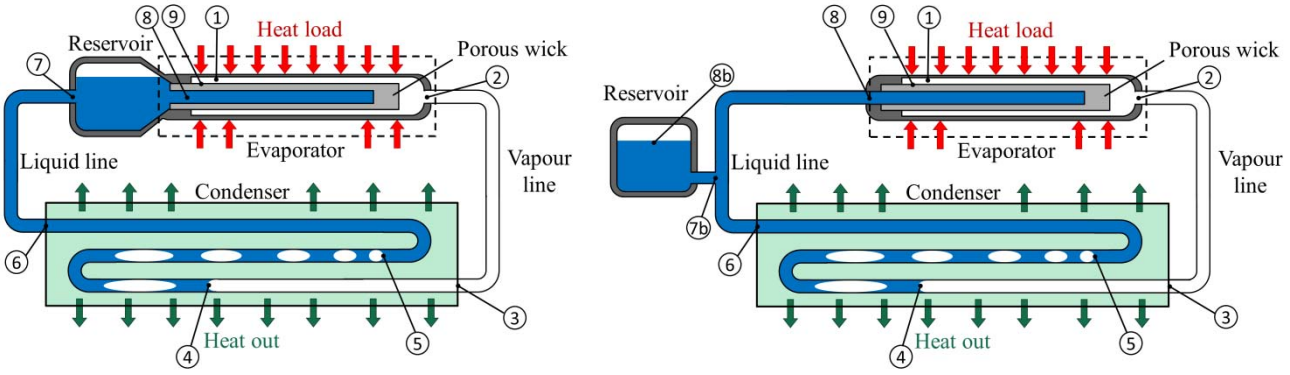

(a) (b)

Figure I.1 – Schematic of (a) a traditional LHP (b) and a traditional CPL.

Electronic devices are positioned near the external surface of the evaporator. The heat flux that needs to be evacuated is transferred by conduction up to the porous wick (located inside the evaporator) through the metallic wall of the evaporator. This induces the vaporisation of the fluid and the formation of

menisci at the surface and/or within the porous wick (point 9). The vapour is evacuated thanks to vapour grooves (points 1 to 2) and is transported in the vapour line (points 2 to 3) up to the condenser where the vapour condenses into liquid and releases the heat absorbed during the vaporisation process (points 3 to 6). At the end of the condenser (point 6), the fluid is in liquid state and reaches the liquid line (LHP: points 6 to 7, CPL: points 6 to 8). The compensation chamber (LHP: points 7 to 8, CPL: points 7b to 8b) ensures the adequate operating condition of the working fluid.

CPL and LHP use capillary forces to move fluid and use the latent heat vaporisation of the working fluid to evacuate the heat. These hydraulic and thermal properties permit them to regulate themselves to the heat load which needs to be evacuated, making them passive auto-regulated systems.

The major distinction between the technologies of these two systems comes from the position and the link between the compensation chamber and the evaporator as shown in Figure I.1. The reservoir is embedded in the evaporator for LHP while it is an independent unit, outside the path of fluid circulation, in the CPL. As a consequence, the primary operational difference is that the CPL suffers from transient start-up problems whereas the LHP starts in a simple and robust manner. That is why, for few years, LHP seems to be the best candidate for the thermal regulation of electronic devices. The reservoir ensures the good operating condition imposing the saturation pressure and saturation temperature at the working fluid. Moreover, it prevents defusing and microleaks of the loop.

I.1.2 Thermodynamic cycle

The thermodynamic cycle of an LHP and a CPL in steady-state operation with no gravity controlled is represented in Figure I.2 in the Pressure-Temperature diagram.

The blue solid lines represent the thermodynamic transformations for the CPL and the LHP when thermodynamic transformations are similar (i.e. for the evaporator, the vapour line, the condenser and the porous structure). As explained in section I.1.1, the main difference between CPL and LHP comes from the location of the reservoir. In consequence, the thermodynamic transformations are different for the two technologies and are represented in green lines in Figure I.2. The green solid lines represent the transformations for the LHP while the green dotted lines are for the CPL. The pink dotted lines denote alternative thermodynamic transformations (depending operating conditions or assumed hypothesis). The numbers in the diagram of Figure I.2 correspond to the physical locations shown in Figure I.1 and are used to describe the thermodynamic steady-state of the fluid inside the loop.

First of all, the particularity of the P-T diagram, presented in Figure I.2 for a given working fluid, is the presence of two liquid-vapour equilibrium curves. Assuming that the vaporisation process occurs only at the wick/groove interface, menisci appear along this boundary, implying a shifting of the saturation curve as shown in Figure I.2. In other words, the meniscus curvature ($r = r_m$) modifies the equilibrium condition compared to a flat interface ($r \to \infty$). For a given pressure, the vaporisation process needs a higher overheating of the liquid than for a flat interface.

Secondly, when the liquid state is qualified as “subcooled”, this refers to the temperature of the fluid compared to the saturation temperature. If the liquid temperature is lower than the saturation temperature, the liquid is considered as “subcooled”. This comment is valid for the entire present manuscript.

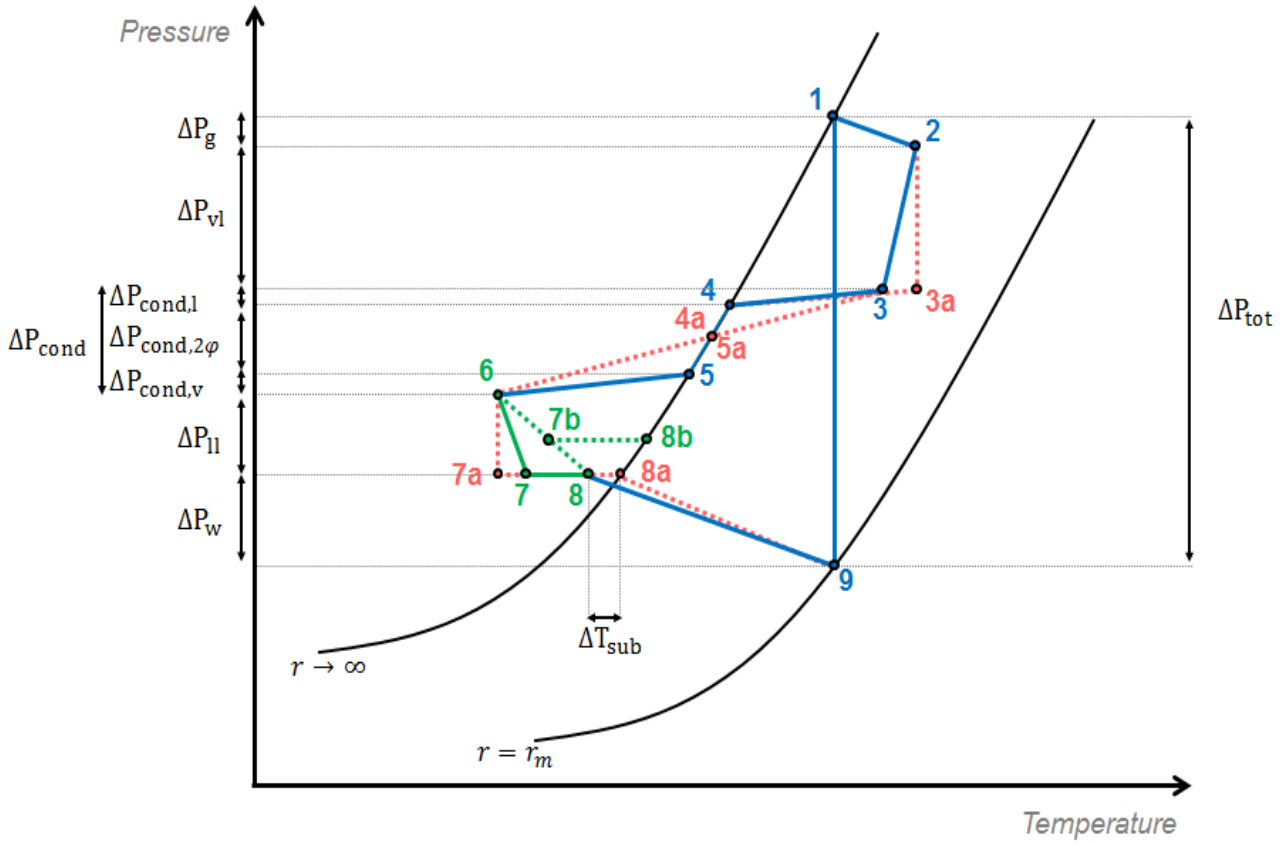

Figure I.2 – Thermodynamic cycle of an LHP/CPL.

Vapour Grooves

1 → 2 : *Blue solid line (LHP/CPL)*

The transformation is characterized by a pressure loss ΔP_g and the superheating of the fluid, which is in the vapour state, along grooves.

Vapour line

2 → 3 : *Blue solid line (LHP/CPL)*

Assuming that the vapour line is not insulated and the ambient temperature is lower than the vapour temperature, the fluid is slightly cooled down by thermal exchange with the ambient. The pressure loss ΔP_{vl} is due to the friction between the walls and the fluid. Note that some studies (Siedel (2014) [11]) show that condensation can also occur in the vapour line.

2 → 3a : *Pink dotted line (Alternative transformation)*

Assuming that the vapour line is thermally insulated from the ambient and can be considered as adiabatic, the pressure decreases at a constant temperature along the component.

Condenser

3 → 6

Two different representations of the transformation inside the condenser can be imagined. The first one assumes that the phase change occurs at a constant pressure and temperature (pink dotted line) while the second, more realistic, considers the pressure drop on the two-phase zone (blue solid line). The total pressure loss in the condenser is noted ΔP_{cond}.

3 → 4 : *Blue solid line (LHP/CPL) or* 3 → 4a : *Pink dotted line (Alternative transformation*)

The vapour is cooled down through the first part of the condenser until it reaches the saturation temperature.

4 → 5 : *Blue solid line (LHP/CPL)*

The vapour condenses along the second part of the condenser. As the phase change occurs at saturation temperature and that the pressure loss is considered, the temperature therefore decreases during the phase-change.

4a → 5a : *Pink dotted line (Alternative transformation)*

Assuming a phase-change at constant pressure and temperature, points 4a and 5a overlap each other.

5 → 6 : *Blue solid line (LHP/CPL) or* 5a → 6 : *Pink dotted line (Alternative transformation)*

The fluid is in liquid state in the last part of the condenser and is subcooled.

Liquid line and compensation chamber

6 → 8

6 → 7 : *Green solid line (LHP)*

Considering a non-insulated liquid line and a higher ambient than the liquid temperature, adding the pressure loss, the temperature of the liquid increases faintly by thermal exchange with the ambient. Like for the vapour line, the pressure drop along the liquid line ΔP_{ll} is due to the friction between the walls and the fluid.

6 → 7a : *Pink dotted line (Alternative transformation)*

Assuming that the liquid line is thermally insulated, the pressure decreases at a constant temperature along the component.

6 → 7b : *Green dotted line (CPL) or 7b → 8 : Green dotted line (CPL)*

The transformation is presented here for a non-insulated liquid line.

7 → 8 : *Green solid line (LHP)*

The liquid does not reach the equilibrium state and remains subcooled compared to the saturation temperature. The mixing between the subcooled liquid arriving from the liquid line and the liquid present within the compensation chamber results in a slightly subcooled liquid at the entrance of the evaporator. This subcooled quantity is noted ΔT_{sub} in Figure I.2. However, the compensation chamber is at the liquid-vapour

equilibrium state as there is no exchange of fluid between the compensation chamber and the evaporator core during the steady-state. Thus, the pressure is at the saturation pressure. Another interest of the subcooling is to prevent the formation of bubbles within the compensation chamber. If vapour occurs at the inlet of the evaporator, vapour bubbles could accumulate and block the path for the liquid at the inlet of the porous wick, resulting in a deprime of the evaporator.

7 → 8a : *Pink dotted line (Alternative transformation)*

The liquid is sufficiently superheated through the liquid line and reaches the saturation temperature. This second representation is less realistic and may dramatically induce the formation of vapour bubbles at the evaporator inlet as explained above.

7b → 8b : *Green dotted line (CPL)*

As already explained, the reservoir in a CPL is outside the liquid path. The point 7b corresponds to the pressure-temperature state at the entrance of the reservoir. An equilibrium condition is established in the condenser and the fluid reaches the pressure-temperature saturation state at point 8b.

Porous material

8 → 9 : *Blue solid line (LHP/CPL)*

The fluid flows through the porous material, generating a pressure drop ΔP_w and an increase in the temperature due to the heat load applied at the external surface of the evaporator. Assuming that the liquid-vapour interface is located only at the wick/groove boundary (point 9), along this interface the liquid is at the saturation temperature. The equilibrium curve is shifted due to the presence of menisci as already explained above.

Total pressure loss

The total pressure drop ΔP_{tot} corresponds to the capillary pressure at the liquid-vapour interface $\Delta P_{tot} = P_1 - P_9$. This pressure drop must compensate for the total pressure loss in the remainder of the loop.

To summarise, the relation between the pressure losses along the loop can be written using the following relation:

$$\Delta P_{tot} = \Delta P_g + \Delta P_{vl} + \Delta P_{cond} + \Delta P_{ll} + \Delta P_w \quad \textbf{(I-1)}$$

I.1.3 Operating conditions

I.1.3.1 LHP start-up scenarios

Ku (1999) [4] discussed the four major start-up scenarii (Figure I.3) of a loop heat pipe. Each condition has its unique start-up characteristics, but for more details on start-up scenario, the readers can refer to Ku (1999) [4]. Only the description of the four situations is reported here.

In the situation 1, vapour exists in the vapour grooves and liquid completely fills the evaporator core. In the situation 2, vapour exists in the vapour grooves and in the evaporator core. In the situation 3, liquid completely fills the vapour grooves and the evaporator core. In the situation 4, liquid fills the vapour grooves and the evaporator core is vapour (two-phase). The last situation 4 presents the most difficult condition for LHP start-up.

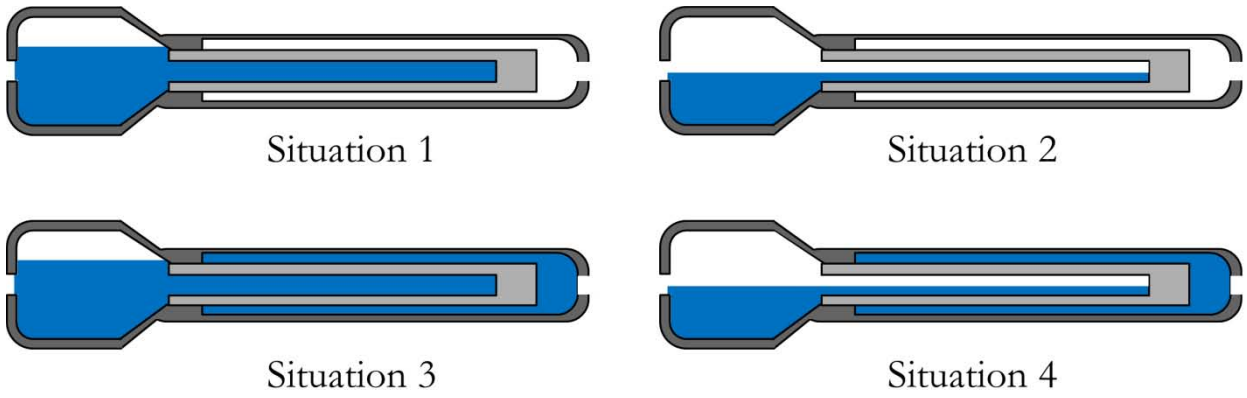

Figure I.3 – Different start-up conditions in the evaporator, adapted from Ku (1999) [4].

I.1.3.2 LHP operating curve

The operating temperature is usually defined as the evaporator temperature corresponding to the maximal temperature of this component. The maximum temperature is located at the external surface of the metallic envelope. The typical operating curve (evaporator temperature versus heat load) of a LHP can be U-shaped or flat-shaped (Figure I.4). In steady-state condition, the loop heat pipe can operate in two modes called and defined as follows:

- **The variable conductance mode (VCM)**
  For low heat load, the condenser and the compensation chamber work under two-phase condition. As the heat load increases, the mass flow rate of the subcooled liquid increases at the inlet of the compensation chamber, resulting in a reduction of the evaporator temperature. Under the VCM, the length of the two-phase zone in the condenser increases with increasing heat loads (red dashed curve in Figure I.5). The evaporator temperature decreases when the heat load increases until reaching a minimal value.

- **The fixed conductance mode (FCM)**
  For higher heat load, the two-phase zone reaches the exit of the condenser (red dashed curve in Figure I.5) and the temperature rises linearly with the heat load (blue solid curve in Figure I.5).

Added to the flat-shaped or U-shaped, a linear behaviour of the operating curve can also be observed when the compensation chamber is already full of liquid, thereby not allowing the condensation length in the condenser to increase. This could be the scenario if the LHP slop is negative (evaporator below the condenser) as Chernysheva et al. (2007) [12] explained.

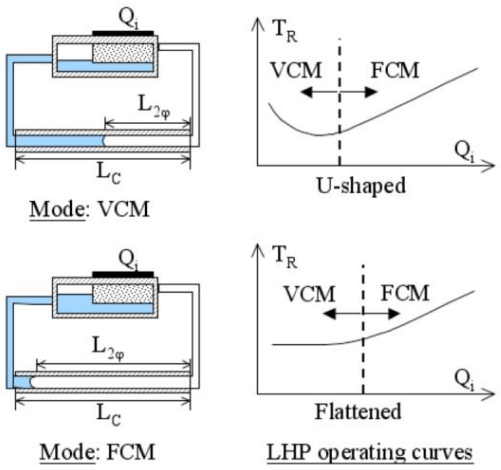

Figure I.4 – Typical LHP operating curves from Launay et al. (2008) [13].

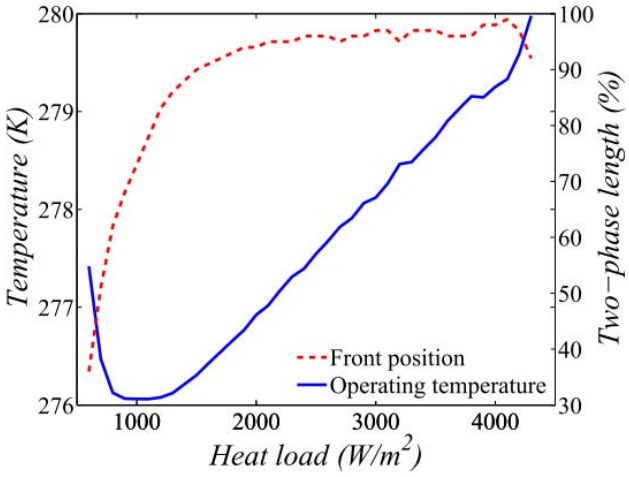

Figure I.5 – Operating temperature (blue solid curve) and length of the two-phase zone into the condenser (red dashed line) versus the applied heat load (Louriou (2010) [3]).

I.1.3.3 CPL operating curve

Similarly that for the LHPs, the CPLs operate under two conductance modes: the variable conductance mode and the fixed conductance mode. However, under the variable conductance mode, the operating curve is flattened, meaning that there is no variation of temperature. As the compensation chamber has no hydraulic link with the evaporator, the liquid-vapour interface within the reservoir fixes the operating condition inside the loop. As the heat load increases, the length of the two-phase zone adapts itself in the condenser. Beyond a given heat load, the CPL operates under fixed conductance mode, meaning that the length of the two-phase zone within the condenser is fixed. In this case, the saturation condition in

the reservoir adapts itself to the applied heat load. Finally, the overall typical operating curve of the CPL is the same as the flat-shaped curve for the LHP (Figure I.4).

I.1.3.4 Orientation of the device

For terrestrial application, the orientation of the loop in the gravity field plays a significant role. In 2007, three mains orientation, i.e. LHP slope defined by Θ, had been distinguished by Chernysheva et al. [12] and the conventions are details below:

- $\Theta = +90°$: vertical orientation with the evaporator located above the condenser
- $\Theta = 0°$: horizontal orientation, the condenser and the evaporator are as the same level
- $\Theta = -90°$: vertical orientation with the evaporator located below the condenser

The same year, in their review, Launay et al. (2007) [6], based on the work of Chuang (2003) [14], defined two parameters to characterize the influence of gravity on the performance of LHP:

- The elevation refers to the relative position of the evaporator compared to the condenser:
  - The positive elevation refers to the situation where the evaporator is below the condenser;
  - The adverse elevation refers to the situation where the evaporator is above the condenser.
- The tilt refers to the relative position of the evaporator compared to the compensation chamber:
  - The positive tilt refers to the situation where the evaporator is below the compensation chamber;
  - The adverse tilt refers to the situation where the evaporator is above the compensation chamber.

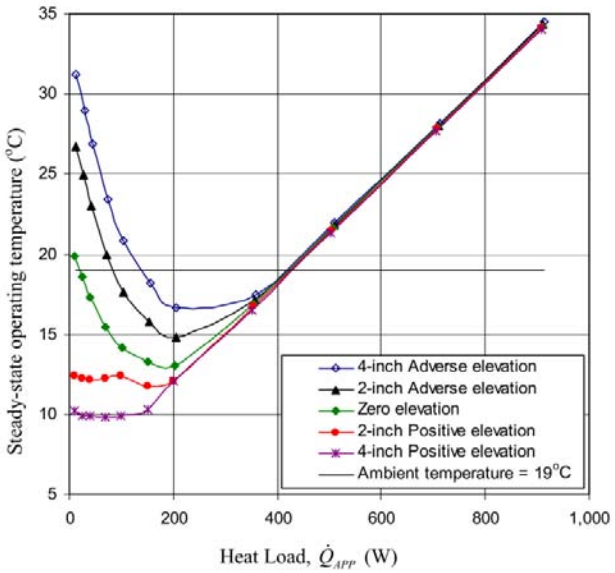

Figure I.6 – Effect of elevation on the trend of steady-state operating curve (Chuang (2003) [14]).

Let's note that the elevation parameter defined by Launay et al. (2007) [6] and used by some authors ([6], [14]) is the totally opposite convention than that defined by Chernysheva et al. (2007) [12].

Chuang et al. (PhD thesis (2003) [14] and published article (2014) [15]) analysed the LHP elevation effects on steady-state performance. The authors highlight that the elevation has a great impact on the LHP operation curve at low heat flux as shown in Figure I.6.

I.1.4 Thermal performance indicators of a capillary two-phase loop

The total thermal loop resistance R_{LHP} (or R_{CPL}) (equation (I-2)) represents the thermal performance of the overall loop (Maydanik et al. (2005) [16]).

$$R_{LHP/CPL} = \frac{T_{ev} - T_{cond}}{Q} \quad \textbf{(I-2)}$$

where T_{ev} is the evaporator maximal temperature (located on the external surface of the casing under normal operating conditions), T_{cond} is the condenser temperature, Q is the flux applied to the evaporator envelope. Therefore, the lower the total thermal resistance, the better the thermal performance of the capillary two-phase loop.

I.1.5 Operating limits

During the steady-state or transient operation, a capillary two-phase loop system could encounter several heat transport limitations (Faghri (1995) [17], Launay et al. (2007) [6]) related to the geometry, the working fluid, the wick structure or the operating temperature. These limitations could induce a loop deprime (a failure of the system operation) or a damage of material. Only the main limitations are listed below:

- Capillary limit
- Boiling limit (linked to the superheated liquid limit)
- Overheat limit
- Sonic limit
- Entrainment limit
- Viscous limit
- Condenser limit

Only the first three ones will be discussed in details as they are the most commonly encountered. For more details on the others, the reader can refer to Faghri (1995) [17], Hamdan (2003) [18] and Launay et al. (2007) [6].

I.1.5.1 Capillary limit

The ability of a capillary structure to provide the circulation for a given working fluid is limited and is called the capillary limitation. In other words, the porous material within the evaporator must have a sufficient capillary pumping. As explain in section I.1.2, the capillary pressure must compensate for the

total pressure loss in a capillary two-phase loop for ensuring the good operation of it. This pressure balance is due to the automatic adjustment of the menisci curvatures along the liquid-vapour interface. The capillary pressure ΔP_{cap} is defined by the Young-Laplace equation (equation (I-3)):

$$\Delta P_{cap} = \frac{2\sigma}{r_m} \quad \textbf{(I-3)}$$

where r_m is the meniscus curvature and σ is the surface tension. Equation (I-3) shows how the pressure difference across a liquid-vapour interface is related to the curvature of the interface. Thereby, the maximum heat transfer that a CPL/LHP can expect depends on the maximum admissible value of the capillary pressure. For a given working fluid and a given porous structure, assuming a cylindrical pore shape and a constant surface tension, the minimum meniscus curvature can be expressed as a function of the pore radius r_p and the cosine of contact angle θ as $r_m = r_p/cos\theta$. As a result, the maximum capillary pressure $\Delta P_{cap,max}$ is directly dependent of the pore size and can be expressed by equation (I-4):

$$\Delta P_{cap,max} = \frac{2\sigma}{r_p} cos\theta \quad \textbf{(I-4)}$$

The maximum capillary pressure $\Delta P_{cap,max}$ must be greater than the total pressure loss inside the loop (neglected statistic pressure drop due to gravity) (equation (I-5)) to avoid the vapour-liquid interface rupture.

$$\Delta P_{cap,max} \geq \Delta P_{tot} = \Delta P_{vl} + \Delta P_{cond} + \Delta P_{ll} + \Delta P_{w} \quad \textbf{(I-5)}$$

All terms in equation (I-5) have been defined in section I.1.2. If ΔP_{tot} exceeds the maximum capillary pressure value, the pressure jump at the interface will cause the liquid-vapour interface to recede and force it to leave the porous structure, resulting in a deprime of the loop. Equation (I-5) highlights an important comment concerning the porous structure properties. Indeed, a great control and knowledge of the pore size distribution within the wick is essential, given that the capillary limit is highly dependent on the pore radius.

I.1.5.2 Boiling limit and superheated liquid

The boiling limit and the superheated liquid are directly correlated (Hamdan (2003) [18]). The boiling limit is directly related to bubble formation in the fluid inside the porous structure. In order for a bubble to exist and grow, a certain liquid superheat is required. Moreover, the size of bubbles has to be greater than a critical value, otherwise the bubbles may be trapped inside the porous structure and thus block the liquid return. The result can be a dryout of the evaporator and a deprime of the loop.

Two nucleation processes are generally distinguished:

- **Homogenous nucleation** refers to the formation of vapour bubbles within the liquid without any pre-existing vapour nuclei and not on any solid surfaces in proximity.
- **Heterogeneous nucleation** refers to the formation of vapour bubbles within the liquid on a heated surface.

As explained in section I.1.1, electronic devices are close to the metallic casing. By conduction, the heat flux applied is transferred to the porous structure. Assuming that the wick is fully saturated with liquid, above a certain heat flux, nucleation will occur in the wick at the wick/casing interface. Thus, heterogeneous nucleation is more expected to occur than homogenous nucleation in the two-phase loop wick.

However, based on the Kwak and Panton theory (1985) [19], Mishkinis and Ochterbeck (2003) [20] and later Kaya and Goldak (2007) [21] studied the homogeneous nucleation within the capillary structure of an evaporator to determine the superheat of liquid ΔT_{nucl} (equation (I-6)) from which vapour could appear under the fin. These studies assume that the nucleation is initiated by vapour embryo trapped in the microcavities at the fin–wick interface. They found very high theoretical values of the order of 50K to 90K for the liquid superheat. These theoretical values are valid for a two-phase loop with a high purity working fluid and good contact at the wick–casing interface.

$$\Delta T_{nucl} = \frac{2\sigma T_{sat}}{\rho_v h_{lv}} \left(\frac{1}{r_n} - \frac{1}{r_p} \right) \quad \textbf{(I-6)}$$

where T_{sat} is the saturation temperature, ρ_v is the vapour density, h_{lv} is the latent heat of vaporisation, r_n is the nucleation radius of the vapour bubble and r_p is the pore radius.

In reality, the boiling can initiate at small superheat values (of the order of the Kelvin) and this value depends on several parameters. Therefore, it is difficult to predict the superheat value. In practice, it will be reduced to the choice of a certain level of overheating (a difference of some kelvins compared to the saturation temperature) from which it is assumed that there is occurrence and development of the vapour in the porous medium [21].

Following all these comments, it is clear that this problematic remains an issue to be addressed.

I.1.5.3 Overheat limit

For thermal regulation, capillary two-phase loops are more often limited by the maximum temperature that electronic devices and equipment can reach without damage. This maximal admissible temperature is called overheat limitation. Indeed, electronic devices are located near the evaporator envelope and they can be affected by the temperature reached by it. Moreover, the evaporator body is often thin and a too high temperature can induce its deformation. The common maximum value that the evaporator envelope can reach is often around 100°C ($T_{max,c}$). In practice, this is often the first limitation reached by capillary two-phase loops, even if the system is able to evacuate a higher heat load.

I.1.6 Working fluid selection

The selection of the working fluid is often based on the figure of merit number (Figure I.7). The merit number combines several thermal and hydraulic properties of the working fluid such as the liquid density, the vapour density, the latent heat of vaporisation, the vapour viscosity, the liquid viscosity, the surface tension, the liquid thermal conductivity or the liquid specific heat. The expression of the merit number depends on the conductance mode of the two-phase loop. The thermal performances of the fluid are regarded as best for high merit number. Based on Figure I.7 and knowing the range of desired

operating temperature, the user can easily choose the most appropriate working fluid. The ammonia is the best known working fluid in the range of 0°C-100°C, explaining the common choice of this fluid [7]. The others common working fluids are the propylene, the ethanol, the water, the methanol and the acetone [7]. The users may also pay attention to the chemical compatibility of the fluid with the wick and others loop component materials and read the paper of Mishkinis et al. (2010) [22] for more details.

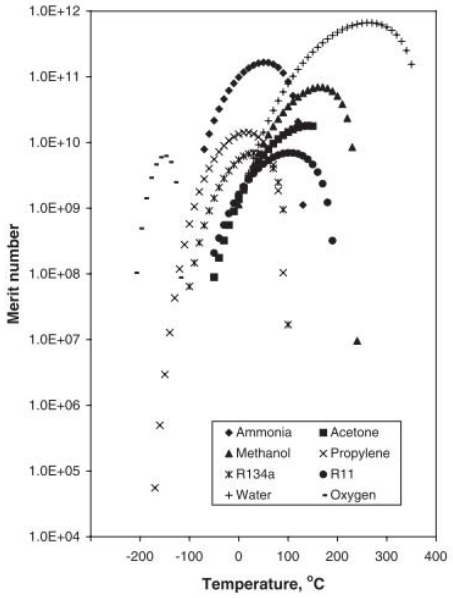

Figure I.7 – Figure of merit number for various working fluid, from Adoni et al. (2012) [23].

I.2 Capillary evaporator of LHP

The major component of a capillary two-phase loop is the evaporator since the vaporisation appears therein. The evaporator is often called "capillary evaporator" due to the presence of the porous material within it. Two roles are expected from it:

- Evacuation of the heat;
- Fulfilling of the pump role.

As explained in section I.1.1, CPLs suffer from a start-up problem due to the location of the compensation chamber. This impacts the operation of the capillary loops and the thermodynamic cycle, especially in the evaporator/reservoir zone, as described in section I.1.2. Moreover, for several decades, it seems that space industry is more interested by LHP technologies, resulting in a larger number of scientific publications studying LHPs instead of CPLs. The context of the present work by the way focusses on LHP system and this explains why only an LHP capillary evaporator description will be discussed below.

I.2.1 Thermal performance indicators of a capillary evaporator

The thermal evaporator resistance R_{ev} (equation (I-7)) and the evaporator heat transfer coefficient h_{ev}, also called the evaporator conductance, (equation (I-8)) both represent thermal performance of an

evaporator (Maydanik et al. (2005) [16]). R_{ev} is inversely proportional to h_{ev} (equation (I-9)). Almost each study, either experimental or numerical, investigates at least one of these two parameters.

$$R_{ev} = \frac{T_{ev} - T_g}{Q} \quad \textbf{(I-7)}$$

$$h_{ev} = \frac{q}{T_{ev} - T_g} \quad \textbf{(I-8)}$$

$$R_{ev} = \frac{1}{h_{ev} S_c} \quad \textbf{(I-9)}$$

where T_{ev} is the evaporator maximal temperature (located on the external surface of the casing under normal operating conditions), T_g is the vapour groove temperature, Q, respectively q, is the flux, respectively the heat density, applied to the envelope and S_c the area of the input surface.

Note that some authors choose to talk in terms of thermal contact conductance $h_{contact}$ (Choi et al. (2013) [24] and Adoni et al. (2012) [23]) as defined in equation (I-10):

$$h_{contact} = \frac{Q}{(T_{ev} - T_g) S_{fin/wick}} \quad \textbf{(I-10)}$$

where $S_{fin/wick}$ is the area contact between the casing and the wick. Assuming that the heat input is applied uniformly along a defined casing length and that the fin has the same length, one can define a value $\gamma = L_{fin}/L_{casing}$ as the ratio between the width of the fin and the width of the casing. Therefore, note that $h_{ev} = h_{contact}\gamma$. Adoni et al. (2012) [23]proposed a new formula (equation (I-11)), reused by Fang et al. (2014) [25], to determine the thermal contact conductance.

$$h_{contact} = \frac{1}{\frac{T_{ev} - T_g}{q} - \frac{A_t}{C_{evap}}} \quad \textbf{(I-11)}$$

where $A_t = S_{fin/wick}$ is the area contact between the casing and the wick and C_{evap} is the thermal conductance from the surface of the evaporator to the interface with the wick. C_{evap} is calculated using an independent code and is then used as a constant.

Therefore, the lower the thermal evaporator resistance, hence the higher the evaporator heat transfer coefficient, the better the thermal evaporator performance.

I.2.2 Classification of capillary evaporators

Three main evaporator/reservoir shapes exist (Figure I.8) and have been reported in literature (Maydanik (2005) [5], Launay and Vallée (2011) [7] and Maydanik et al. (2014) [9]):

- Cylindrical evaporator (CE) (Figure I.8a)
- Flat evaporator ([9]) (FE)
    - With reservoir in the thickness, i.e. with opposite replenishment (OR) (Figure I.8b)
    - With reservoir in the length, i.e. with longitudinal replenishment (LR) (Figure I.8c).

Note that the evaporator of a CPL could also be cylindrical or flat.

The flat evaporator can have three different shapes (Figure I.9):

- The rectangular (or square) shape with OR or LR;
- The flat-oval shape with OR or LR;
- The disk-shaped with OR.

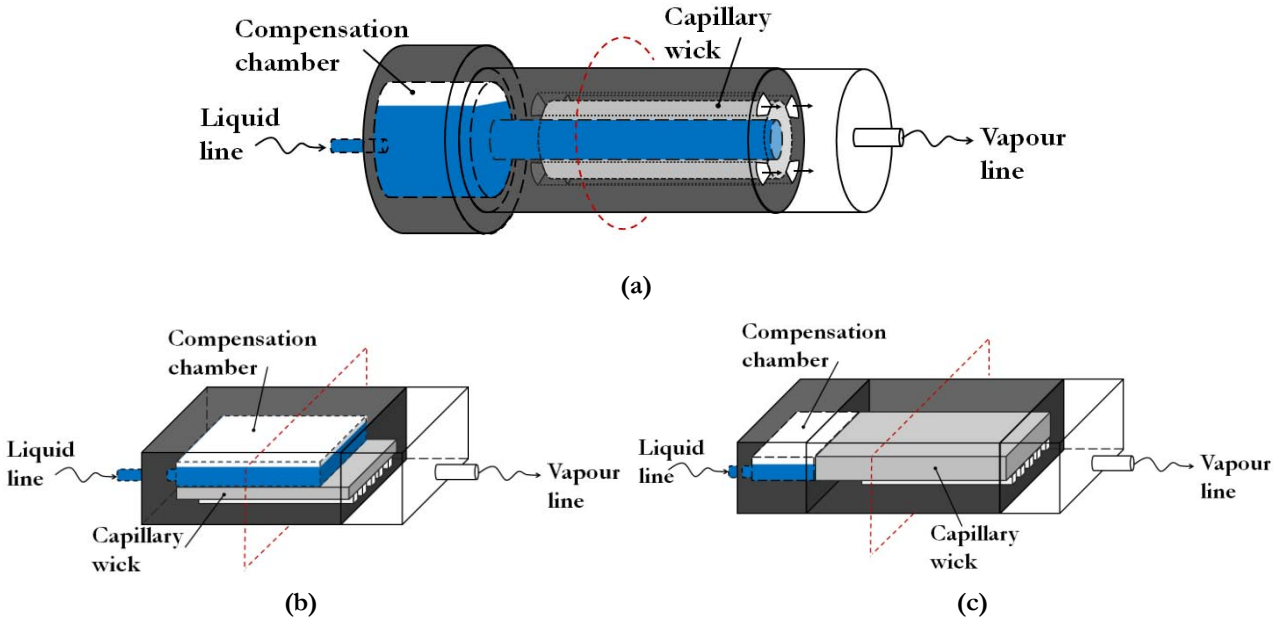

Figure I.8 – Main evaporator/reservoir shapes: (a) Cylindrical shape, (b) Flat shape with opposite replenishment, and (c) Flat shape with longitudinal replenishment. The compensation chamber is sketched under two-phase zone state.

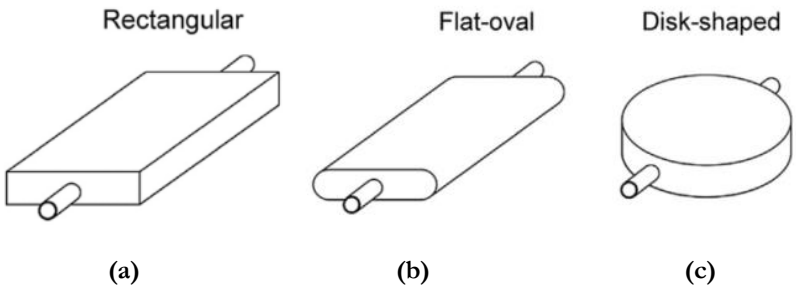

Figure I.9 – Main shapes of flat evaporators: (a) rectangular shape; (b) oval shape and (c) disk shape, from Maydanik et al. (2014) [9].

Cylindrical evaporator was the first to be developed. However, cylindrical evaporators generally require a special saddle to properly attach them to a flat surface (i.e. electronic devices). This saddle design creates an additional thermal resistance and increases the total mass of the LHP. In front of the challenge of miniaturization and the non-matched geometry described previously, the flat evaporators have naturally appeared. Indeed, their thicknesses can be much lower than those of cylindrical evaporators. For more details, a review on flat evaporator was published recently by Maydanik (2014) [9]. However, the

cylindrical shape has a better mechanical strength which is not negligible for the use of a fluid like ammonia.

The terminology in literature is not very clear. Some authors called the flat evaporator the "flat-plate type" evaporator and it seems that this term is mainly used to designate CPLs evaporator. However, no clues are given to know if they speak about rectangular or disk-shaped evaporator.

I.2.3 General description of a capillary evaporator

Both types of evaporator (cylindrical or flat) consist of:

- a porous structure called the wick;
- vapour-evacuation grooves (also called vapour removal channels);
- and a metallic casing (the envelope of the evaporator, also called in literature the wall).

The cylindrical evaporator, as well as the flat evaporator with OR are also constituted by a liquid core. A sectional view of each type of evaporator, defined by the red dashed line in Figure I.8, is sketched in Figure I.10 .

The heat flux that needs to be evacuated is applied at the external surface of the metallic casing. The heat is transferred by conduction up to the porous wick through a fin. This induces the evaporation of the liquid within the wick and/or at the wick/grooves interface. The menisci along the interface adjust themselves to balance the total pressure loss in the loop. The produced vapour is collected and evacuated thanks to vapour grooves towards the vapour line.

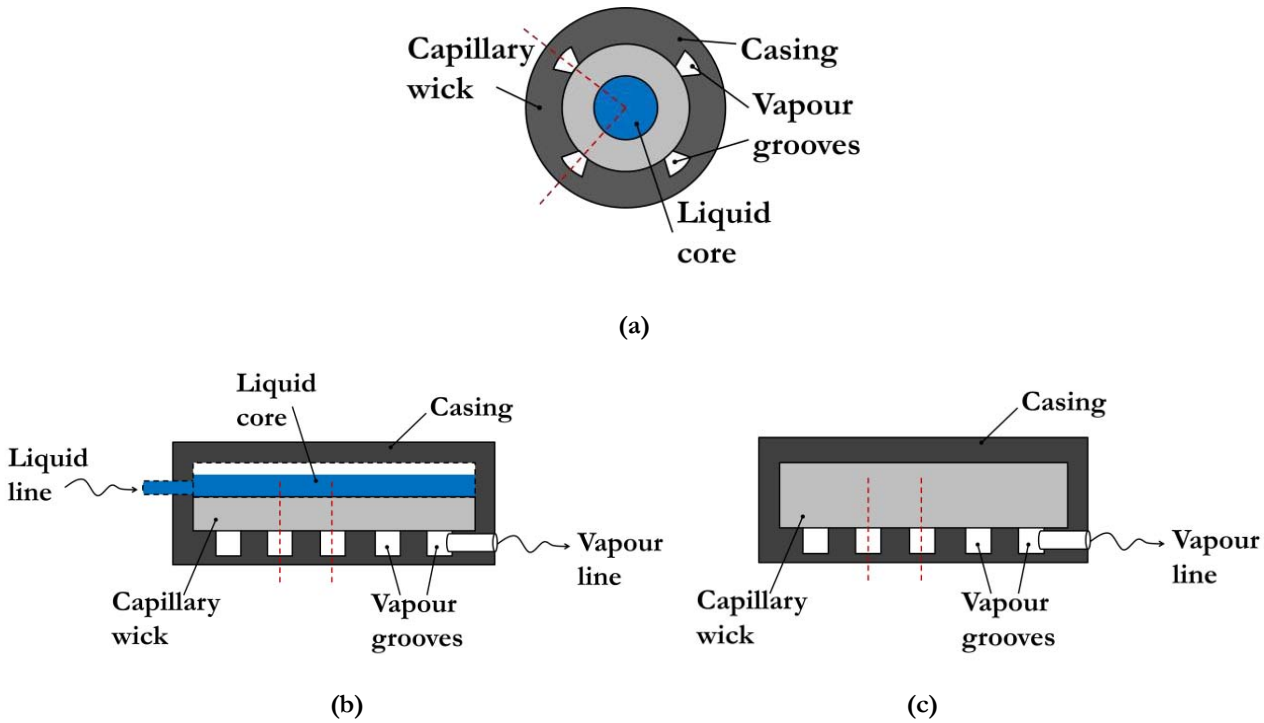

Figure I.10 – Sectional view of main evaporators: (a) Cylindrical shape, (b) Flat shape with opposite replenishment, and (c) Flat shape with longitudinal replenishment.

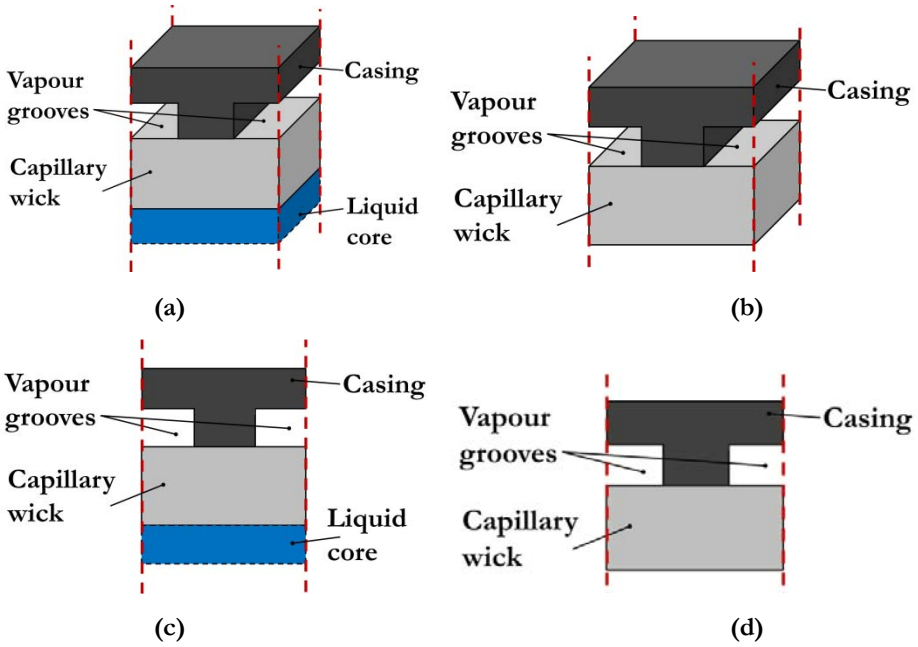

Figure I.11 – Shared unit cell of capillary evaporator: (a) Three-dimensional and (c) two-dimensional unit cell of a CE/FEOR; (b) Three-dimensional and (d) two-dimensional unit cell of a FELR.

Unwrapping the cylindrical evaporator leads to a structure close to a flat evaporator with reservoir in the thickness. Following this representation, it is possible to extract a shared unit cell which is therefore representative of both types of evaporator. The evaporator unit cells (Figure I.11) are defined by dashed line in Figure I.10 and are the unit cells generally studied by all authors in numerical/analytical evaporator works. Different geometries for the unit will be again discussed in section I.2.5.3. Note that the choice was made to centre the unit cell on the fin, but it is also possible to choose to centre it on the groove (Figure I.12). Finally, one can also consider a half unit cell, as it is symmetrical. The choice is made in this manuscript to use the whole unit cell for the reason detailed in section III.2.1.

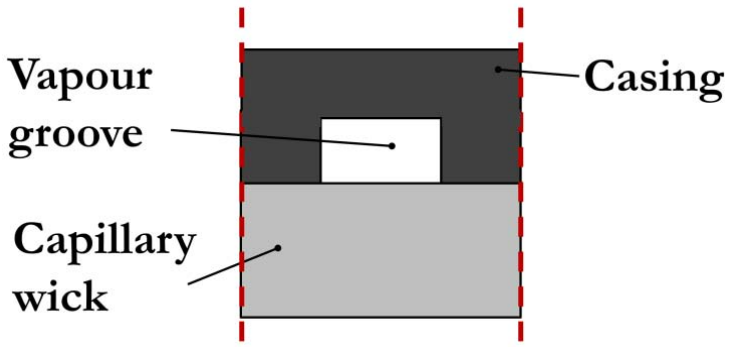

Figure I.12 – Two-dimensional unit cell of capillary evaporator centred on the groove.

I.2.4 Flux balance and parasitic heat flux

In steady-state operation, the whole heat flux Q (sometimes noted Q_{in} or Q_{load}) imposed at the bottom of the casing is not only used to vaporise the liquid inside the wick (named Q_{evap}). Indeed, a part of it is used to overheat the liquid, respectively the vapour, within the wick, and they are noted Q_l, respectively Q_v. Another part is lost by convection in the vapour removal channel and is noted Q_{conv}. The last part, noted Q_{cond} and also called the parasitic heat fluxes, is lost by conduction towards the compensation chamber. A scheme of the flux balance is represented in Figure I.13 for a FEOR. The amount of parasitic heat flux is composed of two parts (designation: CE/FEOR):

- **The radial/transverse leak**
  It refers to the heat conducted from the evaporator metallic wall to the compensation chamber through the porous structure.
- **The axial/longitudinal leak**
  It refers to the heat conducted from the evaporator metallic wall to the compensation chamber through the evaporator wall. It depends on the configuration and the type of connection between the compensation chamber and the evaporator. Therefore, the hydraulic link between the compensation chamber and the evaporator has a direct impact on the thermal performance.

The total balance can be expressed by equation (I-12):

$$Q = Q_v + Q_l + Q_{cond} + Q_{conv} + Q_{evap} \quad \textbf{(I-12)}$$

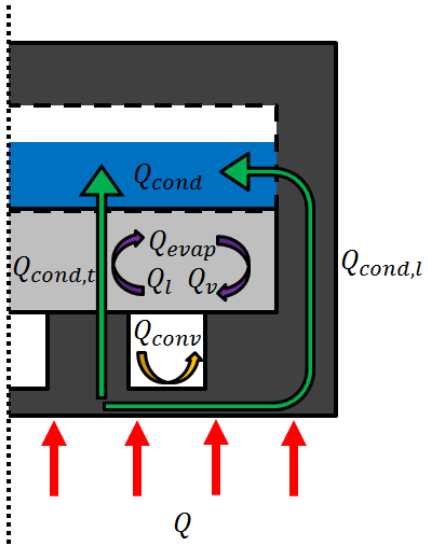

Figure I.13 – Heat flux balance in the evaporator. $Q_{cond,t}$, respectively $Q_{cond,l}$, refers to the transverse, respectively longitudinal, heat leak.

For example, the heat flux distribution extracted from Coquard (2006) [1] is reported in Figure I.14. Until around 95 000W/m2 , the main part of the total flux Q is used to vaporise the liquid. Evaporation heat flux Q_evap is between 80 and 90%. The flux used to overheat the liquid Q_l is almost negligible. The flux loss by convection inside grooves Q_conv and the flux used to overheat the vapour Q_v are less than 10% of the total heat flux. It is not very high but not negligible though. It is also important to note that the parasitic flux Q_cond (flux loss by conduction through the wick in [1]) is always between 5% and 15% and becomes higher than 20% for very high heat flux. The parasitic heat flux indirectly dictates the amount of heat flux used for the vaporisation. Indeed, when the parasitic heat flux is high, the evaporation heat flux becomes limited, inducing a decrease in the mass flow rate and an increase in the operating temperature. Therefore, it is important to decrease as much as possible this parasitic flux. For minimising the amount of parasitic heat flux, the principal advices are to use a low thermal conductivity for the wick and/or the metallic wall and to reduce the section between the reservoir and the evaporator [7].

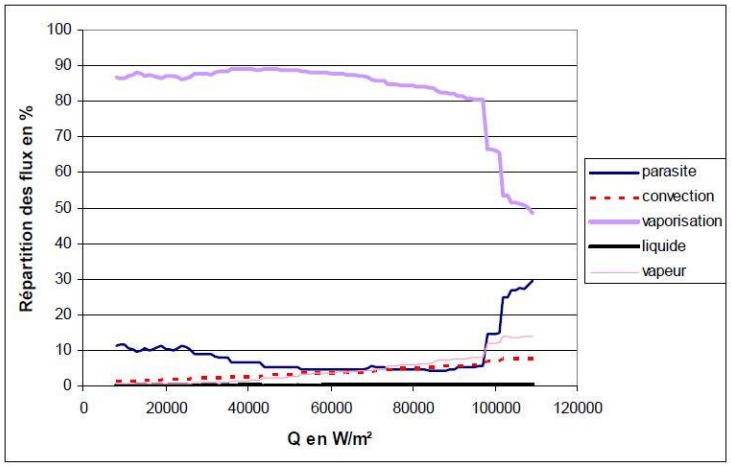

Figure I.14 – Heat flux distribution for an effective thermal conductivity equal to 8W/m/K and pore diameter between 4µm and 10µm, from Coquard (2006) [1]. *Parasite* curve is Q_{cond}; *convection* curve is Q_{conv}; *vaporisation* curve is Q_{evap}; *liquid* curve is Q_l and *vapeur* curve is Q_v.

I.2.5 Components constituting a capillary evaporator

I.2.5.1 Thermohydraulic link between the reservoir and the evaporator

To ensure the continuity of the liquid flow and an homogeneous replenishment of the capillary wick, experimental studies in literature reported two main techniques ([7], [8]): the use of a secondary wick and/or the use of a bayonet (Figure I.15).

The evaporator shape with a secondary capillary wick is sketched in Figure I.15a. This technique ensures that the primary wick is always fed with liquid and it provides a good thermal and hydraulic link between the compensation chamber and the primary wick. Classical secondary wick has a low thermal conductivity and a high permeability. The use of a secondary wick is mainly found in space application.

The bayonet is an extension of the liquid line to the evaporator core (Figure I.15b). The role of the bayonet is to route the liquid in the core of the evaporator. Wang and Ochterbeck (2006) [26] presented a numerical steady-state model to investigate two different cylindrical evaporator geometries, i.e. with

and without a bayonet. From this study, the presence of a bayonet affects the flow and heat transfer in the liquid core and helps to prevent vapour bubbles formation in the liquid core. The bayonet could also be coupled with a secondary wick (Figure I.15c).

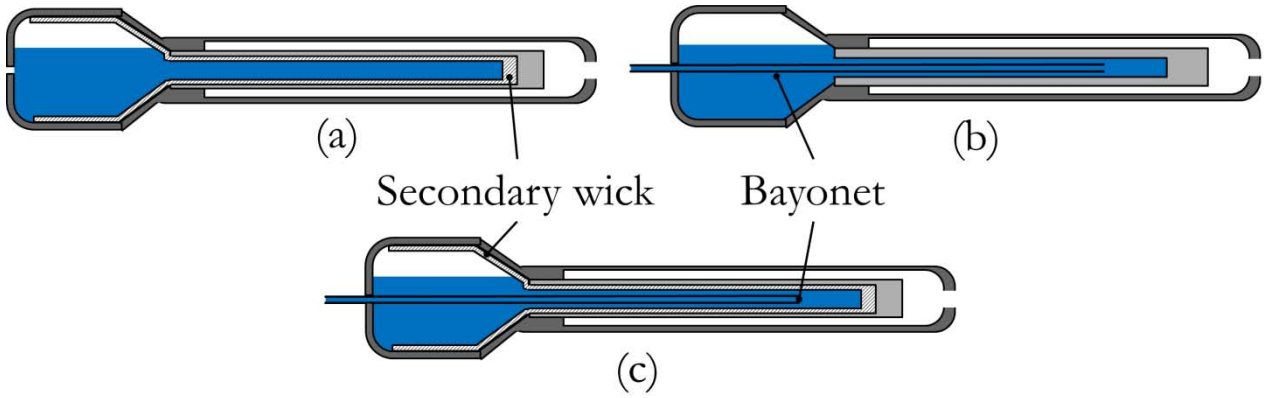

Figure I.15 – Different thermohydraulic links between the reservoir and the evaporator. (a) Secondary wick; (b) Bayonet and (c) Secondary wick and bayonet for a cylindrical evaporator.

I.2.5.2 Metallic casing

The metallic envelop of the evaporator have to have sufficiently high strength and high thermal conductivity. The experimental review of Launay et al. (2011) [7] and Table II-2 reveal that the common casing materials are stainless steel, copper and aluminium. Note that some rare works use nickel, silicon or carbon steel materials.

The ranges, found in literature, for the thermal conductivity k, the Young modulus E, the yield strength σ_y, the tensile strength σ_{ts} and the fracture toughness K_{Ic} are reported in Table I-1. The Young modulus E measures the force that is needed to stretch or compress a material sample. The fracture toughness K_{Ic} is the ability of a material to resist to a fracture when a crack is present. A high value of Young modulus E leads to a stiff material, in opposition to a flexible material, while a high fracture toughness K_{Ic} leads to a tough material, in opposition to a fragile material. The yield strength σ_y is the value of the stress from which a material begins to deform plastically without returning to its original shape. Prior to the yield point, the material deforms elastically without permanent deformation. Finally, the tensile strength σ_{ts} is the force required to lead the material to the breaking point. A high value of the yield strength σ_y leads to a hard material, in opposition to a soft material, while a high tensile strength σ_{ts} leads to a ductile material, in opposition to a brittle material. The metallic envelop of the capillary evaporator needs to be stiff, hard, ductile and tough in addition to have a high thermal conductivity. The analysis of Table I-1 shows that a compromise has to be done between the thermal properties and the mechanical properties of the metallic wall. The thermal conductivity is the highest for the copper and the aluminium but their strength properties are relatively poor. The stainless steel has relatively high strength properties, but the thermal conductivity is low. The silicon has a dramatically low value of fracture toughness K_{Ic} but, in both times, the best yield strength σ_y. The nickel seems to have satisfactory intermediate values for both thermal and mechanical properties.

	k (W/m.K)	E (MPa)	σ_y (MPa)	σ_{ts} (MPa)	K_{Ic} (MPa/m$^{1/2}$)
Stainless Steel	16 - 25	189 - 210	170 - 1000	480 - 2240	62 - 280
Copper	380 - 403	112 - 148	30 - 500	100 - 550	30 - 90
Aluminium	237 - 240	68 - 82	30 - 500	58 - 550	22 - 35
Nickel	~ 90	190 - 220	70 - 1100	345 - 1200	80 - 110
Silicon	140 - 150	140 - 155	3200 - 3460	160 - 180	0.83 - 0.94
Carbon Steel	36 - 54	200 - 215	250 - 395	345 - 580	41 - 82

Table I-1 – Thermal conductivity and strength of the common casing material. Green boxes, respectively red boxes, denote the best values, respectively the worst values of the concerned variables. Orange boxes denote intermediate values.

I.2.5.3 The vapour grooves and impact on the fin geometry

Two main roles of the grooves should be mentioned: they collect the vapour produced in the wick and they play a role in the thermal transfer of the heat load towards the wick. That is why many authors focus their attention on their geometrical characteristics: their locations, their dimensions and their shapes. Readers can refer to Launay et al. (2007) [6] concerning the effect of the groove design on the LHP operation. Changing the groove geometrical properties directly influence the shape of the porous structure as well as the size of the wick/casing surface area.

I.2.5.3.1 Positions and locations

Positions

Vapour grooves can be manufactured either at the inner surface of the casing (geometry A) or at the outer surface of the porous wick (geometry B) as sketched in Figure I.16.

Even if its manufacture is more delicate, numerical studies reported that geometry B compared to geometry A has better thermal performances (Coquard (2006) [1]), operates at lower temperature (Zhang et al. (2012) [27]) and delays the vapour breakthrough at the inlet of the wick (Boubaker (2014) [28]). Note that from the experimental review of Launay et al. (2011) [7], no experimental data comparing geometry A and geometry B are reported in literature.

Mazuik et al. (2000) [29] and Chernysheva and Maydanik (2008/2009) [30], [31] proposed an alternative design of geometry B with grooves inside the wick. A capillary strip is kept between the groove/casing interface and the porous wick (geometry C in Figure I.16). To the best of our knowledge, these two studies are the only ones which treat this variant of groove position. Mazuik et al. (2000) [29] compared geometry A, B and C using a 2D finite element method and showed that geometry C permits to keep a lower temperature of the evaporator envelope than geometry A and B. Geometry A exceeds the maximum temperature T_{max} of the casing defined in section I.1.5.3 while geometry B, respectively geometry C, are around 5°C, respectively 15°C, lower than T_{max}. Chernysheva and Maydanik (2008/2009) [30], [31] compared a 2D mathematical model and experimental results using geometry C. The prediction of the casing overheating is in accordance with experimental results. Unfortunately, no more details are given either on experimental setup or on the motivation for the choice of this geometry.

Several questions remain: How they have manufactured such groove geometry? Are the wick and the capillary strip manufactured from the same materials? Do they have the same properties?

A last rare geometry, geometry D, has been numerically investigated by Khrustalev and Faghri (1995) [32] and later experimentally tested by Choi et al. (2013) [24]. It combines geometry A and B consisting in grooves machined in the casing and in the wick. Thus, the casing interpenetrates the wick. Choi et al. (2013) [24] explained that geometry D extends the contact area between the casing and the wick and thus increases the thermal contact conductance $h_{contact}$ defined in section I.2.1.

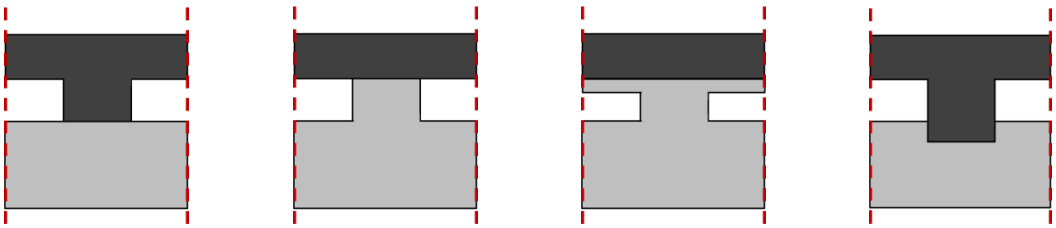

(a) Geometry A (b) Geometry B (c) Geometry C (d) Geometry D

Figure I.16 – Vapour grooves positions. (a) Geometry A: at the inner surface of the casing; (b) Geometry B: at the outer surface of the porous structure; (c) Geometry C: within the capillary structure and (d) Geometry D: at the inner surface of the casing interpenetrating the porous structure.

Locations

Cylindrical evaporator and Flat rectangular/oval evaporator with OR /LR

The classical CE has axial grooves as depicted in Figure I.8a. For few years, some authors (Riehl and Dos Santos (2008) [33]; Santos et al. (2012) [34]) investigated the influence of circumferential grooves added to the axial grooves (Figure I.17) for studying the thermal performance of the evaporator. However, axial grooves stay nowadays the classical and main using design.

Flat evaporator (rectangular or oval) with OR/LR has longitudinal grooves as sketched in Figure I.8b and Figure I.8c.

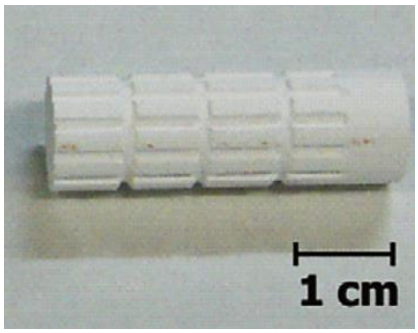

Figure I.17 – Ceramic wick machined with several axial and circumferential grooves for a cylindrical evaporator (CPL) (Santos et al. (2012) [34]).



Figure I.18 – Top view of vapour groove locations for a flat disk-shaped evaporator with OR, adapted from Kiseev et al. (2010) [35]: (a) Radial grooves; (b) Radial/annular grooves and (c) Longitudinal (i.e. parallel) grooves.

Flat disk-shaped evaporator with OR

Flat disk-shaped evaporator with OR can have radial, concentric (i.e. annular) or longitudinal (i.e. parallel) grooves (Figure I.18). Longitudinal groove is the most classical geometry (Choi et al. (2013) [24]). Kiseev et al. (2010) [35] proposed a new design of wick with combined types of groove (concentric and radial). The authors highlighted that for concentric grooves, the heat transfer of a flat disk-shaped evaporator is improved by about 10 to 30% with the grooves manufactured inside the casing rather than in the capillary structure.

I.2.5.3.2 Shapes

The shape of grooves can be rectangular, trapezoidal or triangular [17], which also has an impact on the geometry of the fin. A non-exhaustive list of groove/fin shapes is sketched in Figure I.19. Rectangular grooves (Figure I.19a), respectively trapezoidal grooves (Figure I.19b and Figure I.19c), lead to rectangular fins, respectively trapezoidal fins. Triangular grooves lead to trapezoidal fins (Figure I.19e and Figure I.19f) for classical non-penetrating casing.

Rectangular and trapezoidal grooves (Figure I.19a-c) (engraved in the wick or the casing) are the traditional design and are the most investigated in literature (Kiseev et al. (2010) [35]; Choi et al. (2013) [24]). Moreover, the rectangular shape of removal channel is less complex to machine than triangular or trapezoidal shape and requires less level of precision. Triangular grooves manufactured within the casing were numerically studied by Hamdan (2003) [18] (Figure I.19e) and the ones manufactured within the wick (Figure I.19f) were experimentally investigated by Choi et al. (2013) [24] and Kiseev et al. (2010) [35]. As explained by the latest, triangular grooves within the wick enlarge the surface area for vaporisation implying an enhancement of the evaporation rate. The interpenetrating casing within the wick for triangular fins (Figure I.19d) was numerically studied by Khrustalev and Faghri (1995) [32], and was experimentally tested by Choi et al. (2013) [24] for rectangular fins.

I.2.5.3.3 Dimensions

The grooves and the fins are also characterized by their dimensions. Kiseev et al. (2010) [35] compared experimentally the influence of groove shape and location on the thermal performance of the evaporator, showing that a correct choice of the vapour groove configurations can intensify the heat transfer. They stipulated that the optimum ratio between the total area of vapour grooves and the total area of the input wall is around [0.4;0.5].

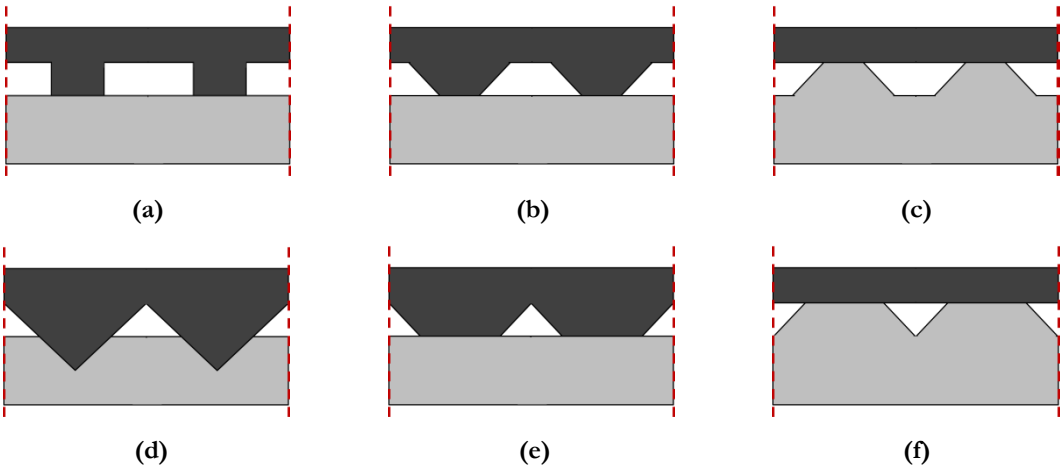

Figure I.19 – Groove and fin shapes. Dark grey sketches the casing and light grey sketches the wick. (a) Rectangular grooves and fins; (b) and (c) Trapezoidal grooves and fins; (d) Triangular grooves and fins with interpenetrating fin within the wick; (e) and (f) Triangular grooves and trapezoidal fins.

Only the influence of rectangular groove dimension is discussed here as they are the classical shape. Rectangular grooves are defined by their height H and their width W. Zhang et al. (2012) [27] defined two parameters α and β for characterizing the impact of groove geometry on the temperature wall (Figure I.20). α is the ratio between the height and the width of the groove and β is the ratio between the fin width and the groove width. Their results predict the lower wall temperature for $\alpha = 1$ and $\beta = 0.5$. These lead to a square vapour groove and a fin twice thinner than the width of the vapour groove.

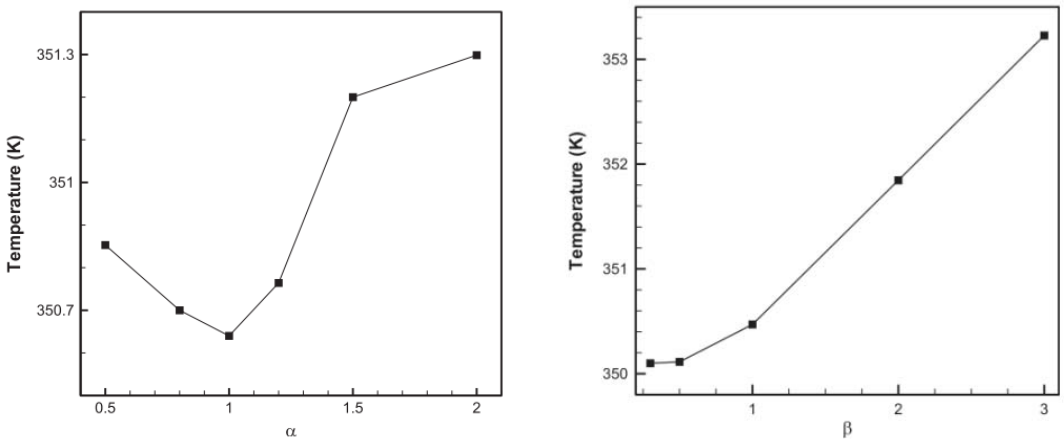

(a) (b)

Figure I.20 – Averaged temperature of the evaporator wall for different (a) α and (b) β from Zhang et al. (2012) [27].

I.2.5.4 Porous structure

The porous wick structure plays several roles as listed below:

- supplying the liquid from the compensation chamber;
- ensuring the evaporation process;
- ensuring a sufficient capillary pressure to compensate for the pressure drops in others loop components;
- and limiting the parasitic heat flux.

All these aspects highlight the necessity of a good selection of the wick material and properties. The main characteristics which influence the loop steady-state operation are the porosity, the permeability, the pore size distribution and the material, as discussed in Launay et al. (2007) [6] and in Launay and Vallée (2011) [7].

I.2.5.4.1 Single-layer and two-layer porous structure

The classical wick is constituted by a single layer (one material with associated properties). In literature, some authors studied numerically ([1], [36], [37]) or experimentally ([38], [39], [40]) an evaporator with a two-layer (also called bilayer or double-layer) wick. Actually, this configuration can be linked to the presence of a secondary wick as described in section I.2.5.1. The secondary wick has generally a low thermal conductivity and a high permeability. The pore size distribution of each layer differs in each study.

A bilayer capillary structure was proposed by Coquard in 2006 [1] and summarized by Mottet et al. (2014) [37] based on numerical analysis. The casing overheating (section I.1.5.3) and the parasitic heat flux (section I.2.4) are two important limiting parameters. Insulating wick ensures a weak heat loss whereas a conductive wick reduces the risk of overheating. Based on this numerical analysis, combining a conductive layer and an insulating layer is proposed (Figure I.21). The insulating layer has smaller pore size than the conductive layer, thus playing the role of a capillary lock. The impact of the size of each layer is also investigated, highlighting that the size of the conductive layer does not seem to have a significant incidence on the casing overheating.

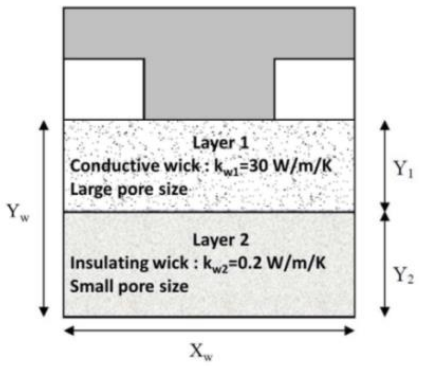

Figure I.21 – Schematic model of a bilayer wick proposed by Coquard (2006) [1].

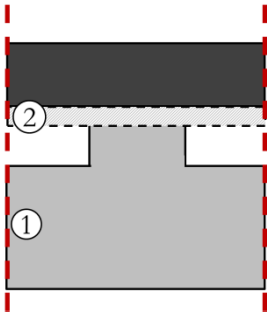

Figure I.22 – Sketch of a potential bilayer wick, based on Mazuik et al. (2000) [29] and Chernysheva and Maydanik (2008/2009) [30], [31] numerical studies. (1) is the primary wick and (2) is the second layer characterized by a capillary strip.

Bai et al. (2009) [36] investigated the influence of a two-layer wick on LHP. The proposed bilayer wick is almost the same as the one suggested numerically by Coquard (2006) [1], except concerning the choice of the pore size. The first outside wick layer is a nickel structure with a small pore radius. The second inner layer has a low thermal conductivity and a large pore radius. Their conclusions are the same as Coquard (2006) [1] concerning the overheating of the casing and the parasitic heat flux.

Singh et al. (2009) [38] and later Wu et al. (2011) and (2013) [39], [40] tested a two-layer wick composed by a monoporous and a biporous layer. The biporous layer is near the heated casing and the monoporous layer is below. The authors showed that this configuration permits to reduce the vapour temperature at the outlet of the evaporator as well as the evaporator wall temperature in comparison with a monolayer wick characterized by a monoporous pore size distribution.

As already explained in section I.2.5.3.1, Mazuik et al. (2000) [29] and Chernysheva and Maydanik (2008/2009) [30], [31] proposed an original design of the wick as sketched in Figure I.22. Unfortunately, no more details are given on the properties of the wick. Several questions remain: How they have manufactured such groove geometry? Are the wick and the capillary strip manufactured from the same materials? Do they have the same properties? A potential answer could be that the wick is in reality a two-layer wick structure (Figure I.22), thus implying that the capillary strip and the primary wick are not necessarily composed by the same material and could have different properties (such as porosity, permeability and size pore distribution).

I.2.5.4.2 Wick Material

The major wick materials are metal, plastic and ceramic. For more details, the reader can refer to [7] and [8] for the summarize of experimental studies and to Table II-2 for numerical studies. The classical manufacturing process of the porous wick is the sintering of metal. Nickel (Ni) (Figure I.23) is the most commonly used metal but some studies tested titanium (Ti) (Figure I.24b) and less frequently brass (Cu-Zn), copper (Cu) (Figure I.24a), stainless steel (SS) and iron (Fe). These kinds of wick have high porosity and low average pore size diameters. PTFE ([41], [42]), polyethylene (PE) and polypropylene (PP) are the most encountered plastic in experimental test ([7]). Finally, ceramic [34] is also used to manufacture porous wick. Plastic and ceramic have the advantage to have a low thermal conductivity, thus reducing the heat leak towards the compensation chamber. However, their porosity is small and the overheating limit is low.

A new kind of wick using a metalloid material was proposed by Hamdan (2003) [18]. A Coherent Porous Silicon (CPS) wick (Figure I.25) is characterized by extruded micro cylindrical channels with a constant spacing. The fabrication process has the advantage to have a high precision control of the porosity and the pore size.

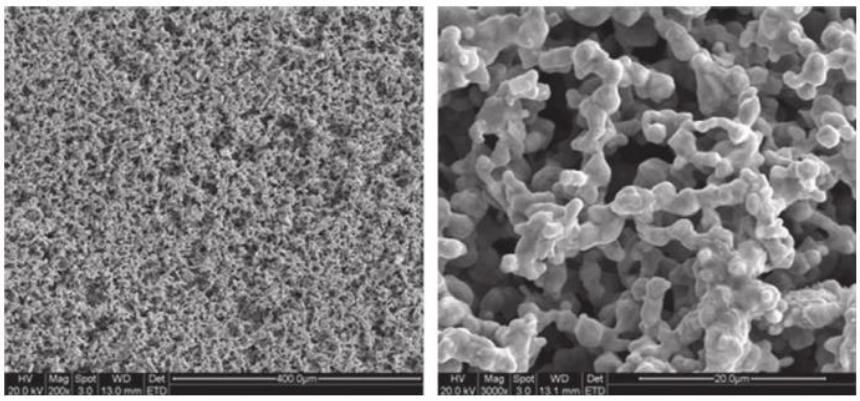

(a) 200 magnitude (b) 3000 magnitude

Figure I.23 – SEM picture of a Nickel wick, from Li et al. (2012) [43].

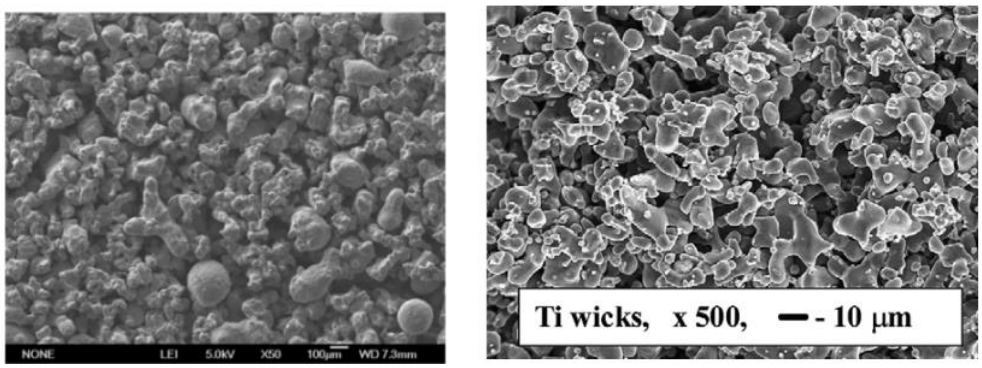

(a) **(b)**

Figure I.24 – SEM picture of a (a) Copper wick, from Li and Peterson (2011) [44], and (b) a Titanium wick, from Kiseev et al. (2010) [35].

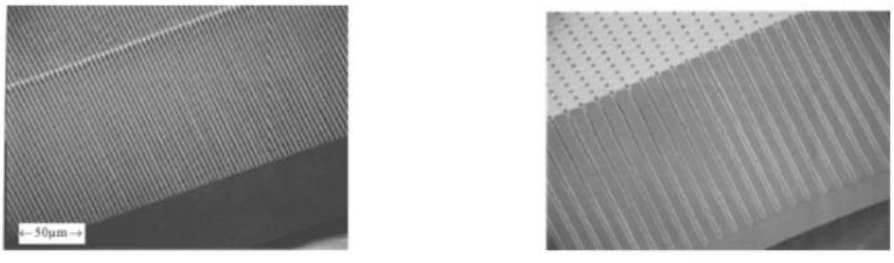

(a) (b)

Figure I.25 – Coherent porous silicon (CPS) wick with (a) 2µm pore size and 4µm spacing and (b) 5µm pore size and 20µm spacing, from Hamdan (2003) [18].

I.2.5.4.3 Porosity and permeability

Porosity

The porosity ε of a porous medium is defined as the ratio of the volume of void space (called the pores) to the total volume of the sample (equation (I-13)). The porosity has no unit and is between 0 and 1 (or 0 and 100%). This property needs to be determined experimentally.

$$\varepsilon = \frac{V_{void}}{V_{total}} \quad \textbf{(I-13)}$$

The porosity of sintered metal and plastic reported in experimental and numerical studies are summarized in Table I-2. Nickel and titanium porous structures, which are the most encountered for metal wicks, have higher porosity than plastics. A high porosity is often looked for in capillary evaporator application as it provides a high flow rate of liquid through the wick.

		Experimental studies	Numerical studies
Metals	Ni	55 - 86%	50 - 78%
	Ti	55 - 78%	~ 60%
	Cu	45 - 70%	50 - 70%
	SS	~ 30%	~ 60%
	CuZn	~ 40%	×
	Fe	~ 30%	×
Plastics	PTFE	~ 50%	44 - 50%
	PE	35 - 50%	35 - 50%
	PP	40 - 50%	×

Table I-2 – Porosity of wick material used in experimental and numerical studies, adapted from Launay et al. (2011) [7]for experimental data and Table II-2 for numerical data.

Permeability

The permeability K is the ability of a porous medium to transmit fluids in the presence of a pressure gradient. This property is directly related to the geometry of the considered sample (such as the pore size, the porosity and its dimensions) and the liquid properties. The permeability is generally determined experimentally for the considered sample, but some well-known relations exist. For example, the Kozeny relation (equation (I-14)) determines the permeability of a packed bed of spherical solid beads.

$$K = \frac{d_{bead}^2 \varepsilon^3}{\Psi(1-\varepsilon)^2} \quad \textbf{(I-14)}$$

where d_{bead} is the diameter of the solid beads and Ψ is a geometrical factor depending on the powder and process used and the resulting tortuosity of the porous structure. Historically, Kozeny proposed $\Psi = 72$. Few years later, Carman, respectively Ergun, proposed $\Psi = 180$, respectively $\Psi = 150$ for random packed beds of spherical particles. These two common relations are called the Carman-Kozeny equation and the Blake-Kozeny equation. Noted that some authors used $\Psi = 37.5$ for a sintered structure ([45]).

The permeability of metals and plastics reported in experimental and numerical studies are summarized in Table I-3. However, most of the time, the permeability is not given in literature. For a loop system, the permeability has to be as high as possible to provide a good liquid flow within the wick. In literature, its value varies from 10^{-15} to 10^{-12} m^2.

		Experimental studies	Numerical studies
Metals	Ni	$1.4\times10^{-14} – 1\times10^{-11}$	$2\times10^{-14} – 1.1\times10^{-11}$
	Ti	$2\times10^{-14} – 2\times10^{-13}$	×
	Cu	$\sim 7\times10^{-12}$	$5.2\times10^{-11} – 6.075\times10^{-11}$
	SS	$2.5\times10^{-14} – 1.5\times10^{-13}$	$\sim 6\times10^{-13}$
	CuZn	×	×
	Fe	×	×
Plastics	PTFE	×	$\sim 1.3\times10^{-14}$
	PE	$1.1\times10^{-12} – 1\times10^{-13}$	$\sim 1\times10^{-13}$
	PP	×	×

Table I-3 – Permeability (m^2) of wick material used in experimental and numerical studies, adapted from Launay et al. (2011) [7] for experimental data and Table II-2 for numerical data.

I.2.5.4.4 Pore size distribution

The pore size distribution is usually given in terms of mean (or maximum) pore size and standard deviation. The pore size distribution is directly related to the maximal capillary pressure (see equation (I-4) in section I.1.5.1). The wick has to have small pore size to ensure a large capillary driving pressure. The mean pore diameters of common materials are reported in Table I-4 and are between 1 to 20µm for usual wick and can reach 120µm for copper. The usual experimental setup to determine the pore size distribution is the mercury intrusion technique. A typical curve distribution is presented in Figure I.26 (pink line). The mean pore diameter in this example is 10µm and the standard deviation is ±5µm. Some authors investigated biporous wicks (green line in Figure I.26) which are characterised by two types of pore size in the wick at the same time. These kinds of structure will be discussed in details in Chapter V.

		Experimental studies	Numerical studies
Metals	Ni	1.8 – 20µm	0.9 – 7µm
	Ti	5 – 24.4µm	×
	Cu	20 – 130µm	3 – 21µm
	SS	19 – 20µm	~ 25µm
	CuZn	~ 9.6µm	×
	Fe	~ 1.6µm	×
Plastics	PTFE	1.2 – 4µm	2 – 10µm
	PE	7 – 12µm	~ 6µm
	PP	×	×

Table I-4 – Mean pore diameters of wick material used in experimental and numerical studies, adapted from Launay et al. (2011) [7] for experimental data and Table II-2 for numerical data.

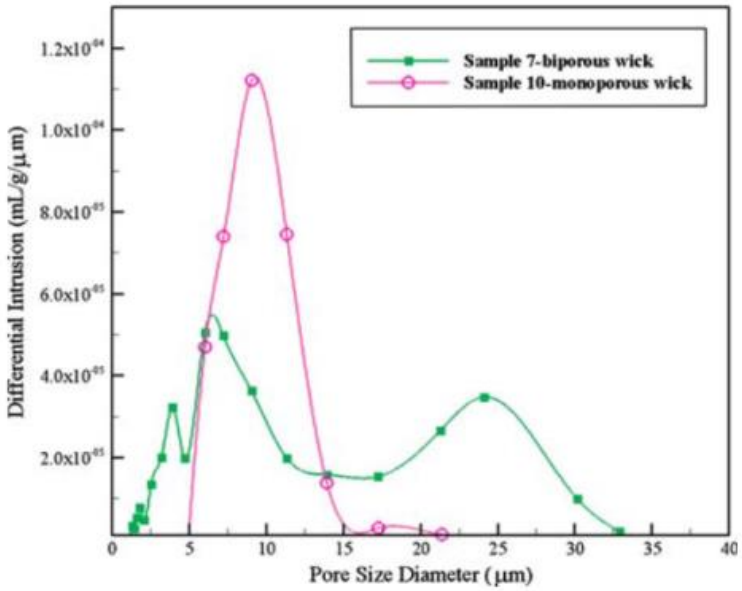

Figure I.26 – Pore size distribution of monoporous and biporous wick, from Yeh et al. (2008) [46].

I.2.5.4.5 Effective thermal conductivity

The effective thermal conductivity k^* is also a crucial parameter which determines the thermal properties of the capillary structure: the heat transport from the casing to the evaporation zone and the heat conducted towards the reservoir (parasitic heat flux). A sintered wick has the same conductivity in each direction, i.e. the porous structure is isotropic. The effective thermal conductivity is a function of the porosity and the thermal conductivity of both the solid matrix and the fluid, noted k_l^* for a liquid-saturated wick. Several authors (Kaya and Goldak (2006) [21], Mo et al. (2006) [47], Coquard (2006) [1], Singh et al. (2009) [38], Li and Peterson (2011) [44], Chernysheva and Maydanik (2008, 2009, 2012) [30], [31], [48], Lin et al. (2011) [49]) reported several correlations. Some of them compared predicted values with experimental results (Mo et al. (2006) [47], Singh et al. (2009) [38]) and others compared the influence of correlation on the overall evaporator temperature (Kaya and Goldak (2006) [21], Lin et al. (2011) [49]). The main used correlations are reported in Table I-5 and they are plotted in Figure I.27.

The two usual models are the parallel model (arithmetic mean) (equation (I-15)) and the series model (harmonic mean) (equation (I-16)), defining respectively the upper and the lower limit value of the effective conductivity. The parallel model is the most encountered model in numerical literature (Figus et al. (1999) [50], Huang et al. (2005) [51], Liu et al. (2007) [52], Wan et al. (2007, 2008 and 2011) [52–54], [52] Nishikawara et al. (2013) [53], Fang et al. (2014) [25], Boubaker et al. (2015) [54]). Coquard (2006) [1] used the average between the series model and the parallel model to calculate the effective thermal conductivity (equation (I-17)). Chaudary and Bhandari proposed a correlation based on the parallel and series model (equation (I-18)) and which corresponds to the geometric mean. The coefficient n is usually between 0.42 and 0.51 in literature but can be adjusted to fit experimental results. Bai et al (2009) [36], as well as Li and Peterson (2011) [44] and Zhang et al. (2012) [27], used $n = 0.42$ for a copper powder wick, while Mo et al. (2006) [47] used $n = 0.51$ for a nickel powder wick.

Parallel model (maximum, arithmetic mean)	$k_{max} = \varepsilon k_l + (1-\varepsilon)k_w$	**(I-15)**
Series model (minimum, harmonic mean)	$k_{min} = \dfrac{k_l k_w}{\varepsilon k_w + (1-\varepsilon)k_l}$	**(I-16)**
Average model	$k_l^* = \dfrac{k_{max} + k_{min}}{2}$	**(I-17)**
Chaudary and Bhandari's model (geometric mean)	$k_l^* = (k_{max})^n (k_{min})^{1-n}$	**(I-18)**
Goring and Churchill's model	$k_l^* = \dfrac{k_l\left((2k_l + k_w) - 2(1-\varepsilon)(k_l - k_w)\right)}{(2k_l + k_w) + (1-\varepsilon)(k_l - k_w)}$	**(I-19)**
Maxwell's model	$k_l^* = k_s\left[\dfrac{2 + k_l/k_w - 2\varepsilon(1 - k_l/k_w)}{2 + k_l/k_w + \varepsilon(1 - k_l/k_w}\right]$	**(I-20)**
Alexander's model	$k_l^* = k_l \left(\dfrac{k_l}{k_w}\right)^{-(1-\varepsilon)^{0.59}}$	**(I-21)**
Odelevski's model	$k_l^* = k_w(1-\varepsilon)(1+\varepsilon)^{-2.1} + \varepsilon k_l$	**(I-22)**

Table I-5 – Usual correlations for the calculation of the effective thermal conductivity. k_w, respectively k_l, is the thermal conductivity of the wick material, respectively of the liquid. ε is the porosity.

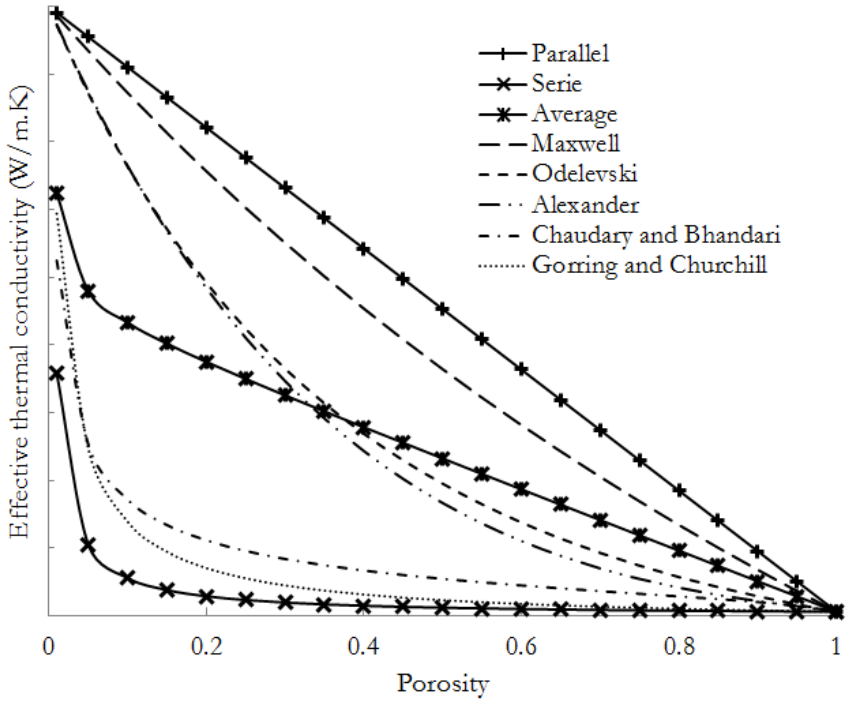

Figure I.27 – Variation of the effective thermal conductivity as the function of the porosity for different correlation.

Goring and Churchill proposed a formula for a powder metal wick (equation (I-19)). However, this model is valid for a constant powder diameter and a single-point contact between two powders. The effective thermal conductivity predicted by Goring and Churchill's model is underestimated and is not relevant for a sintered wick. The Maxwell's model (equation (I-20)) determined the effective thermal conductivity for heterogeneous wick. Singh et al. (2009) [38] showed that the Maxwell's model overestimated the effective thermal conductivity by several times the experimental value. Alexander's model is proposed for a sintered wick (equation (I-21)) and is used for example by Siedel et al. (2013) [45] for a nickel sintered wick. Singh et al. (2009) [38] concluded that Alexander's correlation is the most appropriate (amongst the ones they studied) for a copper powder wick even if the predicted value is twice higher than the experimental one. Chernysheva and Maydanik (2008, 2009, 2012) [30], [31], [48] used the formula proposed by Odelevski (equation (I-22)) to predict the effective thermal conductivity of a copper wick. The others numerical studies of heat and mass transfer within a capillary evaporator used directly the effective thermal conductivity as an input of their model (Demidov and Yatsenko (1994) [55], Maziuk et al. (2000) [29], Khrustalev and Faghri (1995) [32], Yan and Ochterbeck (2003) [56], Ren et al. (2007) [57]).

Mo et al. (2006) [47] and Singh et al (2009) [38] investigated the influence of the correlation on the effective thermal conductivity and compared their predicted results with experimental data. Mo et al. (2006) [47] highlighted that the choice of the correlation depends on the working fluid. Therefore, they proposed a polynomial equation (as a function of the working fluid thermal conductivity) to determine the effective thermal conductivity of a nickel sintered wick and this, whatever the working fluid. Singh et al. (2009) [38] stated that Alexander's correlation is the most appropriate for a copper powder wick even if this statement is debatable. Kaya and Goldak (2006) [21] and later Lin et al. (2011) [49] investigated the influence of the choice of the correlation on the overall evaporator temperature. They both reported that the choice of the correlation has a low influence on the maximum wall temperature and the temperature distribution within the wick (Figure I.28).

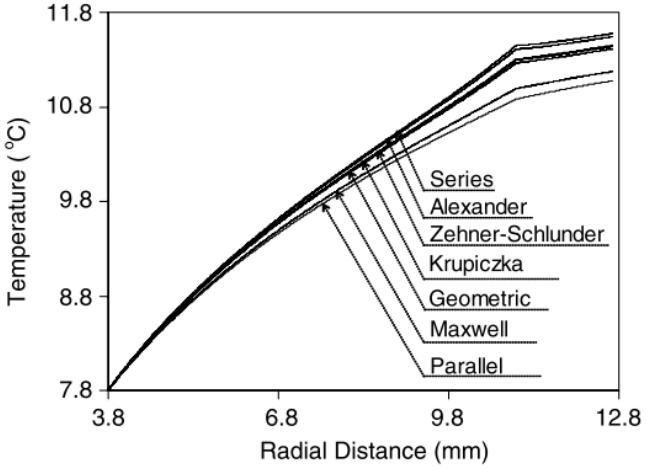

Figure I.28 – Temperature profile as a function of the radial distance from the inner diameter of the wick to the outer diameter of the casing for different effective thermal conductivity relations, from Kaya and Goldak (2006) [21].

Chapter II Literature review

Chapter II Literature review 37
II.1 Analytical studies 38
II.2 Modelling of the whole loop system 39
II.3 Visualisation experiment of the evaporation process 48
II.4 Modelling of the capillary evaporator 51
II.5 Synthesis and conclusion of the chapter 71

This literature review focuses on numerical studies and is organized as follows. Firstly, the existing analytical models are presented. Two kinds of analytical studies are distinguished: the ones which determined the operating temperature, i.e. the wall evaporator temperature; and the ones describing the heat and mass transfer within the capillary evaporator only. In a second time, several steady-state and transient models of the whole loop are discussed with a detailed description of their evaporator model. In the last part, the focus is made on works where only the capillary evaporator is modelled. All the models presented in this section are summarized in Table II-1, Table II-2 and Table II-3.

II.1 Analytical studies

II.1.1 Analytical LHP studies

Chernysheva et al. (2007) [12] investigated two compensation chamber operating modes: the fully liquid-saturated state and the two-phase state for studying the influence of the cooling fluid distribution in the loop. They assumed that the compensation chamber is in a two-phase state during the variable conductance mode (VCM), while it becomes fully saturated with liquid when the LHP operates in the fixed conductance mode (FCM). The operating temperature T_{ev}, corresponding to the evaporator temperature, is analytically determined for both operating modes. The intersection point between the two curves obtained from the two expressions of T_{ev} corresponds to the transition point between the VCM and the FCM. This study highlights that the evaporator temperature depends on the operating mode (fully or partially saturated reservoir) of the device and is higher when the LHP operates with a partially-filled compensation chamber. The authors provided two simple expressions of the evaporator temperature. However, they are semi-empirical and the various heat transfer coefficients, as well as the compensation chamber temperature, need to be determined experimentally as for example Li et al. (2011) [58] did.

Launay et al. (2008) [13] proposed two analytical expressions to determine the operating temperature of a loop heat pipe under the variable and fixed conductance mode based on the simplification of a steady-state numerical model. Their temperature expressions have been validated for different fluids, wick effective thermal conductivities, evaporator geometries (flat and cylindrical) and elevations contrary to those provided by Chernysheva et al. (2007) [12]. However, in the manner of [12], some parameters, such as the evaporator thermal resistance, must be determined experimentally.

Recently, Siedel et al. (2015) [59] improved the steady-state analytical model proposed by Launay et al. (2008) [13]. The transfer by conduction within the evaporator is treated as a 2D problem, while a 1D representation of the liquid flow in the wick is adopted. The heat transfer equation in the evaporator/reservoir is solved using a Fourier series development. The evaporation rate is controlled by the kinetic evaporation theory, and the accommodation coefficient is equal to 0.1. This analytical model is more accurate than Chernysheva et al. (2007) [12] and Launay et al. (2008) [13], but the determination of the operating temperature is more complex.

II.1.2 Analytical evaporator study

Cao and Faghri (1994) [60] developed an analytical steady-state solution to determine the temperature and the pressure fields within capillary structure partially heated at the upper surface (Figure II.1). The heat flux applied is uniform and the porous structure is rectangular. Even if the heat load is directly applied at the top of the porous media, this geometry can be directly related to the unit cell of an LHP/CPL evaporator (see section I.2.3).

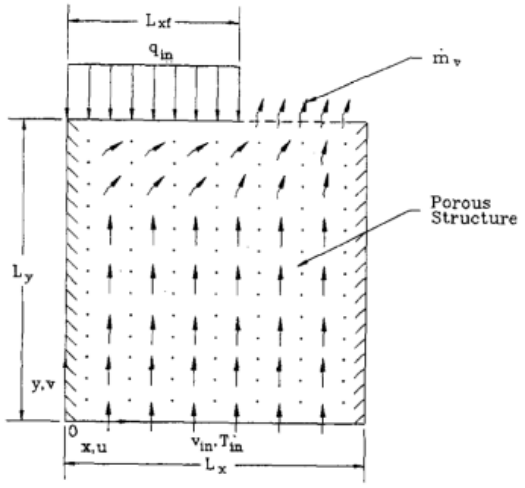

FIG. 1. Porous structure with partial heating and evaporation on the upper surface.

Figure II.1 – Computational domain constituted by the capillary structure heating at the upper surface from Cao and Faghri (1994) [60].

The analytical solution provided is valid for a fully liquid-saturated and homogeneous wick. Therefore, the evaporation process occurs at the upper unheated wick interface only. The liquid flow analytical solution is obtained combining the two-dimensional Darcy's law and the continuity equation. The analytical solution of the energy equation is based on an adimensionalized energy equation where properties of the working fluid and the wick structure appear. Both (energy and flow solutions) are finally obtained using the method of separation of variables. A good agreement between their analytical model and a numerical resolution has been shown concerning the temperature field in the porous wick structure. Until reaching the middle section of the wick, the velocity field of the liquid is almost one-dimensional and the temperature field is quasi uniform. The authors also investigated the influence of three different effective thermal conductivities emphasising that a low effective thermal conductivity implied a sharp variation of the temperature at the upper surface.

II.2Modelling of the whole loop system

Several steady-state and transient mathematical models to predict the operational characteristics of two-phase loops have been published. Only the most recent works and/or the most relevant as regards to the present study are presented here. All these models are based on the energy conservation in the compensation chamber and on the calculation of pressure loss along each component of the loop. As this work thesis concerns the evaporator, the synthesis of work will mainly focus on the evaporator representation. The reader can refer to the Siedel's review (2015) [10] for a more extensive analysis and more exhaustive references.

II.2.1 Steady-state modelling

Kaya and Hoang (1999) [61] proposed a steady-state LHP model based on energy balance and pressure drop on each component of the loop to determine the operating temperature of the system. The model

was validated experimentally and results are in good agreement for high heat flux. Despite this model can predict quite accurately the operating temperature, the evaporator model is basic. The heat and mass transfer in the wick is supposed to be unidirectional and the heat leak in the wick is determined analytically from the conductive heat equation.

Chuang et al. (PhD thesis (2003) [14] and published article (2014) [15]) analysed the LHP elevation effects on steady-state performance. The convention used in this work is defined in section I.1.3.4. The author suggested that the LHP can operate in two different modes at a positive elevation:

- Gravity-controlled mode:
  The LHP operates at low heat flux and is characterized by a two-phase flow in the removal channel within the evaporator. The liquid-vapour interface at the wick/groove location is flat.
- Capillary-controlled mode:
  The LHP operates at high heat flux and is characterized by a fully vapour flow in the removal channel within the evaporator. The liquid-vapour interface at the wick/groove location is curved.

The hypothesis of the existence of the gravity-controlled mode was confirmed experimentally using neutron radiography technique. Thereafter, Chuang (2003) [14] developed a 1D steady-state model which takes into account the two operating modes mentioned previously. The model is suitable for an adverse and a positive elevation of the device. Moreover, the originality of this model stays in the investigation of several pressure drop correlations which take into account the phase change and the singular pressure loss in the bends of the liquid line and the vapour line. The comparison between experimental and numerical results shows a good agreement when the device is horizontal. However, a deviation in predicted results is observed at the gravity-controlled mode, i.e. for low heat load. Furthermore, the evaporator model is very simple and cannot describe accurately the phenomena which take place in it. The heat exchange and the flow in the porous structure are assumed to be unidirectional and the wick is fully saturated with liquid. The pressure field is calculated using the analytical solution of the Darcy's law, while the temperature field is calculated using the analytical solution of the conductive heat transfer equation.

Hamdan (2003) [18] developed a theoretical steady-state model to predict the maximum evaporator temperature, the condenser temperature and the maximum power that can be dissipated by an LHP constituted by a CPS wick (see section I.2.5.4.2 concerning the CPS structure). The evaporator is flat with an opposite replenishment (Figure II.2). The model is based on the conservation equations (mass, energy and momentum balances) and thermodynamic considerations to evaluate the capillary limit and the boiling limit for a whole LHP. Using an hydrodynamic model and analytical expressions, the author explained that decreasing the pore size increases the capillary pressure in the wick until an optimum value, depending on the heat flux, for which the pressure dramatically fall down due to the friction (Figure II.3). In 2009, Hamdan et al. [62] investigated the parasitic heat flux from the evaporator to the compensation chamber. They pointed out that the subcooled liquid needs to balance the heat leak to prevent a failure of the LHP operation. Their model permits to evaluate the subcooled temperature required for a stable operation of the LHP.

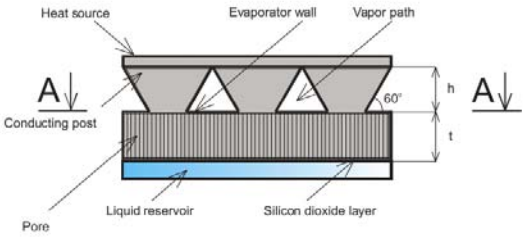

Figure II.2 – Sectional view of the FEOR studied by Hamdan (2003) [18] (scheme from Alexseev (2003) [63]).

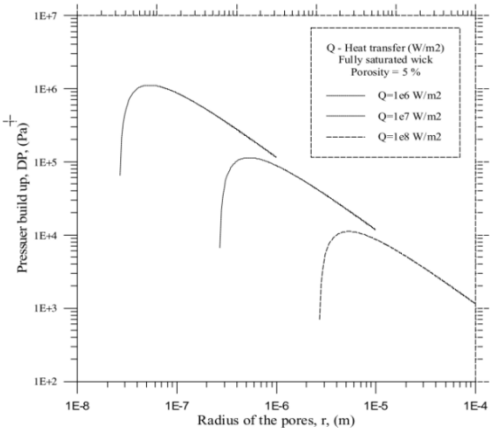

Figure II.3 – Pressure across the wick versus the pore size for different heat fluxes, from Hamdan (2003) [18].

In complement to the previous studies, Alexseev (2003) [63] studied the pressure drop and the temperature distribution in a triangular groove using analytical and numerical calculation. The wick is a coherent porous silicon structure (CPS) supposed to be fully saturated with liquid. A method to determine the optimal design of this triangular-shaped groove with a CPS capillary structure is proposed. The author recommends using a pitch (distance between two neighbour pore centres) to pore diameter ratio as small as possible to keep a low evaporator temperature.

However, both evaporator models in [18] and [63] are simplistic: they considered a fully saturated wick and a 1D steady-state analytical model in the wick.

Atabaki (2006) [64] presented a mathematical steady-state model based on the fluid flow and the heat transfer in the whole loop using a nodal network method. The authors considered two evaporator geometries: LHP with a CE and CPL with a FE. This model was further extended by Jesuthasan (2011) [65] for a LHP with a FEOR who implemented a more accurate model (a quasi-three-dimensional finite volume method) for the fluid flow and the heat transfer inside the grooves. The model predicts the steady-state operating temperature and the mass flow rate along the loop as well as the length of the two-phase region in the condenser. The system of equations is solved in one-dimension and uses semi-empirical correlations. The assumption of saturated wick is made and a uniform injection velocity and temperature at the wick/groove interface is imposed as boundary condition for the vapour flow in the groove.

Bai et al. (2009) [36] established a steady-state mathematical model considering a two-layered wick structure (see section I.2.5.4.1) within a cylindrical evaporator of an ammonia LHP. The evaporator model is based on a nodal network approach, as sketched in Figure II.4, from which an energy balance at each node is considered. The thermal conductances are either fitted on experimental data or calculated from the analytical solution of the 1D energy conservation equation. They investigated the influence of a two-layer wick on LHP performance assuming an annular flow model for the condenser and a liquid-saturated wick within the evaporator. For a high heat flux when the device operates in the fixed conductance mode (FCM), the authors have noted that the bilayer structure has no effect on the operating temperature compared to a single-layer structure.

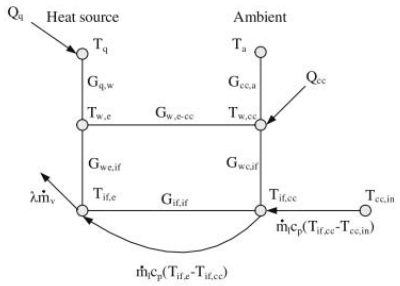

Figure II.4 – Thermal network of the evaporator and reservoir used by Bai et al. (2009) [36].

Adoni et al. (2010) [66] developed a steady-state mathematical model for determining thermohydraulic performances of an ammonia LHP. The flat evaporator is constituted by a disk-shaped sintered nickel wick and the compensation chamber is in the thickness. The grooves are machined in the aluminium heater plate. Their model solved a system of equations based on the heat transfer, the pressure loss and the mass balance in each component of the loop. They fitted the model using experimental data: the conductance due to the heat exchange (parasitic flux) by conduction through the wall from the evaporator to the compensation chamber is deduced experimentally. Figure II.5 shows a better agreement between their mathematical model and experiment for a conductance of 0.9W/K (high thermal coupling) than for $10^{-3}\mathrm{W/K}$ (weak thermal coupling).

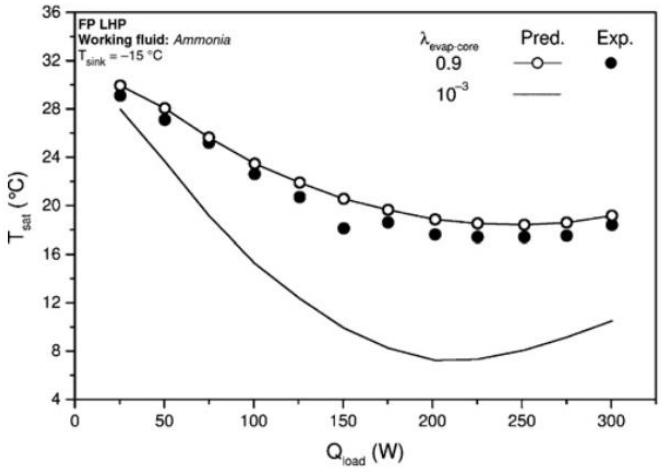

Figure II.5 – Influence of the parasitic heat flux to the compensation chamber on the operating temperature, from Adoni et al. (2010) [66].

Lachassagne (2010) and (2013) [67], [68] proposed a steady-state modelling of a whole CPL under gravity composed by three evaporators (Figure II.6). Trapezoidal grooves are machined within the nickel-sintered wick in the direction of the evaporator width. The model is based on a nodal network and the equations are transposed using an electrical network. Only the evaporator model is described below. The flow in the wick is supposed to be unidirectional and the liquid-vapour interface is located at the wick/groove interface only. A staggered mesh is used as described in Figure II.7a. The evaporator is discretized into 4 nodes: the liquid core node (noted "art"), the porous structure node (noted "por"), the trapezoidal grooves node (noted "can") and the two lateral grooves node (noted "canlat"). The thermal network of the evaporator using the electrical analogy is given in Figure II.7b. One can see that three conductances are introduced in this electrical network: the evaporator conductance G_{evap}, the trapezoidal grooves conductance G_{can} and the lateral grooves conductance G_{canlat}.

The model was validated by experiment. The main advantage of this electrical analogy representation, compared to other loop models available in the literature, is that it is able to predict condensation or vaporisation in every part of the loop, especially in the liquid and the vapour lines. However, the model is fitted to experimental results by the way of the evaporator conductance. Note that the compensation chamber conductance, not expressed here, is also determined using experimental data. Indeed, as their evaporator model is elementary (no vapour recession in the porous wick, 1D flow in the wick…), they cannot evaluate numerically these two conductances.

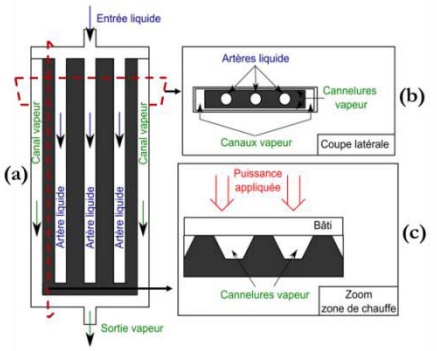

Figure II.6 – Sectional (a) top, (b) transverse and (c) longitudinal views of the evaporator studied by Lachassagne (2010) [67], Lachassagne et al. (2013) [68] and Blet (2014) [69]. The blue legend refers to the liquid path and the green legend refers to the vapour grooves. The grey part depicts the wick structure. Scheme from Blet (2014) [69].

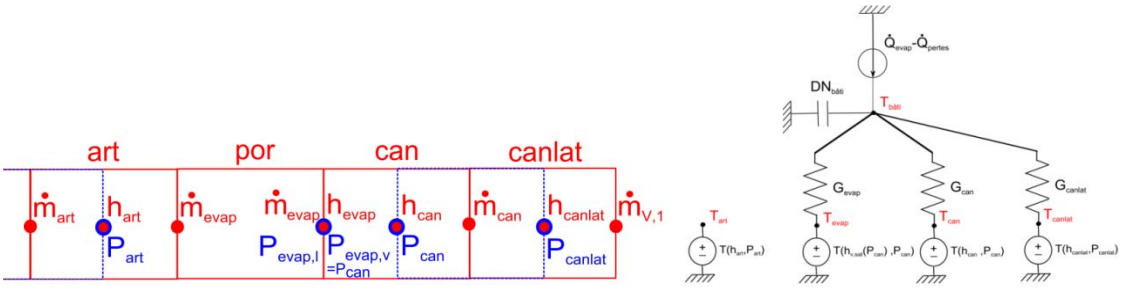

(a) **(b)**

Figure II.7 – (a) The one-dimensional discretization of the evaporator using a staggered mesh (red meshes: energy and mass balance; blue meshes: momentum balance) and (b) the thermal network of the evaporator using an equivalent electrical representation used by Lachassagne (2010) [67], Lachassagne et al. (2013) [68] and Blet (2014) [69] for the evaporator representation. Schemes from Blet (2014) [69].

Siedel et al. (2013) [45] developed a steady state model to investigate the thermohydraulic behaviour of a whole LHP with a disk-shaped evaporator with an opposite replenishment. Governing equations of the evaporator are discretized in 2D for an evaporator unit cell and solved using a finite difference method (Figure II.8) while governing equations of other loop components are discretized in 1D. This description of the complete LHP permits a better description of the transfers and the parasitic heat flux through the wick. The liquid flow within the wick is described using the Darcy's law and the convection-diffusion equation is used for calculating the temperature field. The applied heat load is supposed to be sufficiently low for considering the wick fully saturated with liquid. The evaporation occurs at the wick/groove interface only and there is no vapour recession within the capillary structure.

It is interesting to focus our attention on the choice of the boundary condition for the wick/groove interface (noted F in Figure II.8). The expression of the boundary condition along this interface introduces an interfacial resistance expressed using a mixed boundary condition (i.e. a convective boundary condition). The evaporative heat transfer coefficient h_{ev} is determined by the kinetic evaporation theory.

The authors studied the influence of the accommodation parameter on the operating temperature (Figure II.9a). For a given heat load, multiplying the accommodation coefficient by 100 induces a rising of the operating temperature of about 5 to 10K. Moreover, for low wick thermal conductivity ($\lambda < 5\mathrm{W/m.K}$), the accommodation coefficient value seems to have no effect on the heat flux of evaporation. However, for a conductive wick ($\lambda > 5\mathrm{W/m.K}$), if the evaporation rate is restricted, meaning a low accommodation coefficient, then an increase in the evaporation heat flux is observed while it continues to decrease for a higher accommodation coefficient (Figure II.9b). Therefore, this coefficient needs to be fitted on experimental data and the discussion on the legitimacy to take into account an interfacial resistance at the wick/groove interface when the wick is saturated with liquid is open .

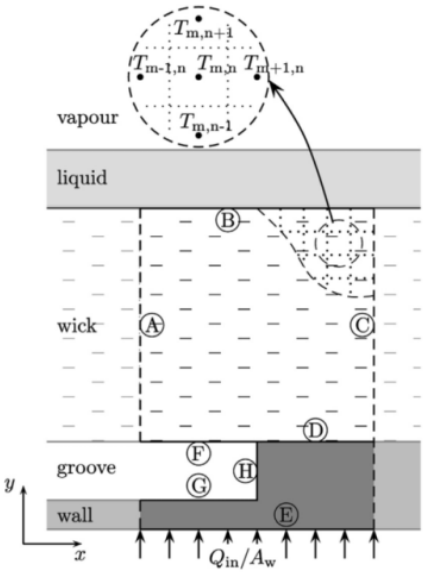

Fig. 3. Heat and mass transfer in the wick.

Figure II.8 – Computation domain of the heat and mass transfer of Siedel et al. (2013) [45].

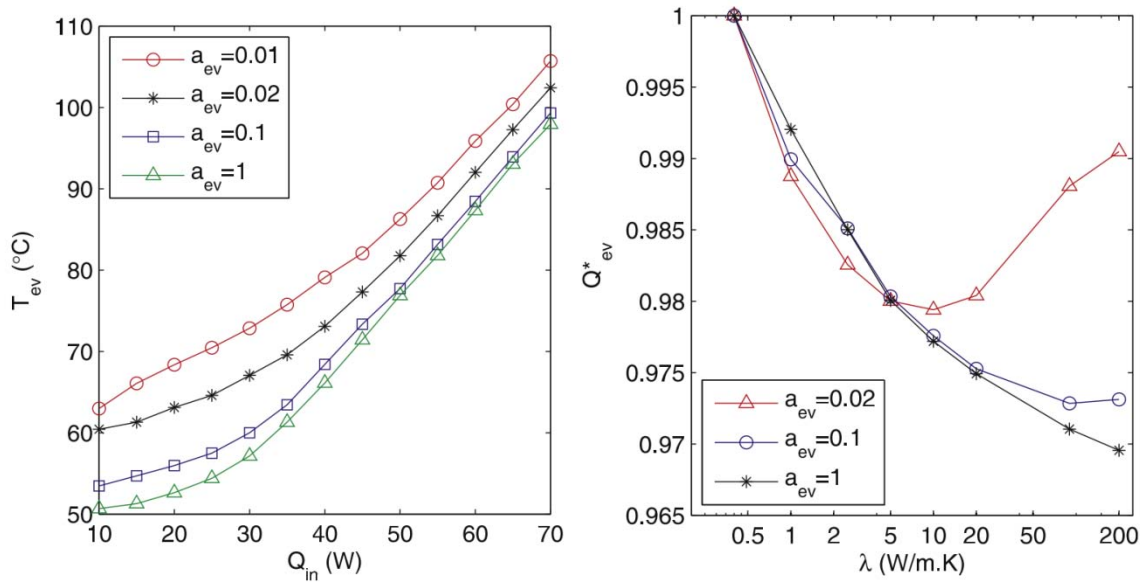

(a) **(b)**

Figure II.9 – Influence of the accommodation coefficient (a) on the operating temperature and (b) on the evaporation rate, from Siedel et al. (2013) [45]. Q_{in} is the applied heat flux, Q^*_{ev} is the evaporation heat flux as defined in section I.2.4.

II.2.2 Transient modelling

Launay and al. (2007) [70] developed a transient overall model to describe the oscillating behaviour of a standard loop heat pipe. The model is based on the transient mass, momentum and energy equation for all components of loop (compensation chamber, condenser, evaporator, liquid and vapour lines). A liquid-vapour interface is present in the compensation chamber and the liquid core, the wick is fully saturated with liquid and the removal channels are filled with vapour (thus corresponding to the situation 2 in section I.1.3.1). The heat transfer in the evaporator is simplified using a thermal nodal network, and five thermal resistances are introduced: the conductive thermal resistance R_{vap} between the evaporator casing and the wick; the conductive thermal resistance R_{ax} between the evaporator and the reservoir; the conductive thermal resistance R_w through the wick; the convective thermal resistance R_{conv} between the fluid and the reservoir casing; and the convective/radiative thermal resistance R_{amb} between the reservoir casing and the ambient. R_{vap} and R_{amb} are fitted on experimental data, then numerical results are compared with experimental data. Even though the difference between the predicted temperature and measured ones does not exceed 3.5K, a numerical time lag exists for low heat flux. The authors explained that it is certainly due to the approximation done in the evaporator/reservoir model.

Kaya et al. (2008) [71] proposed a transient loop model using a nodal network to estimate the average temperature of the evaporator wall (i.e. the operating temperature). The transient mass, momentum and energy equation on each component are solved using a staggered grid. The fluid is considered as compressible. It is assumed that the wick is always saturated with liquid and no boiling is allowed within

the capillary structure. The heat transfer (equation (II-1)) and the pressure drop (equation (II-2)) within the wick are unidirectional and the evaporator is discretized using annular volume element.

$$\dot{Q}_i = \frac{2\pi k_{eff} l_w}{\ln\left(D_{i,ext}/D_{i,int}\right)}\left(T_i - T_{i-1}\right) \quad \textbf{(II-1)}$$

$$\Delta P_w = \frac{\dot{m}_{evap}\mu_l}{2\pi l_w \rho_l K}\ln\left(\frac{D_{w,ext}}{D_{w,int}}\right) \quad \textbf{(II-2)}$$

where $\dot{Q}_i$ represents the heat transfer from the node $i-1$ to the node i, k_{eff} is the effective thermal conductivity, l_w is the wick length, $D_{i,ext}$ is the exterior diameter of the node i, $D_{i,int}$ is the interior diameter of the node i, $D_{w,ext}$ is the external diameter of the wick, $D_{w,int}$ is the external diameter of the wick, T_i is the temperature at the node i, $\dot{m}_{evap}$ is the evaporation mass flow rate, μ_l is the liquid viscosity and ρ_l is the liquid density.

This model was compared with an experiment. The numerical response time of the LHP is always faster than what is observed experimentally, especially for low heat load. This is explained by the inaccuracy of the heat leak determination in the evaporator. Thus, they must fit numerical solution using experimental data. Indeed, they had to multiply the calculated heat leak through the wick by 0.07 to reproduce the correct start-up time.

The same year, Vlassov and Riehl (2008) [72] proposed a transient model to study the overall LHP. The condenser, the liquid and the vapour lines are spatially discretized, while the compensation chamber and the evaporator are described using an equivalent thermal nodal network (Figure II.10). This nodal representation introduces several conductances which need to be experimentally determined: $G_{w,e}$ (conductance between the evaporator wall and the liquid vapour interface), $G_{w,r}$ (conductance between evaporator wall and reservoir wall), $G_{if,r}$ (conductance between reservoir wall and vapour–liquid interface in the reservoir), $G_{if,if}$ (conductance between vapour–liquid interfaces in the evaporator and reservoir through the capillary structures) and ς_e (the fraction of the enthalpy of the incoming cold fluid directed to the evaporator core). Therefore, this model is not able to give accurate results without any preliminary ground test of the considered loop.

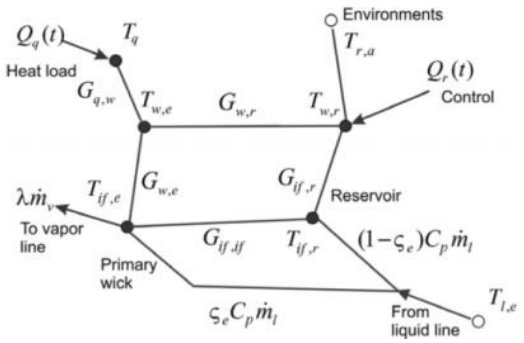

Figure II.10 –Equivalent thermal network of the evaporator-reservoir, from Vlassov and Riehl (2008) [72].

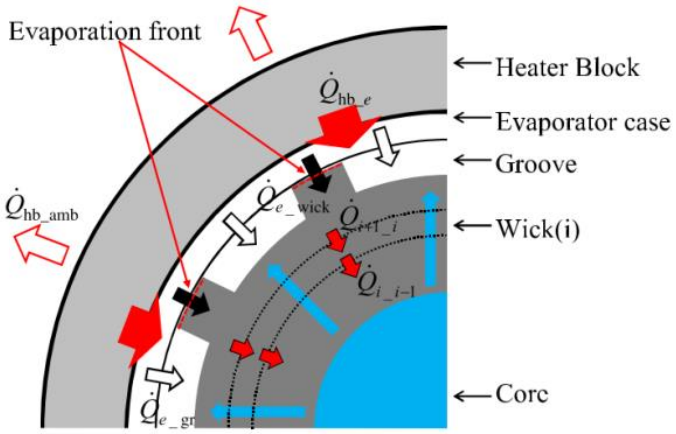

Figure II.11 – Schematic of the evaporator cross-section, from Nishikawara et al. (2013) [73].

Nishikawara et al. (2013) [73] improved the model proposed by Kaya et al. (2008) [71] and established a transient loop model with a more accurate evaporator description. Figure II.11 summarizes the heat exchanges within the evaporator. The evaporator is discretized into 11 nodes. The energy conservation equation of the compensation chamber, of the heater block, of the evaporator casing, of the grooves and of the wick are combined to compute the compensation chamber temperature, the heater block temperature, the evaporator casing temperature, the groove temperature and the wick temperature.

Several heat fluxes are distinguished: the leak $\dot{Q}_{wick,cc}$ from the evaporator to the compensation chamber; the conductive flux $\dot{Q}_{e,cc}$ from the evaporator through the evaporator; the heat exchange $\dot{Q}_{cc,bay}$ inside, across and outside the bayonet; the heat exchange $\dot{Q}_{cc,amb}$ between the compensation chamber and the ambient; the amount $\dot{Q}_{sub}$ of returning liquid subcooling; the heat load $\dot{Q}_{apply}$ applied at the external surface of the evaporator casing; the heat exchange $\dot{Q}_{hb,e}$ between the heater block and the evaporator casing; the convective heat flux $\dot{Q}_{e,wick}$ between the heater block and the ambient; the flux $\dot{Q}_{e,gr}$ due to the convection in the vapour removal channels; the heat exchange $\dot{Q}_{e,amb}$ between the evaporator casing and the ambient; and the heat conduction $\dot{Q}_{i+1,i}$ within the wick between nodes i and $i+1$. Most of the thermal conductances used in the calculation of the heat fluxes are determined experimentally. Unlike other transient loop model, the numerical response time is in good agreement with experimental results. However, numerical results predict some temperature overshoots which are not observed experimentally and the compensation chamber temperature is always under- or over-estimated. These phenomena can be attributed to the evaporator model which is too basic assuming a unidirectional flow and heat transfer and a saturated wick.

Recently, Blet (2014) [69] extended the model developed by Lachassagne (2010) and (2013) ([67] and [68]) to a transient model. This model is based on a nodal network with a 1D spatial discretization. On each node, mass, energy and momentum balances are performed. As Lachassagne (2010) and (2013) ([67] and [68]) did, the originality of this model resides in the fact that the equations are transposed using an electrical network analogy. Even though the model was improved with the addition of the transient loop behaviour, the conclusion is the same as Lachassagne (2010) and (2013) ([67] and [68]). The evaporator representation is not sufficiently detailed and the evaporator conductance is still determined

experimentally. However, the proposed model is a useful tool to pre-design a whole CPL and to predict the operating condition.

II.2.3 Summary of whole loop models

All the cited models are based on the energy conservation and the calculation of pressure loss along each component of the loop. The evaporator is discretized in one-dimension, expected for Siedel et al. (2013) [45]. The pressure drop within the wick is generally determined analytically. The heat load applied to the evaporator is divided into several heat fluxes computed from conductances which are themselves mainly determined experimentally or analytically.

The comparisons with experiments show a general good agreement but only under specific operating conditions (high heat fluxes, horizontal orientation…). Moreover, numerical response time is most of the time faster than the experimental observation. All the previously cited studies determine several parameters of the model experimentally and/or using accommodation coefficients to fit the experimental results. All the authors agree to say that their evaporator models are too simplistic. Indeed, they all consider a wick fully saturated with liquid, meaning that the evaporation only occurs at the external surface of the wick, and unidirectional flow and transfers within the evaporator.

II.3 Visualisation experiment of the evaporation process

As reported previously, in all loop system models, the authors consider a fully liquid-saturated wick. However, two works on the visualisation of the evaporation process within the capillary structure, discussed below, disproved the fully saturated state of the wick for high heat flux.

Liao and Zhao (1999) [74] and later in (2000) [75] conducted a three-dimensional experiment to observe and understand the evaporation process in a two-dimensional porous medium partially heated by a grooved block. Liao and Zhao (1999) [74] showed that a relation exists between the heat transfer coefficient behaviour, the applied heat flux and the evaporation process in the porous structure (constituted by spherical glass beads) (Figure II.12). The phase change behaviour was discussed in details based on flow visualisation in Liao and Zhao (2000) [75] where the porous structure is constructed with circular cylinders.

At low heat flux, bubbles are generated in the capillary structure below the heated surface of the block. They move downwards in the porous structure. As the imposed heat flux increases, the number of bubbles increases and coalesced bubble is formed. This coalesced bubble grows and spurts into the vapour grooves. In consequence, the liquid replenished the overall wick and the cycle of bubble generation began again. This cycle process (bubble growth, collapse and liquid replenishment) has a high-frequency which virtually led to a vapour-liquid co-existing zone, i.e. a two-phase zone. The authors observed that firstly the two-phase zone grows vertically, then it extends horizontally in a second stage. When the imposed heat flux is further increased, the surface under the fin becomes dry.

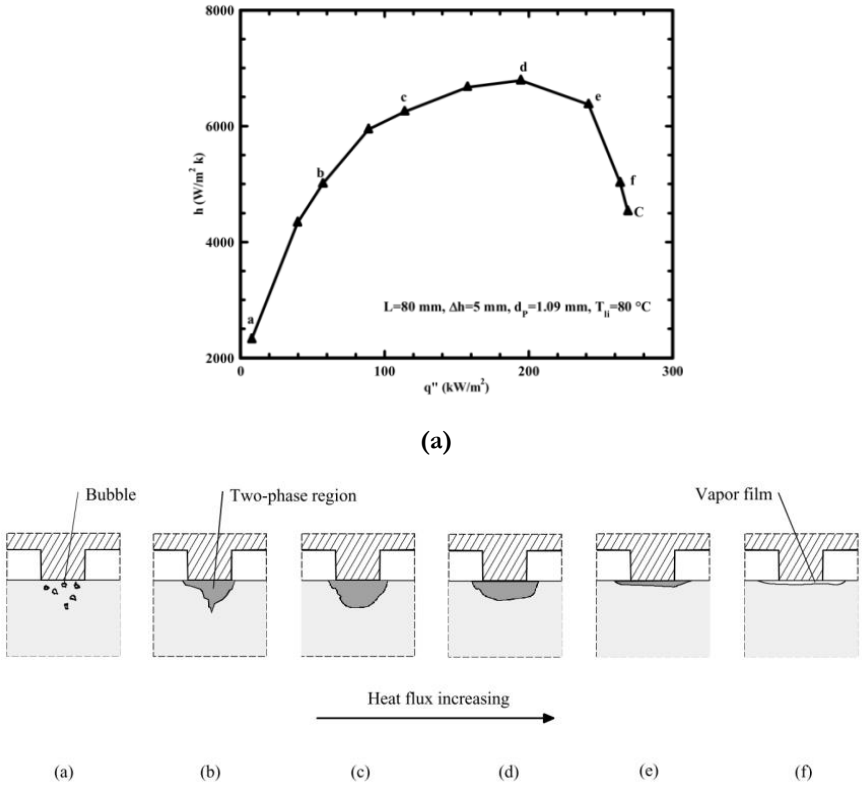

Figure II.12 – (a) Variation of the heat transfer coefficient vs the imposed heat flux. (b) Phase-change events below the heated surface when the heat flux increases, from Liao and Zhao (1999) [74].

A typical variation of the heat transfer coefficient is presented in Figure II.12a where the letter labels represent the corresponding phase-change behaviour illustrated in Figure II.12b. With the increase in the imposed heat flux, the heat transfer coefficient increases to a maximum value and then decreases afterwards. The best thermal performance is reached when a two-phase zone exists under the fin. When the heat flux becomes too high, bubbles collapse faster thus creating a vapour pocket under the casing. The lower thermal conductivity of the vapour film causes a decay of thermal performance. The authors experimentally highlighted that a two-phase zone can exist and persist under steady-state condition below the fin of the heated casing for a large range of heat flux. The occurrence of the two-phase zone is positively correlated with the best thermal performance of the device.

Coquard (2006) [1] and Mottet et al. (2015) [76] experimentally studied a quasi-two-dimensional micromodel (Figure II.13) in order to perform visualization of the invasion of the wick by vapour. The porous medium is formed by a monolayer of steel beads of 1mm diameters fixed on a brass support. The beads are randomly distributed. The metallic casing is in brass and is linked to an electric heating element to impose a heat flux. These elements are sandwiched between two Plexiglas plates and the working fluid is the Fluorinert. The experiments were carried out inside a temperature controlled enclosure. A high definition camera is used to visualize and record the evolution of the phase distribution within the wick. The dimensions of the micromodel are about one order of magnitude greater than in a real evaporator unit. Also the pore sizes are between one and two orders of magnitude

greater that in the wicks of LHP evaporator. However, the forces controlling the phase distributions, namely the capillary and viscous forces, are in the same order.

Figure II.14 shows the growth of the vapour region in the wick with an applied flux of 2W. The invasion of the wick by the vapour starts relatively close to the casing/groove/wick contact line (Figure II.14a) and grows laterally until reaching the other groove (Figure II.14b). Then vapour continues to invade the porous medium (Figure II.14c and Figure II.14d) keeping an approximately symmetric shape relative to the fin. The vapour continues to move towards the wick inlet. Finally, viscous fingers begin to appear (Figure II.14e) until vapour breakthrough (Figure II.14f).

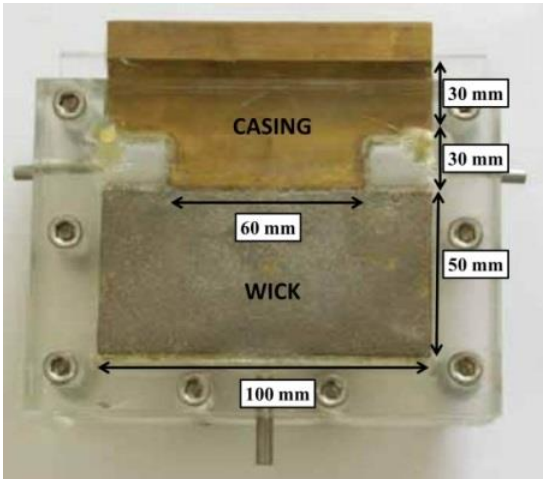

Figure II.13 – Two-dimensional model evaporator unit cell, from Coquard (2006) [1].

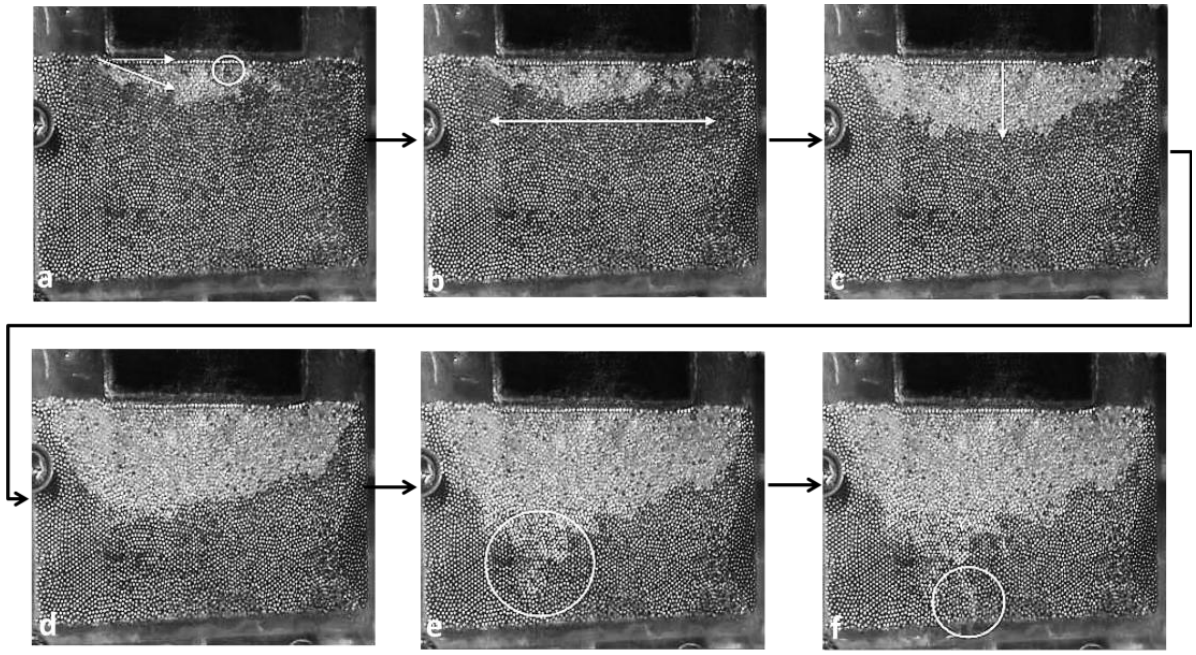

Figure II.14 – Evolution of phase distribution within the wick for a heat load of 2W. The growing zone in light grey is the region occupied by the vapour. From Coquard (2006) [1].

To summarize, under a certain heat load, the evaporation process is no longer located at the wick/groove interface and vapour occurs within the capillary structure. Considering a two-dimension unit cell, the vapour forms a vapour blanket (i.e. pocket) under the fin (Coquard (2006) [1]). However, the evaporator unit cell is expected to be three-dimensional and the 3D experiment conducted by Liao and Zhao (1999) and (2000) ([74] and [75]) predicted a two-phase zone, i.e. coexistence of the liquid and the vapour in a same region, under the heated fin.

II.4 Modelling of the capillary evaporator

As shown, there is a lack in the evaporator modelling in the whole loop system study. The evaporation process is supposed to occur at the wick/groove interface, whatever the heat load and most of the authors suppose the heat flow and the heat transfer as unidirectional. A better understanding of the processes which occur inside the capillary evaporator is needed to improve the existing loop models. To meet this need, several authors focused their attention on the key component of the two-phase loop system: the evaporator.

This section is divided into three parts as explained in the following. The first part reports the works considering a fully saturated wick, meaning that the heat load is sufficiently low to have no vapour recession. The second part discusses the evaporator model considering the occurrence of a vapour blanket under the heated fin. Actually, the first part, and even further the second, regroups the majority of the available evaporators' studies in literature. Finally, the last part itemises the few studies assuming a two-phase zone within the capillary structure.

II.4.1 Without vapour within the wick

Cao and Faghri (1994) [77] proposed a pseudo three-dimensional numerical model where the liquid flow inside the wick is computed as a 2D problem and the vapour flow inside the grooves is considered as a fully 3D problem. The fluid flow within the capillary structure is determined using a Navier-Stokes analogy equation which takes into account the convective and the viscous transport term in addition to the Darcy's law. The temperature field is computed using an advection-diffusion equation. The governing equations are solved using a finite difference approach. The flow and heat transfer problem is performed for a unit cell of a CPL evaporator as shown in Figure II.15. It is assumed that the liquid-vapour interface is located at the wick/groove interface. In other words, there is no vapour recession within the capillary structure. Moreover, it is interesting to note that the liquid-vapour mass flux $\dot{m}$ is determined using the equation (II-3) which is based on the kinetic limit of evaporation.

$$\dot{m} = \frac{2\beta}{2-\beta}\sqrt{\left(\frac{1}{2\pi R_g}\right)}\left(\frac{p_l^*}{\sqrt{T_l}} - \frac{p_v}{\sqrt{T_v}}\right) \quad \textbf{(II-3)}$$

where β is the accommodation coefficient taken equal to 0.1, p_l^* is the equilibrium saturation pressure corresponding to the interfacial liquid temperature T_l and is calculated using Clausius-Clapeyron relationship, p_v is the vapour pressure, T_v is the vapour temperature and R_g is the gas constant. The use of this relation supposes that the evaporation is controlled by the thin film region located at the junction of a pore and a meniscus. A discussion on the legitimacy to take into account the kinetic limit of

evaporation in evaporator field of application seems to be necessary as some authors use it while others not. The advantage of this formulation seems to be the occurrence of an accommodation coefficient which is used as an artificial key to control numerically the evaporation rate.

Firstly, the authors discussed the boiling limit. According to the authors, four main evaporator regimes can be distinguished depending on the heat load applied at the external envelope (Figure II.16). They described that at high fluxes, boiling may start at the wick/casing interface generating some bubbles (Figure II.16c). These bubbles may coalesce (Figure II.16d) and form a vapour blanket under the fin. These operating conditions are the same as described experimentally by Liao and Zhao (1999) and (2000) ([74] and [75]). However, the authors added that the bubbles thus created, could be expulsed at such high pressures that they may destroy the capillary meniscus and the boiling limit is reached. However, this last affirmation is not based on experimental or numerical investigations which approve or disapprove this theory. As the recession of the vapour within the wick is not included in their model, they cannot discuss the real influence of the occurrence of vapour inside the wick on the evaporator thermal performance or on the system depriming.

The main conclusion of Cao et Faghri (1994) [77] is that a 2D modelling of a unit cell evaporator is satisfying. This can be justified by the fact that the working fluids (ammonia and Freon) investigated in [77] have relatively high latent heat of vaporisation inducing a low mass flow rate of vapour within the removal channels. Therefore the vapour pressure in the grooves can be considered as uniform. They concluded that a 2D model is satisfying as long as the vapour velocity is sufficiently low.

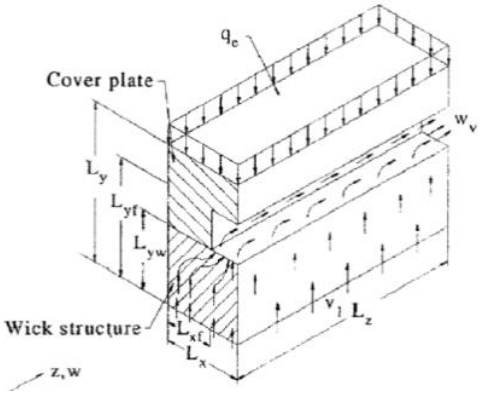

Figure II.15 – Schematic of the CPL evaporator unit cell studied by Cao and Faghri (1994) [77].

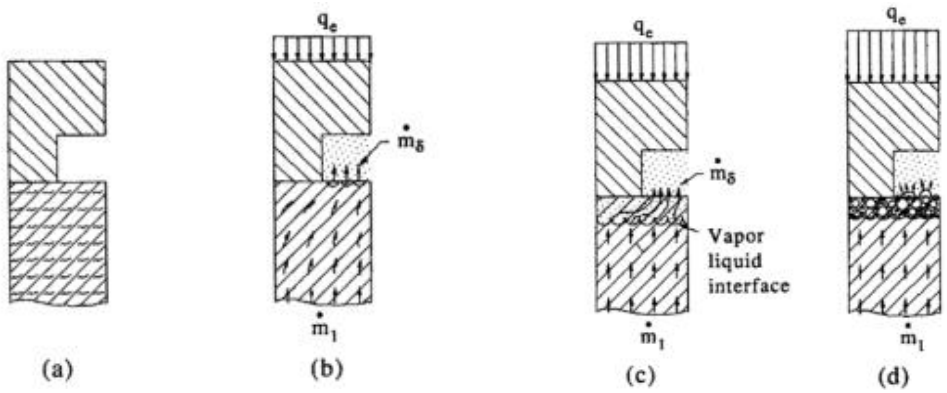

Figure II.16 – Description of different operating conditions for a CPL evaporator, by Cao et Faghri (1994) [77].

Maziuk et al. (2000) [29] compared the first three variants of groove locations defined in section I.2.5.3 (see Figure I.16). They proposed a two-dimensional steady-state model with a liquid-saturated wick to compare evaporator performances. The governing equations are discretized using a 2D finite element method. The heat flow density at the wick/groove interface, i.e. at the liquid-vapour interface, is determined by heat dissipation as equation (II-4) reflects.

$$q_g = \frac{L^2 p_v (T_{cs} - T_v) \mu^{\frac{3}{2}} \Pi}{\sqrt{2\pi R T_v}\, R T_v^2} \quad \textbf{(II-4)}$$

However, no more information is given to justify this choice. The authors showed that geometry C permits to keep a lower temperature of the evaporator envelope than geometry A and B (Figure II.17). Geometry A exceeds the maximum temperature T_{max} of the casing defined in section I.1.5.3 while geometry B, respectively geometry C, are around 5°C, respectively 15°C, lower than T_{max}.

Chernysheva and Maydanik (2008) [78] investigated the start-up process of a cylindrical evaporator (LHP). The choosen start-up scenario is as follows: there is no liquid in the central core, the wick is fully saturated with liquid and the removal channels are filled with liquid (similar to situation 4 in section I.1.3.1). The aim is to determine conditions that ensure the sucessful start-up of the device and the boiling-up of the working fluid in vapor removal channels. The authors highlight the existence of a minimum heat load assuring a sucessful start-up. Under this value, the boiling-up in the vapour removal channels cannot be achieved and the LHP never starts. The critical heat flux depends on the conditions of heat exchange between the compensation chamber and the environment as well as the geometry and the hydraulic link between the reservoir and the wick. Let's note that the problem is solved using a one-dimensional transient heat conduction model with a mesh constituted by 28 nodal points in the wick/casing for the calculation of the temperature field.

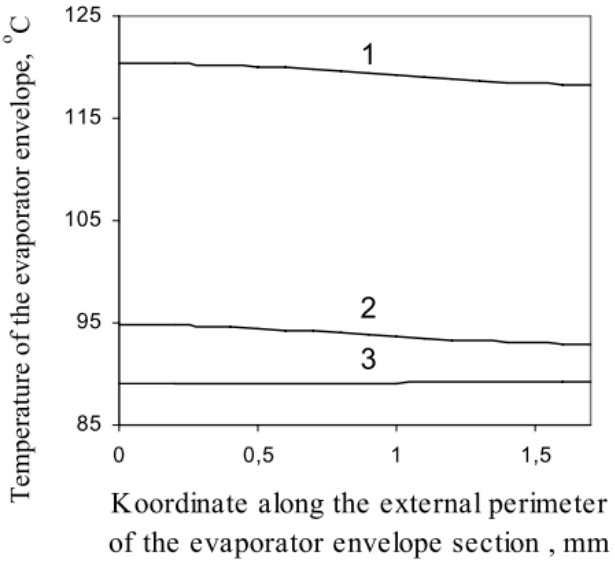

Figure II.17 – Temperature distribution on the evaporator envelop for the water LHP, from Maziuk et al. (2000) [29]. The curve number *1* refers to geometry A, the number *2* refers to geometry B and the number *3* refers to geometry C. Geometries A, B and C are defined in Figure I.16.

Li and Peterson (2011) [44] developed a three-dimensional continuum numerical model to study the heat and mass transfer of a square flat evaporator with an opposite replenishment under steady-state condition. Due to the symmetry of the structure, the computational domain is the evaporator unit cell including the liquid core, the wick, the vapour groove and the metallic casing. The wick is assumed to be fully saturated with liquid and vapour removal channels are machined in the capillary structure. The advection-diffusion equation is used to solve the temperature field within the wick, the vapour removal channel and the compensation chamber. The liquid flow within the wick is solved using the Darcy's law while the vapour flow in grooves is calculated using an analytic expression. The inlet pressure of the wick is determined from a loop model and the analytical expression of the evaporator temperature given by Chernysheva et al. (2007) [12]. All the experimental parameters needed in the analytical expression have been determined in Li et al. [58]. The governing equations are solved using a finite volume method and the upwind scheme was used for the convective term. The pressure, velocity and temperature fields are then computed. The authors showed that for a fully saturated wick, the temperature field has not any obvious difference in the vapour flow direction (in the order of 2×10^{-3}K) (Figure II.18).

The authors compared numerical results of the evaporator wall temperature with the experimental study from Li et al. (2010) [79]. Their model overestimates for high heat load or underestimates for low heat load the operating temperature by about 10 to 20K. The present model is valid as long as the heat load applied to the casing in not too high, meaning that no vapour occurs within the capillary structure. This model is not complete enough in terms of evaporation process.

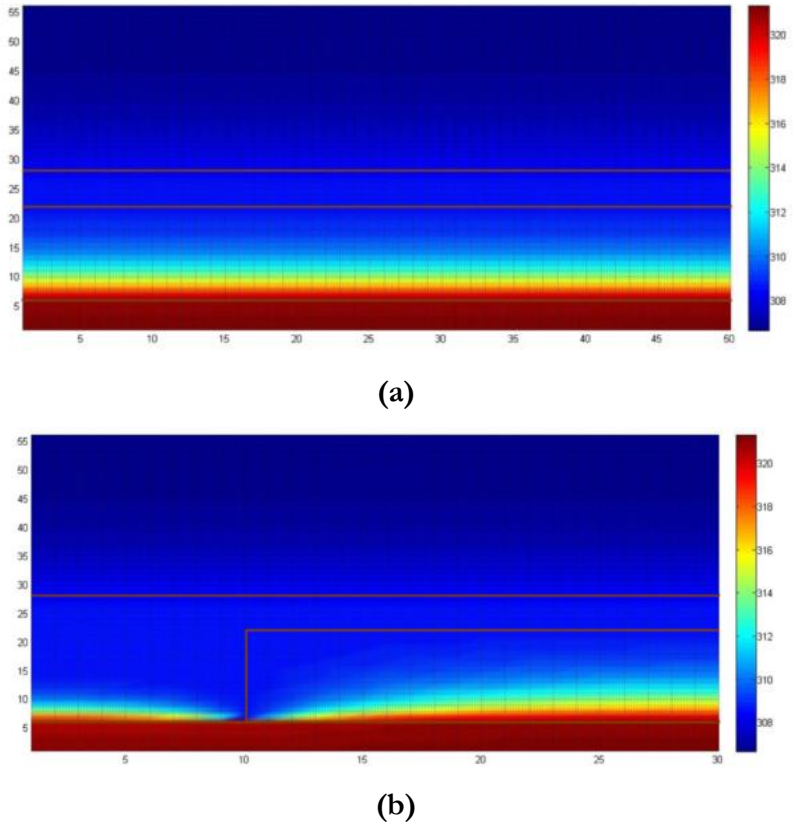

(a)

(b)

Figure II.18 – Temperature distribution in the evaporator along (a) a longitudinal section and (b) a transverse section, from Li and Peterson (2011) [44]. The computation domain, from the top to the bottom, is constituted by the compensation chamber, the wick, the vapour groove and the casing.

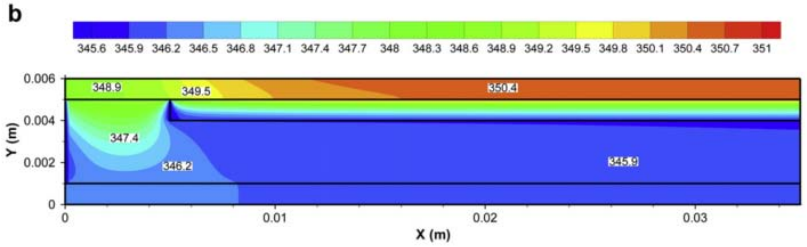

Figure II.19 – Temperature distribution in the evaporator along a longitudinal section, from Zhang et al. (2012) [27]. The computation domain, from the top to the bottom, is constituted by the upper casing, the vapour groove, the wick and the lower casing.

An almost similar three-dimensional steady-state model was published the next year by Zhang et al. (2012) [27]. The authors investigated the heat and mass transfer in the unit cell of a flat rectangular evaporator with a longitudinal replenishment of an LHP. The computation domain includes the evaporator wall, the vapour groove and the capillary structure. The vapour flow in the removal channel is modelled by the Navier-Stokes equation and an analogy Navier-Stokes equation is used for the liquid flow within the wick. Note that the wick is considered as being saturated with liquid. The exiting pressure in the grooves is determined using a loop model and the inlet wick temperature is calculated by the analytical expression proposed by Chernysheva et al. (2007) [12]. Governing equations are discretized using a finite volume method. The pressure, velocity and temperature fields are then computed. An example of temperature field is shown in Figure II.19.

The temperature along the top casing increases smoothly from 348.9K to 350.5K. In other words, the maximum temperature difference is equal to 1.6K. As evaporation occurs at the wick/groove interface, the temperature along this boundary is lower than that of the wick in contact with the casing. The authors investigated the influence of the groove dimension and location on the thermal performance of the evaporator and the wall temperature. The wall temperature is higher with grooves manufactured within the casing under the same operating conditions.

The same year, two similar papers were published by the same group using the lattice Boltzmann method. Xuan et al. (2011) [80], respectively Li et al. (2011) [81], developed a 2D, respectively a 3D, transient model for studying the heat and mass transfer within a unit cell of a cylindrical capillary evaporator of a CPL. A Navier-Stokes analogy equation and the advection-diffusion equation are used to describe the liquid flow and the heat transfer within the wick. The capillary structure is assumed to be fully saturated with liquid as the applied heat flux remains relatively low. A convective boundary condition based on the kinetic evaporation theory is used at the wick/groove interface. Governing equations and associated boundary conditions are solved using a lattice Boltzmann method (LBM). A random porous structure is generated by the Quarter-sweep Gauss-Seidel (QSGS) method. These two combined methods (LBM and QSGS) permit to take into account the complex stochastic structure of a capillary porous wick. The authors thus obtained the temperature field (Figure II.20a) and the liquid velocity field (Figure II.20b). The isotherms and the velocity streamlines are wavy. This is due to the complex structure of the wick. This effect cannot be observed with a traditional CFD method based on continuum approach. The authors also investigated the temperature contour versus time as well as the influence of the working fluid (water, ammonia and Freon-11) and the wick material (stainless steel and nickel).

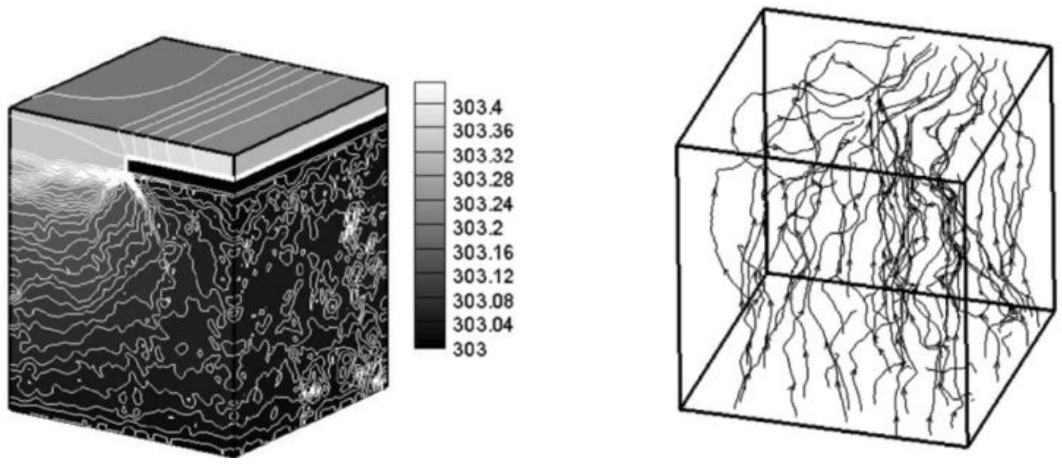

(a) **(b)**

Figure II.20 – (a) Temperature distribution and (b) liquid velocity distribution within the three-dimensional evaporator unit cell studied by Li et al. (2011) [81].

Recently Chernysheva and Maydanik (2016) [82] studied the influence on the temperature field of the convective term in the wick energy equation. Their analysis is conducted on a two-dimensional unit cell of a disk-shaped evaporator for a wick saturated with liquid. The authors concluded that the convective term can be neglected at low heat load and for conductive materials (wick and casing).

II.4.2 With vapour within the wick

Demidov and Yatsenko (1994) [55] presented a heat and mass transfer model to simulate the steady-state evaporation process and the vapour zone within a capillary structure heated by a grooved block.

They considered two operating conditions (Figure II.21):

- From low to moderate heat load, the vapour zone does not exceed the fin and two thin liquid meniscuses are located at the junction of the wick and the casing within the grooves.
- From moderate to high heat load, the vapour zone exceeds the fin and reaches the grooves. The liquid meniscuses disappear.

Both situations assume the occurrence of a vapour zone under the fin of the casing which represents the main and important assumption of this work. The vapour is assumed to be incompressible and the convective heat exchange is neglected. A vapour front of zero thickness is assumed which implies that their results are consistent for an extremely narrow pore size distribution.

The authors analysed the distribution of evaporation intensity and reported that the evaporation from the liquid meniscus could be two or three times higher than that from the surface of the wick. Moreover, when a vapour zone is developed in the capillary structure and reaches the vapour groove, the evaporation intensity decreases significantly. Combining these observations, liquid meniscuses are favourable and the authors advised to use designs which facilitate the formation of these meniscuses.

Khrustalev and Faghri (1995) [32], investigated the heat and mass transfer processes in the capillary structure heated by a triangular fin which interpenetrates the wick under steady-state condition (Figure

II.22a). For high heat flux, a stable vapour blanket within the wick under the fin is assumed and the capillary structure is characterized by a single pore size distribution. The mathematical model is 1D and is based on the kinetic theory (i.e. thin-film evaporation theory) to determine the heat flux of vapour at the liquid-vapour interface (equation (II-5)).

$$q_\delta = -\frac{2\alpha}{2-\alpha}\frac{h_{fg}}{\sqrt{2\pi R_g}}\left(\frac{p_{v\delta}}{\sqrt{T_v}} - \frac{p_{sat}}{\sqrt{T_\delta}}\right) \quad \textbf{(II-5)}$$

where α is the accommodation coefficient taken equal to 0.05, p_{sat} is the equilibrium saturation pressure corresponding to the thin liquid film temperature T_δ and is calculated using Kelvin relationship, $p_{v\delta}$ is the vapour pressure, T_v is the vapour temperature, h_{fg} is the latent heat of vaporisation and R_g is the gas constant.

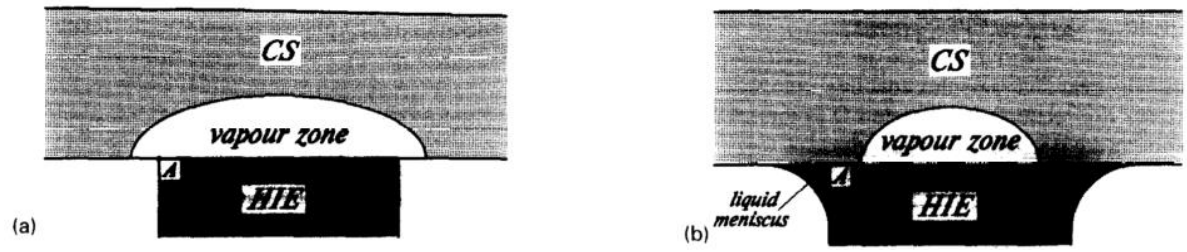

Figure II.21 – Schematic representation of the vapour zone within the evaporator unit cell studied by Demidov and Yatsenko (1994) [55]. (a) "Large" vapour zone for moderate to high heat load and (b) "small" vapour zone for low to moderate heat load. CS: capillary structure; HIE: heat input element.

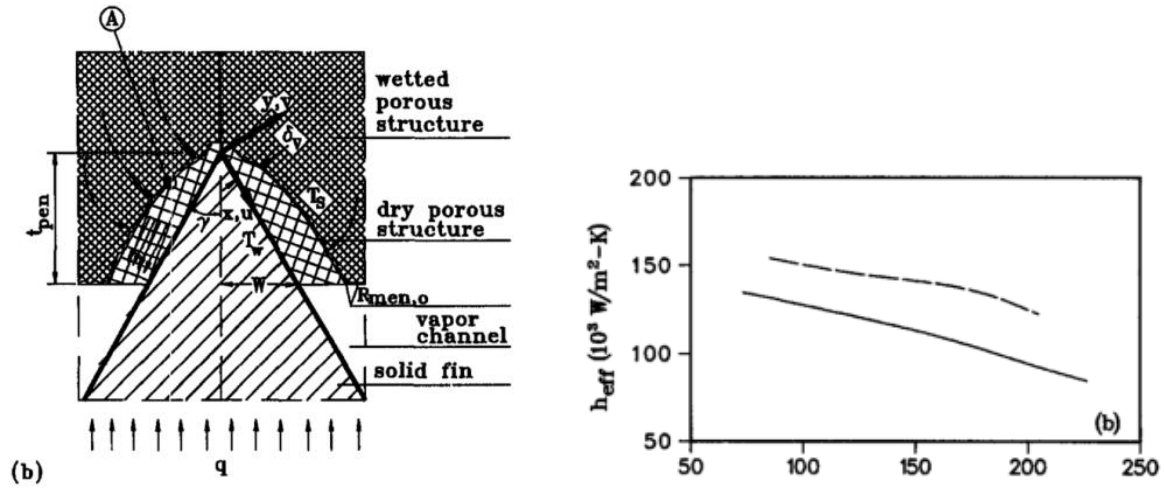

(a) **(b)**

Figure II.22 – (a) The evaporator unit cell studied by Khrustalev and Faghri (1995) [32] with interpenetrating fin within the capillary structure. (b) The variation of the heat transfer coefficient versus the applied heat load (W/cm²). Dashed curve, respectively solid curve, corresponds to a permeability equal to 1×10^{-12} m², respectively 0.5×10^{-12} m².

The authors showed that the increasing thickness of the vapour pocket in the wick resulted in the reduction of the effective heat transfer coefficient at high heat flux (Figure II.22b). Indeed, the vapour blanket forms a thermal resistance in the wick structure causing decay in thermal performance.

Figus et al. (1999) [50] compared two models to investigate the heat and mass transfer in an evaporator unit cell: a pore network model and a continuum model. Both models are solved in two-dimension, under steady-state condition and out of the gravity field. The two-phase zone, the heat transfer in the casing as well as the convective transfers in the wick were neglected. The liquid and the vapour are considered as incompressible. In both models, two main regimes are distinguished:

- For low to moderate heat loads, the wick is fully saturated with liquid. The vaporisation takes place at the wick/groove interface.
- For moderate to high heat load, a vapour pocket appears within the capillary structure. The vaporisation takes place at the wick/groove interface and within the wick.

The continuum model is based on the macroscopic equation of Darcy and the heat conduction equation. The initialization of the liquid-vapour interface within the wick is chosen arbitrarily to coincide with the saturation temperature isotherm determined by solving the temperature field in a liquid-saturated wick. Then, a finite element front tracking method based on a moving structured grid was used to obtain the liquid-vapour interface. The porous structure is characterized by a single pore size implying a smooth liquid-vapour front of zero thickness.

The originality of the second model, called the pore network model (PNM), lies in the fact that the capillary structure is depicted as a network of pores interconnected by throats (bonds) (Figure II.23) with a random size distribution. A more detailed discussion on the pore network model is available in Chapter III. A mass balance is performed at each nodes of the grid centred on the pores, while an energy balance is performed in a thinner grid centred on the throats, the pores and the solid phases. The temperature and pressure fields are determined for a fully saturated wick. Based on the nucleation theory, when the liquid reaches a given overheating, the entire first row of pores under the fin becomes in vapour state. The capillarity is treated using the Laplace's law. Thus the throats located on the liquid-vapour interface are invaded by vapour if the local pressure difference between the liquid and the vapour is greater than the capillary pressure. Then, the procedure is repeated until the stationary solution is obtained. The pores and the throats are characterized by a local hydraulic conductance depending on the local geometry. These heterogeneities lead to a sharp liquid-vapour interface.

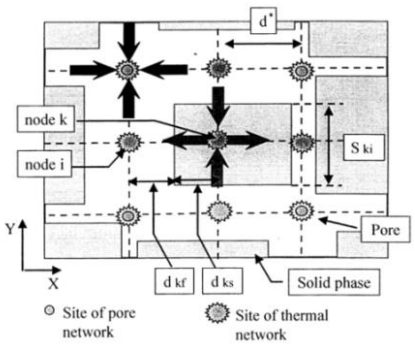

Figure II.23 – Sketch of the pore network model used by Figus et al. (1999) [50].

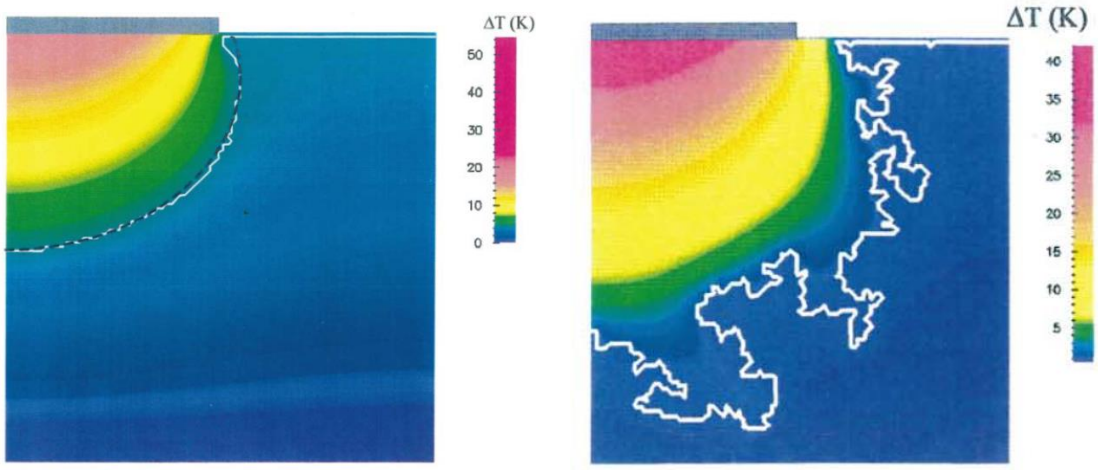

(a) **(b)**

Figure II.24 – Temperature distribution within the wick for heat load and pore size distribution. (a) Heat load of 5 000W/m² and a single pore size and (b) Heat load of 195 000W/m² for a non-uniform pore size distribution, from Figus et al. (1999) [50]. The location of the liquid-vapour interface is depicted by the white solid line for the network model and by the black dot line for the continuum model.

For a single pore size, both methods lead to the same location of the liquid-vapour interface which is smooth (Figure II.24a). The PNM highlights that the non-uniformity of the pore size distribution could lead to a premature deprime of the loop. Actually, the fractal type fronts, not predictable by the continuum model, could present capillary fingers and could cause the vapour breakthrough in the direction of the wick inlet (Figure II.24b). Moreover, the recession of the liquid-vapour interface within the wick increases with the increase in the heat load and/or with the increase in the standard deviation of the pore and throat diameter distribution. The last interesting result, reported by the authors, is the absence of correlation between the liquid-vapour interface shape and its location with the wick thermal conductivity.

Kaya and Goldak (2006) [21] developed a two-dimensional model to study the heat and mass transfer in a cylindrical evaporator unit cell under steady-state condition. Unlike Demidov and Yatsenko (1994) [55] and Figus et al. (1999) [50], the convective term in the energy equation (advection-diffusion) for the wick is taken into account. Darcy's law is used to describe the flow inside the wick. The formulation of the problem supposes a vapour region within the wick under the fin and a single pore size distribution. Consequently, the liquid-vapour front has a zero thickness.

The problem is written in polar coordinates and governing equations (mass, momentum and energy equations) are solved using the finite element method. An interfacial resistance is introduced at the wick/groove boundary when the wick is in liquid state. The calculation of this coefficient is based on the kinetic evaporation theory introducing an accommodation coefficient taken equal to 0.1. The authors reported that the value of the accommodation coefficient does not influence strongly the maximum temperature of the system located at the external surface of the casing. However, nothing is said concerning the change, or not, on the overall temperature in the wick. The authors investigated the influence of the choice of the correlation to predict the effective thermal conductivity of the porous

medium and they highlighted that the overall temperature distribution is not strongly affected by the choice of the correlation (see section I.2.5.4.5).

The important discussion broached in this study concerns the boiling limit as already discussed in section I.1.5.2. The nucleation is expected to start in microcavities at the wick-casing interface for small liquid superheat value. In this study, this value is taken equal to 4K. However, the authors asserted that if the contact between the fin and the wick is improved, this value could be much larger. Thus, Kaya and Goldak (2006) [21] followed the same approach as Mishkinis and Ochterbeck (2003) [5] based on the Kwak and Panton theory (1985) [19] (cluster nucleation theory) to determine the required superheating of the liquid to initiate nucleation in a porous medium. They obtained superheat values in the order of 70K. They concluded that a vapour region could exist and provide an escape path for the bubbles towards the grooves. Moreover, the initiation of boiling below the liquid-vapour interface is very unlikely and the boiling limit is, in practice, never reached.

Coquard (2006) [1] extended the pore network model proposed by Figus et al. (1999) [50]. The convective heat transfer within the wick and the heat transfer in the casing are taken into account. Moreover, the vapour is considered as slightly compressible. The model presented in [50] is called a mixed pore network approach since it differs lightly from [1] in terms of model formulation: the pressure and temperature fields are computed using mean field approach whereas the capillarity is managed using a classical pore network approach. Thus, the macroscopic parameters such as the permeability or the effective thermal conductivity were directly used as input parameters. The transition from the saturated liquid wick to the vapour-liquid wick is assumed to occur when a given superheat value is reached somewhere under the fin, which is the hottest region within the wick. The pore network model used in the present work is almost the same as Coquard (2006) [1] and will be discussed in details in chapter II. This model was experimentally validated for a two-dimensional porous structure as presented in section II.3. As shown in Figure II.25, Coquard (2006) [1] explained that the presence of vapour within the wick is positively correlated with the increasing of the thermal performance of the evaporator. Even though the occurrence of vapour within the wick seems to be favourable for the transfers, when the heat load increases, the evaporation heat transfer coefficient reduces when the liquid-vapour interface recedes into the wick.

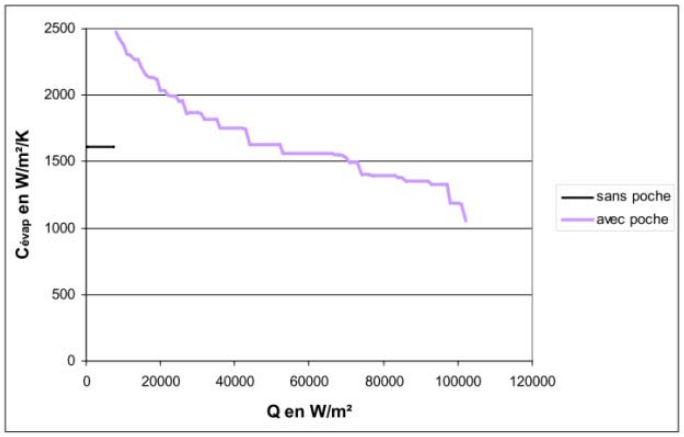

Figure II.25 – Variation of the heat transfer coefficient versus the heat load, from Coquard (2006) [1]. Black line depicts the saturated wick state and the purple line depicts the liquid-vapour wick state.

Liu et al. (2007) [52] proposed the study of heat and mass transfer within a flat evaporator of a CPL. The computational domain is limited to the capillary structure. Thermal and dynamic problems within the porous wick have been solved using the field synergy principle. The initial phase distribution inside the wick is given, 61% of the porous media is liquid, supposing a vapour pocket under the metallic casing. The influence of heat load and geometry have been investigated, showing that the width of the fin and the thickness of the wick have a great influence on flow and thermal transfer.

Wan et al. (2007, 2008 and 2011) ([83], [84] and [85]) published three similar papers where they investigated the heat and mass transfer of an overall flat plate CPL evaporator with a two-dimensional representation under steady-state condition. The liquid-vapour interface is supposed to have a zero thickness. An interface tracking method based on a moving structured grid is used to localize the liquid-vapour interface. The flow in the porous structure is described using the Brinkman-Darcy-Forcheimer equation. Governing equations are discretized using a finite difference method and solved with the SIMPLE algorithm. As the results, the authors obtained the liquid velocity field (Figure II.26) and the temperature field. The advantage of this representation is that the computational domain contains several grooves permitting to investigate the evolution of the liquid-vapour interface within the wick. As shown in Figure II.26, vapour zones are located under the fins of the casing and at the left wall side. The originality of this article is the introduction of the side wall effect heat transfer limit. Indeed, for flat evaporator, this phenomenon can induce the occurrence of vapour within the liquid grooves, which feed the wick with liquid. This effect is disastrous for the good operation of a fluid loop and can be balanced by the subcooling of the inlet liquid.

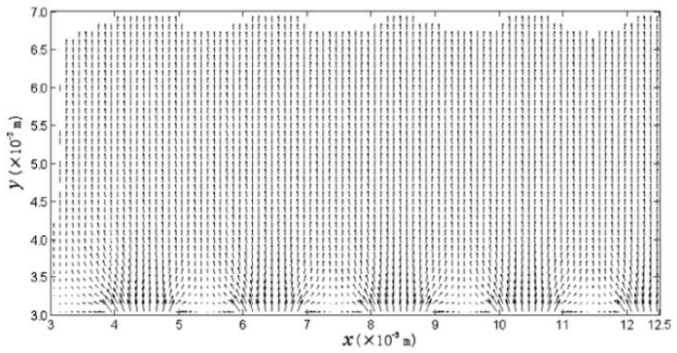

Figure II.26 – Liquid velocity vectors in the wick structure heated in the top surface ($q=3\times10^4 W/m^2$), from Wan et al. (2011) [85].

Ren and al. (2007) [57] investigated both stationary and transient problems of heat and mass transfer in the porous wick of a cylindrical evaporator (LHP) using a mixture multiphase model. The heat transfer in the casing is neglected and the computational domain is limited to a part of the evaporator. Governing equations are discretized using a finite volume method. Several interesting results are presented in this paper. This method can catch the position of the liquid-vapour interface during the transient process (Figure II.27a) and confirm that the vapour pocket moves downwards within the wick before to stabilize. For low heat flux, the liquid-vapour interface does not vary monotonously ($q=20W/m^2$ in Figure II.27c). This behaviour refers to the cycle phenomenon of "bubble growth/collapse/liquid replenishment/bubble growth" described experimentally by Liao and Zhao (2000) [75]. This is confirmed by the oscillatory heat fluxes with time as shown in Figure II.27b.

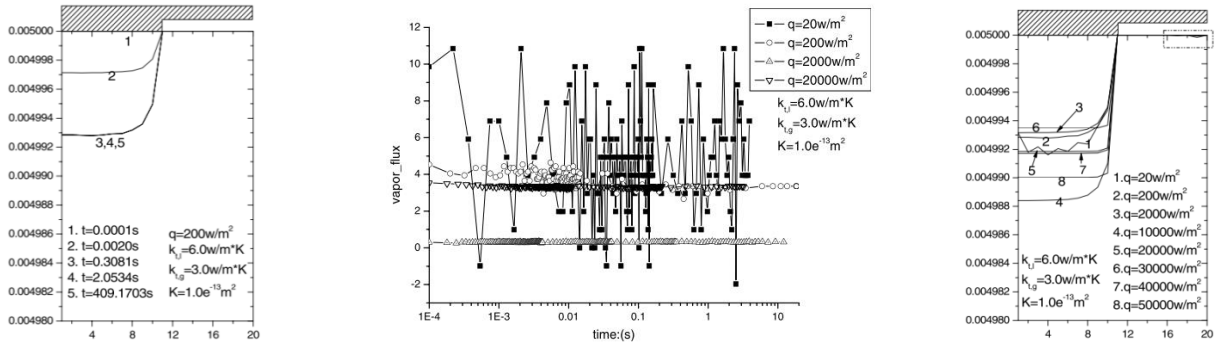

(a) **(b)** **(c)**

Figure II.27 – (a) Evolution of the position of the liquid-vapour interface during the transient process. (b) Vapour fluxes during the transient process for different heat load. (c) Location of the liquid-vapour interface at steady-state under different heat load. Extract from Ren et al. (2007) [57].

The interface behaviour with the increase in the heat load is also interesting. Indeed, as the heat flux rises, the liquid-vapour interface is first pushed back downwards the wick before retracting and becoming thinner for higher fluxes (Figure II.27c). This phenomenon is the results of the combining effect of evaporation, heat conduction and convection. The vapour blanket invades more deeply within the wick when the effect of evaporation and heat conduction is stronger than the effect of convection and less deep otherwise.

A classical pore network approach was used by Louriou (2008) [3] for simulating the transient behaviour of the vapour growth within the wick. The model is based on the classical pore network imbibition and drainage rules in two-dimension. An experiment has validated this model. The author has shown that the vapor growth in the context of a capillary evaporator is essentially controlled by the pressurisation.

A 3D steady-state numerical model for a flat copper-water evaporator with opposite replenishment is proposed by Chernysheva and Maydanik (2012) [48]. All main elements of the evaporator, including the wick, the barrier layer, the vapour removal channel, the vapour collector, the evaporator body as well as the compensation chamber are examined. The model is based on the solution of the thermal energy equation using the finite difference method. Later (first presented in (2011) [86] and then published in (2012) [87]), the authors used the same model for investigating the influence of a uniform and a concentrating heating on the external surface of the evaporator envelope. Figure II.28 depicts the temperature field of evaporator upper surface for concentrated and uniform heating. One could observe that the temperature is considered as uniform in the compensation chamber. The authors justified this choice by the agitation within the reservoir ensured by the liquid that arrives from the liquid line.

In the above model [48], the wick surface is either saturated or dried, inducing that no evaporation occurs at the spots considering as dried. This hypothesis has a direct impact on the evaporation rate as it is shown in Figure II.29 and Figure II.30. At low heat load, the evaporation takes place under the whole surface of the heater, but when the vapour occurs within the wick, the evaporation front falls down and the evaporation essentially comes from the peripheral sections of the evaporator.

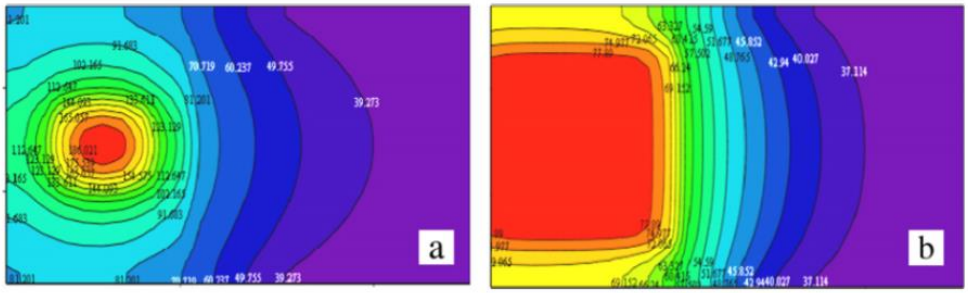

Figure II.28 – Temperature field of evaporator upper surface at heat load of 590W for (a) concentrated heating and (b) uniform heating, from Chernysheva and Maydanik [87].

It is commonly accepted that the thermal link between the evaporator and the compensation chamber plays an important role on the operating temperature of the LHP. In the continuity of previously cited works, the authors studied in more details the heat exchange in the compensation chamber filled by liquid (Chernysheva et al. (2013) [88]) for two different orientations (vertical position $\Theta = +90°$ and horizontal position $\Theta = 0°$). The temperature field of the evaporator is done in Figure II.31. The inlet liquid mass flow rate within the reservoir is equal to the vapour mass flow rate at the exit of the vapour collector. Thus, an increase in the heat load causes the decrease in the subcooled liquid temperature within the reservoir.

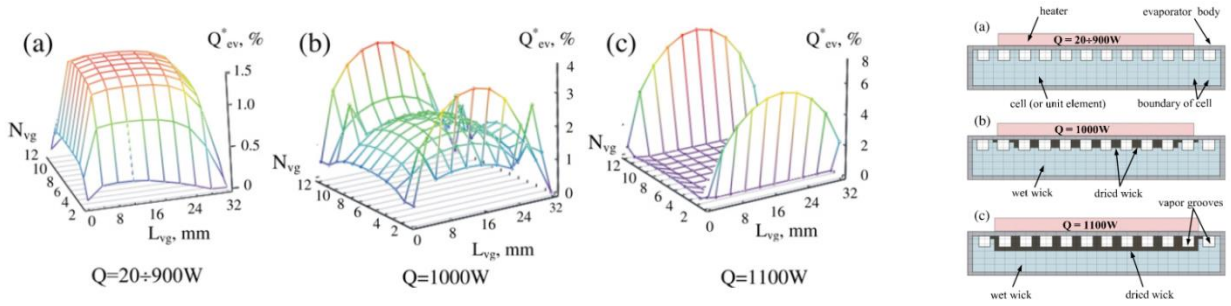

Figure II.29 – (a) Variation of the evaporating surface in active zone and (b) the corresponding phase distribution in the wick, with increasing heat load for uniform heating. From Chernysheva and Maydanik [48], [86], [87].

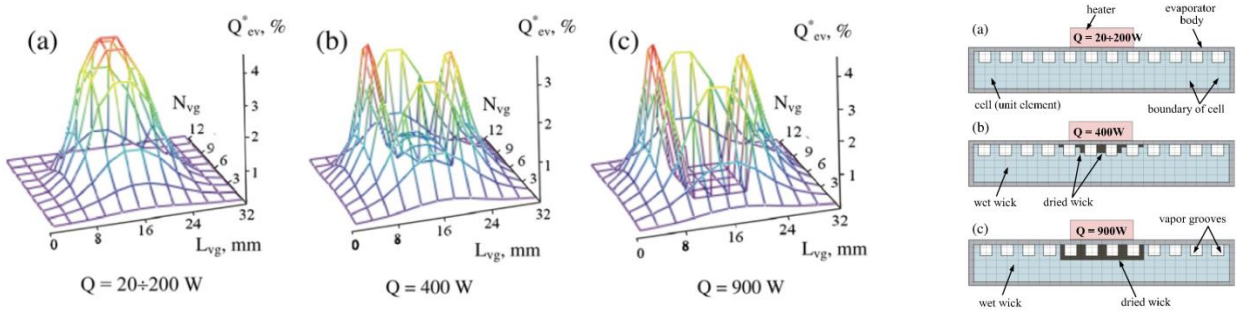

Figure II.30 – (a) Variation of the evaporating surface in active zone and (b) the corresponding phase distribution in the wick, with increasing heat load for concentrated heating. From Chernysheva and Maydanik [48], [86], [87].

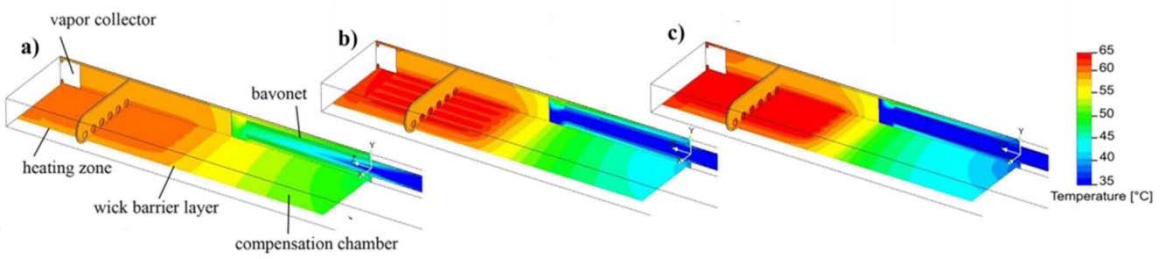

Figure II.31 – Temperature distribution in the evaporator for different heat loads (a) 100W, (b) 300W and (c) 500W, from Chernysheva et al. [88].

Through these studies ([48], [87], [88]), the authors presented an accurate three-dimensional heat and mass transfer model at the scale of the evaporator. However, in this model [48], the wick surface is either saturated or dried, inducing that no evaporation occurs at the spots considered as dried. The partially invaded wick scenario is not considered. Moreover, convective heat transfer within the wick is ignored. In the more recent study [88], the CFD software used simulates the porous material as a solid body, thus the liquid flow within the wick is not simulated.

Fang et al. (2014) [25] studied the heat and mass transfer within a flat evaporator under steady-state condition to investigate the influence of non-uniform heat load on evaporator thermal performance. The governing equations are solved using Fluent and a two-dimensional dynamic mesh model. The entire evaporator is represented in 2D: the vapour and liquid grooves, the capillary structure as well as the metallic casing. The heat transfer within grooves occurs only by conduction while the convective terms are taken into account within the capillary structure. The gravity is neglected and the fluid is considered as incompressible. The liquid-vapour interface could recede within the capillary structure. The applied heat load $q(x) = f(q_{load}, \gamma)$ is a function of q_{load} the average heat flux on the heating surface and γ the degree of heat concentration. They obtain the temperature field of the studied system for different non-uniform heat loads (Figure II.32). Comparing Figure II.32a and Figure II.32c, one can show that the vapour interface retreats within the wick for concentrated heat load. Under the same heat concentration, when the average heat load increases, the vapour flow increases, inducing a larger recede of the vapour within the capillary structure (Figure II.32b-d). The authors compared the evaporative heat transfer coefficient (defined as Adoni et al. (2012) [23], see section I.2.1) for different γ and q_{load} (Figure II.33).

For a given heat concentration, the thermal performance of the evaporator decreases when the heat load increases. On the other side, for a given heat load, it seems that it exists an optimum heat concentration leading to the best performance of the evaporator before its performance deteriorates. These two tendencies are positively correlated with the occurrence of vapour within the wick.

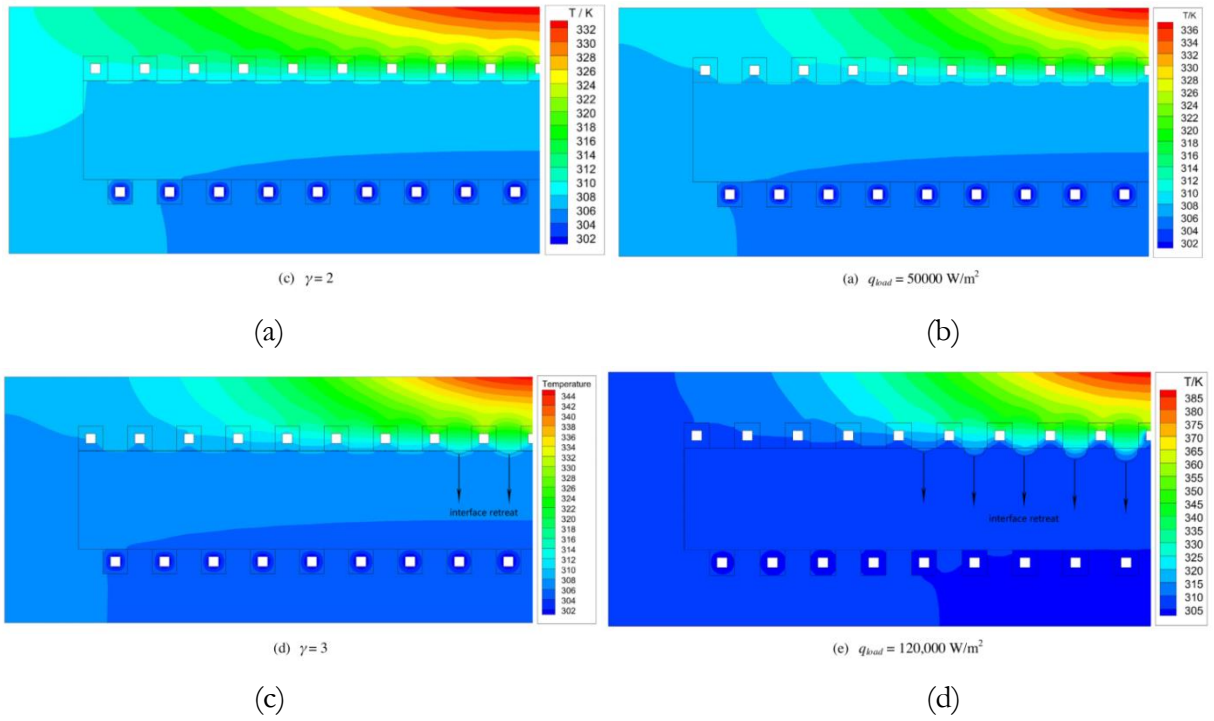

Figure II.32 –Temperature contours under different heat concentrations and different heat loads, from Fang et al. (2014) [25]. (a) q_{load}=60 000W/m² and γ=2; (b) q_{load}=50 000W/m² and γ=3; (c) q_{load}=60 000W/m² and γ=3 and (d) q_{load}=120 000W/m² and γ=3.

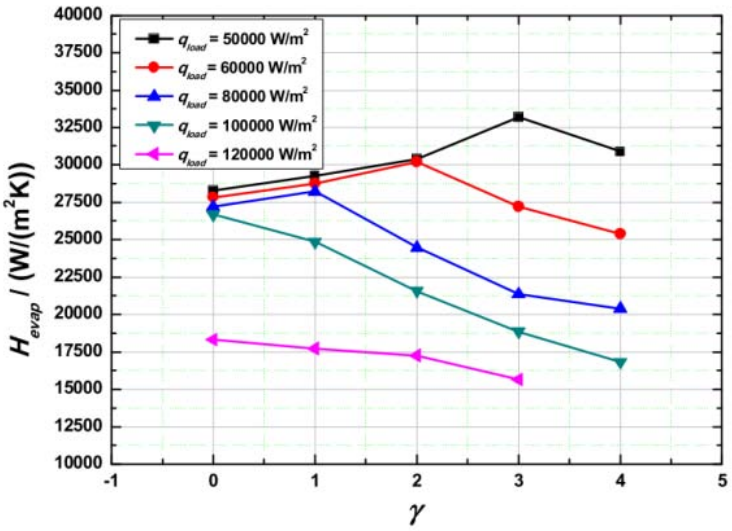

Figure II.33 – Evaporative heat transfer coefficient under different average heat fluxes with different concentrations, from Fang et al. (2014) [25].

Recently, Boubaker (2014) [28], Boubaker et al. (2015) [54] and Boubaker and Platel (2015) [89] investigated heat and mass transfer in a flat rectangular capillary evaporator [54] coupling with a complete loop model [89]. The authors proposed a transient two-dimensional separate phase model (SFM) using the volume-averaged technique to simulate the dynamic growth and stabilization of the vapour pocket within the capillary structure [54]. Darcy's law combined with the continuum equation is solved to describe the fluid flow on the porous wick, while energy equation is solved in the wick as well

as in the casing. The governing equations are solved by the finite element method. Several main assumptions are made in this model and are listed below:

- The liquid relative permeability, respectively vapour relative permeability, is taken equal to the liquid volumetric fraction, respectively vapour volumetric fraction.
- The fluid (vapour or liquid) is incompressible and has constant properties.
- The liquid-vapour transition takes place at a front of zero thickness, i.e. the porous structure is characterized by a uniform pore size distribution.

The liquid-vapour phase change within the porous wick is governed by the Langmuir's law (equation (II-6)) expressing the amount of liquid which becomes vapour at the interface.

$$\dot{\Gamma} = aS_w \sqrt{\frac{M}{2\pi RT}} \left(p_{sat}(T) - p_v\right) \quad \textbf{(II-6)}$$

where a is an accommodation coefficient taken equal to 4×10^{-4} in [28], [54], [89]. Like Cao and Faghri (1994) [77] and Kaya and Goldak (2006) [21] did, the evaporation rate is controlled by the kinetic limit of evaporation.

The diameter and the depth of the vapour zone during its growth are investigated in [54] (Figure II.34). Whatever the heat flux applied, the depth of the vapour reaches its maximal value after 10 seconds, while the diameter stabilizes after 20 seconds. This observation permits to highlight two different steps in the dynamic growth of the vapour. In a first time, the vapour grows simultaneously in the lateral and the depth direction. Then, in a second stage, the vapour continues to stretch in the lateral direction towards the grooves. In [28], Boubaker discussed the influence of the accommodation coefficient a introduced by the Langmuir's law (equation (II-6)). A small variation of this coefficient has a significant impact on the vapour pocket depth. For example, taken $a=1\times10^{-4}$, respectively $a=4\times10^{-4}$, the vapour depth is 0.52mm, respectively 0.94mm. The transient parasitic heat flux loss by conduction towards the inlet of the wick is also discussed in [54]. Their analysis provides to use a high porosity and a low wick thermal conductivity to avoid heat leak (Figure II.35a). The last results was also highlighted by Coquard (2006) [1] under steady-state conditions (Figure II.35b).

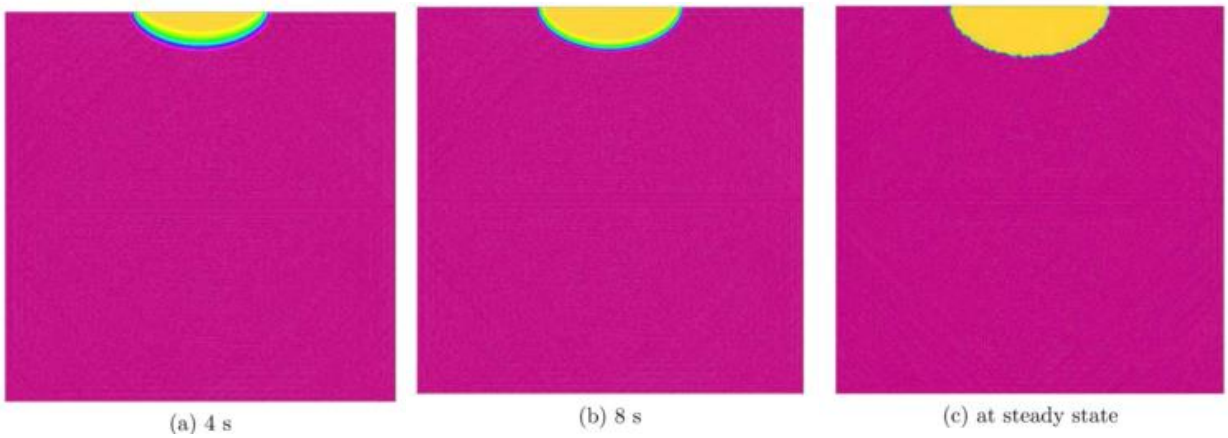

Figure II.34 – Dynamic behaviour of vapour pocket for 20W/cm², from Boubaker et al. (2015) [54].

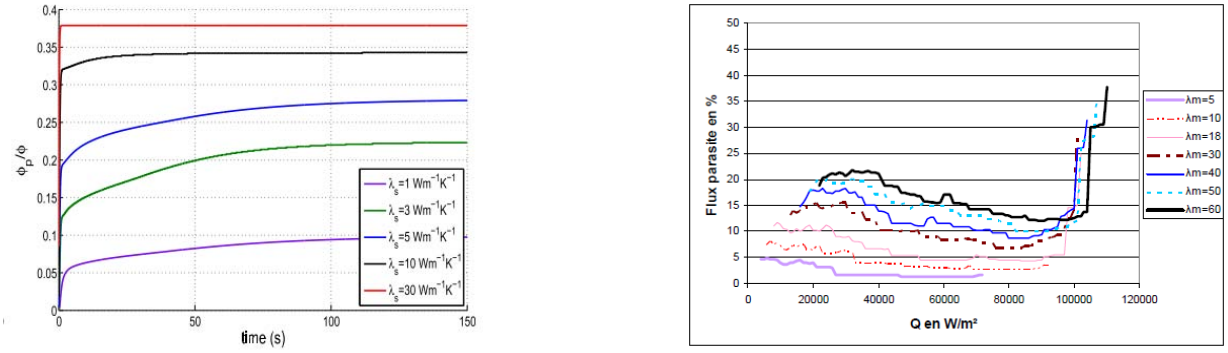

(a) (b)

Figure II.35 – Evolution of the parasitic heat flux for different thermal conductivities (a) during transient process from Boubaker et al. (2015) [54] and (b) under steady-state condition from Coquard (2006) [1].

Based on [54], Boubaker and Platel (2015) [89] have coupled the evaporator model described above and a loop model. The authors highlighted an unexpected result which is however very interesting. The shape, comprising the depth and the diameter, of the vapour zone seems to stay the same whatever the heat load applied to the evaporator envelope. This result is explained as follows: increasing the heat load implied a higher vapour mass flow rate at the exit of the evaporator (Figure II.36a). Therefore, the inlet mass flow rate of vapour at the condenser inlet also increases, resulting in a lower liquid temperature at the exit of the condenser (Figure II.36b). The subcooled liquid flows through the liquid line and the reservoir to reach the evaporator inlet. Thus, the temperature of the liquid at the inlet of wick decreases when the heat load increases. These two effects tend towards stabilizing the vapour pocket within the capillary structure. Ren et al. (2007) [57] did almost the same observation: as the heat load increases, the vapour pocket become thinner. However, their model was not coupled with a loop model. It appears from these two studies [57], [89] that some phenomena tend to stabilize the shape of the vapour within the wick.

These works [28], [54], [89] permit to highlight the presence of a vapour zone within the wick contrary to usual assumption in whole CPL/LHP models. It is the first time in literature where a whole loop model is coupled with an evaporator model taking into account the phase change within the porous wick.

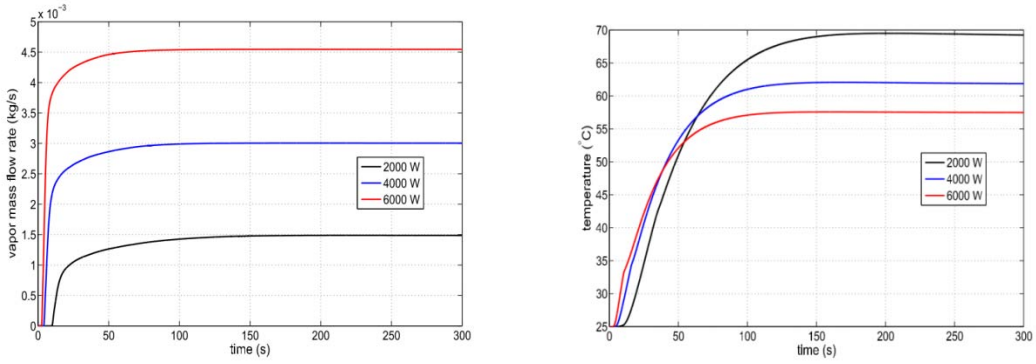

(a) (b)

Figure II.36 – (a) Vapour mass flow rate and (b) liquid temperature at the porous wick inlet for different heat loads, from Boubaker and Platel (2015) [89].

II.4.3 With a two-phase zone within the wick

Based on their above observations [74], [75], Zhao and Liao (2000) [90] developed a one-dimensional heat transfer model divided into two distinct formulations: one when the capillary structure is fully saturated with liquid (no vapour bubble) and the other when vapour bubbles occur within the wick. The transition heat flux, from which the second formulation is used, is determined experimentally. The occurrence of a vapour pocket under the fin is not investigated. As the heat load is sufficiently low, the evaporation occurs at the wick/groove boundary and the liquid saturation of the wick is equal to 1. When the heat load is higher, the saturation field of liquid is solved from the length of the two-phase zone (Figure II.37).

As shown in Figure II.37, for an applied heat load equal to 208.75kW/m^2, respectively 259.58kW/m^2, the top surface of the wick is saturated with liquid, by about 93%, respectively 63% and the length of the two-phase zone is about 3mm, respectively 9mm. The length of the two-phase zone increases with the heat load, while the wick becomes more invaded by vapour.

Based on the kinetic evaporation theory and the determination of the liquid saturation field, the temperature of the liquid film and thus the wall temperature are computed to determine the heat transfer coefficient. Their model agrees with experimental results of the heat transfer coefficient with a maximum relative difference of 11.2%.

Yan and Ochterbeck (2003) [56] developed a two-dimensional two-phase mixture model under steady-state operation. The computational domain (Figure II.38a) considers the liquid core and the capillary structure. The metallic casing is neglected and the heat flux is directly applied at the top of the wick. The velocity, pressure, liquid saturation and temperature fields are computed on the overall computation domain. This approach leads to significant variations of the saturation within the wick (Figure II.38b) and thus to the existence of an important two-phase liquid-vapour region. The influences of heat load, liquid subcooling and effective thermal conductivity of the wick structure on the evaporator performance was also studied with a special attention on the behaviour of the liquid core. The authors showed that a minimum liquid subcooling is required to avoid occurrence of vapour inside the liquid core, which could result in the dysfunction of the pumped loop.

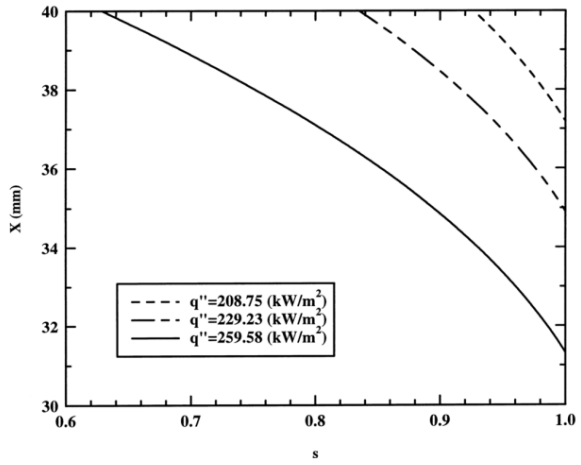

Figure II.37 – Liquid saturation distribution for different heat fluxes, from Zhao and Liao (2000) [90].

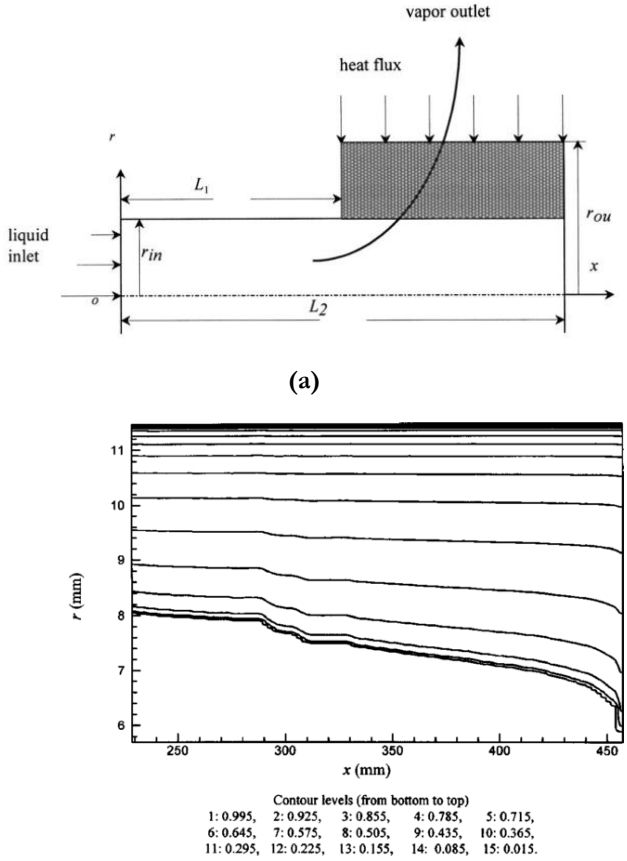

Figure II.38 – (a) Computational domain studied by Yan and Ochterbeck (2003) [56] and (b) liquid saturation field within the wick structure from Yan and Ochterbeck (2003) [56].

Huang et al. (2005) [51] and Huang and Liu (2005) [91] developed a two-dimensional mathematical model to study the heat and mass transfer with phase change in the wick of a CPL capillary evaporator. They considered that the wick can be divided into three zones: a vapour saturated zone, a liquid saturated zone and a two-phase zone located between the two previously cited zones. Primary variables of their model are the temperature, the liquid saturation, the pressure, the liquid velocity, the vapour velocity and the phase change rate. According to the liquid saturation field (Figure II.39), the usual assumption of a liquid-vapour front with zero thickness is not suitable for a large range of heat flux. However, the two-phase zone, and thus the vapour zone, recedes into the wick when the heat load is increased and the two-phase zone tends to be concentrated in a narrow scope.

In addition to these works assuming a two-phase zone, note that two other models developed by Chernysheva and Maydanik (2008) and (2009) ([30] and [31]) and by Lin et al. (2011) [49] also assume the coexistence of the liquid and the vapour within the wick. These models have been developed for a biporous wick structure. Like the Chapter V is especially dedicated to the biporous structure, these studies will be discussed in details in the previously cited section, but they are part of studies assuming a two-phase zone.

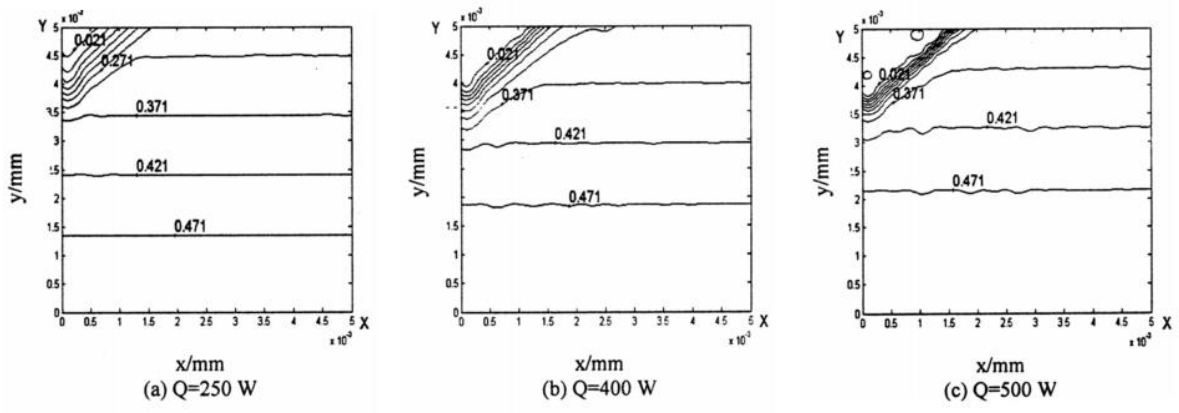

Figure II.39 – Liquid saturation field for different heat loads, from Huang et al. (2005) [51].

II.4.4 Summary of capillary evaporator models

The evaporator models available in literature and cited in the section II.4 can be divided into three mode approaches:

- **Wick saturated mode**
  The wick is assumed to be fully saturated with liquid. The evaporation process occurs at the wick/groove interface. Several three-dimensional studies are available in literature as this operating condition is simple to numerically implement in three-dimension. This representation is suitable as long as the heat flux applied at the external surface of the evaporator stays relatively low.
- **Vapour pocket mode**
  Under a certain heat load, vapour occurs within the capillary structure under the fin, creating a vapour pocket, also called a vapour blanket. The transition between the saturated and the unsaturated mode is determined arbitrarily using a given superheat from which the liquid becomes a vapour pocket. Almost all the studies are carried out in two-dimension under single pore size distribution hypothesis, i.e. a zero thickness liquid-vapour interface. The vapour pocket is valid as long as the pore size is uniform and as long as the unit cell is constituted by a single layer of pore. However, the real evaporator unit cell is three-dimensional. Thus, the vapour pocket behaviour seems to be unlikely. Note that it exists almost one three-dimensional model ([48], [87], [88]) assuming a vapour blanket.
- **Two-phase mode**
  Under a certain heat load, vapour occurs within the capillary structure. Unlike the previously described mode, a two-phase zone is formed in the wick, meaning that the liquid and the vapour coexist in the same zone. This assumption is in accordance with the experiment carried out by Liao and Zhao (1999) [74] and later in (2000) [75]. The primary variables of the two-phase models are the pressure, the temperature and the liquid saturation. However, the effective parameters, such as the relative permeability or the capillary pressure curve, are determined arbitrarily.

II.5 Synthesis and conclusion of the chapter

Two-phase loops are complex systems with several coupled mechanisms at different scales. However, the key of the loop is the evaporator component as the vaporisation process occurs inside.

The literature review was focused on numerical studies and all the models presented are summarized in Table II-1, Table II-2 and Table II-3. The review of the whole loop system model highlights that all authors considered a fully saturated wick within the capillary evaporator and unidirectional transfers. Moreover, they fitted their numerical results on experimental data by the way of conductances. Two visualisation experiments of the evaporation process within a unit cell of a capillary evaporator highlighted that a vapour blanket, respectively a two-phase zone, occurs for a two-dimensional unit cell, respectively a three-dimensional unit cell of the evaporator. As the major weak point of the loop models stays in the modelling of the evaporator, several authors focused their attention on this component. Three kinds of studies can be distinguished: the one assuming a liquid saturated wick, the one assuming a vapour pocket within the wick and the last one assuming a two-phase zone in the capillary structure.

It seems that there is still a doubt about the legitimacy of the choice between the hypothesis of a two-phase zone and/or a vapour pocket since some authors used the second one and rare others the first one. One of the challenges of this work is to confirm or deny the occurrence of a vapour pocket or a two-phase zone within the capillary structure. The pore network model seems to be the best candidate to answer this question since the pore size distribution can be non-uniform. Moreover, this method permits to simulate and to follow a non-symmetric liquid-vapour interface.

Legend for Table II-1

CE	Cylindrical Evaporator
FEOR	Flat Evaporator with Opposite Replenishment
FE	Flat Evaporator
FELR	Flat Evaporator with Longitudinal Replenishment
DOR	Disk-shaped evaporator with Opposite Replenishment
LM	Loop Model
E	whole Evaporator model
UC	Unit Cell of an evaporator
E/UC+LM	model of an Evaporator or a Unit Cell coupled with a Loop Model
L	Liquid saturated wick
L+V	occurence of Liquid and Vapour phase in the wick assuming a vapour pocket
L&V	occurence of Liquid and Vapour phase in the wick assuming a two-phase zone
$\dot{m}$	liquid-vapour mass flux based on the kinetic theory
h	convective coefficient based on the kinetic theory

Legend for Table II-2

*	Effective thermal conductivity of the wick
CS	Carbon Steel
Cu	Copper
Ni	Nickel
PE	Polyethylene
PTFE	Polytétrafluoroéthylène
Si	Silicon
SS	Stainless Steel
Ti	Titanium

Legend for Table II-3

R: H×W×L	Rectangular groove: Height×Width×Length
T: H×w×W×L	Trapezoidal groove: Height×small Width×long Width×Length
T: H×A×W×L	Trapezoidal groove: Height×Angle×Width×Length
CE: Do/Di×L	Cylindrical Evaporator: outer Diameter/inner Diameter×Length
FE: H×W×L	Flat Evaporator: Height×Width×Length
DE: D\H	Disk-shaped Evaporator: Diameter\Height

Authors	Ref	Year	Loop		Evap geometry				Grooves location		Grooves shape			Model				Condition		Wick state			Dimension			Computational domain			Kinetic limit			Specificity		
			LHP	CPL	CE	FEOR/FE	FELR	DOR	Wick	Casing	Rectangular	Trapezoidal	Other	LM	E	UC	E/UC+LM	Steady-state	Transient	L	L+V	L&V	1D	2D	3D	Groove	Casing	Wick	$\dot{m}$	h	Value	Gravity	Convection	Compressibility
Kaya and Hoang	[61]	1999	×	-	×	-	-	-	-	-	-	-	-	×	-	-	-	×	-	×	-	-	×	-	-				-	-	-	×	-	-
Chuang	[14]	2003	×	-	×	-	-	-	-	×	×	-	-	×	-	-	-	×	-	×	-	-	×	-	-				-	-	-	×	×	-
Hamdan	[18]	2003																																
Hamdan and Elnajjar	[62]	2009	×	-	-	×	-	-	-	×	-	×	-	×	-	-	-	×	-	×	-	-	×	-	-				-	-	-	-	×	-
Atabaki	[64]	2006	×	×	×	×	-	-	-	×	-	×	-	×	-	-	-	×	-	×	-	-	×	-	-				-	-	-	×	-	-
Bai et al.	[36]	2009	×	-	×	-	-	-	-	-	×	-	-	×	-	-	-	×	-	×	-	-	×	-	-				-	-	-	-	×	-
Adoni et al.	[66]	2010	×	-	-	-	-	×	-	×	×	-	-	×	-	-	-	×	-	×	-	-	×	-	-				-	-	-	-	×	-
Jesuthasan	[65]	2011	×	-	×	×	-	-	-	×	×	-	-	×	-	-	-	×	-	×	-	-	×	-	-				-	-	-	×	-	-
Lachassagne et al.	[68]	2013	-	×	-	×	-	-	×	-	-	×	-	×	-	-	-	×	-	×	-	-	×	-	-				-	-	-	×	-	-
Siedel et al.	[45]	2013	×	-	-	-	-	×	-	×	×	-	-	×	-	-	-	×	-	×	-	-	-	×	-				-	×	0.01 to 1	-	×	-
Launay et al.	[70]	2007	×	-	×	-	-	-	-	-	-	-	-	×	-	-	-	-	×	×	-	-	×	-	-				-	-	-	-	×	-
Kaya et al.	[71]	2008	×	-	×	-	-	-	-	-	-	-	-	×	-	-	-	-	×	×	-	-	×	-	-				-	-	-	-	-	-
Vlassov and Riehl	[72]	2008	×	-	×	-	-	-	×	-	-	×	-	×	-	-	-	-	×	×	-	-	×	-	-				-	-	-	×	-	-
Nishikawara et al.	[73]	2013	×	-	×	-	-	-	×	-	×	-	-	×	-	-	-	-	×	×	-	-	×	-	-				-	-	-	×	-	-
Blet	[69]	2014	-	×	-	×	-	-	×	-	-	×	-	×	-	-	-	-	×	×	-	-	×	-	-				-	-	-	×	-	-
Cao and Faghri	[77]	1994	-	×	-	×	-	-	-	×	×	-	-	-	-	×	-	×	×	×	-	-	-	×	×	×	×	×	×	-	0.1	-	×	×
Maziuk et al.	[29]	2000	×	-	-	-	-	-	×	×	×	-	-	-	-	×	-	×	-	×	-	-	-	×	-	-	×	×	-	-	-	-	-	-
Chernysheva and Maydanik	[78]	2008	×	-	×	-	-	-	×	-	×	-	-	-	×	-	-	-	×	×	-	-	×	-	-	-	×	×	-	×	?	-	-	×
Li and Peterson	[44]	2011	×	-	-	×	-	-	×	-	×	-	-	-	-	×	×	×	-	×	-	-	-	-	×	×	×	×	-	-	-	-	×	-
Xuan et al.	[80]	2011	-	×	×	-	-	-	-	×	×	-	-	-	-	×	-	-	×	×	-	-	-	×	-	-	×	×	-	×	0.1	-	×	-
Li et al.	[81]	2011	-	×	×	-	-	-	-	×	×	-	-	-	-	×	-	-	×	×	-	-	-	-	×	-	×	×	-	×	0.1	-	×	-
Zhang et al.	[27]	2012	×	-	-	-	×	-	×	×	×	-	-	-	-	×	×	×	-	×	-	-	-	-	×	×	×	×	-	-	-	-	×	×

Table II-1 – Summary of the LHP/CPL models presented in Chapter II. See page 73 for the legend.

			Loop		Evap geometry				Grooves location		Grooves shape			Model				Condition		Wick state			Dimension			Computational domain			Kinetic limit			Specificity		
Authors	Ref	Year	LHP	CPL	CE	FEOR/FE	FELR	DOR	Wick	Casing	Rectangular	Trapezoidal	Other	LM	E	UC	E/UC+LM	Steady-state	Transient	L	L+V	L&V	1D	2D	3D	Groove	Casing	Wick	$\dot{m}$	h	Value	Gravity	Convection	Compressibility
Demidov and Yatsenko	[55]	1994	-	-	-	-	-	-	-	×	×	-	-	-	-	×	-	×	-	-	×	-	-	×	-	-	-	×	-	×	?	-	×	-
Khrustalev and Faghri	[32]	1995	-	-	-	-	-	-	×	×	×	-	×	-	-	×	-	×	-	-	×	-	×	-	-	-	×	×	×	-	0.05	-	-	-
Figus et al.	[50]	1999	-	×	×	-	-	-	-	×	×	-	-	-	-	×	-	×	-	-	×	-	-	×	-	-	-	×	-	-	-	-	-	-
Kaya and Goldak	[21]	2006	×	-	×	-	-	-	-	×	-	×	-	-	-	×	-	×	-	-	×	-	-	×	-	-	×	×	-	×	0.1	-	×	-
Coquard	[1]	2006	×	-	×	-	-	-	×	×	×	-	-	-	-	×	×	×	-	-	×	-	-	×	-	-	×	×	-	-	-	-	×	×
Liu et al.	[52]	2007	-	×	-	×	-	-	-	×	×	-	-	-	-	×	-	-	×	-	×	-	-	×	-	-	-	×	-	×	?	-	×	×
Wan et al.	[83]	2007																																
	[84]	2008	-	×	-	×	-	-	-	×	×	-	-	-	×	-	-	×	-	-	×	-	-	×	-	×	×	×	-	-	-	-	×	-
	[85]	2011																																
Louriou	[3]	2008	×	-	×	-	-	-	-	×	×	-	-	-	-	×	×	-	×	-	×	-	-	×	-	-	-	×	-	-	-	-	×	×
Chernysheva and Maydanik	[86]	2011																																
	[87]	2012	×	-	-	×	-	-	×	-	×	-	-	-	×	-	×	×	-	-	×	-	-	-	×	×	×	×	-	×	?	-	×	-
	[48]	2012																																
Fang et al.	[25]	2014	×	-	-	?	-	?	-	×	×	-	-	-	×	-	-	×	-	-	×	-	-	×	-	×	×	×	-	-	-	-	×	-
Boubaker et al.	[54], [89]	2015	-	×	-	×	-	-	-	×	×	-	-	×	-	×	×	-	×	-	×	-	-	×	-	-	×	×	×	-	4×10^{-4}	×	×	-
Zhao and Liao	[90]	2000	-	-	-	×	-	-	-	×	×	-	-	-	-	×	×	×	-	-	-	×	×	-	-	-	-	×	×	-	0.03	×	-	-
Yan and Ochterbeck	[56]	2003	-	×	×	-	-	-	-	-	-	-	-	-	-	×	-	×	-	-	-	×	-	×	-	-	-	×	-	-	-	-	×	-
Huang et al.	[51], [91]	2005	-	×	-	×	-	-	-	×	×	-	-	-	-	×	-	×	-	-	-	×	-	×	-	-	-	×	-	-	-	-	×	-
Ren et al.	[57]	2007	×	-	×	-	-	-	-	×	×	-	-	-	-	×	-	-	×	-	-	×	-	×	-	-	-	×	-	-	-	-	×	×
Chernysheva and Maydanik	[30]	2008	×	-	-	-	-	-	×	-	×	-	-	-	-	×	×	×	-	-	-	×	-	×	-	-	×	×	-	-	-	×	-	-
	[31]	2009																																
Lin et al.	[49]	2011	×	-	×	-	-	-	×	-	×	-	-	-	-	×	×	×	-	-	-	×	×	×	-	-	-	×	-	-	-	-	-	-

Table II-1 – Summary of the LHP/CPL models presented in Chapter II. See page 73 for the legend.

			Material properties							
			Wick					Casing		
Authors	Ref	Year	Material	ε (%)	$K\ (m^2)$	d_{pore} (µm)	k_w	Material	k_c	Working fluid
Kaya and Hoang	[61]	1999	Ni	-	-	1.2	-	CS	-	ammonia
Chuang	[14]	2003	Ni	-	2×10^{-14}	1.6	-	Al	-	ammonia
Hamdan	[18]	2003	Si	20	3.81×10^{-14}	2.5	140	Si	140	water
Hamdan and Elnajjar	[62]	2009								
Atabaki	[64]	2006	Ni	50	2.7×10^{-10}	1.2	-	-	-	water ammonia
Bai et al.	[36]	2009	Ni	55 - 60	1.23×10^{-14}	1.5	91.4	SS	-	ammonia
			Ceramic		1.1×10^{-11}	35	1.1			
Adoni et al.	[66]	2010	Ni	60	-	5	-	Al/SS	-	ammonia
Jesuthasan	[65]	2011	Ni	50	2.7×10^{-14}	1.2	-	-	-	ammonia
Lachassagne et al.	[68]	2013	Ni	73	6.53×10^{-13}	6.8	-	SS	-	ethanol
Siedel et al.	[45]	2013	Ni	75	-	3 - 5	0.5 200	Cu	398	water
Launay et al.	[70]	2007	Ni	65	7.5×10^{-14}	1.5	*14.3	Al	-	ammonia
Kaya et al.	[71]	2008	Ni	60	2×10^{-14}	0.9	-	SS	-	ammonia
Vlassov and Riehl	[72]	2008	PE	50	1×10^{-13}	6	-	SS	-	acetone
Nishikawara et al.	[73]	2013	PTFE	50	1.3×10^{-14}	2	-	SS	-	ethanol acetone
Blet	[69]	2014	Ni	73	6.53×10^{-13}	6.8	-	SS	-	methanol
Cao and Faghri	[77]	1994	-	60	1×10^{-11}	50	10	-	38.4	ammonia freon-11
Maziuk et al.	[29]	2000	Ni	-	-	-	*8	SS	14	water acetone
Chernysheva and Maydanik	[78]	2008	Cu - Ni - Ti	60	-	-	30 - 7 - 3	Cu	380	water - ammonia
								SS	17	acetone
Li and Peterson	[44]	2011	Cu	50	6.075×10^{-11}	-	*10.36	Cu	-	water
Xuan et al.	[80]	2011	Ni	70	-	10	91	SS	25	ammonia
Li et al.	[81]	2011	Ni	70	-	10	91	SS	25	ammonia
Zhang et al.	[27]	2012	Cu	50	5.2×10^{-11}	-	*10.2	Cu	387.6	water

Table II-2 – Wick properties, casing properties and working fluid used in models presented in Chapter II. See page 73 for the legend.

Authors	Ref	Year	Material properties							Working fluid
			Wick					Casing		
			Material	ε (%)	$K\ (m^2)$	d_{pore} (µm)	k_w	Material	k_c	
Demidov and Yatsenko	[55]	1994	Cu	-	1×10^{-13}	4-10	*25	Cu	380	water
Khrustalev and Faghri	[32]	1995	-	50	1×10^{-12}	20	*10	-	438	water
Figus et al.	[50]	1999	-	40	1×10^{-13}	10	0.4	-	-	ammonia
Kaya and Goldak	[21]	2006	-	60	4×10^{-14}	-	*6.073 14.5	-	14.5	ammonia
Coquard	[1]	2006	-	25	4×10^{-14}	7	0.2 to 90	-	22	ammonia
Liu et al.	[52]	2007	-	-	1.869×10^{-10}	-	27	-	-	methanol
Wan et al.	[83]	2007								
	[84]	2008	SS	61.1	6.616×10^{-13}	-	15.2	Cu/SS	-	methanol
	[85]	2011								
Louriou	[3]	2008	Ni - PTFE	44	1.1×10^{-12}	7 - 10	0.2 - 90	-	-	ammonia
Chernysheva and Maydanik	[86]	2011								
	[87]	2012	Cu	66	-	-	-	Cu	-	water
	[48]	2012								
Fang et al.	[25]	2014	SS	61.1	-	25	-	SS	-	methylalcohol
Boubaker et al.	[54], [89]	2015	Ni	73	6.5×10^{-13}	-	5	Ni	90	methanol
Zhao and Liao	[90]	2000	Glass	36.85	-	-	*0.706	Cu/SS	-	water
Yan and Ochterbeck	[56]	2003	-	60	7.16×10^{-15}	30	*1 - *10	-	-	ammonia
Huang et al.	[51], [91]	2005	-	50	1.869×10^{-11}	-	27	-	-	ammonia
Ren et al.	[57]	2007	Ni	50	1×10^{-13}	1	*6	-	-	ammonia
Chernysheva and Maydanik	[30]	2008				3-12				water methanol
	[31]	2009	Cu	70	-	4-17 7-21	-	Cu	-	
Lin et al.	[49]	2011	Ni	70	3×10^{-13}	3.5	-	-	-	ammonia
				78	1.1×10^{-11}	1-12				

Table II-2 – Wick properties, casing properties and working fluid used in models presented in Chapter II. See page 73 for the legend.

			Groove		Wick	Casing
Authors	Ref	Year	Number	R: H×W×L or H×W T: H×w×W×L or H×A×W×L	CE: Do/Di×L FE: H×W×L DE: D\H	CE: Do/Di×L FE: H×W×L DE: D\H
Kaya and Hoang	[61]	1999	-	-	-	-
Chuang	[14]	2003	43	-	19.1mm / 9.5mm × -	24.1mm / 19.1mm × 61cm
Hamdan	[18]	2003	-	-	0.2mm × 1cm²	1mm × 1cm²
Hamdan and Elnajjar	[62]	2009				
Atabaki	[64]	2006	16	4mm² × -	10mm / 6mm × -	25.4mm / 10mm × 150mm
Bai et al.	[36]	2009	-	-	18mm / 6mm × 148mm 18mm / 12mm / 6mm × 148mm	20.4mm / 18mm × 175mm
Adoni et al.	[66]	2010	-	-	102mm \ 6mm	102mm \ -
Jesuthasan	[65]	2011	16	4mm² × -	-	-
Lachassagne et al.	[68]	2013	-	0.6mm × 0.6mm × 1.2mm × -	16mm × 68mm × 283mm	1mm × 81mm × 320mm
Siedel et al.	[45]	2013	15	1mm² × -	30mm \ 3mm	30mm \ 2mm
Launay et al.	[70]	2007	-	-	19mm / 9.9mm × -	-
Kaya et al.	[71]	2008	4	-	14mm / 6mm × -	17mm / 14mm × 200mm
Vlassov and Riehl	[72]	2008	15	2mm × 26° ×2.5mm × -	16.5mm / 7mm × 67mm	19mm / 16.5mm × 100mm
Nishikawara et al.	[73]	2013	12	1mm × 1mm × 45mm	9.5mm / 5mm × 50mm	12mm / 9.5mm × 75mm
Blet	[69]	2014	-	0.6mm × 0.6mm × 1.2mm × -	16mm × 68mm × 283mm	1mm × 81mm × 320mm
Cao and Faghri	[77]	1994	-	0.25mm × 1.5mm × 50mm	0.75mm × 3mm × 50mm	0.75mm × 2.5mm × 50mm
Maziuk et al.	[29]	2000	-	2mm × 2mm	5mm × 2mm 7mm × 2mm	UC : 3mm × 2mm 1mm × 2mm
Chernysheva and Maydanik	[78]	2008	-	0.25mm × 0.25mm	10mm / 2mm × 80mm	12mm / 10mm × 80mm
Li and Peterson	[44]	2011	-	4mm × 3mm × 25mm	5.5mm × 4.5mm × 25mm	1.5mm × 4.5mm × 25mm
Xuan et al.	[80]	2011	-	0.0625mm × 0.0125mm	0.125mm × 0.125mm	0.125mm × 0.125mm
Li et al.	[81]	2011	-	0.0725mm × 0.0125mm	0.1475mm × 0.1475mm × -	0.1475mm × 0.025mm × -
Zhang et al.	[27]	2012	-	1mm × 1mm × 30mm	4mm × 2mm × 35mm	1mm × 2mm × 35mm

Table II-3 – Groove, wick and casing geometry dimensions in models presented in Chapter II. See page 73 for the legend.

			Groove		Wick	Casing
Authors	Ref	Year	Number	R: H×W×L or H×W T: H×w×W×L or H×A×W×L	CE: Do/Di×L FE: H×W×L or H×W DE: D\H	CE: Do/Di×L FE: H×W×L DE: D\H
Demidov and Yatsenko	[55]	1994	-	70µm × 130µm	200µm × 200µm	70µm × 70µm
Khrustalev and Faghri	[32]	1995	-	-	-	-
Figus et al.	[50]	1999	-	3mm × -	5mm × 5mm	-
Kaya and Goldak	[21]	2006	-	-	21.9mm / 14.66mm	25.4mm / 21.9mm
Coquard	[1]	2006	-	1.5mm × 4mm	5mm × 10mm	3mm × 10mm
Liu et al.	[52]	2007	-	-	5mm × 5mm	-
Wan et al.	[83]	2007				
	[84]	2008	-	0.5mm × 0.5mm	4mm × 18.5mm	-
	[85]	2011				
Louriou	[3]	2008	-	-	1.4mm × 1.4mm	-
Chernysheva and Maydanik	[86]	2011				
	[87]	2012	12	1.8mm × 1.8mm × 32mm	6mm × 41mm × 40mm	0.5mm × 42mm × 80mm
	[48]	2012				
Fang et al.	[25]	2014	19	1mm × 1mm	4mm × 37mm	3mm × 43mm
Boubaker et al.	[54], [89]	2015	-	0.16mm × 0.33mm	1mm × 1mm	0.33mm × 1mm
Zhao and Liao	[90]	2000	-	1.5mm × 1.5mm × 1.5mm	-	31mm × 100.5mm × 28mm
Yan and Ochterbeck	[56]	2003	-	-	22.9mm / 11.4mm × 228.6mm	-
Huang et al.	[51], [91]	2005	-	3mm × -	5mm × 5mm	-
Ren et al.	[57]	2007	8	-	5mm × 1mm	-
Chernysheva and Maydanik	[30]	2008	-	1.4mm × 0.9mm	1.8mm × 1.6mm	0.5mm × 1.6mm
	[31]	2009		1.8mm × 0.9mm	2.2mm × 1.7mm	0.5mm × 1.7mm
Lin et al.	[49]	2011	8	-	12.5mm / 9mm × 40mm	15.5mm / 12.5mm × 40mm

Table II.3 – Groove, wick and casing geometry dimensions in models presented in Chapter II. See page 73 for the legend.

Chapter III Pore network modelling

Chapter III Pore network modelling 81
III.1 Pore network model 82
III.2 Mathematical model 85
III.3 Numerical method 94
III.4 Model validation and effective thermal conductivity correlation 100
III.5 Results and discussions 108
III.6 Synthesis and conclusion of the chapter 115

This chapter presents the mixed pore network model developed in this thesis. The computational domain corresponds to the three-dimensional unit cell of the evaporator. The model takes into account the heat and mass transfer within the wick and the heat transfer in the casing as well as the fluid flow in the capillary structure. The model is validated from a comparison with an experiment found in literature. This comparison led us to open a discussion on the effective thermal conductivity correlation. Finally, a discussion is performed on the evaporator thermal performances from the analysis of the liquid-vapour phase distribution in the 3D evaporator unit cell.

III.1 Pore network model

III.1.1 General description

At microscopic level, a porous medium is composed of solid material and voids as explained in section I.2.5.4 (see Figure I.23 and Figure I.24). A two-dimensional scheme of a porous medium is depicted in Figure III.1. The void space is represented as a network of sites, called the pores, (i.e. the larger voids) connected by throats, also called bonds (i.e. the constrictions of the pore space). Two main types of pore network can be distinguished: unstructured (as illustrated in Figure III.1b and Figure III.1c) or structured. While unstructured pore networks are a priori more representative of a real structure because they follow the skeleton of the pore space, structured pore networks will be used in the present work because they are simpler and computationally more efficient. More precisely, the porous microstructure will be represented by: a square pore network in 2D (Figure III.2a) or a cubic pore network in 3D (Figure III.2b). In this classical representation, each pore has four neighbours in the square network, and six in the cubic network. In 3D networks the pores are generally represented as spheres and the throats as cylinders leading to the so-called sticks and balls representation (Figure III.2b). Pores can be also represented by cubes and throats by rectangular cuboid shapes (Figure III.2c). The pore/throat diameters are distributed randomly according to a given probability distribution function (p.d.f.). The distance between two pores, i.e. nodes, is the lattice spacing, noted a and is constant in each direction.

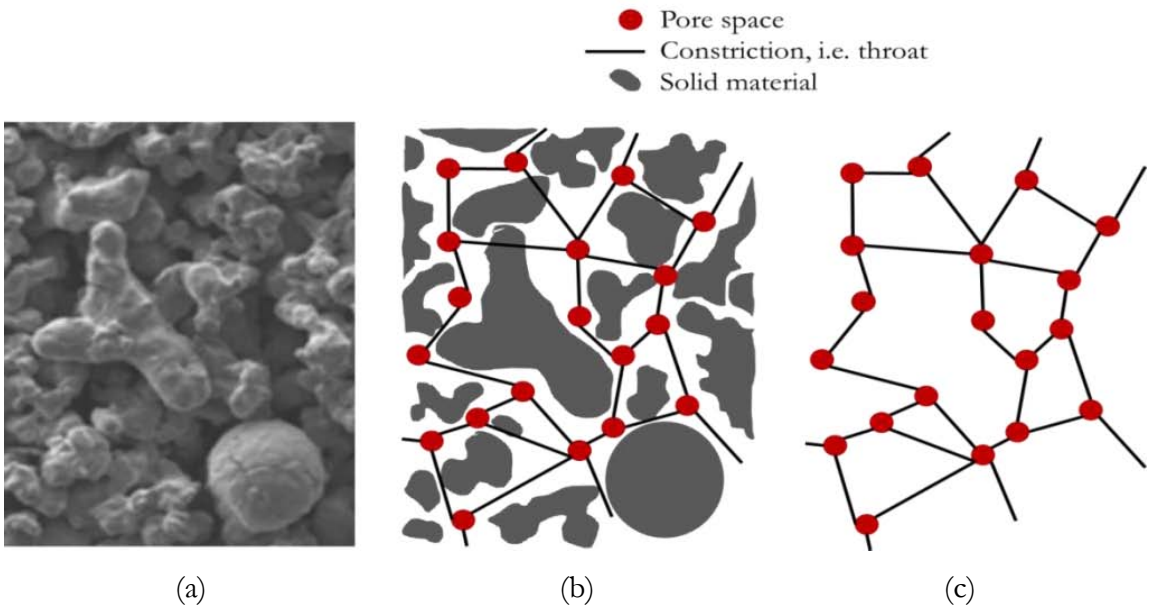

Figure III.1 – (a) Part of an SEM picture of a copper wick from Li and Peterson (2011) [44]. (b) and (c) Schematic of a pore network. The pore space is represented as a network of sites (red circles) connected by throats (black lines) (corresponding to the constrictions of the pore space).

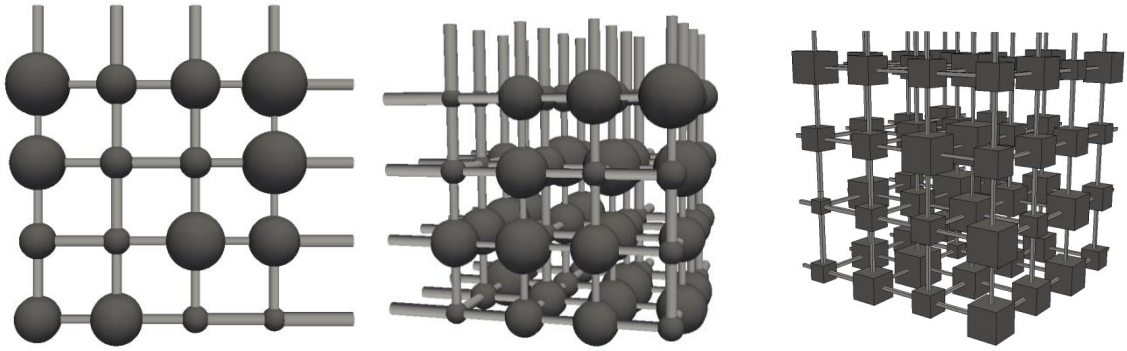

(a) (b) (c)

Figure III.2 – Pore network representation of a porous microstructure by a 2D square network with cylindrical throats and spherical pores (a), a 3D cube network with cylindrical throats and spherical pores (b), and a 3D cube network with cuboid throats and cubic pores (c).

III.1.2 Classical pore network model

In the classical pore network approach, the mass flow rate between two adjacent nodes i and j is expressed as:

$$q_{ij} = \rho \frac{g_{ij}}{\mu} (P_i - P_j) \quad \textbf{(III-1)}$$

where ρ is the density of the fluid, μ is the dynamic viscosity, g_{ij} is the hydraulic conductance and P_i and P_j are the pressures in the pore i and j respectively.

For cylindrical throats, the hydraulic conductance is expressed assuming a Poiseuille flow in the throat and is a function of the local geometry dimensions (equation (III-2)).

$$g_{ij} = \frac{\pi d_{ij}^4}{128 l_{ij}} \quad \textbf{(III-2)}$$

where d_{ij} is the diameter of the throat and l_{ij} its length.

Note that for cuboid throats, the hydraulic conductance is expressed by equation (III-3) (Gostick et al. (2007) [92]).

$$g_{ij} = \frac{0.1425\, d_{ij}^4}{2 l_{ij}} \quad \textbf{(III-3)}$$

The pressure field (liquid or vapour) is computed from the mass balance expressed at each node of the network (equation (III-4)).

$$\sum_j q_{ij} = 0 \quad \textbf{(III-4)}$$

where i is the considered node and j denotes the four (six respectively) neighbour nodes for a square (cubic respectively) representation.

III.1.3 Mixed pore network model

With the approximation of mixed pore network model the throat hydraulic conductance $\bar{g}$ is taken as a constant, i.e. is the same for every throat. The mass flow rate in a throat is defined by

$$q_{ij} = \rho u_{ij} a^2 \quad \textbf{(III-5)}$$

where u_{ij} is the fluid velocity in the considered throat.

Considering the classical Darcy model for the flow in a porous structure (equation (III-6)), a classical finite volume discretization leads to equation (III-7).

$$\mathbf{u} = -\frac{K}{\mu}\nabla P \quad \textbf{(III-6)}$$

$$u_{ij} = -\frac{K}{\mu}\frac{\left(P_j - P_i\right)}{a} \quad \textbf{(III-7)}$$

where K is the permeability.

Finally, combining equation (III-5) and equation (III-7), the mass flow rate between two adjacent nodes can be expressed by equation (III-8).

$$q_{ij} = \rho a \frac{K}{\mu}\left(P_i - P_j\right) \quad \textbf{(III-8)}$$

Comparing equation (III-1) and equation (III-8) leads to express the mean hydraulic conductance $\bar{g}$ as

$$\bar{g} = aK \quad \textbf{(III-9)}$$

The mean hydraulic conductance is a function of the permeability, i.e. a macroscopic parameter. The pressure field is then computed, as in the classical pore network approach, from the mass balance expressed at each node. Hence, the mixed pore network approach can be regarded as a mean field approximation of the flow in the considered disordered porous structure, and the method is actually fully equivalent to the finite volume discretized form of the Darcy's formulation.

III.2Mathematical model

III.2.1 Hypothesis and computational domain

Operating conditions

The model is developed under steady-state operating condition assuming negligible gravity effects. The radiative effects are neglected. The liquid core is fully saturated with liquid. The temperature is considered as uniform in the compensation chamber due to the agitation within the reservoir due to the liquid arriving from the liquid line. The heat load applied at the external surface of the casing is uniform.

Capillary wick

The wick structure is rigid, isotropic and homogeneous. The local thermal equilibrium between the porous structure and the working fluid is assumed. The pores can be spherical or cubic and the throats can be cylindrical or parallelepipedal. Both representations are implemented in the numerical code and the choice has no influence on numerical results.

Working fluid

The working fluid is Newtonian. The liquid, considered as perfectly wetting, is incompressible and has constant properties. The vapour is slightly compressible and the ideal gas law is used to determine the vapour density (equation (III-10)).

$$\rho_v = \frac{P_v M}{RT} \qquad \textbf{(III-10)}$$

Computational domain

The computational domain is depicted in Figure III.3. It corresponds to the three-dimensional evaporator unit cell defined in section I.2.3 and depicts in Figure I.11b.

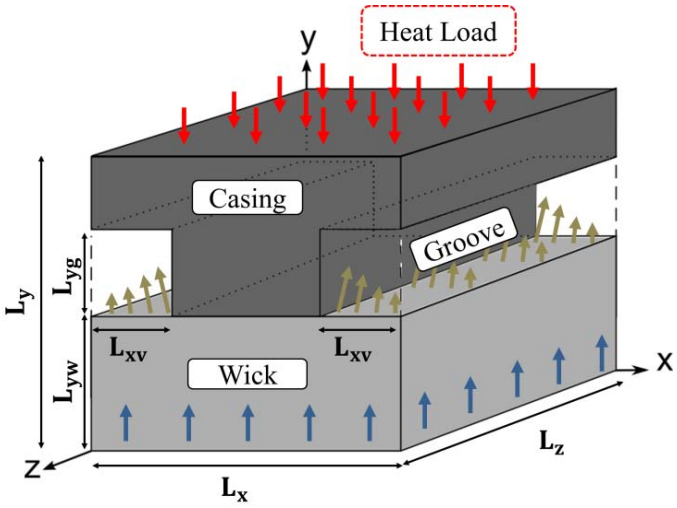

Figure III.3 – Three-dimensional computational domain with the grooves in the casing.

The representative unit cell is taken far enough from the wall separating the wick from the compensation chamber. There is hence no wall side effect. The liquid core/compensation chamber is not studied and is justified by the hypothesis of a uniform temperature within the reservoir. Compared to the pressure drop inside each component of the loop, the groove pressure loss is negligible. Therefore, the transfers and the flow within the vapour removal channel are not solved, and the temperature/pressure is uniform in the vapour grooves.

A shown in Figure III.3, the computational domain is considered as centred on the fin with two half groove on each side. Since the beginning of the present manuscript, the choice was made to consider unit cells as sketched in Figure III.3, instead of half unit cell. This choice is justified by the non-symmetrical distribution of the pore size within the wick. Indeed, the pore sizes and throat sizes are randomly distributed. As a result, the pore/throat size distributions are not symmetrical within the wick.

III.2.2 Governing equations

III.2.3 Flow in the porous structure

As explained in section III.1.3, the flow is described using Darcy's law (equation (III-11)) combined with the continuity equation (equation (III-12)).

$$\mathbf{u_i} = -\frac{K}{\mu_i}\nabla P_i \qquad \textbf{(III-11)}$$

$$\nabla.(\rho_i \mathbf{u_i}) = 0 \qquad \textbf{(III-12)}$$

where i denotes the liquid l or the vapour phase v depending on whether the considered node is occupied by the liquid or the vapour. The permeability K is determined using the classical pore network approach as explained in Appendix C.

The adequacy of the Darcy law, instead of Darcy-Brinkman or Darcy-Brinkman-Forcheimer laws, for describing the fluid behaviour within the wick of a capillary evaporator is discussed in Kaya and Goldak (2006) [21]. The authors concluded that Darcy's law is sufficient as each non Darcy's terms (viscous transport term, convective transport term, inertia term…) is negligible.

III.2.4 Heat transfer

Casing

Heat transfer is considered to occur by conduction in the metallic wall of the evaporator,

$$\nabla.(k_c \nabla T) = 0 \qquad \textbf{(III-13)}$$

where k_c is the thermal conductivity of the casing.

Wick

Heat transfer occurs by conduction and convection within the wick,

$$(\rho_i c_{p,i})\mathbf{u_i}.\nabla T = \nabla.(k_i^* \nabla T) \quad \textbf{(III-14)}$$

where i denotes the liquid l or the vapour v phase depending on whether the considered node is occupied by the liquid or the vapour, $(\rho_i c_{p,i})$ is the heat capacity and k_i^* is the effective thermal conductivity (see section I.2.5.4.5) of the wick filled with the phase i.

Simulations presented in this thesis will be performed for different wick and casing material and for a somewhat large range of heat flux. Therefore, in accordance with the discussions in Chernysheva and Maydanik (2016) [82], the convective term is kept into the energy equation.

III.2.5 Boundary conditions

III.2.5.1 Inlet of the wick

The temperature and the pressure at the inlet of the wick are specified as expressed by equation (III-15). They correspond to the pressure and the temperature in the compensation chamber. A subcooling value ΔT_{sub} can be introduced.

$$T = T_{sat} - \Delta T_{sub} = T_{cc},\ P = P_{sat}(T_{sat}) = P_{cc} \quad \textbf{(III-15)}$$

III.2.5.2 External surface of the evaporator wall

The heat load is applied at the external surface of the metallic casing (equation (III-16)).

$$(k_c \nabla T).\mathbf{n} = q \quad \textbf{(III-16)}$$

where $\mathbf{n}$ is the interface normal unit vector and q (W/m^2) the heat flux applied to the casing.

III.2.5.3 Lateral sides

Spatially periodic boundary conditions are imposed on the lateral sides of computational domain.

III.2.5.4 Grooves

The groove pressure (equation (III-17)) is determined as the sum of the compensation chamber pressure P_{cc} and the total pressure drop inside the loop ΔP_{loop}. ΔP_{loop} is computed using the loop model presented in Li and Peterson (2011) [44] and reported in details in section III.2.6. The approximation is made that the temperature in the groove T_g is close to the saturation temperature at the pressure P_g in the groove (equation (III-18)). The groove temperature is determined using the Clausius-Clapeyron relationship.

$$P_g = P_{cc} + \Delta P_{loop} \quad \textbf{(III-17)}$$

$$T_g = T_{sat}(P_g) \quad \textbf{(III-18)}$$

III.2.5.5 Casing/groove interface

A convective boundary condition is used at the casing/groove interface (equation (III-19)).

$$(k_c \nabla T).\mathbf{n} = h_g\left(T - T_g\right) \quad \textbf{(III-19)}$$

The heat transfer coefficient h_g between the casing and the vapour flow within the groove is computed using the correlation given by Sleicher and Rouse (1975) [93]. This correlation is expressed in terms of the Nusselt number and is valid for a fully developed flow inside a rectangular pipe. The Nusselt number is expressed by equation (III-20).

$$Nu = 5 + 0.015\, Re^a\, Pr^b \quad \textbf{(III-20)}$$

where a and b are determined using equation (III-21) and equation (III-22).

$$a = 0.88 - \frac{0.24}{4 + Pr} \quad \textbf{(III-21)}$$

$$b = \frac{1}{3} + 0.5\exp(-0.6\, Pr) \quad \textbf{(III-22)}$$

The Prandtl number Pr is the ratio between the momentum diffusivity and the thermal diffusivity of the vapour (equation (III-23)).

$$Pr = \frac{\mu_v c_{p,v}}{k_v} \quad \textbf{(III-23)}$$

where μ_v is the dynamic viscosity of vapour, $c_{p,v}$ is the vapour specific heat and k_v is the vapour thermal conductivity.

The Reynolds number Re is the ratio between the momentum forces and the viscous forces (equation (III-24)).

$$Re = \frac{u_v \rho_v D_H}{\mu_v} \quad \textbf{(III-24)}$$

where u_v is the vapour velocity and D_H is the hydraulic diameter.

The hydraulic diameter is defined from the perimeter P and the surface S of the groove (equation (III-25)).

$$D_H = \frac{4S}{P} \quad \textbf{(III-25)}$$

Combining equations (III-20) to (III-25), the convective coefficient h_g can be computed using the Nusselt number definition (ratio of convective to conductive heat transfer) (equation (III-26)).

$$h_g = \frac{Nu\, k_v}{D_H} \quad \textbf{(III-26)}$$

III.2.5.6 Casing/wick interface

The contact between the wick and the casing is considered as ideal. In other words, there is no contact resistance. Hence, energy conservation is expressed at the junction between the wick and the fin (equation (III-27)). Moreover, as the casing is viewed like a wall, a no pressure gradient condition is implemented (equation (III-28)).

$$(-k_i^* \nabla T).\mathbf{n} = (-k_c \nabla T).\mathbf{n} \quad \textbf{(III-27)}$$

$$\nabla P.\mathbf{n} = 0 \quad \textbf{(III-28)}$$

where i denotes the liquid l or the vapour v phase depending on whether the considered node is occupied by the liquid or the vapour.

To take into account the abrupt changes in conductivity at the wick/casing interface, a compound value of the thermal conductivity is used. Thus, the thermal conductivity is determined using a harmonic mean between the effective thermal conductivity of the wick and the thermal conductivity of the casing.

III.2.5.7 Wick/groove interface

The boundary condition at the wick/groove interface depends on the fluid occupying the considered pore.

If the pore is in liquid state

Energy conservation (equation (III-29) is expressed together with the temperature continuity (equation (III-30)) if the pore is in liquid state at the wick/groove interface.

$$(-k_l^* \nabla T).\mathbf{n} = \rho_l h_{lv} \mathbf{u}_l.\mathbf{n} \quad \textbf{(III-29)}$$

$$T_l = T_g \quad \textbf{(III-30)}$$

where h_{lv} is the latent heat of vaporisation.

If the pore is in vapour state

A convective boundary condition is used if the pore is in vapour state at the wick/groove interface (equation (III-31)).

$$(k_v^* \nabla T).\mathbf{n} = h_g(T - T_g) \quad \textbf{(III-31)}$$

The heat transfer coefficient h_g is the same as the one defined in section III.2.5.5 and is calculated using the relation given by Sleicher and Rouse (1975) [93].

III.2.5.8 Liquid-vapour interface

The liquid-vapour interface can be located at the wick/groove interface and/or within the capillary structure. If the liquid-vapour interface is located at the wick/groove interface, the boundary conditions are the ones described in section III.2.5.7 if the pore is occupied by liquid

Energy conservation (equation (III-32)), temperature continuity (equation (III-33)) and flow continuity (equation (III-34)) are implemented at the liquid-vapour interface within the wick.

$$\left(-k_{w,l} \nabla T\right).\mathbf{n} - \left(-k_{w,v} \nabla T\right).\mathbf{n} = \rho_l h_{lv} \mathbf{u}_\mathrm{l}.\mathbf{n} = \rho_v h_{lv} \mathbf{u}_\mathrm{v}.\mathbf{n} \quad \textbf{(III-32)}$$

$$T_l = T_v = T_{sat}(P_v) \quad \textbf{(III-33)}$$

$$\rho_v \mathbf{u}_\mathrm{v}.\mathbf{n} = \rho_l \mathbf{u}_\mathrm{l}.\mathbf{n} \quad \textbf{(III-34)}$$

The Clausius-Clapeyron relationship (equation (III-35)) is used to link the temperature and the vapour pressure along the liquid-vapour interface.

$$P_{sat}(T_{sat}) = P_{ref} \exp\left(-\frac{h_{lv} M}{R}\left[\frac{1}{T_{sat}} - \frac{1}{T_{ref}}\right]\right) \quad \textbf{(III-35)}$$

The liquid-vapour interface is actually discrete and formed by a series of menisci located at the entrance of throats. The maximum pressure difference between the liquid and the vapour across such a meniscus is given by Laplace's law (equation (I-4)) as already explained in section I.1.5.1.

$$\Delta P_{cap,max} = \frac{2\sigma}{r_p} cos\theta \quad \textbf{(III-36)}$$

As the liquid is supposed to be perfectly wetting, the contact angle is equal to 0°.

III.2.6 Loop model

The mixed pore network model is coupled with a loop model to determine the pressure in the groove (equation (III-17)). The loop model described below is the one proposed in Li and Peterson (2011) [44].

Note, however, that the saturation pressure inside the compensation chamber is fixed in our model whereas this is an output in Li and Peterson approach. We recall that we have the following elements between the exit of the groove and the liquid chamber: the vapour line, the condenser and the liquid line, denoted by the subscript vl, $cond$ and ll respectively.

III.2.6.1 Mass flow rate along the loop

The mass flow rate entering the wick is expressed as (equation (III-37)):

$$\dot{m}_l = \rho_l u_l S \quad \textbf{(III-37)}$$

where S is the wick inlet area.

The mass flow rate is conserved $\dot{m}_l = \dot{m}_v$ all along the loop in the steady-state regime.

III.2.6.2 Expression of the groove pressure

The pressure losses in the loop should be balanced by the action of capillary forces (equation(I-1)) as explained in section I.1.2.

$$\Delta P_{cap} = \Delta P_g + \Delta P_{vl} + \Delta P_{cond} + \Delta P_{ll} + \Delta P_w \quad \textbf{(III-38)}$$

Using the notations of the section I.1.2, we have the following relations

$$\begin{cases} \Delta P_g = P_1 - P_2 \\ \Delta P_{vl} = P_2 - P_3 \\ \Delta P_{cond} = P_3 - P_6 \\ \Delta P_{ll} = P_6 - P_7 \\ \Delta P_w = P_8 - P_9 \end{cases} \quad \textbf{(III-39)}$$

$$\Delta P_{cap} = P_1 - P_9 \quad \textbf{(III-40)}$$

with $P_7 = P_8$ corresponding to the compensation chamber pressure, i.e. the inlet pressure of the wick P_{cc}. Combining equation (III-38), equation (III-39) and equation (III-40), the unknown pressure P_g (i.e. P_1) in the vapour removal channel can be determined from equation (III-41).

$$P_g = P_{cc} + \Delta P_g + \Delta P_{vl} + \Delta P_{cond} + \Delta P_{ll} \quad \textbf{(III-41)}$$

Thus, ΔP_{loop} defined in equation (III-17) is the sum of the pressure losses in the vapour removal channel, the vapour line, the condenser and the liquid line (equation (III-42)).

$$\Delta P_{loop} = \Delta P_g + \Delta P_{vl} + \Delta P_{cond} + \Delta P_{ll} \quad \textbf{(III-42)}$$

III.2.6.3 Expression of pressure drop along the loop

Liquid line

Assuming a circular pipe of diameter d_{ll}, the pressure drop inside the liquid line ΔP_{ll} is determined by equation (III-43) (Poiseuille's law).

$$\Delta P_{ll} = \frac{128 l_{ll} \nu_l \dot{m}_l}{\pi d_{ll}^4} \quad \textbf{(III-43)}$$

where l_{ll} is the length of the liquid line and ν_l is the kinematic viscosity of the liquid.

Vapour line

Similarly, assuming a circular pipe of diameter d_{vl}, the pressure drop inside the liquid line ΔP_{vl} is determined by equation (III-44).

$$\Delta P_{vl} = \frac{128 l_{vl} \nu_v \dot{m}_v}{\pi d_{vl}^4} \quad \textbf{(III-44)}$$

where l_{vl} is the length of the liquid line and ν_v is the kinematic viscosity of the liquid.

Condenser

The pressure drop inside the condenser of diameter d_{cond} can be calculated as the sum of two pressure drops: the liquid pressure drop $\Delta P_{l,cond}$ (equation (III-45)) and the vapour pressure drop $\Delta P_{v,cond}$ (equation (III-46)). The Poseuille's law in a circular pipe is assumed.

$$\Delta P_{l,cond} = \frac{128 l_{l,cond} \nu_l \dot{m}_l}{\pi d_{cond}^4} \quad \textbf{(III-45)}$$

$$\Delta P_{v,cond} = \frac{128 l_{v,cond} \nu_v \dot{m}_v}{\pi d_{cond}^4} \quad \textbf{(III-46)}$$

$l_{l,cond}$ ($l_{v,cond}$ respectively) is the length of the liquid (the vapour respectively) within the condenser.

Vapour groove

The pressure drop inside the groove is computed using equation (III-47) from Li and Peterson (2011) [44].

$$\Delta P_g = 2 \frac{\rho_v \, \nu_v \, \gamma \, \bar{u}_v}{D_H} l_{vg} \quad \textbf{(III-47)}$$

where D_H is the hydraulic diameter, $\bar{u}_v = \dot{m}_v/(NHW\rho_v)$ is the mean velocity of vapour with N the number of grooves, H the height of the groove and W the width of the groove, $\gamma = 4.7 + 19.64\, G$ with $G = (A^2+1)/(A+1)^2$ and $A = H/W$.

III.2.7 Flux balance

As explained in section I.2.4, at steady-state the whole heat flux Q imposed at the external surface of the casing can be expressed by equation (I-12).

$$Q = Q_v + Q_l + Q_{cond} + Q_{conv} + Q_{evap} \quad \textbf{(III-48)}$$

These different fluxes can be expressed as follows.

Q_{evap}, vaporisation of the liquid

$$Q_{evap} = \dot{m}_l h_{lv} \quad \textbf{(III-49)}$$

Q_l, heating of the liquid

$$Q_l = \int_{l-v} (\rho_l c_{pl})(u_n)_l T dS + \int_{g/w,l} (\rho_l c_{pl})(u_n)_l T dS - \int_{inlet} (\rho_l c_{pl})(u_n)_l T dS \quad \textbf{(III-50)}$$

where $l-v$ is the liquid-vapour interface within the wick ,$g/w, l$ is the groove/wick interface occupied by liquid and $inlet$ is the inlet of the wick; $(u_n)_l$ is the liquid velocity.

Q_v, heating of the vapour

$$Q_v = \int_{l-v} (\rho_v c_{pv})(u_n)_v T dS - \int_{g/w,v} (\rho_v c_{pv})(u_n)_v T dS \quad \textbf{(III-51)}$$

where $l-v$ is the liquid-vapour interface within the wick ,$g/w, v$ is the groove/wick interface occupied by vapour and $(u_n)_v$ is the vapour velocity.

Q_{conv}, flux lost by convection

The flux Q_{conv} is the flux lost by convection within the vapour removal channel.

$$Q_{conv} = \int_{\mathrm{g/c}} h_g (T - T_g) dS + \int_{g/w,v} h_g (T - T_g) d\,S \quad \textbf{(III-52)}$$

where g/c is the groove/casing interface and T_g is the groove temperature.

Q_{cond}, flux lost by conduction

The flux Q_{cond} refers to the transversal leak of the parasitic heat flux (equation (III-53)). It corresponds to the heat conducted from the evaporator metallic wall to the compensation chamber through the porous structure.

$$Q_{cond} = \int_{inlet} k_l^* \frac{\partial T}{\partial y} dS \quad \textbf{(III-53)}$$

III.3Numerical method

III.3.1 Finite volume method

The governing equations and associated boundary conditions are discretized using the finite volume method (Patankar (1980) [94]). The mesh used for this study is structured and the grid points are centred on pores. Hence, the volumes controls are conditioned by the distance between two pores and the geometry of the wick. The whole computational domain (wick, casing and grooves) is then meshed. An upwind scheme is used for the convective term in the energy equation (equation (III-14)). The use of such scheme involves a non-symmetric linear system to be solved.

III.3.2 Programming language and linear solver

In order to solve the linear system, an iterative home-made code written in Fortran90 has been developed. PETSc solver [95] is used to solve the linear systems constructed from governing equations and boundary conditions. The selected linear solver is the stabilized version of BiConjugate Gradient (Bi-CGStab), as this method is suitable for the resolution of non-symmetric linear systems. The preconditioner is the incomplete LU factorization with no fill-in (ILU(0)).

III.3.3 Method of solution and computational chart

The solution depends on the pressure drop in the other components of the loop (equation (III-42)) and the velocity field (equation (III-14)). Moreover, when vapour enters the wick, the position of the liquid-vapour interface is not known a priori. Hence, an iteration procedure is necessary to obtain the steady-state solution.

For low heat flux, no vapour occurs within the wick, solving the problem is easier and the flowchart is given in Figure III.4.

If the heat flux becomes sufficiently high, vapour can invade the wick and two different scenarios must be considered. The first scenario corresponds to the situation where the pressure jump across some menisci at the wick/groove interface exceeds the maximum capillary pressure given by Laplace's law, (equation (I-4)). Such a meniscus cannot stay at the wick/groove interface and recedes into the wick.

This scenario corresponds to the capillary limit described in section I.1.5.1. The second scenario is the possible nucleation of vapour in pores (as explained in section I.1.5.2). According to nucleation theory this is possible when the temperature becomes sufficiently high in some pores for nucleation to occur. In this case, pores can be invaded by vapour not necessarily at the wick-groove interface but inside the wick. The temperature T_{nucl} marking the onset of nucleation can be expressed as

$$T_{nucl} = T_{sat}(P_v) + \Delta T_{nucl} \quad \textbf{(III-54)}$$

where P_v is the pressure corresponding to the formation of a bubble of radius r_b in a pore and ΔT_{nucl} is the nucleation superheat, which depends on several factors such as the operating conditions, the nature of the fluid, the porous material, the pore wall topography, etc.

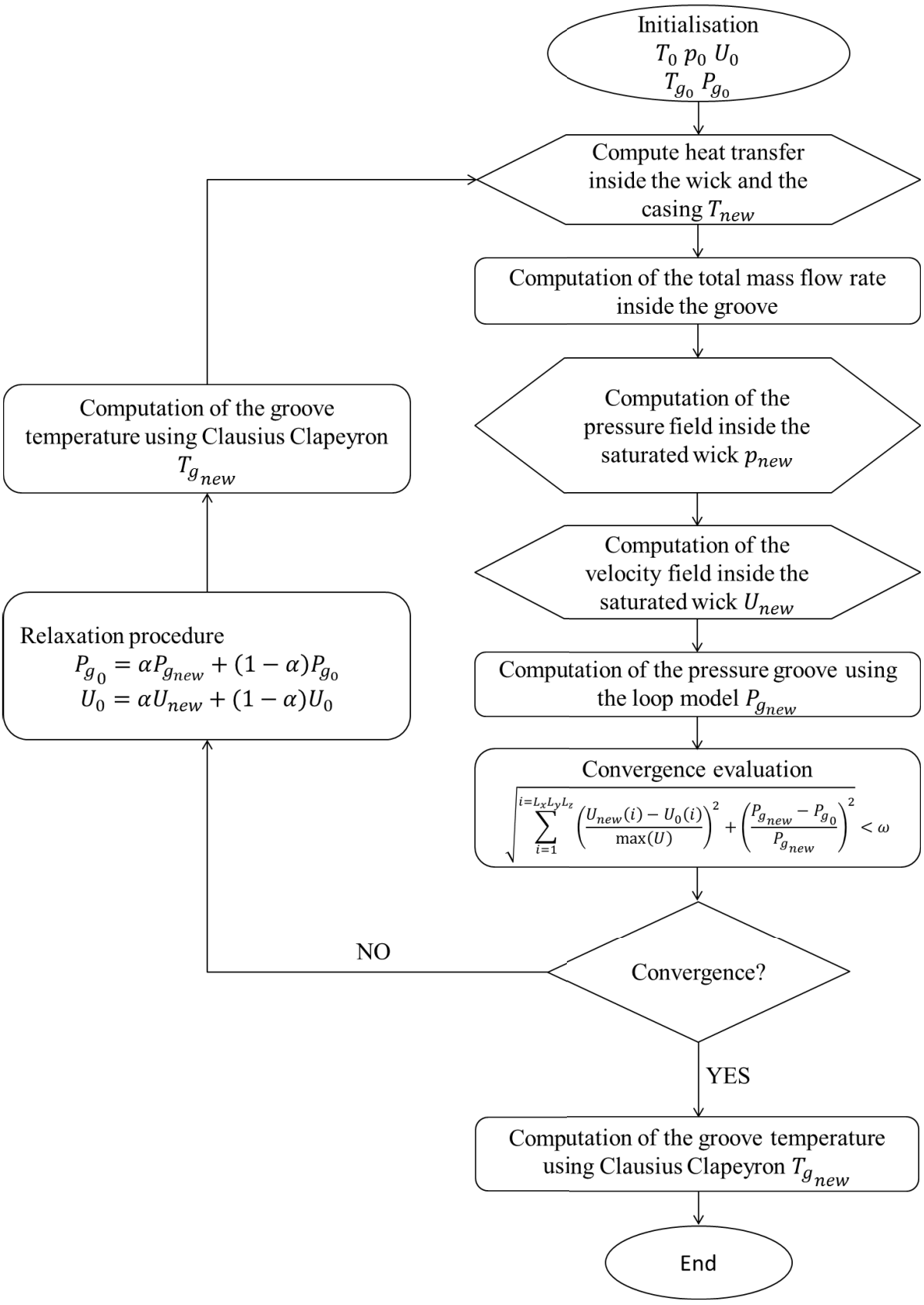

Figure III.4 – Computational chart for the case with a liquid saturated wick.

Hence, P_v can be expressed using equation (III-55).

$$P_v = P_l + \frac{2\sigma}{r_b} \quad \textbf{(III-55)}$$

where P_l is the liquid pressure in the pore prior nucleation, i.e. the pressure computed assuming a fully saturated zone. A problem is to estimate the bubble radius r_b since r_b is supposed to correspond to the minimum size of embryo leading to the bubble formation. In the absence of more information, a simple rule is to take $r_b \approx r_p$ where r_p is the pore radius. The advantage of this approach is to make the nucleation criterion depend on the local liquid pressure. A difficulty remains: the evaluation of ΔT_{nucl}. This is still an open problem. As in previous works, i.e. [1], [50], [96] and in accordance with the discussion in [21], a few Kelvin superheat is assumed. We took ΔT_{nucl} between 3K and 4K for the simulations presented in this thesis.

The procedure is then as follows after the nucleation step. The model cannot handle vapour pressurization steps, which can occur as long as the vapour has not reached the grooves when nucleation takes place inside the wick. Actually, simulations show that nucleation takes place at the casing/wick interface which is the place of highest temperatures in the wick. Starting from the node corresponding to $\max(T - T_{nucl})$ with of course $T - T_{nucl} > 0$, a vapour cluster percolating to one of the two grooves is formed using the standard invasion algorithm (Wilkinson and Willemsen (1983) [97]) in the 2D layer of pores in contact with the casing. The distribution so-obtained is the initial guess for the computation of the liquid-vapour interface within the wick.

Once equations are solved, the pressure jump $\Delta P = p_v - p_l$ across each meniscus at the liquid-vapour interface is computed. For each meniscus, this value is compared to the capillary pressure threshold defined by equation (I-4). If $\Delta P > \Delta P_{cap,max}$, the meniscus is then moved into the adjacent pore and all equations are then solved again until convergence for this new phase distribution. This procedure is then repeated until the criterion of meniscus stability, i.e. $\Delta P \leq \Delta P_{cap,max}$, is fulfilled for each meniscus present in the wick.

Once the menisci are stable, a procedure verifies that the temperature of every pore occupied by liquid is lower than the nucleation temperature. If this condition is not satisfied for some pores, the pore corresponding to $\max(T - T_{nucl})$ is removed from the list of liquid pores and considered as vapour. If this new vapour pore is not directly connected to the vapour cluster and/or the grooves, the invasion percolation rules are used to link it to the main vapour cluster and/or to the grooves.

Actually, the procedure can be performed using various rules as regards the moving menisci. For example, we can move at each step only one meniscus, the less stable one corresponding to $\max(\Delta P - \Delta P_{cap,max})$. On the contrary, we can move all the menisci such that $\Delta P - \Delta P_{cap,max} > 0$ or some fraction of these menisci. Tests indicate that the obtained steady-state solution is only slightly dependent on this choice. Since the solution is not very sensitive to this aspect of the procedure, the procedure leading to the shortest computational times is adopted, namely the one where all menisci detected as unstable are moved at each step.

The iterative method leading to the solution for an unsaturated wick is summarized in Figure III.5.

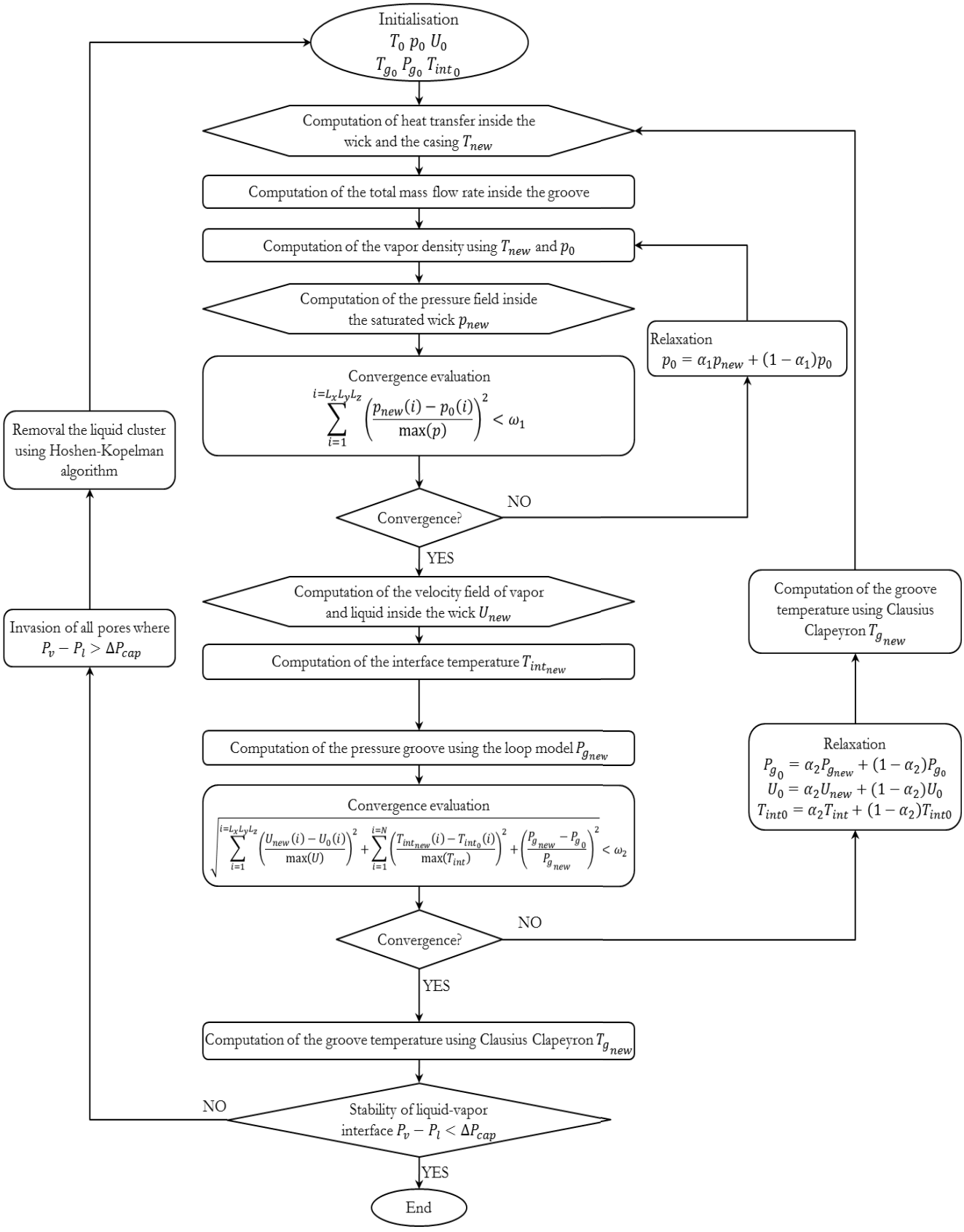

Figure III.5 – Computational chart for the case with an unsaturated wick.

III.3.4 Hoshen-Kopelman algorithm: cluster location

Once the invasion of one or several new pores is performed, isolated liquid clusters disconnected from the liquid reservoir have to be found and deleted. This calculation step is named "removal the liquid clusters using Hoshen-Kopelman algorithm" in Figure III.5. Under steady-state condition, liquid clusters are not stable and therefore disappear as soon as they are formed. The Hoshen-Kopelman (HK) algorithm (Hoshen and Kopelman (1976) [98]) is used to identify and remove these clusters as explained in the following. One advantage of this method is to browse the network only once through a labelling method. The general idea of this algorithm is based on a scan of the grid looking for occupied cells and the union-find method. Cells of the grid refer to pores in the present pore network approach. "Occupied" cell means that the pore is in liquid state, whereas "unoccupied" means that the pore is in vapour state. Finally, a label is assigned to each occupied cell. It corresponds to the cluster to which the cell belongs.

The procedure of the HK algorithm for a two-dimensional $n_j \times n_i$ grid is detailed in the following. First of all, defining the column by i and the row by j, a counter l is created such as $l = (j-1) \times n_i + i$ to assign a unique number to each pore defined by its coordinates (j, i). A vector $label$ is created and has the dimension l. As it is easier to explain the HK algorithm based on an example, the following explained steps will be supported by the example given in Figure III.6 (8×5 grid dimensions).

1) The first pore at coordinates $(1,1)$, i.e. $l = 1$, is checked. If the state is occupied, the value 1 is assigned to $label(0)$, otherwise 0. In the example in Figure III.6a, the pore is vapour and it takes the value 0.

2) The first row is considered in the ascending order of the column number, i.e. $2 \leq i \leq n_i$ and $j = 1$. If the considered pore is vapour, the value 0 is assigned to $label(l)$. For each occupied cell, the left neighbour, i.e. the pore located at $i - 1$, is checked. If the left neighbour is not occupied, the cell $label(l)$ takes the label equal to l at this grid location; otherwise it takes the neighbour's label. Figure III.6b illustrates this step.

3) The first column is considered in the ascending order of the row number, i.e. $2 \leq j \leq n_j$ and $i = 1$. If the considered pore is vapour, the value 0 is assigned to $label(l)$. For each occupied cell, the bottom neighbour, i.e. the pore located at $j - 1$, is checked. If the bottom neighbour is not occupied, the cell $label(l)$ takes the label equal to l at this grid location; otherwise it takes the neighbour's label. Figure III.6c illustrates this step.

4) The rest of the grid is examined in the ascending order of the row number, then in the ascending order of the column number, i.e. $2 \leq i \leq n_i$ and $2 \leq j \leq n_j$. If the considered pore is vapour, the value 0 is assigned to $label(l)$. For each occupied cell, the left and bottom neighbour, i.e. the pore located at $(j-1, i)$ and $(j, i-1)$, are checked. At this stage, several options can be encountered:

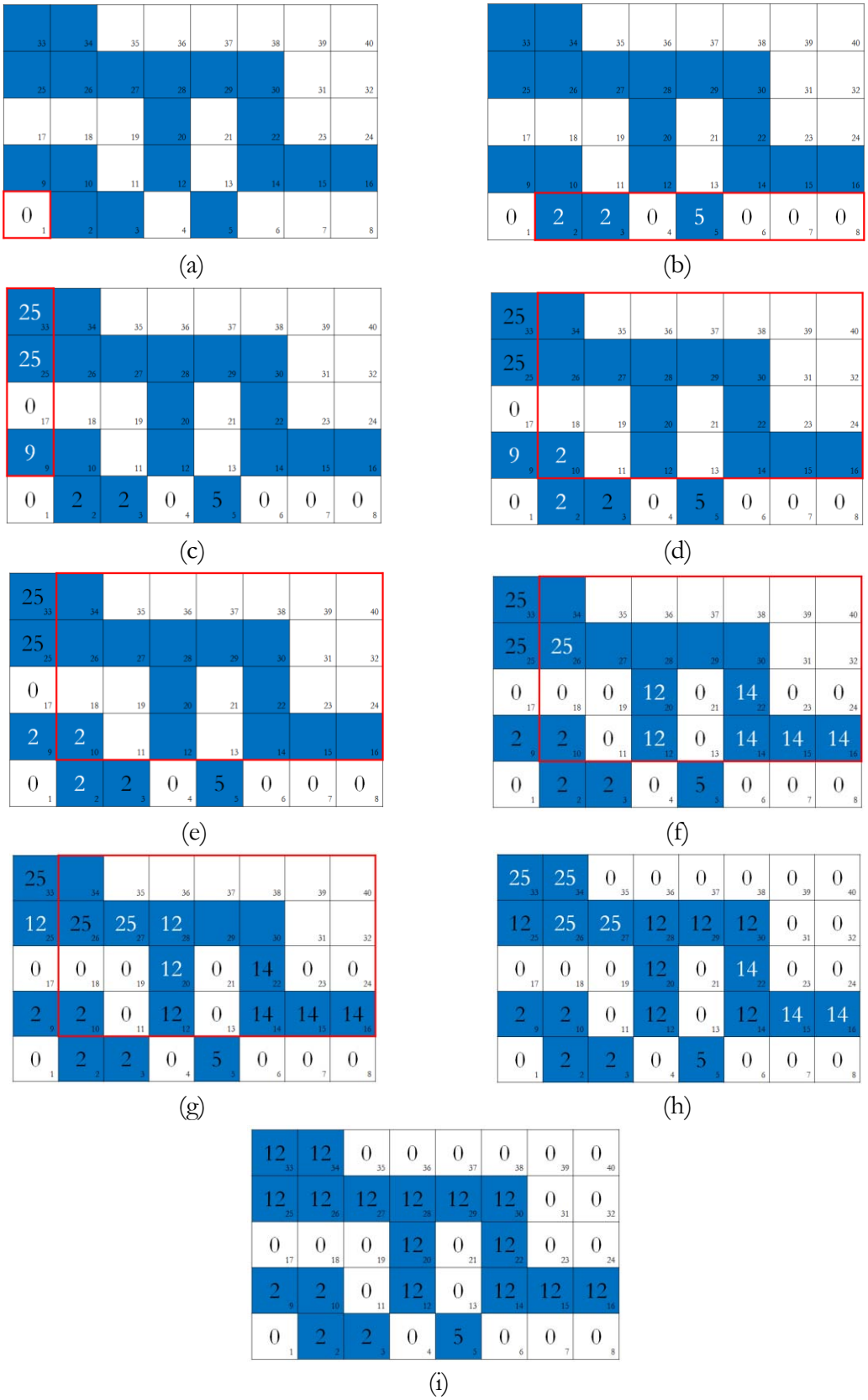

Figure III.6 – Various steps of the Hoshen-Kopelman procedure based on a two-dimensional example over a 8×5 grid. Cells in blue means "occupied cells", i.e. pores in liquid state; and cells in white means "unoccupied cells", i.e. pores in vapour state. Numbers in the right bottom corner in each grid cells are the unique number assign to each pores. The number in the centre of each cell is the label assigned to the cells corresponding to the cluster label.

- If both neighbours are in occupied state (with labels equal to $label_{min}$ and $label_{max}$), the considered cell takes the minimal label number $label_{min}$ (Figure III.6d) and the value $label_{min}$ is also assigned to the cell $label(label_{max})$ (Figure III.6e). This situation is also sketched in Figure III.6g: the cell $l = 28$ has two occupied neighbours with $label_{min} = 12$ and $label_{max} = 25$, thus the considered cell takes the value $label(28) = 12$ and the label of the cell $label_{max} = 25$ becomes 12, i.e. $label(label_{max}) = label(25) = label_{min} = 12$.
- If no neighbour is occupied, the cell $label(l)$ takes the label equal to l at this grid location, like the cells at $l = 12$ and $l = 14$ in Figure III.6f.
- If only one neighbour is occupied by liquid, the cell $label(l)$ takes the neighbour's label, like the cells at $l = 15$ and $l = 20$ in Figure III.6f.

This procedure is repeated until reaching the point at coordinates (n_j, n_i). At the end of this stage, all the liquid pores have a label number. However, as depicted in Figure III.6h, a given cluster can have several label numbers which is not suitable (the considered cluster is identified by the labels 12, 14 and 25).

5) The last step consists in updating the cluster label to have a unique identifier for each of them. The vector $label$ is scanned. If the value of $label(l)$ is not null, then the value $label(l)$ is replaced by the value of the corresponding label at the location $label(l)$, i.e. $label(l) = label\big(label(l)\big)$. Considering the cell at $l = 27$ in Figure III.6h: its current value is 25 ($label(27) = 25$), however, this cell belongs to cluster labelled 12. This label value is replaced as follows: $label(27) = label\big(label(27)\big) = label(25) = 12$. This procedure is repeated until reaching the end of the size of the $label$ vector. Once this step is ended, the whole network is correctly labelled as sketched in Figure III.6i.

This algorithm is applied to the present network model extended to the third dimension. If there are liquid clusters with another label than the one linked to the wick inlet, then they are removed.

III.4 Model validation and effective thermal conductivity correlation

III.4.1 Input parameters

The present mixed pore network model is compared to an experiment from Li et al. (2011) [58], for a validation purpose. The authors proposed their own three-dimensional model in Li and Peterson (2011) [44] (see section II.4.1 for the summary of their model). Their numerical results are also compared with our model. They studied a flat rectangular evaporator using water as working fluid. All necessary properties for the wick, the liquid, the vapour, the casing and the loop model are given in Table III-1. Note that one of the main differences between the model presented in [44] and the current mixed pore network approach is the prediction of the occurrence of vapour within the wick. Indeed, Li and Peterson's model is valid for a fully liquid saturated wick while our model can predict the recession of vapour within the wick.

The porosity and the permeability are numerically computed as explained in Appendix A and Appendix C and are equal to 0.52 and 3.5×10^{-10} m^2. Note that Li and Peterson (2011) [44] used equation (I-14) with $\Psi = 150$ (Blake-Konzeny equation) to calculate the permeability. With an average powder size equal to 128µm±2µm and a porosity of 0.5±0.1, the authors calculated a permeability equal to 6.075×10^{-11} m^2. Our computed permeability is greater than the one from Li and Peterson (2011) [44]. However, from Blake-Konzeny equation, the permeability is of order 10^{-10} for a porosity equal to 0.6. Therefore, the numerically computed permeability is not unrealistic and is used as input in our model.

Wick properties (Copper powder)		
d_{throat} (µm)	65±5	
Throat diameter p.d.f	Normal	
Thermal conductivity (W/m/K)	340	
	Experiment [44]	Numerical
Porosity	0.5±0.1	0.52
Permeability (m^2)	6.075×10^{-11}	3.5×10^{-10}
Casing property (Copper)		
Thermal conductivity (W/m/K)	340	
Fluid properties (Water)		
	Liquid	Vapour
Thermal conductivity ((W/m/K)	0.6	0.0192
Viscosity (Pa.s)	7.03×10^{-4}	1×10^{-5}
Specific heat capacity (J/kg/K)	4178.5	1880.8
Heat latent of vaporisation (kJ/kg)	2416	
Liquid density (kg/m^3)	993.67	
Molar mass (kg/mol)	0.018	
Surface tension (N/m)	70×10^{-3}	
Inlet temperature/pressure		
P_{cc} (Pa)	6000	
$T_{sat}(P_{cc})$ (K)	309	
Geometry dimensions (mm) (see Figure III.3 for definitions)		
L_x	4.5	
L_y	7	
L_z	3.5	
L_{xv}	1.5	
L_{yw}	1.5	
L_{yg}	4	
Loop dimensions		
Number of grooves / Length of grooves (mm)	6 / 25	
Length (mm)/ inner diameter (mm) of the vapour line	120/5	
Length (mm)/ inner diameter (mm) of the liquid line	120/5	
Length (mm)/ inner diameter (mm) of the condenser	540/5	

Table III-1 – Porous material properties, fluid properties, geometrical dimensions and loop dimensions used in simulations.

III.4.2 Model validation: overheating of the casing

The evaporator wall temperature as a function of the heat load applied to the casing is shown in Figure III.7 and is compared to experimental data from [58]. The numerical results have been simulated using the Alexander's model (equation (I-21)) to compute the effective thermal conductivity. The predicted casing temperature correlates quite well and the trend of the temperature variation is in accordance with the experimental results as shown in Figure III.7. The maximum difference between the experimental results and the numerical prediction of the evaporator wall temperature is about 3K. We conclude that the mixed pore network model presented in section III.2 is an accurate tool to investigate the heat and mass transfer of an LHP/CPL evaporator.

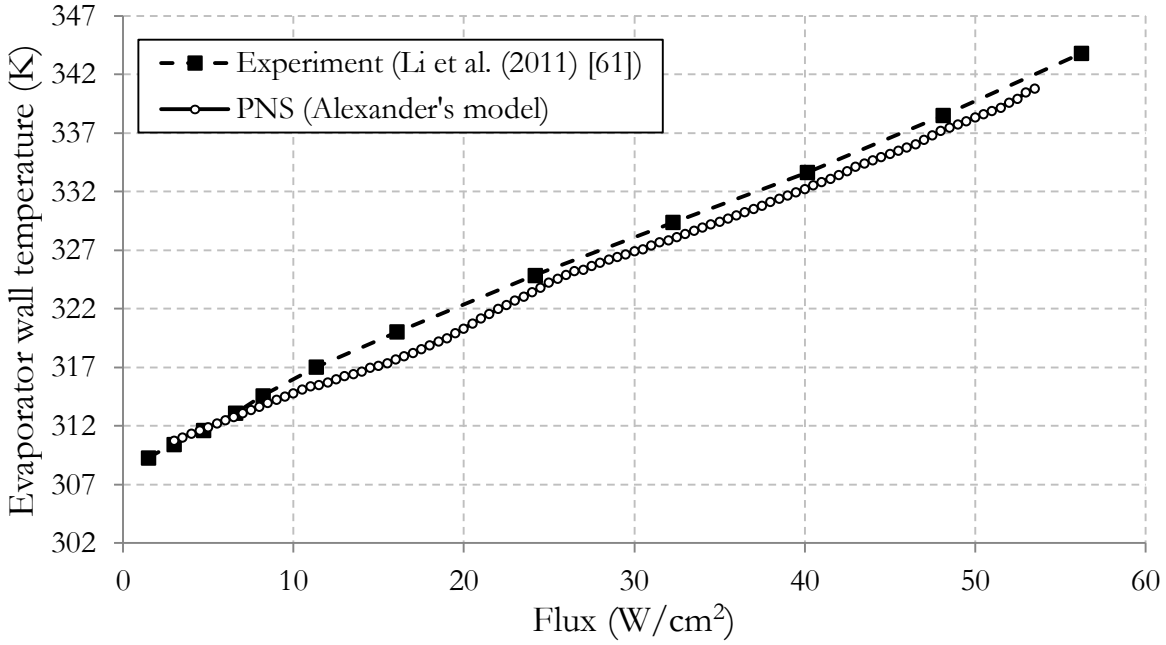

Figure III.7 – Variation of the evaporator wall temperature, i.e. the casing temperature, as a funtion of the heat load. PNS stands for pore network simulation.

III.4.3 Influence of the correlation for the effective thermal conductivity

III.4.3.1 Value of the effective thermal conductivity

In this section, similarly as in Li and Peterson (2011) [44], three heat fluxes (4.5W/cm^2, 15.5W/cm^2 and 31W/cm^2) were investigated and compared with the experimental data from Li et al. (2011) [58]. Their numerical results from [44] and their experimental results from [58] are reported by the dashed lines in the figures presented in this section. Correlations presented in Table I-5 (section I.2.5.4.5) to compute the effective thermal conductivity have been investigated. Table III-2 summarizes the values of the wick effective thermal conductivity saturated with liquid or vapour for the different correlations. First of all, it is clear from this table that the choice of the correlation has a great impact on the predicted value. The effective thermal conductivity of the wick can vary by two orders of magnitude depending on the chosen correlation. In the figures of this section, solid lines correspond to the results obtained with our code and red symbols indicate that vapour has recessed within the wick.

	k_l^*	k_v^*
Parallel	164.61	164.31
Maxwell	130.9	130.5
Average	82.8	82.1
Odelevski	68.7	68.4
Alexander	37.16	11.17
Chaudary and Bhandari (n=0.60)	22.66	5.72
Chaudary and Bhandari (n=0.51)	14.5	2.69
Chaudary and Bhandari (n=0.42)	9.28	1.26
Goring and Churchill	2.26	7.3×10^{-2}

Table III-2 – The effective thermal conductivity values for the liquid and vapor regions computed from the different correlations presented in Table I-5.

III.4.3.2 Goring and Churchill's model: not appropriated

Regarding the prediction of the wall temperature, Goring and Churchill's model is definitively not appropriated. Indeed, compared with experimental results from Li et al. (2011) [58] at 4.5W/cm^2, the use of Goring and Churchill overestimates the wall temperature by about 30K. This trend is worst for higher heat flux: the wall temperature reaches 2513K at 31W/cm^2. The liquid and vapour effective thermal conductivities are 2.3W/K/m and 7.3×10^{-2}W/m/K. As already discussed in section I.2.5.4.5, this correlation underestimates k^* and is not relevant for a sintered capillary structure.

III.4.3.3 Chaudary and Bhandari model: a debatable correlation

The Chaudary and Bhandari's model (i.e. geometric mean) is used in this section with the two current values of n (n=0.42 and n=0.51) and n=0.60. Note that Li and Peterson (2011) [44] used this correlation, with n=0.42. As shown in Figure III.8, for n=0.42 and n=0.51, the wall temperature is overestimated for low heat load. The overestimation becomes rapidly dramatically high with the increase in the heat load. The vapour occurs in the wick for low heat flux and thus rapidly leads to an overheating of the casing due to the additional vapour resistance between the wick and the casing. When n increases (n=0.60), the wall temperature decreases due to higher vapour effective thermal conductivity and seems to correlate better with experimental results for the range of heat flux 4.5W/cm^2 to 31W/cm^2. Unfortunately, such a high value for n was never reported in the literature. Moreover, for higher heat flux, the trend of the temperature variation is the same as the one for lower n value: the dramatic overestimation of the casing temperature is only delayed with the increase in n. Therefore, the legitimacy to use n=0.60 is debatable and the use of Chaudary and Bhandari's model does not seem to be appropriated due to an underestimation of the effective thermal conductivity.

Note that Kaya and Goldak (2006) [21] reported that this correlation is suitable as the predicted temperature wall is of the same order as the one predicted by others correlations. However, they did not stipulate which value of n they used. Moreover, as it will be discussed in more details in section III.4.3.5, their wick material is almost insulating and the choice of the correlation for the effective thermal conductivity has less impact on the temperature field.

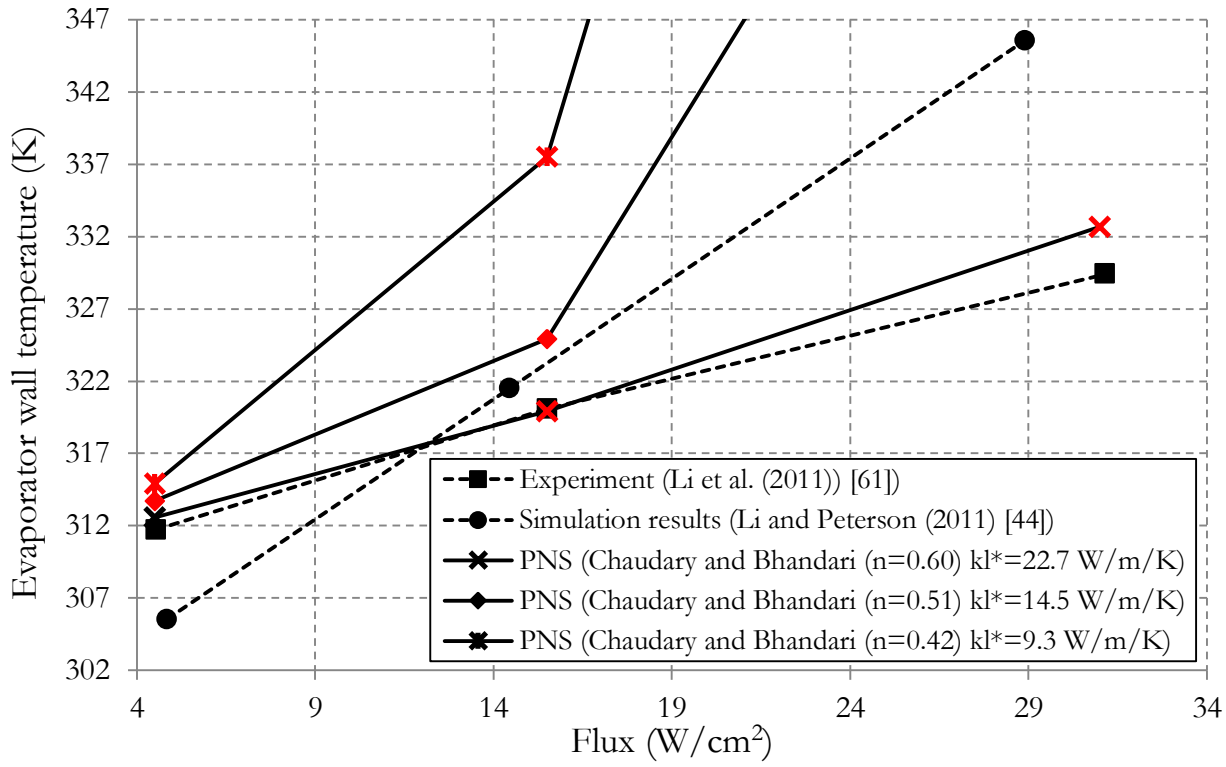

Figure III.8 – Variation of the evaporator wall temperature as a function of the heat load applied to the casing using the Chaudary and Bhandari model for three different values of n. Red symbols indicate that vapour occurs within the wick.

III.4.3.4 Wall temperature deviation and comparison with experiment

Kaya and Goldak (2006) [21] and Lin et al. (2011) [49] (see discussion in section I.2.5.4.5) had already pointed out the impact of the correlation of the effective thermal conductivity on the wall temperature. Kaya and Goldak (2006) [21]compared the influence, amongst others, of Alexander's model, the geometric model, Maxwell's model and the parallel model, while Lin et al. (2011) [49] compared the parallel model, Maxwell's model and Odelevski's model. Their wall temperature deviation was around 0.5K [21] to 2K [49], therefore they concluded that the choice of the correlation does not impact significantly the overall temperature field. In this section, the parallel model, Maxwell's model, the average model, Odelevski's model and Alexander's model are compared using the mixed pore network model. The wall temperature deviation is around 1K (Figure III.9) when the wick is liquid-saturated to several Kelvins (~8K at 31W/cm^2 in Figure III.10) when the vapour recesses within the wick. Hence, the choice of the effective thermal conductivity correlation seems to have a greater impact for the current studying case contrary to discussion in [21] and [49], especially when vapour occurs within the capillary structure. Nevertheless, it is interesting to note that whatever the effective thermal conductivity correlation, the current model reproduces with good agreement the experimental behaviour, i.e. the slope of the temperature curve has the same trend as the measurement results, contrary to the numerical results of Li and Peterson (2011) [44]. Indeed, Li and Peterson (2011) [44] numerical results underestimate (of about 5K) or overestimate (of about 15K) the overheating of the casing, excepted for heat flux around 15.5W/cm^2 (see Figure III.10). Moreover, note that our model predicts the recession of the vapour within the wick (with a vapour saturation lower than 2%), while Li and Peterson (2011) [44] assumed a fully liquid saturated capillary structure.

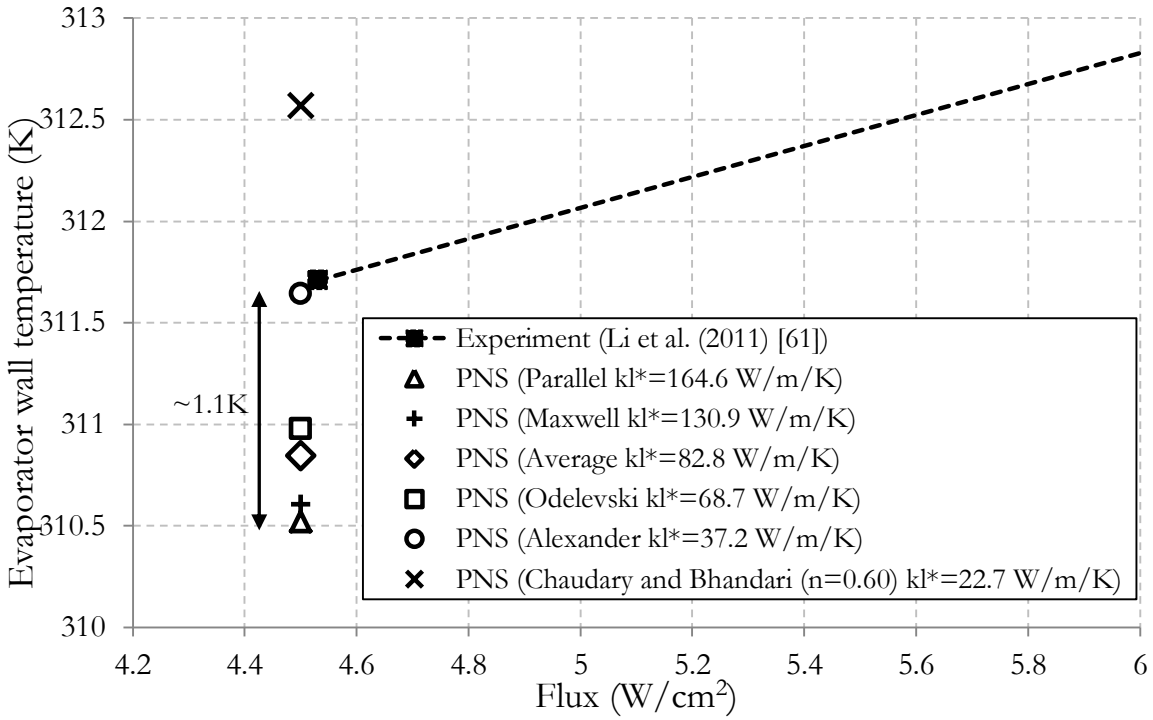

Figure III.9 – Evaporator wall temperature for 4.5W/cm² applied to the casing for different effective thermal conductivity correlations.

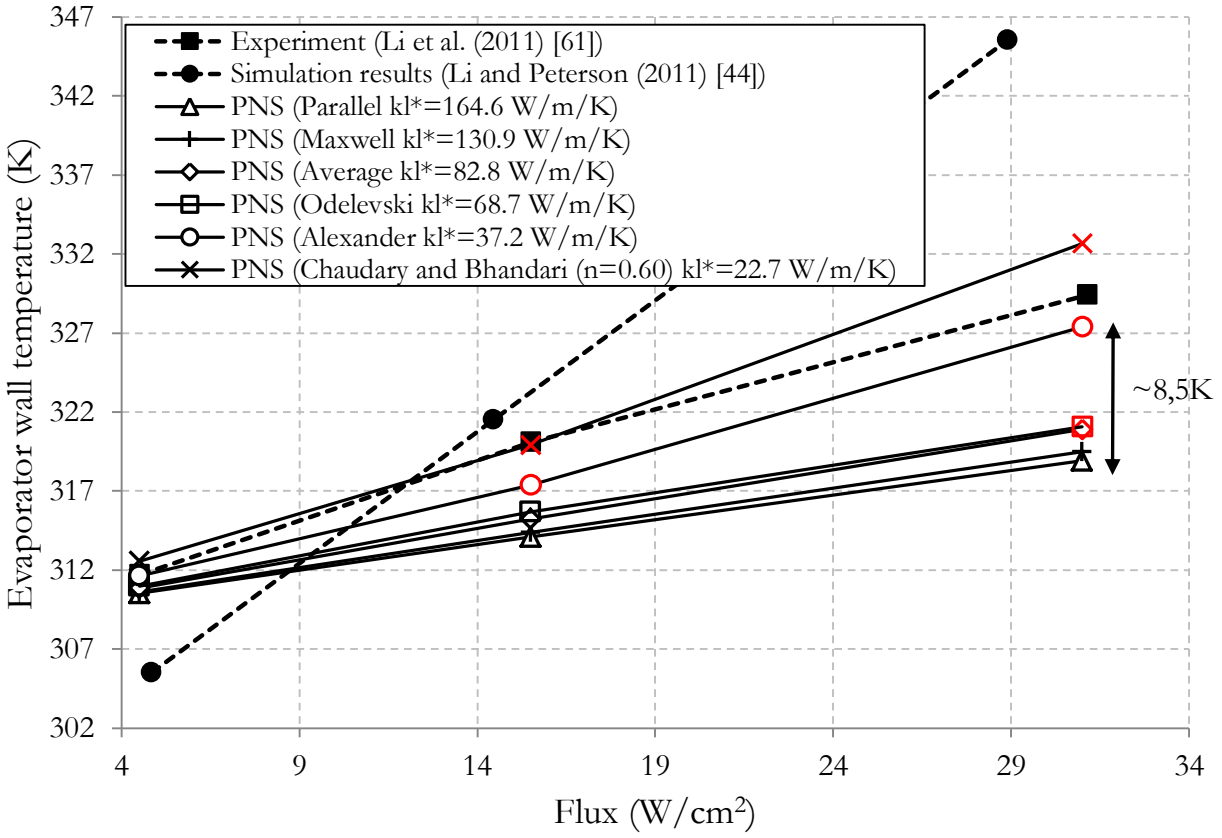

Figure III.10 – Evaporator wall temperature as a function of the heat load applied to the casing for different effective thermal conductivity correlations. Red symbols indicate that vapour occurs within the wick.

The thermal conductivity of the liquid k_l, the vapour k_v and the solid matrix of the porous medium k_w, as well as the ratio k_l/k_w and k_v/k_w for the studies of Kaya and Goldak (2006) [21], Lin et al. (2011) [49] and the current simulation adapted from Li et al. (2011) [58] are reported in Table III-3.

	Kaya and Goldak (2006) [21]	Lin et al. (2011) [49]	Li et al. (2011) [58] Li and Peterson (2011) [44]
Working fluid	Ammonia	Ammonia	Water
k_l (W/m/K)	0.52	0.52	0.6
k_v (W/m/K)	0.024	0.024	0.019
k_w (W/m/K)	Stainless Steel (?): 14.5	Nickel: 91	Copper: 340
ε	60%	~70%	~50%
k_l/k_w	3.6×10^{-2}	5.8×10^{-3}	1.8×10^{-3}
k_v/k_w	1.7×10^{-3}	2.7×10^{-4}	5.6×10^{-5}
Deviation of the wall temperature	~0.5K	~2K	Current model results: ~1K for saturated wick ~8K for unsaturated wick

Table III-3 – Comparison between the thermal conductivity of the working fluid and the wick and their impact on the evaporator wall temperature deviation in three different works ([21], [49] and our model using properties from [44] and [58]).

The working fluid in [21] and [49] is the ammonia, while water is used in [58]. Nevertheless, the liquid and vapour thermal conductivity are of the same order of magnitude, thus the main difference between these studies is the solid material of the wick.

The ratio between the liquid and the solid thermal conductivity is between 10^{-2} and 10^{-3}. For a liquid saturated wick, whatever the choice of the correlation for k_l^*, the solid matrix conductivity has not a significant impact on the wall temperature. The temperature deviation is around 1K (see Figure III.9) and is in accordance with the trend reported in [21] and [49].

When vapour has recessed within the capillary structure (depicted by red symbols in Figure III.10), the wall temperature deviation is much higher, around 8K, with the current model contrary to [21] and [49]. The ratio between the vapour and the solid thermal conductivity permits to explain this trend. Indeed, the ratio is one order of magnitude greater in [21] than in [49], inducing a higher temperature deviation. Compared with the experiment of Li et al. (2011) [58], the ratio is two order of magnitude greater than in [21]. As a consequence, the occurrence of vapour has a significant impact on the temperature field when the wick is conductive, and thereby, the choice of the model for k_v^* also.

III.4.3.5 Wick material and effective thermal conductivity model

It appears from Table III-3 and the discussion in section III.4.3.4 that for an almost insulating wick [21], the correlation of the effective thermal conductivity has a limited impact on the temperature field, whereas the impact is much more pronounced for a conductive wick. For illustrating this purpose, Figure III.11 and Figure III.12 show the variation of the casing temperature for an insulating wick (k_w=4W/m/K) and a conductive wick (k_w=340W/m/K) for two effective thermal conductivity correlations: the average model and the Alexander's model. Anticipating the results presented in section

III.5, results in Figure III.11 and Figure III.12 are presented for the ranges of heat load which correspond to the best thermal performances of the evaporator. For the insulating wick, the casing temperature difference is about 3K for a heat load equal to 5W/cm^2, whereas the deviation of the casing temperature for the conductive wick is about 11K for a heat load equal to 52.5W/cm^2.

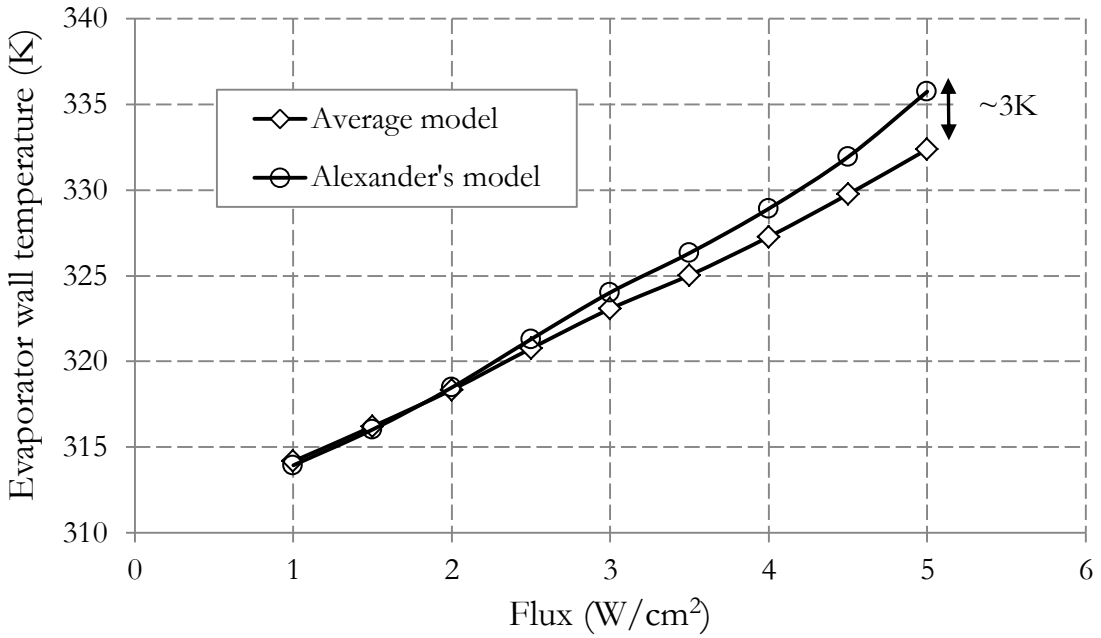

Figure III.11 – Variation of the evaporator wall temperature as a function of the heat load for an insulating wick (k_w=4W/m/K) using the average model and the Alexander's model for the effective thermal conductivity.

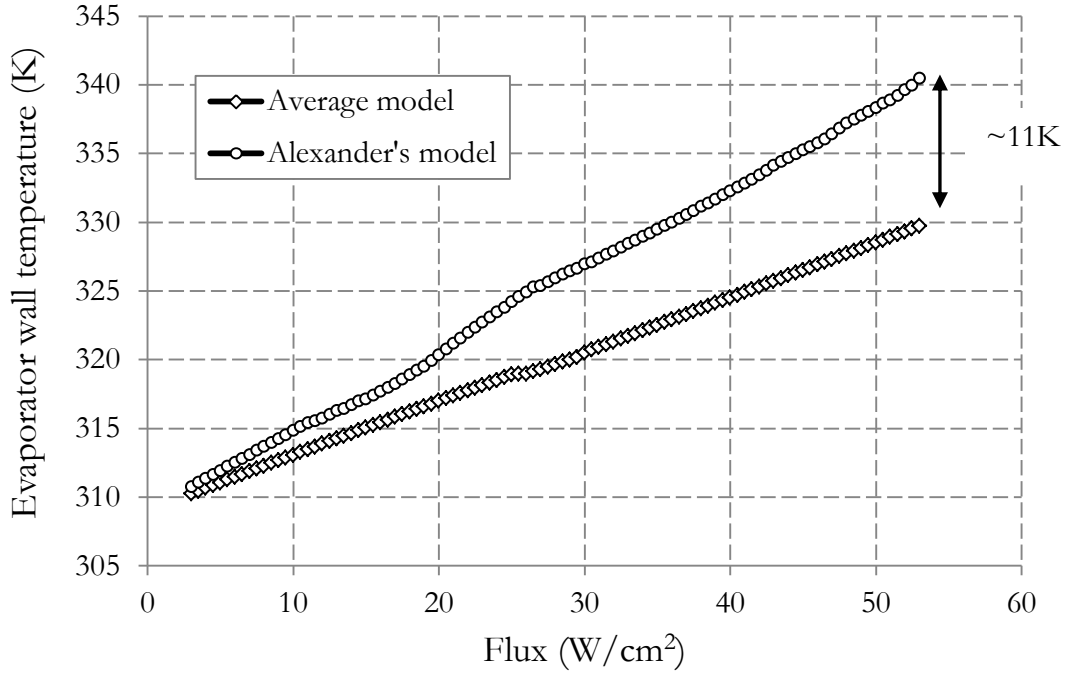

Figure III.12 – Variation of the evaporator wall temperature as a function of the heat load for a conductive wick (k_w=340W/m/K) using the average model and the Alexander's model for the effective thermal conductivity.

III.4.4 Summary

Li and Peterson (2011) [44] numerical results underestimate or overestimate the overheating of the casing, excepted for heat flux around 15.5W/cm^2. The current model, whatever the effective thermal conductivity correlation (Figure III.10), reproduces with better agreement the experimental behaviour, i.e. the slopes of curve have the same trend as the experimental results, with a maximal deviation about 8K. We conclude that the mixed pore network model presented in section III.2 is an accurate tool to investigate the heat and mass transfer of an LHP/CPL evaporator.

In the particular case presented in this section, the use of the Alexander's model for the effective thermal conductivity permits to reproduce quite well the trend of the casing overheating compared with experiment. However, when the wick is insulating, the model for the effective thermal conductivity has much lower impact. In the simulations presented in this thesis two different correlations to compute the effective thermal conductivity have been used: the Alexander's model and the average model. The average model is used when the thermal conductivity of the wick is relatively low, i.e. insulating wick, otherwise the Alexander's model is used.

III.5 Results and discussions

This section is adapted from the section 6 of "Three-dimensional liquid and vapour distribution in the wick of capillary evaporators", L. Mottet et al., IJHMT, 2015, [76]***.***

III.5.1 Input parameters

In this section, results of simulations performed considering the 3D evaporator unit cell are presented. The geometrical dimensions and porous medium properties are indicated in Table III-4. They are representative of an LHP evaporator unit cell. The working fluid is ammonia. Its physical properties are also indicated in Table III-4. No subcooling is considered, i.e. $\Delta T_{sub} = 0\text{K}$. The wick has low thermal conductivity (k_w=4.18W/m/K) and the average model to compute the effective thermal conductivity is used in accordance with discussion in section III.4.3.5. Nucleation is supposed to occur if the temperature in the wick is greater than T_{sat}+4K, where T_{sat} is the saturation temperature in the groove. A grid of 31×49×33 points (leading to a total number of 50127 computational points) is used. The grid has 31×20×33 points (which corresponds to 20460 computational points) located within the wick and 20×13×33+31×16×33 (which corresponds to 16368 computational points) located within the casing.

III.5.2 Liquid-vapour distribution within the wick

A series of steady-state solutions is obtained by varying the heat flux applied to the casing outer surface. As in previous works, e.g. [50], [96], the nucleation temperature is not reached in the wick for sufficiently low heat flux. Vaporisation takes place only at the wick-groove interface and the wick operates in a liquid saturated mode. For higher heat fluxes, partial invasion of the wick by the vapour occurs. This was also predicted in the aforementioned previous works. However, the 3D simulations lead to identify a regime, referred to as regime II, which is fundamentally different from the regimes reported in [50] or [96]. This

regime is obtained for an intermediate range of heat fluxes, sufficiently high for the wick to be partially invaded by the vapour but not too high as discussed hereafter. As illustrated in Figure III.13b, this regime is characterized by the coexistence of the liquid and vapour phases over the casing-wick contact surface. This is in contrast with the results reported in [50] or [96], where only vapour is in contact with the casing as soon as the wick becomes unsaturated.

More details on the variation of phase distribution with heat flux are presented in Figure III.14. This figure shows the fraction of pores right under the casing occupied by either vapour or liquid, the overall vapour saturation in the wick and the depth of the two-phase region, which is the distance between the casing wick interface and the pore occupied by vapour located the closest to the wick inlet, as a function of the heat flux applied to the casing.

Wick properties		
d_{throat} (µm)	2±1	
Throat diameter p.d.f	Uniform	
Thermal conductivity (W/m/K)	4.18	
Porosity	0.59	
Permeability (m^2)	4.3×10^{-14}	
Casing property		
Thermal conductivity (W/m/K)	70	
Fluid properties (Ammonia)		
	Liquid	Vapour
Thermal conductivity ((W/m/K)	0.52912	0.024365
Viscosity (Pa.s)	1.56×10^{-4}	0.963×10^{-5}
Specific heat capacity (J/kg/K)	4675.7	2841.3
Heat latent of vaporisation (kJ/kg)	1225.58	
Liquid density (kg/m^3)	624.46	
Molar mass (kg/mol)	0.017	
Surface tension (N/m)	29.589×10^{-3}	
Inlet temperature/pressure		
P_{cc} (Pa)	615050	
$T_{sat}(P_{cc})$ (K)	283.15	
Geometry dimensions (mm) (see Figure III.3 for definitions)		
L_x	1.9	
L_y	3	
L_z	2	
L_{xv}	0.35	
L_{yw}	1.2	
L_{yg}	0.8	
Loop dimensions		
Number of grooves / Length of grooves (mm)	10/6	
Length (mm)/ inner diameter (mm) of the vapour line	100/3	
Length (mm)/ inner diameter (mm) of the liquid line	100/3	
Length (mm)/ inner diameter (mm) of the condenser	100/3	

Table III-4 – Porous materials properties, fluid properties and geometrical dimensions.

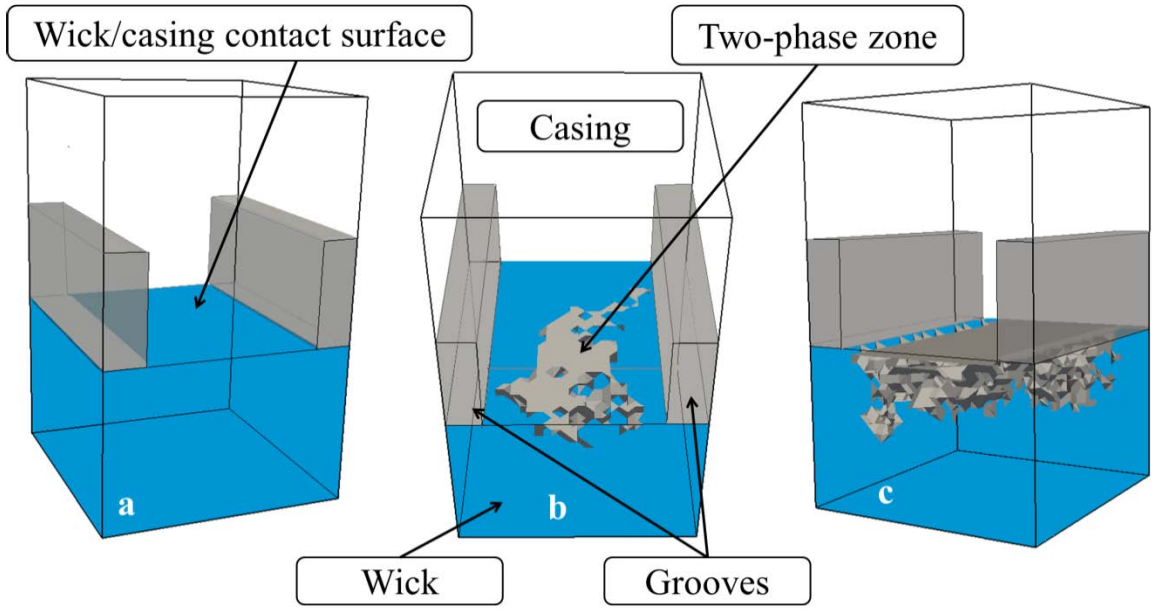

Figure III.13 – The three main operating regimes from pore network numerical visualizations of vapour and liquid phase distribution in the evaporator unit cell: a) Saturated wick regime, b) Two-phase zone regime (referred to as regime II in this paper) and c) Dry-out regime where a vapour blanket has been formed under the casing. The various images were obtained for an applied heat flux of 0.8W/cm² (a), 1W/cm² (b) and 10W/cm² (c) respectively. Vapour phase is in grey and liquid phase is in blue.

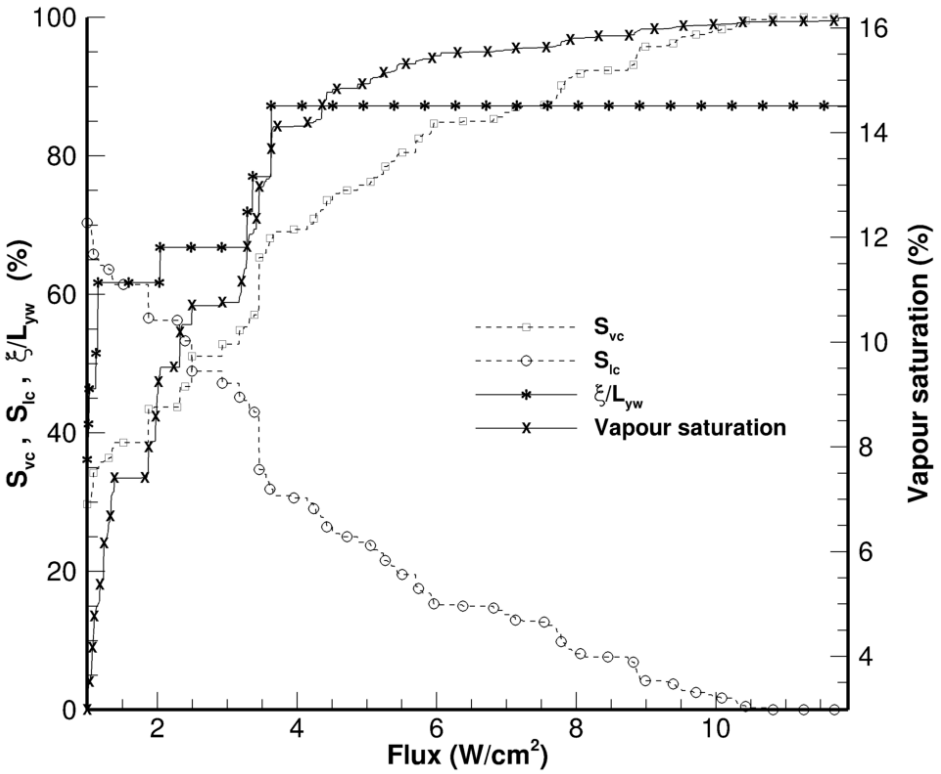

Figure III.14 – Variation of vapour region depth (divided by wick thickness), vapour overall saturation and the occupancy state of pores under the casing as a function of heat flux applied to the casing. S_{vc} is the fraction of pore occupied by vapour right under the casing, S_{lc} is the fraction of pore occupied by liquid right under the casing and ξ/L_{yw} is the depth of the two-phase zone.

As can be seen, regime II, where a two-phase zone is in contact with the casing, extends over a significant range of heat fluxes. The fraction of liquid pores in contact with the casing exceeds the fraction of vapour pores in contact with the casing up to an applied heat flux of 2.5W/cm^2. For this flux, the depth of the two-phase region is already high and reaches 67% of the wick thickness even though only 10% of the wick pore space is occupied by vapour. The wick/casing surface becomes fully dry for heat fluxes greater than 10W/cm^2. The vapour saturation increases rapidly with the applied heat load in this regime but remains relatively low (below 17%), which is in sharp contrast with the 2D simulation results reported in [50] which led to much higher vapour saturations for similar applied heat fluxes. The overall vapour saturation seems to stabilize in Figure III.14. Although not shown here, the vapour saturation continues to increase with the heat flux but less rapidly once a dry vapour region is present under the casing and eventually forms a thick vapour blanket. As can be seen from Figure III.14, the depth of the two-phase region within the wick reaches a plateau in regime II. This plateau corresponds to the growth of the two-phase region in the lateral direction in the wick instead of the depth direction.

In summary, the 3D simulations show the existence of three regimes and not only two as reported in some previous investigations, e.g. [50] or [96]: a regime at low heat load where the wick is saturated by liquid, a regime at high heat load where the wick-casing surface is dry and an intermediate regime (regime II) where both liquid and vapour are in contact with the casing-wick surface. These three regimes are illustrated in Figure III.13.

III.5.3 Vaporisation partition

The mass flow rate of vapour feeding the vapour groove in regime II is shown as a function of the heat flux applied to the casing in Figure III.15. The mass flow rate is divided into two parts: the fraction of the total mass flow rate resulting from vaporisation of the liquid at the wick/groove interface and the fraction of the total mass flow rate resulting from vaporisation within the wick. As can be seen the vapour which feeds the groove mostly comes from the vaporisation process within the wick in regime II. Figure III.15 also shows a significant increase, from 32.7% to 52.6%, in the fraction of vapour mass flow rate resulting from the vaporisation process within the wick at the beginning of regime II when the heat flux varies from 1.38W/cm^2 to 1.385W/cm^2. This corresponds to the situation where the two-phase region becomes connected to the two grooves on both sides of casing fin. For lower heat loads in regime II, the two-phase zone is connected to only one groove.

III.5.4 Maximum temperature

The maximum temperature T_{max} is located on the left and right of the metallic casing outer surface. In practice, this temperature should not exceed some specified value depending on the equipment to be cooled. The maximum temperature can be characterized from the excess temperature $\Delta T_{max} = T_{max} - T_{sat}$, where T_{sat} is the saturation temperature inside the grooves. As shown in Figure III.16, the excess temperature ΔT_{max} is equal to about 26K for a heat load of 11.9W/cm^2, i.e. at the end of regime II. This order of magnitude is widely acceptable for such a system, indicating that regime II is a fully operational regime, i.e. is quite likely in operating LHP. The variation of ΔT_{max} with the heat flux is not perfectly

monotonous in Figure III.16. This is due to the discrete representation of pore space. A slight decrease in ΔT_{max} can happen when a new pore is occupied by vapour at the wick-groove interface.

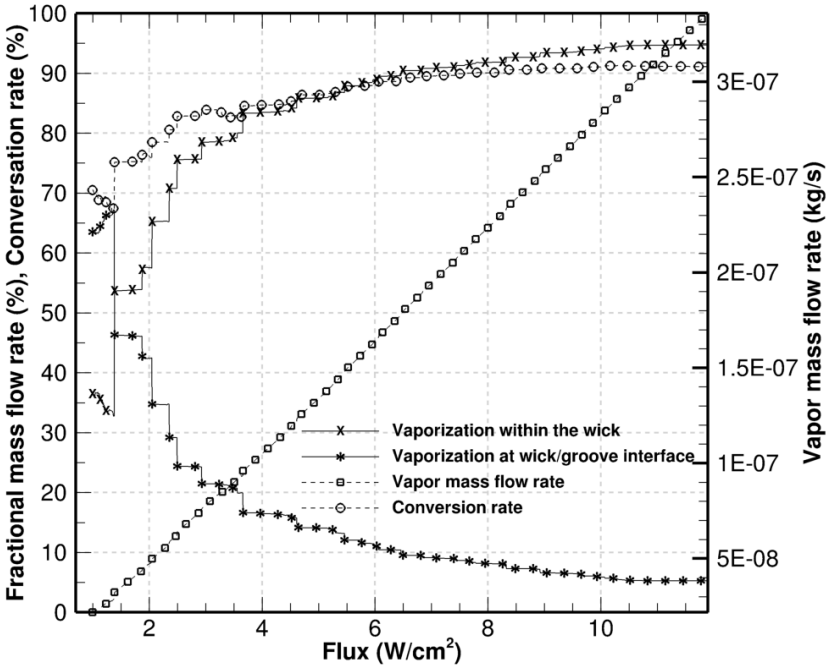

Figure III.15 – Variation of vapour mass flow rate partition, vapour mass flow rate and conversion rate of applied flux as a function of the heat flux applied to the casing in regime II.

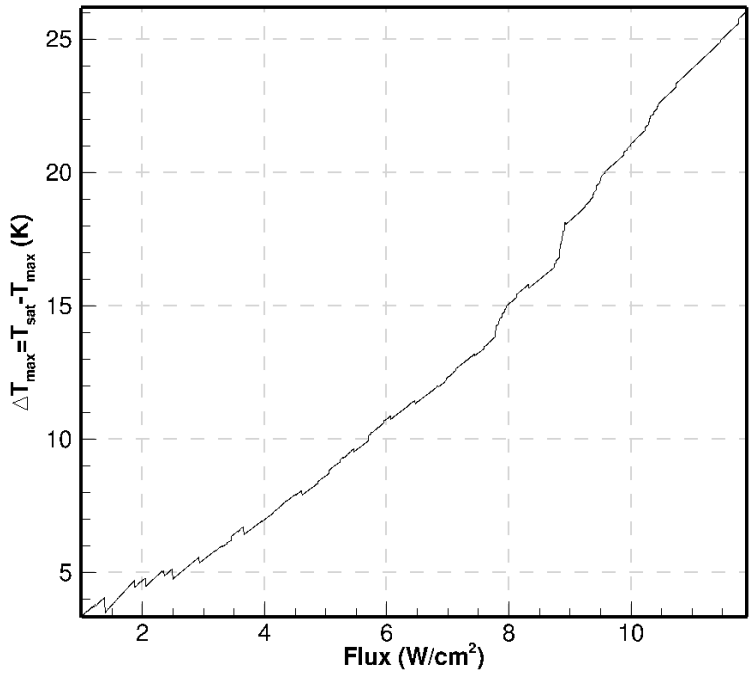

Figure III.16 – Variation of $\Delta T_{max} = T_{max} - T_{sat}$ as a function of the heat load applied to the casing in regime II. T_{sat} is the saturation temperature inside the grooves.

III.5.5 Conductance

The global performance of evaporator can be characterized from the computation of its global conductance (see equation (I-8)). The variation of h_{ev} with the applied heat flux q is shown in Figure III.17.

The results are markedly different from those obtained from 2D PN simulations (see [96]), which indicated that the conductance was maximum in regime I (fully saturated wick) and then decreased as soon as the vapour penetrated in the wick. The 3D simulations reveal that the evaporator conductance is the greatest in regime II, i.e. with a partially saturated wick. Actually, three different ranges of flux can be distinguished in Figure III.17. The conductance, which is constant in regime I (liquid-saturated wick), increases in regime II with the heat load until reaching a maximum (of the order of 0.57W/cm^2/K in our simulations). Note that this maximum is observed over a quite significant range of heat flux in regime II (as shown by the plateau in Figure III.17). The conductance decreases in regime II when the fraction of the casing-wick contact surface in contact with liquid becomes too small. In our simulations, the conductance begins to decrease for an applied heat flux of about 7.8W/cm^2, i.e. when less than about 10% of the pores in contact with the casing are still occupied by liquid (see Figure III.14). From the results reported in Figure III.14 and Figure III.17, the best evaporator performance is observed in the range of heat fluxes [3.7 -7.8W/cm^2] corresponding to a noticeable fraction of pores in contact with the casing occupied by liquid. This fraction varies between 35% and 10% in this range of heat fluxes according to Figure III.14.

Interestingly, the conductance variation shown in Figure III.17 is qualitatively similar to the variation obtained in the experiment of Liao and Zhao (1999) [74], see Figure II.12 in section II.3.

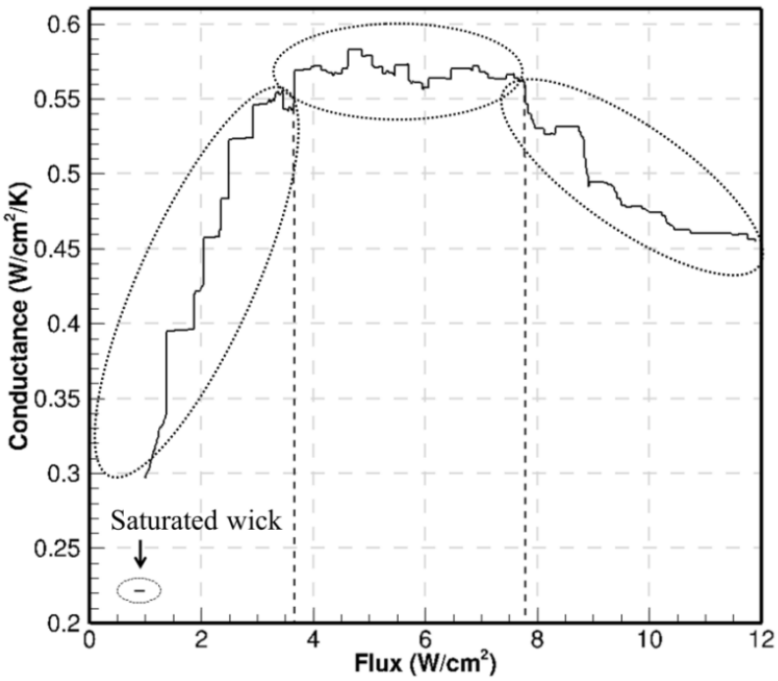

Figure III.17 – Variation of evaporator conductance as a function of the heat load applied to the casing.

The theory of invasion percolation in a gradient, see [99] and references therein, indicates that the size of two-phase region, which roughly corresponds to the depth ξ of two-phase zone should scale as

$$\frac{\xi}{a} \propto \left(\frac{Ca}{\Sigma}\right)^{-1} \quad \textbf{(III-56)}$$

where the capillary number Ca can be expressed as $Ca = \mu_l Q/(h_{lv} L_x L_z \sigma)$ and $\sum = (d_{max} - d_{min})/a$ (where we recall that a is the lattice spacing, which can be seen as the mean distance between two pores). Equation (III-56) thus indicates that a broad pore size distribution (i.e. a relatively large $\sum$) favours the formation of a two-phase zone while a narrow distribution will favour the detrimental formation of a vapour blanket under the casing. In our simulations, the pore size distribution is narrow. Therefore, the occurrence of regime II in a capillary evaporator is actually still more likely than predicted from our simulations.

III.5.6 Conclusion

The 3D simulations indicate that three regimes should be distinguished as regards the distribution of the fluid within the wick when the applied heat load is varied. This is in contrast with several previous works where only two regimes were distinguished. In particular, the 3D simulation indicates that the regime leading to the best evaporator performance is a regime, referred to as regime II, where a two-phase liquid-vapour zone forms within the wick. In this regime, the liquid phase in the wick is in partial contact with the casing at the casing/wick contact surface. Because of fundamental differences between the percolation properties of the liquid and vapour phases in the wick between the 2D case and the 3D case, this regime was completely overlooked in some previous works based on 2D pore network simulations. This regime could also not be studied in the modelling approaches assuming only two regions in the wick separated by a macroscopic sharp interface: a dry region occupied by vapour and a liquid region only occupied by liquid. The 3D simulations indicate that three types of region can in fact exist in the wick (in regime III, i.e. for sufficiently high heat load): dry regions, liquid saturated regions and two-phase regions where vapour and liquid coexist. However, the formation of a dry region along the casing in regime III leads to a significant degradation in the evaporator performance.

Therefore, the 3D simulations suggest that the porous wick should be designed so as to favour the occurrence of regime II over a large range of heat loads.

III.6 Synthesis and conclusion of the chapter

Simulations of heat and mass transfer with phase change in a capillary evaporator representative unit cell were presented. The simulations are based on a mesoscale approach in which the capillary effects are modelled as in classical pore network models but where the pressure and temperature fields are computed using mean field approaches.

This mesoscale model, referred to as a mixed pore network model, was first validated by comparison with experiment from Li et al. (2011) [58]. The satisfactory agreement between the simulations and this experiment is an indicator that the mixed pore network model can be used with confidence to study the heat and mass transfer in the wick of a capillary evaporator.

A discussion was conducted on the effective thermal conductivity correlation. First of all, it appears that when the wick remains saturated with liquid, the choice of the correlation to compute the effective thermal conductivity has a low impact on the temperature field. On the other hand, this choice has a greater impact when there is occurrence of vapour in the capillary structure. Then the average model and the Alexander's model were compared for an insulating and a conductive wick. The main correlations presented in section III.4.3.4 are suitable when the wick thermal conductivity is low (i.e. insulating wick) with a relatively low temperature deviation (~3K), while the choice of the correlation is more critical for a conductive wick with a temperature deviation around 11K. These two cited models are the two correlations used in the simulations presented in this thesis. The comparison between several simulations is always performed using the same correlation. Even if the choice of the correlation is not the optimal one for the considered wick, the comparison and discussions remain accurate. Actually, the prediction of the effective thermal conductivity remains an issue to be addressed. Ideally, it will be more interesting and accurate to use the effective thermal conductivity directly determined from experiment.

In the last part of the chapter, the focus was on the liquid-vapour phase distribution within the capillary structure. Three regimes were distinguished. The first one corresponds to a fully saturated wick with liquid. The second regime is characterized by the occurrence of a two-phase zone, located right under the casing, within the wick. Contrary to a common assumption, it was highlighted that the vapour and liquid phases coexist in a same region. This zone persists for a large range of heat flux and is positively correlated with the best thermal performances of the evaporator. Therefore, this regime is the more interesting in term of thermal performance for a capillary evaporator. Finally, the third regime occurs when the first layer of pores under the casing is in vapour state, corresponding to a dry region. This last regime leads to a significant degradation of the thermal performance.

Chapter IV Sensitivity study (Monoporous wick)

Chapter IV Sensitivity study (Monoporous wick) 117
IV.1 Study of grooves location 118
IV.2 Parametric study 129
IV.3 Synthesis and conclusions of the chapter 146

In this chapter, a sensitivity study is performed using the mixed pore network model presented in the previous chapter. The wick is monoporous for all simulations presented in this chapter. Firstly, the influence of grooves location on the evaporator thermal performances is studied. Hence, three different geometries are studied: grooves within the internal surface of the casing, grooves within the external surface of the wick and grooves within the wick. In a second part, a parametric study is presented. The influence of the wick and the casing material is investigated added to a discussion on the wick properties, such that the porosity and the throat size distribution. Three wick materials, three casing materials, four throat size distributions and two porosities are tested. The variations of the nucleation flux, the evaporator conductance, the evaporator wall temperature, the liquid-vapour phase distribution, the mass flow rate and the flux balance as a function of the heat load are discussed in both sections of this chapter.

IV.1 Study of grooves location

IV.1.1 Input properties

In this section, the position of grooves is investigated with a focus on the evaporator thermal performances and the liquid-vapour phase distribution within the capillary structure. The three geometries A, B and C presented in section I.2.5.3.1 are investigated and are depicted in Figure IV.1. Geometry A and B are the common geometries encountered in literature and they correspond to the grooves manufactured at the inner surface of the casing or at the outer surface of the porous structure. The last geometry, i.e. geometry C, corresponds to the grooves manufactured within the capillary wick. Table IV-1 summarizes the different parameters used in the simulations. L_{yt} is the thickness of the capillary strip in geometry C. All the simulations presented in this section have been performed using the Alexander's model to compute the effective thermal conductivity of the wick. ΔT_{nucl} is equal to 3K for all simulations.

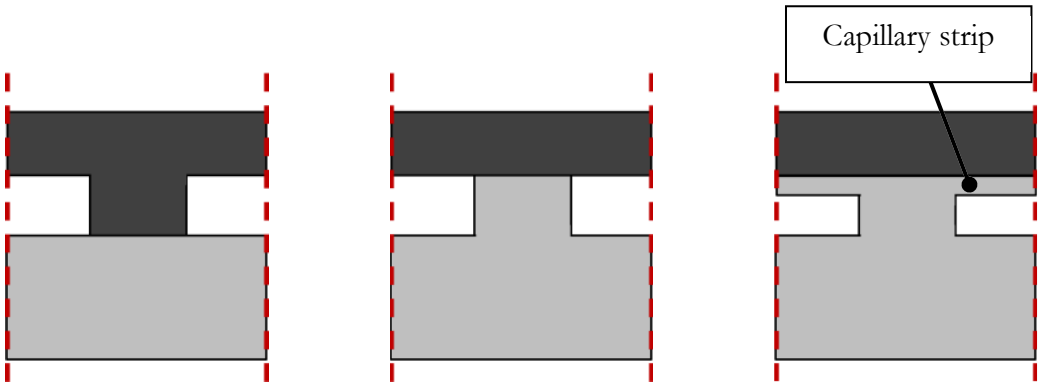

(a) Geometry A **(b)** Geometry B **(c)** Geometry C

Figure IV.1 – Vapour groove positions. (a) Geometry A: at the inner surface of the casing; (b) Geometry B: at the outer surface of the porous structure and (c) Geometry C: within the capillary structure.

Wick properties (Nickel)			
d_{throat} (μm)	2.3±2		
Throat diameter p.d.f	Normal		
Thermal conductivity (W/m/K)	90		
	Geometry A	Geometry B	Geometry C
Porosity	0.805	0.806	0.805
Permeability (m^2)	4.4×10^{-14}	4.6×10^{-14}	4.5×10^{-14}
Casing property (Stainless steel)			
Thermal conductivity (W/m/K)	20		
Fluid properties (Ammonia)			
	Liquid	Vapour	
Thermal conductivity (W/m/K)	0.52912	0.024365	
Viscosity (Pa.s)	1.56×10^{-4}	0.963×10^{-5}	
Specific heat capacity (J/kg/K)	4675.7	2841.3	
Heat latent of vaporisation (kJ/kg)	1225.58		
Liquid density (kg/m^3)	624.46		
Molar mass (kg/mol)	0.017		
Surface tension (N/m)	29.589×10^{-3}		
Inlet temperature/pressure			
P_{cc} (Pa)	615050		
$T_{sat}(P_{cc})$ (K)	283.15		
Geometry dimensions (mm) (see Figure III.3 for definitions)			
L_x	1.9		
L_y	3.4		
L_z	2		
L_{xv}	0.35		
L_{yw}	1.5		
L_{yt}	0.35		
L_{yg}	0.7		
Loop dimensions			
Number of grooves / Length of grooves (mm)	6/25		
Length (mm)/ inner diameter (mm) of the vapour line	200/2		
Length (mm)/ inner diameter (mm) of the liquid line	200/2		
Length (mm)/ inner diameter (mm) of the condenser	200/2		

Table IV-1 – Porous materials properties, fluid properties and geometrical dimensions.

IV.1.2 Results and discussions

IV.1.2.1 Evaporator thermal performances

In this section, discussions on the thermal performances will be conducted. We recall that three regimes have been defined in Chapter III:

- Regime I: the evaporator operates in regime I when the wick is saturated with liquid.

- Regime II: A two-phase zone, i.e. coexistence of liquid and vapour, exists under the casing. The regime can be divided into three parts: a rise, a plateau and a decrease in the conductance. The evaporator reaches its best thermal performances during this regime, i.e. the plateau part.

- Regime III: The first layer of pores under the casing is fully occupied by vapour.

The occurrence of vapour within the capillary structure is desirable to reach the evaporator best performances. Therefore, the nucleation flux corresponding to the heat flux from which the vapour begins to invade the wick (transition from regime I to regime II) should be relatively low in the range of heat load that it is necessary to evacuate.

The nucleation fluxes are equal to 1.74W/cm^2, 3W/cm^2 and 2.415W/cm^2 for geometry A, B and C, respectively. Even though the order of magnitude for the nucleation flux is the same for the three geometries, the occurrence of vapour within the wick is slightly delayed when the grooves are manufactured in the capillary structure (geometries B and C).

The temperature distributions in the unit cell at $z=L_z/2$ are reported in Figure IV.2 at 1.735W/cm^2 and in Figure IV.3 at 2.41W/cm^2. The temperature along the wick/casing – grooves/casing interface is plotted in Figure IV.4 for both fluxes. Actually these two fluxes correspond to the fluxes just before the occurrence of vapour within the wick for geometry A and geometry C respectively, i.e. wicks are still saturated with liquid (regime I). We recall that the heat flux applied at the outer surface of the casing is uniform.

The thickness of the casing for geometry A induces a higher thermal resistance between the wick and the casing, hence the temperature at the wick/groove interface is higher (see Figure IV.2, Figure IV.3 and Figure IV.4). The difference between the maximum temperature obtained from geometry A and geometry B (geometry C respectively) is around 1.2K (0.8K respectively) at 1.735W/cm^2. Therefore, the nucleation occurs in geometry A before in geometries B and C. Finally, the maximum temperature reached along this interface is higher for geometry C than for geometry B due to the porous layer between the casing and the wick: the difference between the maximum temperatures is around 0.4K at 1.735W/cm^2 and 0.5K at 2.41W/cm^2. Actually, the vapour removal channels are at the saturation temperature and lead to a slight decrease in the temperature when the grooves are directly in contact with the casing. Moreover, note that the temperature along the wick/casing interface for geometry C is more uniform than for geometry B (see Figure IV.2, Figure IV.3 and Figure IV.4) due to the capillary strip between the wick and the casing.

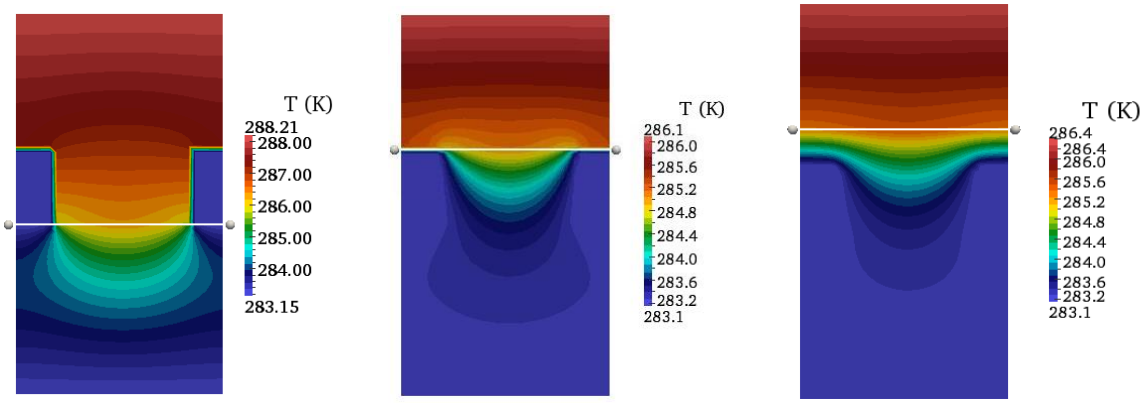

(a) (b) (c)

Figure IV.2 – Temperature distribution (z=L_z/2) at 1.735W/cm² for (a) geometry A, (b) geometry B and (c) geometry C. The white lines show the location of the wick/casing – grooves/casing interface.

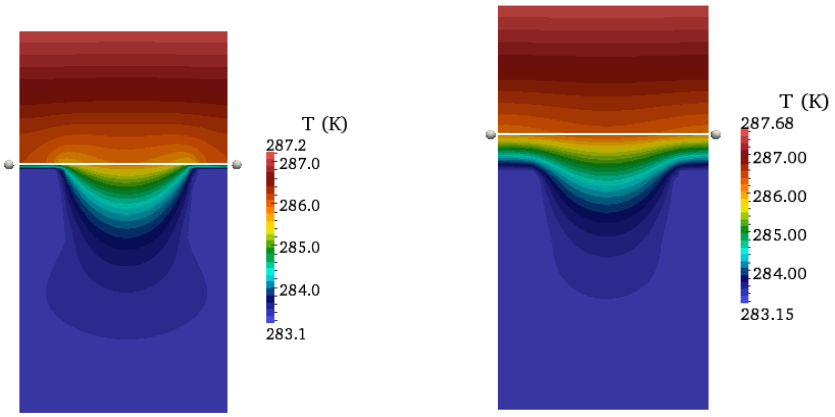

(a) (b)

Figure IV.3 – Temperature distribution (z=L_z/2) at 2.41W/cm² for (a) geometry B and (b) geometry C. The white lines show the location of the wick/casing – grooves/casing interface.

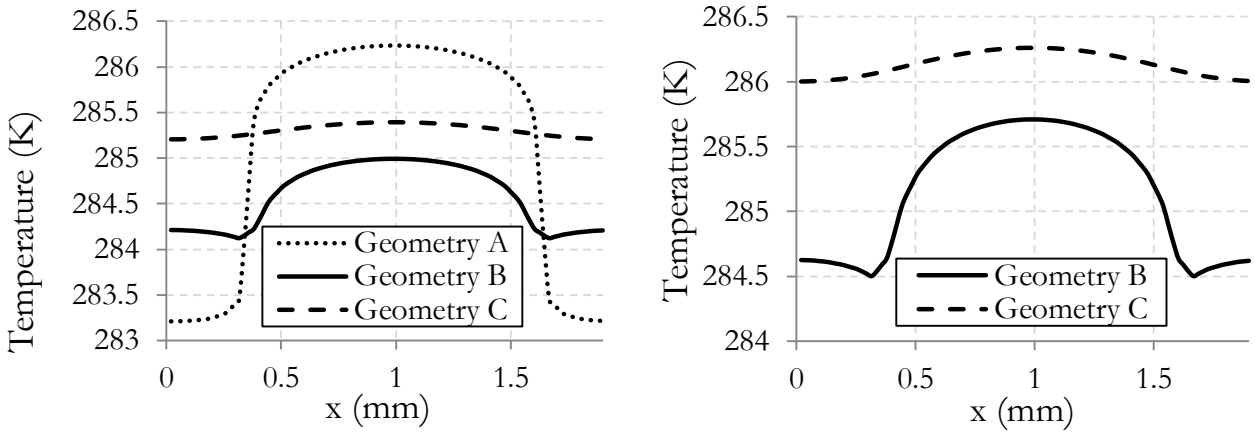

(a) (b)

Figure IV.4 – Variation of the temperature along the wick/casing – grooves/casing interface at (a) 1.735W/cm² and (b) 2.41W/cm².

The following discussion is based on Figure IV.5 and Figure IV.6 which represent the variation of the conductance and the fraction of pores occupied by vapour under the casing as a function of the applied heat load.

The range of heat load where geometry A operates with the best thermal performances, i.e. in regime II, is from 2.875W/cm^2 to 6.01W/cm^2 with a maximum conductance equal to 0.49W/cm^2/K (see Figure IV.5). The corresponding range of fraction of pores occupied by vapour under the casing is from 48.5% to 79.6% (Figure IV.6). Similarly, the range of heat load and fraction of pores occupied by vapour under the casing for geometry B are from 3.885W/cm^2 to 8.5W/cm^2 and from 27.1% to 62.1%. The conductance reaches a maximum of 0.74W/cm^2/K for geometry B. Note that beyond 12.8W/cm^2, the conductance of geometry B becomes lower than the one computed when the wick is saturated with liquid even though a two-phase zone still exists under the casing (vapour occupancy equal to 78%). Finally, geometry C operates with the best thermal performances in regime II for heat fluxes from 4.73W/cm^2 to 8.005W/cm^2 and reaches a maximum conductance equal to 0.83W/cm^2/K. The vapour occupies 45% to 71.9% of the void space under the casing over this range of fluxes.

As already pointed out in other studies (see Coquard (2006) [1]), Figure IV.5 highlights that the evaporator performances are better for grooves manufactured in the wick (geometry B and geometry C) compared to grooves manufactured at the outer surface of the casing (geometry A). Moreover, the conductance reaches higher values for geometry C than for geometry B but for a lower range of fluxes. The groove temperature is computed from the vapour mass flow rate (see section III.2.6). As the vapour mass flow rates for all geometries are almost equivalent (Figure IV.7), the groove temperature of the three geometries are approximately the same for a given heat flux. Therefore, the conductance is mainly impacted by the casing temperature.

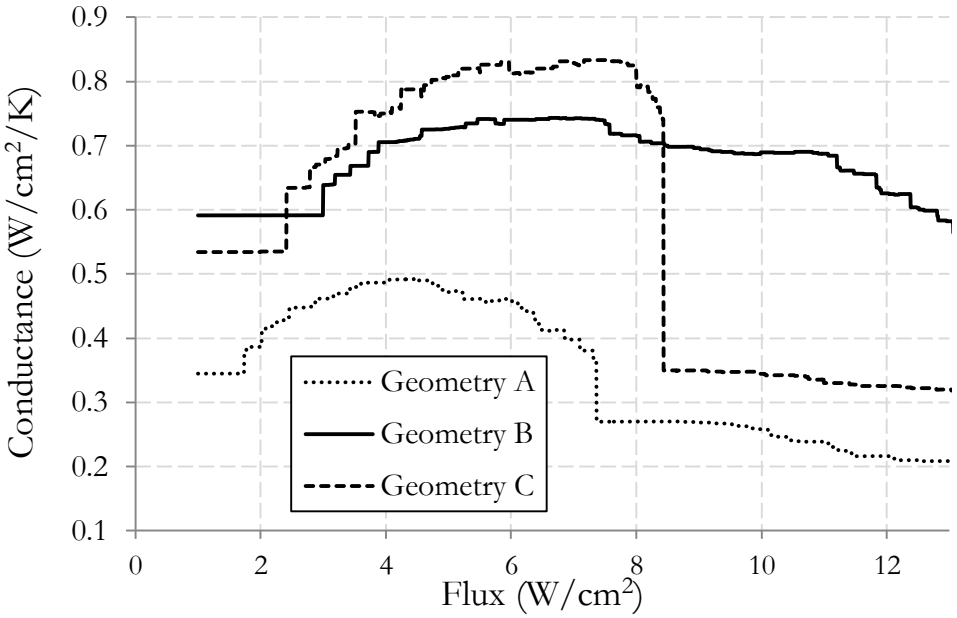

Figure IV.5 – Variation of the conductance as a function of the heat load for geometries A (grooves at the inner surface of the casing), B (grooves at the outer surface of the wick) and C (grooves within the wick).

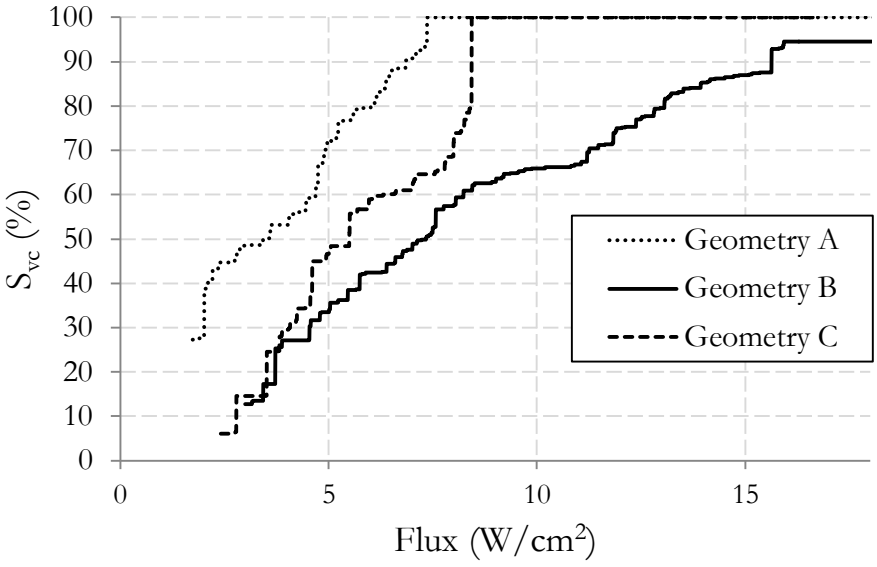

Figure IV.6 – Variation of the fraction of pores occupied by vapour right under the casing (S_{vc}) for geometries A (grooves at the inner surface of the casing), B (grooves at the outer surface of the wick) and C (grooves within the wick). 100% means that a dry region exists under the casing, i.e. the first layer of pores under the casing is in vapour state.

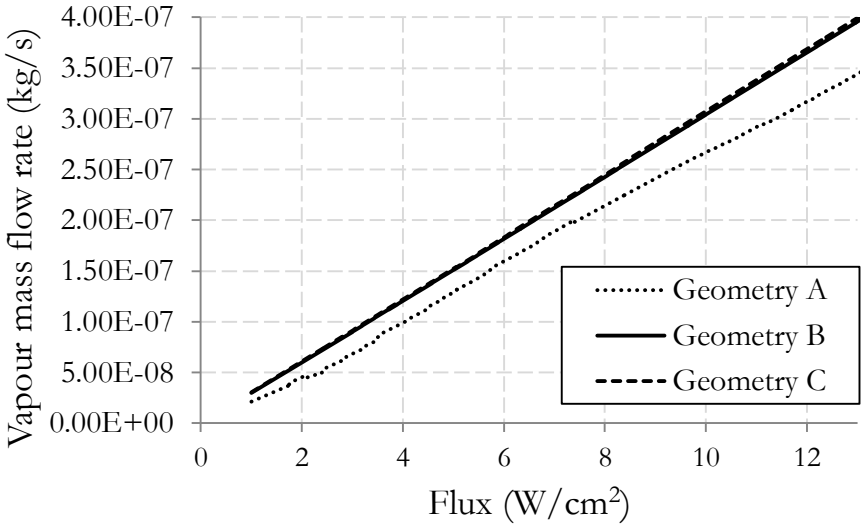

Figure IV.7 – Variation of vapour mass flow rate as a function of the heat load for geometries A (grooves at the inner surface of the casing), B (grooves at the outer surface of the wick) and C (grooves within the wick).

As shown in Figure IV.8, the evaporator wall temperature increases faster for geometry A compared to geometries B and C. Regarding geometry A, the jump of the temperature at 7.365W/cm^2 (the temperature moves from 303.3K to 310.5K) actually corresponds to the occurrence of a dry region under the casing as shown in Figure IV.6. Indeed, at 7.365W/cm^2 the first layer of pore under the casing is occupied by vapour (regime III) for geometry A (corresponding to S_{vc} equal to 100%), while only 50.6% of pores are in vapour state for geometry B (regime II). Actually, the vapour layer formed under the casing induces a higher thermal resistance and lead to the temperature increase. These combined

situations (dry region under the casing and increase in the evaporator wall temperature) cause the drop of the conductance as shown in Figure IV.5. This scenario is exactly the same for geometry C: the temperature increase occurs at 8.435W/cm^2 (Figure IV.8) when a dry region exists under the casing (Figure IV.6).

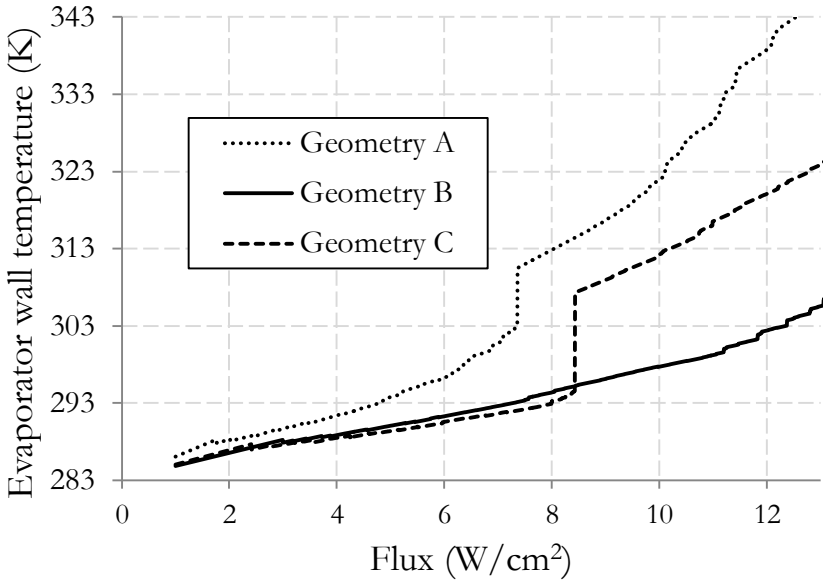

Figure IV.8 – Variation of evaporator wall temperature as a function of the heat load for geometries A (grooves at the inner surface of the casing), B (grooves at the outer surface of the wick) and C (grooves within the wick).

As shown in Figure IV.8, the casing temperature for geometry B is lower than for geometry C for a heat flux lower than 2.415W/cm^2. This flux actually corresponds to the nucleation flux of geometry C. This explains why the conductance of the evaporator, when the wick is saturated with liquid, is lower for geometry C than for geometry B (see Figure IV.5). Between 2.415W/cm^2 and 8.435W/cm^2, the evaporator wall temperature is slightly greater for geometry B compared to geometry C and corresponds to the best thermal performance of geometry C as observed in Figure IV.5. Finally, beyond 8.435W/cm^2 the temperature dangerously increases due to the thermal resistance of the vapour layer under the casing.

In conclusion, the evaporator thermal performances are improved with grooves manufactured in the capillary structure (at the outer surface of the wick or within the wick). Grooves manufactured within the wick lead to better conductance values but for a narrower range of fluxes compared to geometry B. Indeed, the occurrence of a vapour layer under the casing is delayed when the grooves are at the outer surface of the wick and in consequence, the range of heat fluxes corresponding to the best conductances is larger.

IV.1.2.2 Liquid-vapour distribution within the wick

The liquid and the vapour phase distributions within the wick are discussed in this section for the three geometries. Over the whole range of fluxes, the vapour saturation of the wick is always greater for

geometry A than for geometries B and C (see Figure IV.9a), as well as the vapour region depth (Figure IV.9c) and the occupancy of vapour at the wick/groove interface (Figure IV.9d). Figure IV.10 depicts the liquid and vapour phase distributions within the wick for three different heat fluxes: 4W/cm^2, 6W/cm^2 and 9W/cm^2. As can be seen from Figure IV.4, a "hierarchy" exists in the temperature along the wick/groove interface. Even though this discussion was conducted for wicks saturated with liquid, this "hierarchy" is kept whatever the flux applied to the casing as long as a two-phase zone remains under the casing. Consequently, geometry A is always more invaded by vapour than the two others geometries (Figure IV.9a and Figure IV.10).

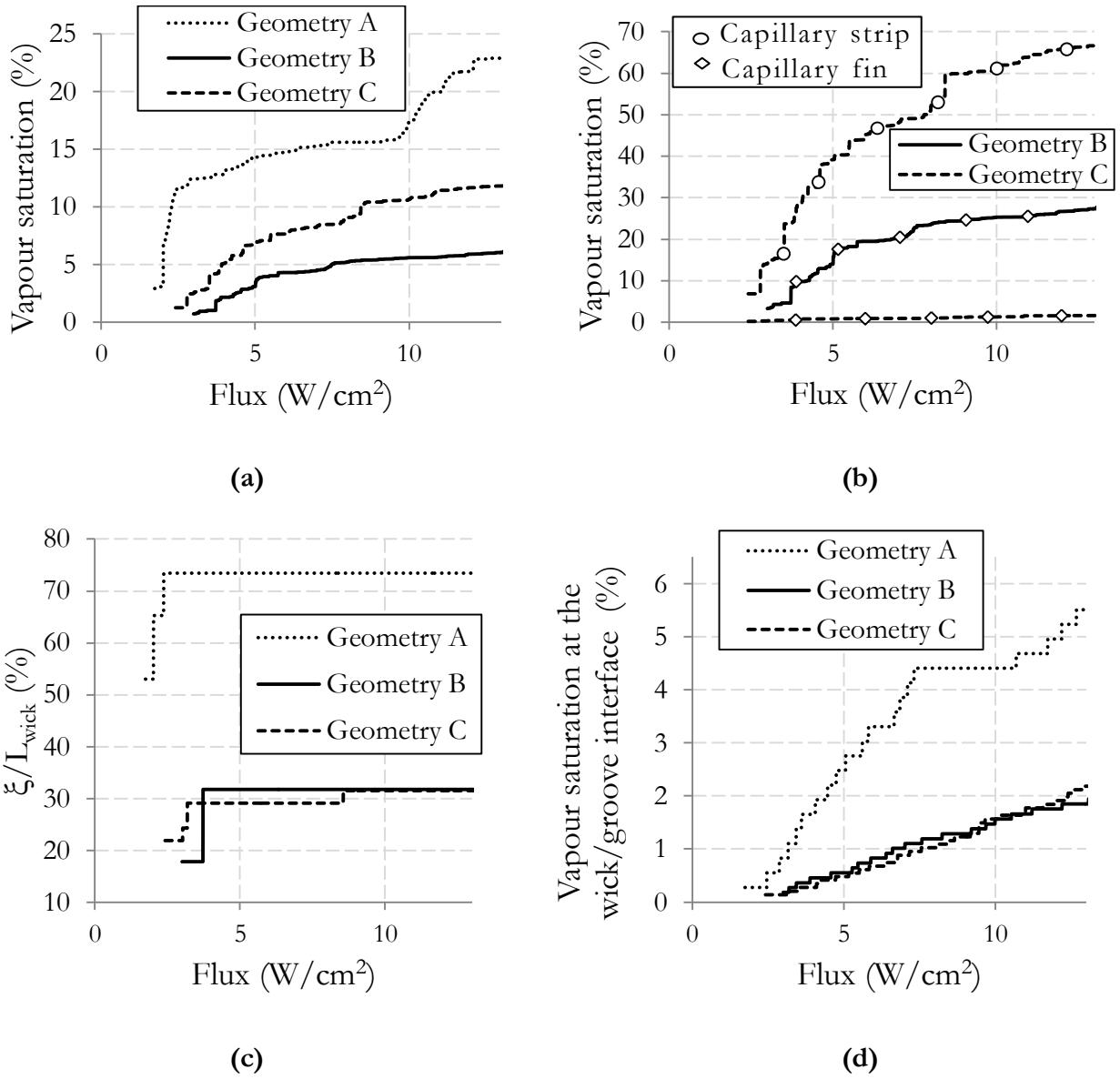

Figure IV.9 – (a) Variation of the vapour overall saturation as a function of the heat load; (c) Variation of the vapour region depth divided by the wick thickness (ξ/L_{wick}) (L_{wick} is equal to L_{yw} for geometry A, $L_{yw} + L_{yg}$ for geometry B and $L_{yw} + L_{yg} + L_{yt}$ for geometry C); and (d) Occupancy of the wick/groove interface by vapour for geometries A (grooves at the inner surface of the casing), B (grooves at the outer surface of the wick) and C (grooves within the wick). (b) Variation of the vapour saturation in the fin region for geometries B and C and in the capillary strip for geometry C.

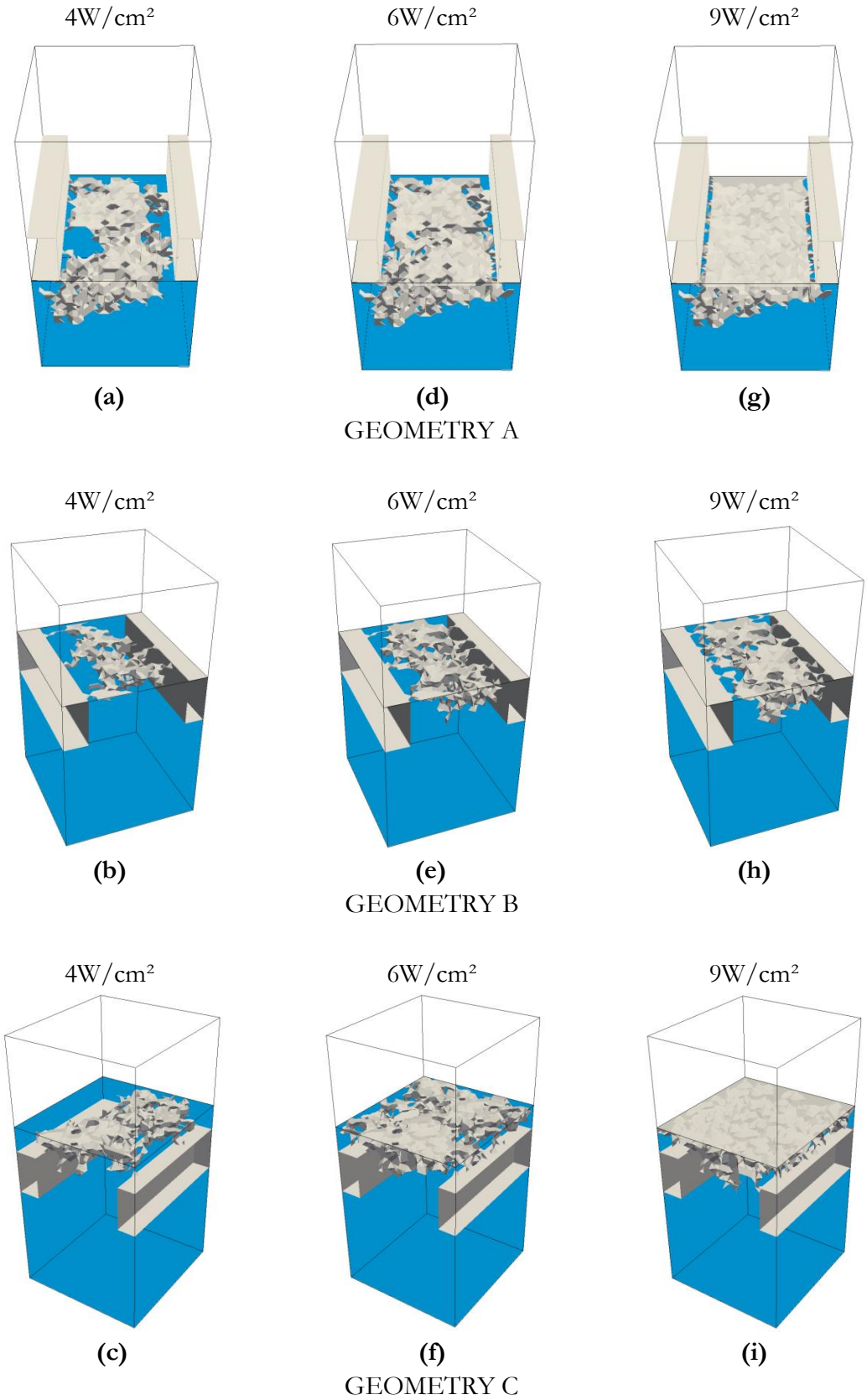

Figure IV.10 – Pore network numerical visualisations of vapour and liquid phase distribution in the evaporator unit cell for the fluxes 4W/cm² (figures (a), (b) and (c)), 6W/cm² ((d),(e) and (f)) and 9W/cm² (figures (g), (h) and (i)) for geometry A (figures (a), (d) and (g)), geometry B (figures (b), (e) and (h)) and geometry C (figures (c), (f) and (i)). Vapour phase is in grey and liquid phase is in blue.

As shown in Figure IV.9c, the vapour region depth is high even for low heat load when the grooves are manufactured in the casing. This configuration is unfavourable for a capillary evaporator application due to the potential vapour breakthrough. However, for all geometries, the vapour region firstly grows towards the inlet of the wick (Figure IV.9c). Then the growth of the vapour region occurs laterally and in the grooves direction (Figure IV.9d). Moreover, the capillary fin (geometries B and C) permits to maintain the vapour in this region and thus prevent the vapour breakthrough (see Figure IV.9b and Figure IV.9c). Indeed, the vapour is completely confined in the fin region for geometry B (Figure IV.9b). Similarly, the capillary strip between the wick and the casing plays a role of capillary lock: as shown in Figure IV.9b, the vapour region is mainly located in this wick part (the vapour saturation in the fin region is less than 2%). However, for geometry C configuration, the flux is homogeneously transmitted towards the wick (see Figure IV.4), favouring the vaporisation of new pores in the capillary strip. Actually, between 38% and 52% of this region are at the vapour state when the evaporator operates with the best thermal performances (Figure IV.6).

IV.1.2.3 Flux balance

The heat load applied to the casing is not completely used to vaporise the liquid within the wick. Figure IV.11 shows the part of the flux actually used for the vaporisation. As explained in section I.2.4, the heat flux is also lost by conduction towards the wick inlet (parasitic flux) (Figure IV.12a) and by convection in the grooves (Figure IV.12b). The parts of the flux used to overheat the liquid and the vapour are always lower than 1% and are not discussed here.

Over the range of fluxes corresponding to the best thermal performance of the evaporator in configuration A, the vaporisation flux is between 74% and 86% (Figure IV.11). Indeed, the part of the flux lost by conduction towards the wick (the parasitic flux) is not negligible and is between 23.5% and 11.2% (Figure IV.12a). Furthermore, around 3% of the flux is lost by convection during this regime (Figure IV.12b). The part of the flux used for the vaporisation reaches a plateau around 85% for fluxes greater than 6W/cm^2. Unfortunately, in this range of fluxes, the evaporator begins to operate in regime III and the thermal performances decrease. Note that the parasitic heat flux reaches reasonable values in this regime (between 5 and 10% of the total heat load), while the flux lost by convection exceeds 6% and becomes the main source of flux loss.

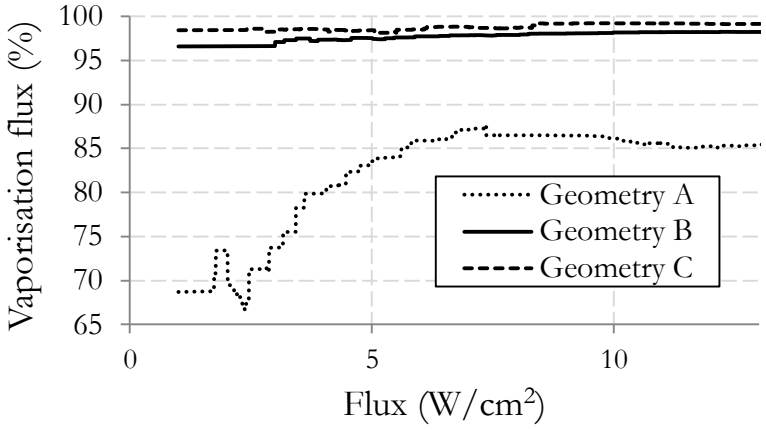

Figure IV.11 – Variation of the vaporisation flux as a function of the heat load for geometries A (grooves at the inner surface of the casing), B (grooves at the outer surface of the wick) and C (grooves within the wick).

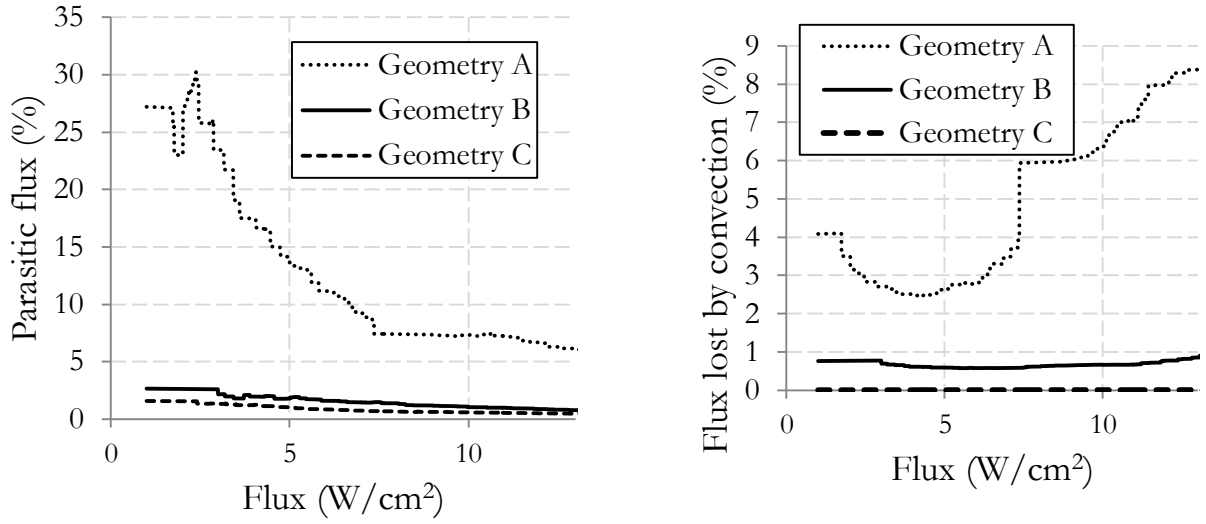

(a) **(b)**

Figure IV.12 –(a) Variation of the parasitic flux and (b) variation of the flux lost by convection within the vapour removal channel as a function of the heat load for geometries A (grooves at the inner surface of the casing), B (grooves at the outer surface of the wick) and C (grooves within the wick).

As shown in Figure IV.11, the part of the flux applied to the casing used to vaporise the liquid is greater than 95% when the grooves are in the wick. Geometries B and C are more favourable to limit the flux losses in the evaporator. In fact, the amounts of flux lost by conduction and by convection are less than 5% and 1% (Figure IV.12). In term of flux loss, geometry C is even better than geometry B insofar as the parts of flux lost by convection and by conduction are lower than 0.3% and 1.6% of the total heat flux as shown in Figure IV.12.

IV.1.3 Summary

Three different positions of the grooves have been studied: at the inner surface of the casing (geometry A), at the outer surface of the wick (geometry B) and within the wick (geometry C). The evaporator thermal performances are better when the grooves are manufactured in the wick.

Geometry A is the worst design in terms of thermal performances, liquid-vapour phase distribution and flux loss. The range of fluxes where the evaporator operates in regime II with the best conductance is narrower than for other geometries. Moreover, the vapour is close to the breakthrough at the inlet of the wick even for low heat load. In addition, the part of the parasitic heat flux remains relatively high during regime II.

Geometry C reaches better values of conductance than geometry B but for a narrower heat flux range. The heat load is transmitted more uniformly towards the wick and unfortunately leads to a premature transition between regime II and regime III. On the other hand, geometry C prevents the loss of heat flux in the evaporator.

IV.2 Parametric study

IV.2.1 Input properties

In this section, the influence of the wick material and the evaporator wall material is discussed as well as the porosity and the throat size distribution on the conductance, the evaporator wall temperature and the parasitic heat flux. Three wick materials (copper, nickel and PTFE) and three casing material (copper, aluminium and stainless steel) commonly encountered in the literature have been tested. Moreover, these materials have been chosen for their different thermal conductivities. The porosity and the throat size distribution used in the simulations have been selected to be in accordance with common values found in literature (see Table I-2 and Table I-4). Note that two average porosities have been imposed: 0.5 and 0.7 and throat sizes used are: 2.3µm±2µm, 5µm±3µm, 10µm±5µm and 20µm±6µm.

Wick properties		
Throat diameter p.d.f	Normal	
Fluid properties (Ammonia)		
	Liquid	Vapour
Thermal conductivity (W/m/K)	0.52912	0.024365
Viscosity (Pa.s)	1.56×10^{-4}	0.963×10^{-5}
Specific heat capacity (J/kg/K)	4675.7	2841.3
Heat latent of vaporisation (kJ/kg)	1225.58	
Liquid density (kg/m^3)	624.46	
Molar mass (kg/mol)	0.017	
Surface tension (N/m)	29.589×10^{-3}	
Inlet temperature/pressure		
P_{cc} (Pa)	615050	
$T_{sat}(P_{cc})$ (K)	283.15	
Geometry dimensions (mm) (see Figure III.3 for definitions)		
L_x	1.9	
L_y	3.4	
L_z	2	
L_{xv}	0.35	
L_{yw}	1.5	
L_{yg}	0.7	
Loop dimensions		
Number of grooves / Length of grooves (mm)	6/25	
Length (mm)/ inner diameter (mm) of the vapour line	200/2	
Length (mm)/ inner diameter (mm) of the liquid line	200/2	
Length (mm)/ inner diameter (mm) of the condenser	200/2	

Table IV-2 – Throat diameter p.d.f, fluid properties, geometrical dimensions and loop dimensions used in simulations.

Table IV-2, Table IV-3 and Table IV-4 summarize the different parameters used in the simulations. All the simulations presented in this section have been performed using the Alexander's model to compute the effective thermal conductivity of the wick. Grooves are located within the wick as this configuration gives the best evaporator thermal performances. Porosities and permeabilities reported in Table IV-4 are those numerically computed. ΔT_{nucl} is equal to 3K for all simulations. In this section, results are labelled using the casing material, the wick material, the porosity and the mean throat diameter. For instance, Al_Ni_0.5_5 will be understood as a simulation performed with an aluminium casing, a nickel wick, a porosity equal to 0.5 and a mean throat diameter equal to 5µm.

	Material	Thermal conductivity
Casing	Al	240 W/m/K
	Cu	380 W/m/K
	SS	20 W/m/K
Wick	Cu	380 W/m/K
	Ni	90 W/m/K
	PTFE	0.2 W/m/K

Table IV-3 – Thermal conductivity of the materials used in simulations.

Simulation	Casing	Wick	Porosity	d_{th} (µm±µm)	Permeability (m^2)	k_l^* (W/m/K)	k_v^* (W/m/K)	Nucleation flux (W/cm^2)
#1	Cu	Cu	0.475	5±3	2.15×10^{-13}	47.44	17.91	38.55
#2	Cu	Cu	0.481	10±5	2.77×10^{-12}	45.98	17.11	37.5
#3	Cu	Cu	0.512	20±6	3.06×10^{-11}	39.31	13.59	32.2
#4	Al	Cu	0.475	5±3	2.15×10^{-13}	47.44	17.91	37.7
#5	Al	Cu	0.481	10±5	2.77×10^{-12}	45.98	17.11	36.6
#6	Al	Cu	0.514	20±6	1.56×10^{-11}	38.87	13.38	31.3
#7	Al	Cu	0.665	5±3	3.94×10^{-13}	16.65	3.85	13.8
#8	Al	Cu	0.668	10±5	4.88×10^{-12}	16.4	3.77	13.6
#9	Al	Cu	0.676	20±6	2.83×10^{-11}	15.63	3.51	13
#10	SS	Cu	0.475	5±3	2.15×10^{-13}	47.44	17.91	31
#11	SS	Cu	0.481	10±5	2.77×10^{-12}	45.98	17.11	30.1
#12	SS	Cu	0.512	20±6	3.06×10^{-11}	39.31	13.59	26.05
#13	SS	Cu	0.665	5±3	3.94×10^{-13}	16.65	3.85	11.9
#14	SS	Cu	0.668	10±5	4.88×10^{-12}	16.40	3.77	11.7
#15	SS	Cu	0.676	20±6	5.67×10^{-11}	15.63	3.51	11.2
#16	Cu	Ni	0.471	2.3±2	1.53×10^{-14}	17.98	6.85	15.03
#17	Cu	Ni	0.475	5±3	2.15×10^{-13}	17.72	6.69	14.9
#18	Cu	Ni	0.665	5±3	3.94×10^{-13}	7.82	1.81	6.7
#19	SS	Ni	0.471	2.3±2	1.53×10^{-14}	17.98	6.85	12.7
#20	SS	Ni	0.475	5±3	1.08×10^{-13}	17.72	6.69	12.6
#21	SS	Ni	0.665	5±3	3.94×10^{-13}	7.82	1.81	6
#22	Cu	PTFE	0.474	2.3±2	1.47×10^{-14}	0.27	0.10	0.26
#23	SS	PTFE	0.471	2.3±2	1.53×10^{-14}	0.27	0.10	0.26

Table IV-4 – Casing materials, wick materials, porosity, throat size distribution, permeability, effective thermal conductivity of the wick computed using the Alexander's model and nucleation flux for the different simulations.

IV.2.2 Results and discussions

In the following sections, the focus is made on the evaporator thermal performances. The influence of the porosity, the wick material, the casing material and the throat size distribution is studied. The discussions will be based on conductances, temperature and pressure fields, evaporator wall temperatures, vapour mass flow rates, parasitic fluxes, occupancies of the vapour under the casing, 3D liquid-vapour phase distributions, length average liquid saturations and the nucleation fluxes. The two last quantities need to be specified.

The occurrence of a two-phase zone under the casing is positively correlated with the best thermal performances of the evaporator. Hence, the flux from which the vapour occurs within the wick (nucleation flux) has an impact on the evaporator performance given that the optimal behaviour of the evaporator is expected for fluxes greater than the nucleation flux. The values of the nucleation flux for the different simulations are reported in Table IV-4 and in Figure IV.13. We recall that this flux corresponds to the transition from regime I to regime II.

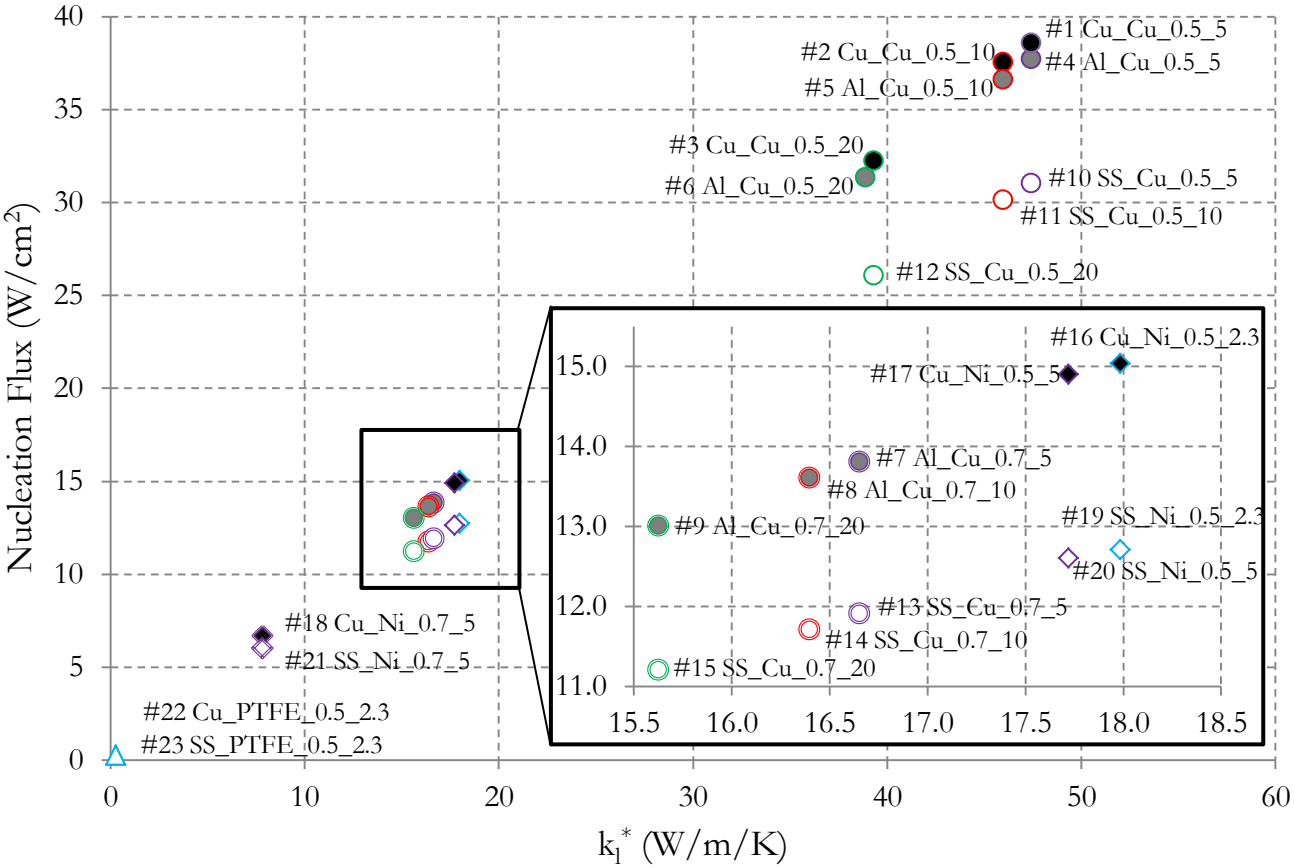

Figure IV.13 – Nucleation flux for different wick materials, casing materials, porosities and throat size distributions. Legend: Circle symbols correspond to copper wick; diamond symbols correspond to nickel wick and triangle symbols correspond to PTFE wick. Blue outlines correspond to throat distribution equal to 2.3±2; yellow outlines correspond to throat distribution equal to 5±3; red outlines correspond to throat distribution equal to 10±5 and green outlines correspond to throat distribution equal to 20±6. Simple outlines correspond to correspond to porosity equal to 0.5 and double outlines correspond to porosity equal to 0.7. White symbols correspond to stainless steel casing; grey symbols correspond to aluminium casing and black symbols correspond to copper casing.

Assuming that the value 1 is assigned to pores occupied by liquid and 0 otherwise, the length average liquid saturation is defined as the sum of the liquid saturation divided by the total number of pores n_k present along each line in the length of the evaporator (in the z-direction) (equation (IV-1)).

$$S_l(i,j) = \left(\sum_{k=1}^{k=n_k} S_l(i,j,k) \right) \Big/ n_k \quad \textbf{(IV-1)}$$

$S_l(i,j,k) = 1$, if the pore is in liquid state;

$S_l(i,j,k) = 0$, otherwise.

A sketch shown in Figure IV.14 summarizes how to compute the map of the length average liquid saturation.

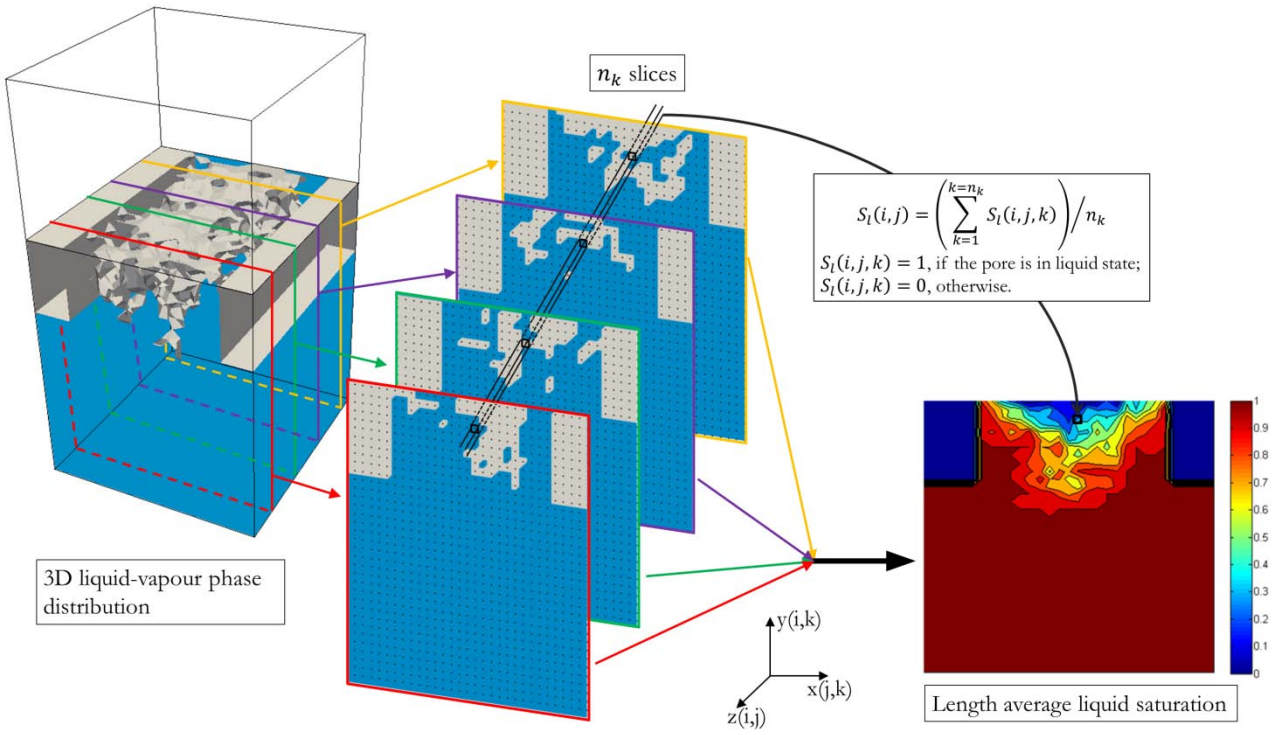

Figure IV.14 – Explanatory diagram for computing the map of the length average liquid saturation

IV.2.2.1 Influence of porosity and wick material

The effective thermal conductivity of the wick depends on the wick material and the porosity among others. That is why the influence of both is discussed in this section. We recall that Alexander's model is used for all simulations and the correlation is given by equation (IV-2).

$$k_i^* = k_i \left(\frac{k_i}{k_w} \right)^{-(1-\varepsilon)^{0.59}} \quad \textbf{(IV-2)}$$

where i denotes the liquid l or the vapour v phase depending on whether the considered node is occupied by the liquid or the vapour. Note that for an insulating wick (low thermal conductivity), the

porosity has not a significant impact on the effective thermal conductivity. For a conductive capillary structure, the effective thermal conductivity increases rapidly with a decreasing porosity.

A low increase in the porosity induces the occurrence of the vapour at a significantly lower heat load. For instance simulations #4 and #7 were performed with the same wick and casing material and for a similar random distribution of throat size, but for porosity equal to 0.475 and 0.665. The nucleation heat flux for simulation #4 is equal to 37.7W/cm^2, whereas the vapour occurs within the wick at 13.8W/cm^2 for simulation #7. A higher porosity induces a lower effective thermal conductivity (see Table IV-4), and as a result a higher temperature within the wick and then under the casing. Indeed, as shown in Figure IV.15, the maximum temperature along the wick/casing interface for simulation #4 is 2K lower at 13.7W/cm^2 than the maximum obtained for simulation #7. Therefore, the vapour within the capillary structure is expected to occur for a low heat flux if the porosity is high and conversely.

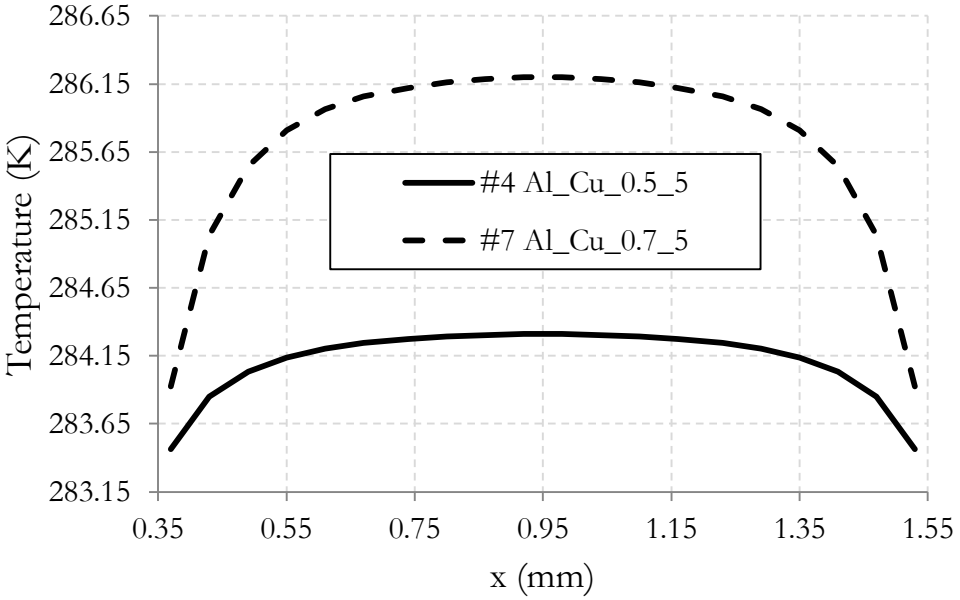

Figure IV.15 – Temperature along the wick/casing interface at 13.7W/cm² for two different porosities: 0.5 (simulation #4) and 0.7 (simulation #7). The wick is made of copper, the casing is made of aluminium and the mean throat diameter is equal to 5µm.

As shown in Figure IV.16, the increase in the porosity causes the reduction of the conductance whatever the throat size, the wick material and the casing material. Simulations #17 and #18 are considered to illustrate the discussion. They correspond to an evaporator made with a nickel wick, a copper casing and a mean throat diameter equal to 5µm. Since the vapour mass flow rate is fully equivalent for both simulations (Figure IV.17), the groove temperature is also the same whatever the porosity. That way, the evaporator wall temperature is the only quantity which influences the conductance. Indeed, the casing temperature is higher for simulation #18 than for simulation #17 explaining the conductance behaviour. The global shape of the two-phase zone is comparable with no obvious noticeable difference (see Figure IV.18 sketched at 24.5W/cm^2) for both simulations and consequently is not the factor which influence the casing temperature. The temperature field along an arbitrary line in the y-direction is plotted in

Figure IV.19 at 24.5W/cm^2. Note that the temperature is almost equivalent in the liquid phase. The temperature rises rapidly in the vapour zone under the casing in both cases. However, this effect is clearly more pronounced when the porosity is high. Of course, this behaviour is directly related to the value of the effective thermal conductivity computed in the vapour zones which is almost 6 times lower for simulation #18 than for simulation #17. Thus, the vapour plays an insulating role between the wick and the casing explaining the overheating of the casing.

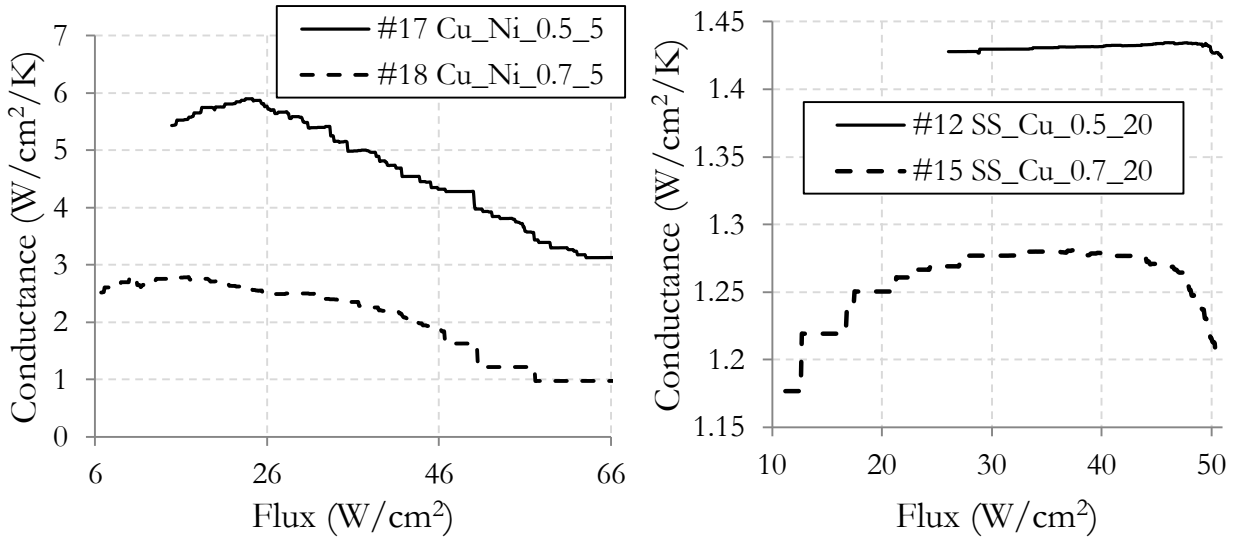

(a) (b)

Figure IV.16 – Variation of the conductance for (a) a Cu-Ni evaporator with a mean throat size equal to 5µm and (b) an SS-Cu evaporator with a mean throat size equal to 20µm for porosities equal to 0.5 and 0.7.

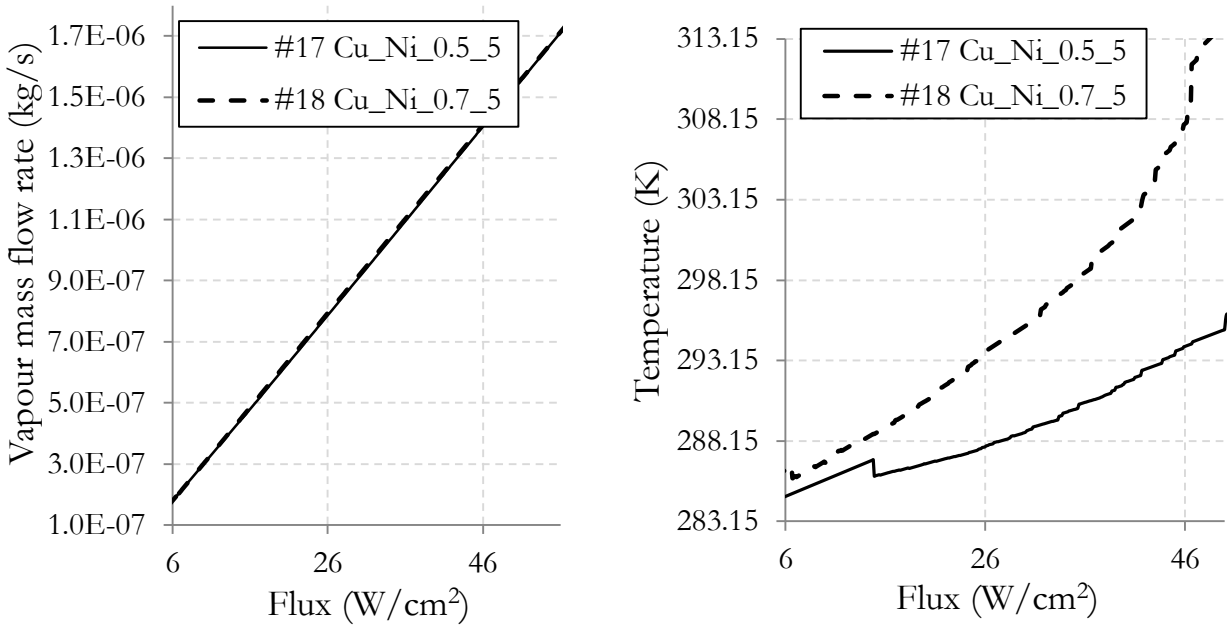

(a) (b)

Figure IV.17 – (a) Variation of vapour mass flow rate and (b) evaporator wall temperature as a function of the heat load for a Cu-Ni evaporator for two different porosities (0.5 and 0.7).

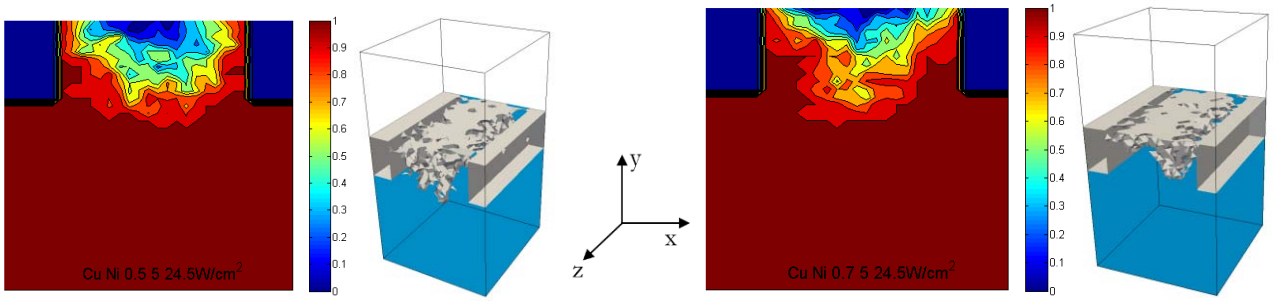

(a1) (b1) (a2) (b2)

Figure IV.18 – (a) Length average liquid saturation for (a1) a porosity equal to 0.5 (simulation #17) and for (a2) a porosity equal to 0.7 (simulation #18). Red zones, i.e. liquid saturation equal to 1, represent a liquid-saturated zone and blue zones, i.e. liquid saturation equal to 0, represent a vapour-saturated zone. (b) Pore network numerical visualisations of vapour and liquid phase distribution in the evaporator unit cell for (b1) a porosity equal to 0.5 (simulation #17) and for (b2) a porosity equal to 0.7 (simulation #18). Vapour phase is in grey and liquid phase is in blue. Figures (a1) to (b2) correspond to a Cu-Ni evaporator with a mean throat size equal to 5µm. Results are shown for a heat load equal to 24.5W/cm².

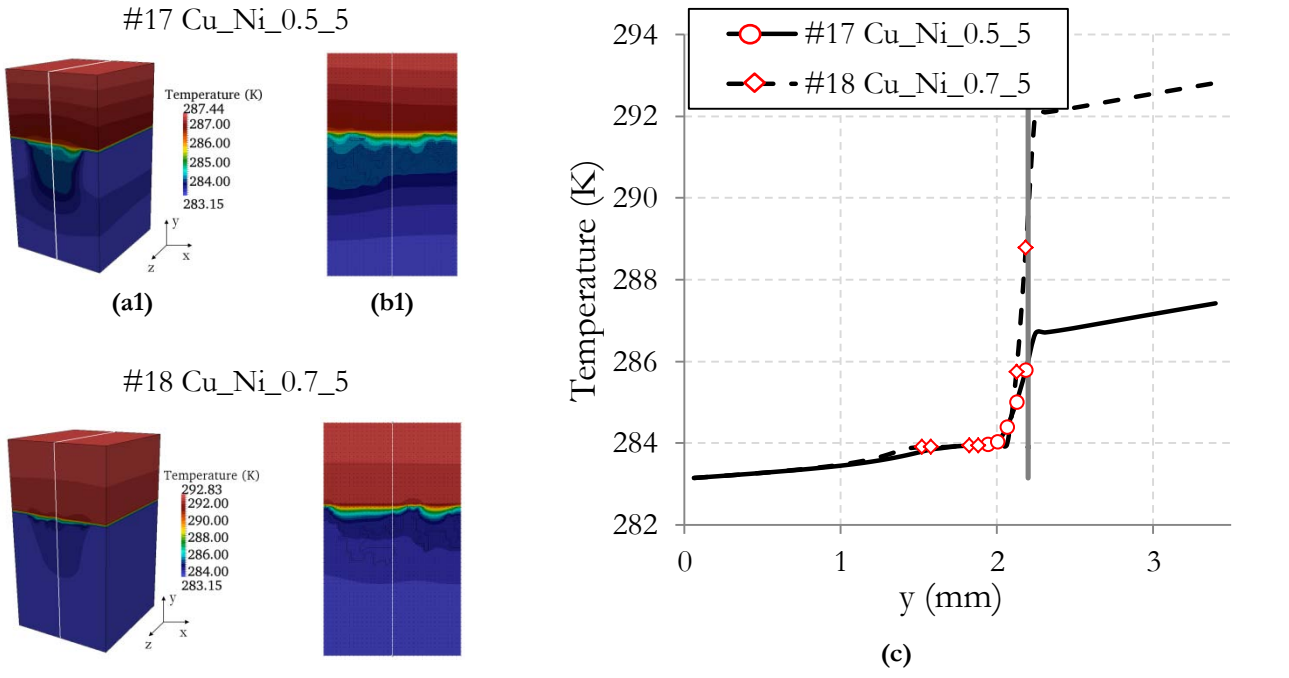

Figure IV.19 – (a) Temperature distribution in the unit cell computed from (a1) a porosity equal to 0.5 (simulation #17) and (a2) a porosity equal to 0.7 (simulation #18). (b) Temperature in the x-y slice corresponding to the white lines in figures (a) for (b1) a porosity equal to 0.5 (simulation #17) and (b2) a porosity equal to 0.7 (simulation #18). Black lines delimit the shape of the vapour phase within the wick. (c) Temperature profiles along the height of the unit cell from the wick inlet to the casing outer surface (in the y-direction). Red symbols indicate that the considered pore is occupied by the vapour. Grey line corresponds to the wick/casing interface location. The location of the line chosen to plot the temperature corresponds to the white lines in figures (b). Figures (a) to (c) correspond to a Cu-Ni evaporator with a mean throat size equal to 5µm. Results are shown for a heat load equal to 24.5W/cm².

For casings manufactured with the same material, the nucleation flux is lower for an insulating wick than for a conductive capillary structure. For example simulations #10 and #20 illustrate this (see Table IV-4). The casing is made of stainless steel, the porosity and the throat size distribution of the wick are equivalent. Simulation #10 was performed for a conductive wick (copper wick) and the nucleation heat flux is equal to 31W/cm^2, while simulation #20 was performed for a nickel wick, which has a lower thermal conductivity, and the nucleation heat flux is equal to 12.6W/cm^2. As for the discussion on the influence of the porosity, the effective thermal conductivity depends on the wick thermal conductivity. Therefore, the maximum temperature under the casing increases with the decrease in the effective thermal conductivity, inducing the occurrence of vapour for lower heat flux.

When the evaporator operates in regime II, the thermal performances are better for a conductive wick. Results for simulations #13 and #21 are used to illustrate this point (see Figure IV.20a). The maximum temperature at the top wall is greater for an evaporator with a nickel wick compared to a copper wick (Figure IV.20a). Figure IV.21 represents the temperature field along a line in the y-direction for simulation #13 and simulation #21 at 16.2W/cm^2. The occurrence of vapour under the casing induces a higher temperature jump when the wick has low thermal conductivity due to the decrease in the effective thermal conductivity (Table IV-4).

The variation of the parasitic heat flux as a function of the heat load is shown in Figure IV.22 for simulations #17 and #18 and simulations #13 and #21. This undesired heat loss towards the wick inlet is reduced with the increase in the porosity and/or the decrease in the wick thermal conductivity because the computed effective thermal conductivity is lower. The wick has to play a role of thermal lock and this requires a high porosity and/or a low wick thermal conductivity.

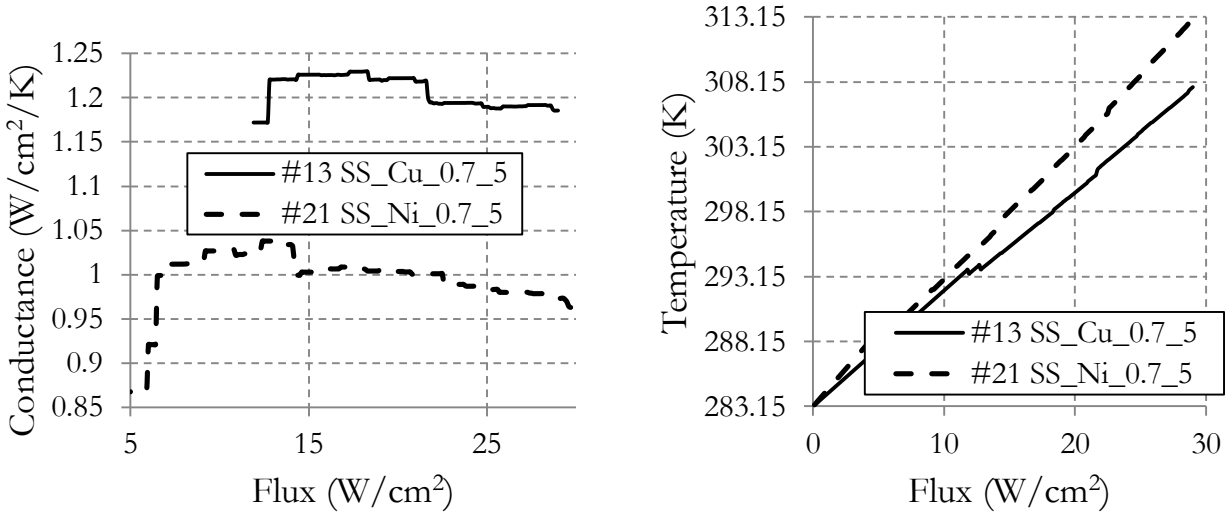

(a) **(b)**

Figure IV.20 – Variation of (a) the conductance and (b) the maximum casing temperature as a function of the heat load for an SS-Cu (simulation #13) and an SS-Ni (simulation #21) evaporator with a porosity equal to 0.7 and a mean throat size equal to 5µm.

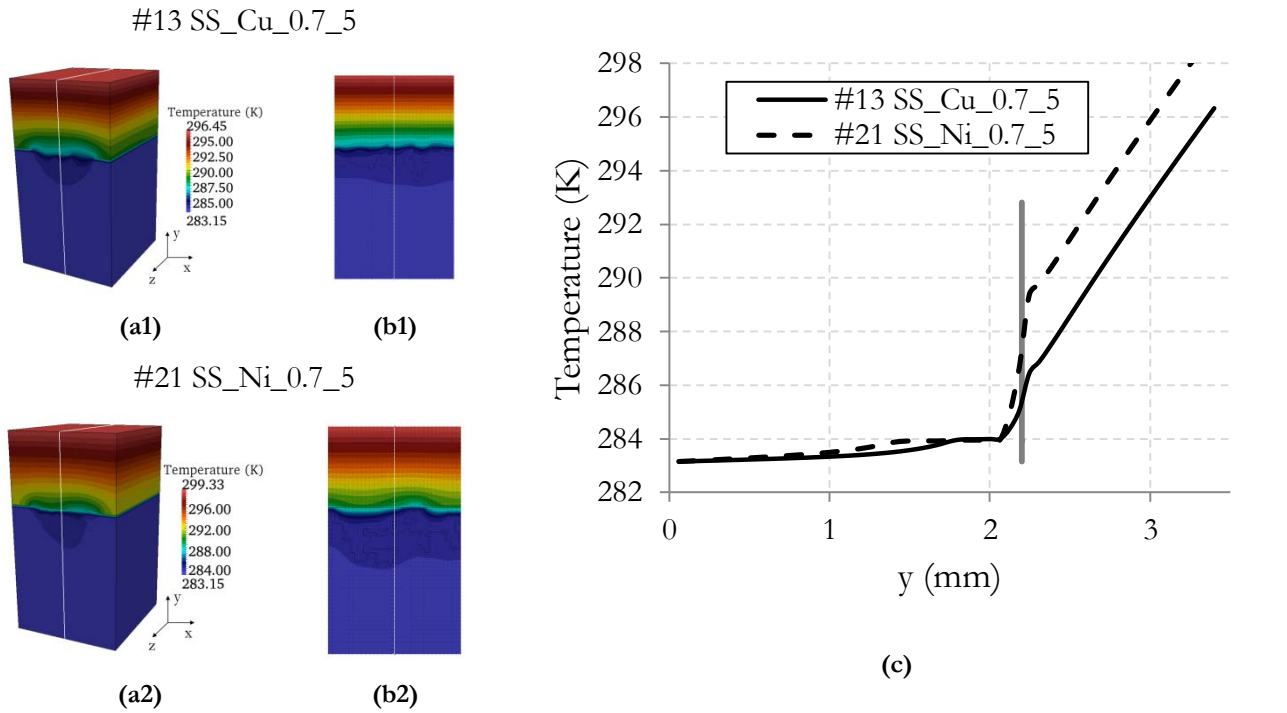

Figure IV.21 – (a) Temperature distribution in the unit cell computed from (a1) a copper wick (simulation #13) and (a2) a nickel wick (simulation #21). (b) Temperature in the x-y slice corresponding to the white lines in figures (a) for (b1) a copper wick (simulation #13) and (b2) a nickel wick (simulation #21). Black lines delimit the shape of the vapour phase within the wick. (c) Temperature profiles along the height of the unit cell from the wick inlet to the casing outer surface (in the y-direction). Grey line corresponds to the wick/casing interface location. The location of the line chosen to plot the temperature corresponds to the white lines in figures (b). Figures (a1) to (c) correspond to an evaporator having a stainless steel casing and a wick with a mean throat size equal to 5µm and a porosity equal to 0.7. Results are shown for a heat load equal to 16.2W/cm².

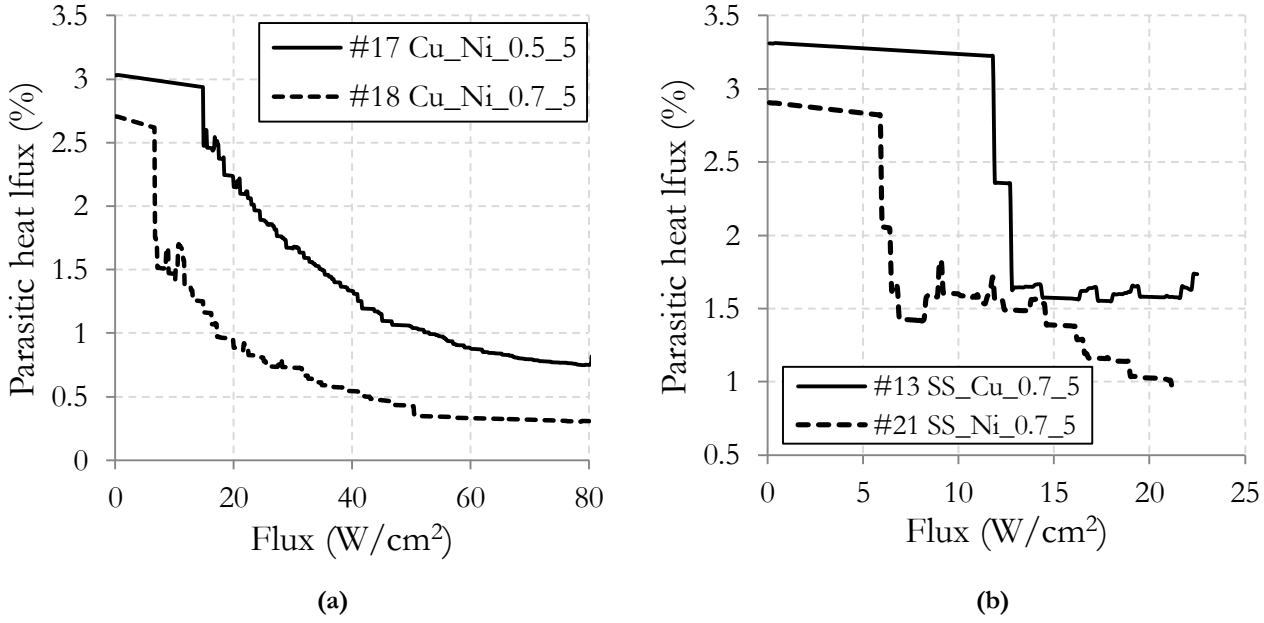

Figure IV.22 – Variation of the parasitic flux as a function of the heat load. (a) Results for a Cu-Ni evaporator having a porosity equal to 0.5 (simulation #17) or equal to 0.7 (simulation #18) (mean throat size equal to 5µm). (b) Results for an evaporator made with a copper wick (simulation #13) and a nickel wick (simulation #21) (stainless steel casing, porosity equal to 0.7 and mean throat diameter equal to 5µm).

In summary, in terms of thermal performances, a high wick thermal conductivity is better, i.e. conductive material and/or a low porosity. Both parameters induce a higher wick effective thermal conductivity which permits a better heat exchange between the casing and the heat sink (i.e. the cold liquid from the compensation chamber). As a result, the maximum evaporator wall temperature is considerably reduced. On the other hand, the flux lost by conduction towards the inlet of the wick increases when the wick is conductive and/or has a low porosity. A desirable objective is to make this parasitic flux as low as possible in order to maximize the efficiency of the capillary evaporator. Therefore, a trade-off needs to be found between a conductive/insulating wick and a high/low porosity to obtain the best evaporator thermal performances and the lowest parasitic heat flux.

IV.2.2.2 Influence of casing material

The more the casing is conductive, the more the flux from which the vapour occurs within the wick is high (see Table IV-4). For example, simulations #2, #5 and #11 have the same porosity, the same throat size distribution and the wick is made of copper material. The vapour occurs within the wick for a heat flux equal to 37.5W/cm^2 when the casing is made of copper, while the nucleation flux is equal to 30.1W/cm^2 when the casing is made of stainless steel. Actually, the maximum temperature under the casing decreases with the rise in the wall thermal conductivity (see Figure IV.23). However, the order of magnitude for the nucleation flux is the same and this trend is all the more true that the casing is conductive (see simulation #2 and simulation #11). Indeed, the maximum temperature under the casing is almost the same at 30W/cm^2 for a casing made of aluminium or copper (maximum temperature equal to 285.76K and 285.7K, respectively).

Moreover, when the wick is insulating, the vapour occurs within the wick for an almost similar heat flux whatever the evaporator wall material. For instance, simulations #22 and #23 were performed with a PTFE wick for two different casing materials (copper and stainless steel) and the nucleation fluxes are both equal to 0.26W/cm^2.

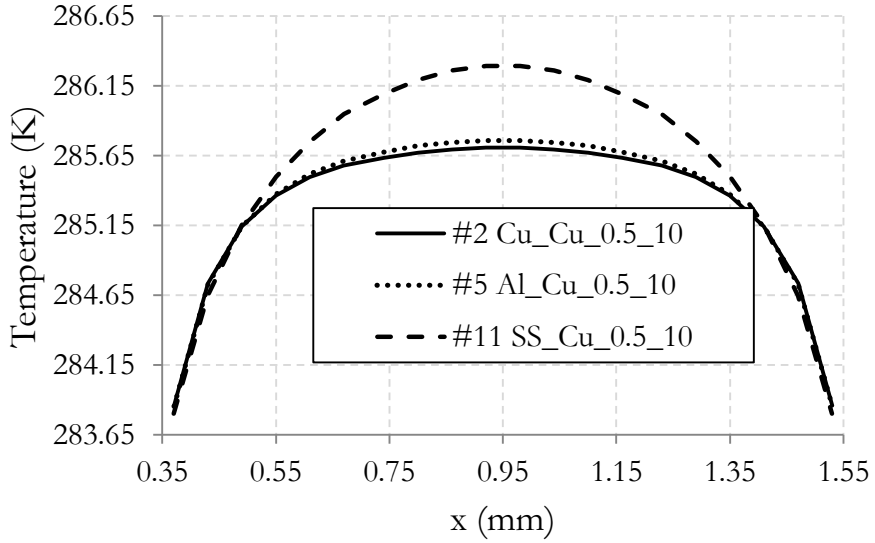

Figure IV.23 – Temperature along the wick/casing interface at 30W/cm² for evaporators having different casing material: copper (simulation #2), aluminium (simulation #5) and stainless steel (simulation #11). The wick is made of copper, the porosity is equal to 0.5 and the mean throat diameter is equal to 10µm.

Figure IV.24 shows the variation of the conductance for an insulating wick (PTFE) and a conductive wick (copper). The conductance is plotted for different evaporator wall materials: copper, aluminium and stainless steel. As can be seen, the evaporator thermal performances are better when the casing is conductive, i.e. with a copper casing. Note that Nishikawara et al. (2015) [100] studied an evaporator made with a PTFE wick and a stainless steel wall. The authors reported experimental conductances between 0.06W/cm²/K and 0.14W/cm²/K. Cao et al. (2002) [101] reported conductances between 2W/cm²/K and 6W/cm²/K for an evaporator with a copper wick and a copper casing. However, the working fluid was water. Values computed from our model seem to be slightly higher. On the whole, the order of magnitude calculated from our mixed pore network model for the conductance (see Figure IV.24) is in accordance with the experimental values reported in literature.

As shown in Figure IV.24a, the conductance behaviour is almost equivalent when the wick is insulating. For example, at 1W/cm^2, the conductance for simulation #22 and simulation #23 is equal to 0.137W/cm^2/K and 0.127W/cm^2/K, respectively. On the contrary, when the wick is conductive (see Figure IV.24b), the thermal performances of the evaporator are duly enhanced when the casing is also conductive. For instance, at 49W/cm^2, the conductance is equal to 1.44W/cm^2/K for simulation #11 (stainless steel casing), while the conductance reaches 12.8W/cm^2/K for simulation #2. The impact of the casing thermal conductivity is clearly more pronounced when the wick is conductive.

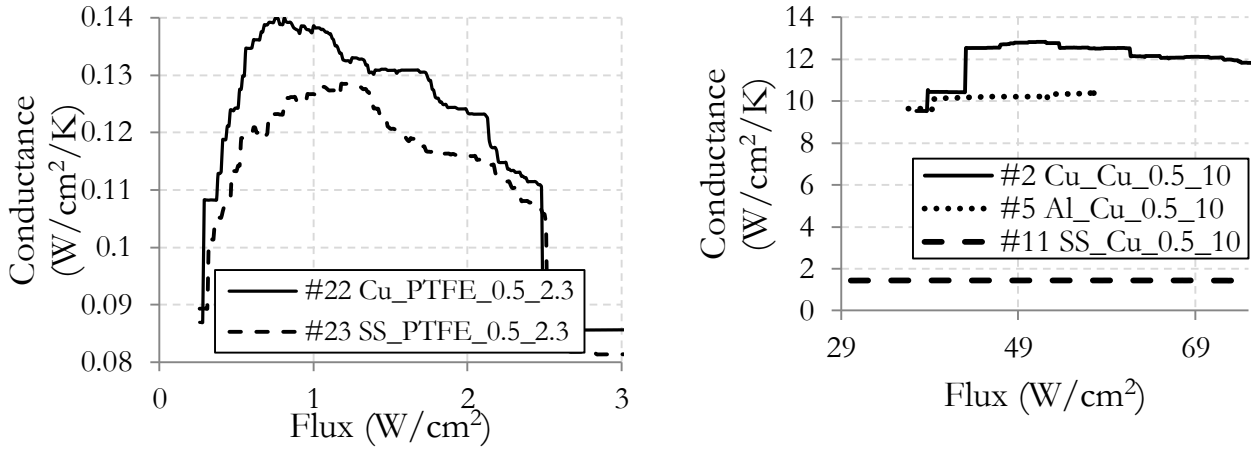

Figure IV.24 – Variation of the conductance for (a) a PTFE wick ($\varepsilon = 0.5$ and d_{th}=2.3µm±2µm) with the casing made of copper (simulation #22) or stainless steel (simulation #23); and (b) a copper wick ($\varepsilon = 0.5$ and d_{th}=10µm±5µm) with the casing made of aluminium (simulation #2), copper (simulation #8), or stainless steel (simulation #11).

Figure IV.25 highlights that the maximum evaporator temperature increases with the rise in the casing thermal conductivity. Figure IV.26 and Figure IV.27 show the temperature distribution in the evaporator for simulations #22 and #23 and for simulations #2, #5 and #11. Because of low thermal conductivity for stainless steel wall, the temperature gradient is larger in the evaporator wall than for a conductive casing, i.e. copper or aluminium casing. This effect is all the more true that the wick is conductive. Indeed the temperature gradient in the stainless steel casing is around 0.5K with a PTFE wick

(simulation #23 in Figure IV.26b), while it reaches 30K with a nickel wick (simulation #11 in Figure IV.27c). Note that the study of the casing material influence was also conducted by Wan et al. (2011) [85] (see Figure 8 in [85]) and their results are in accordance with the ones presented in this section.

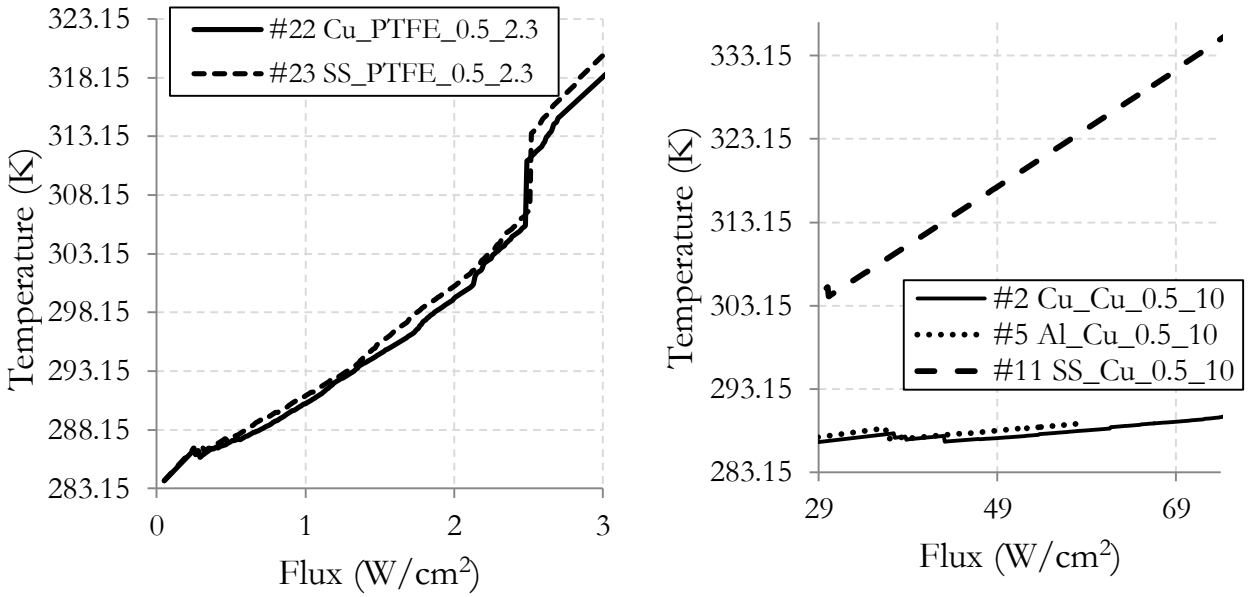

(a) **(b)**

Figure IV.25 – (a) Variation of the evaporator wall temperature for a copper (simulation #22) and a stainless steel (simulation #23) casing. The wick is made of PTFE, with a porosity equal to 0.5 and a mean throat diameter equal to 2.3µm. (b) Variation of the evaporator wall temperature for a copper (simulation #2), an aluminium (simulation #5) and a stainless steel (simulation #11) casing. The wick is made of copper with a porosity equal to 0.5 and a mean throat diameter equal to 10µm.

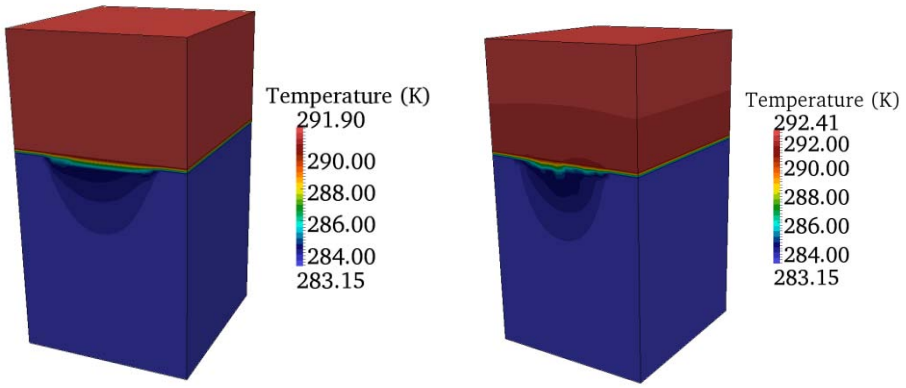

(a) **(b)**

Figure IV.26 – Temperature distribution in the evaporator unit cell (a) with a copper casing (simulation #22) and (b) with a stainless steel casing (simulation #23) at 1.17W/cm². The wick is made of PTFE (ε=0.5 and d_{th}=2.3±2µm).

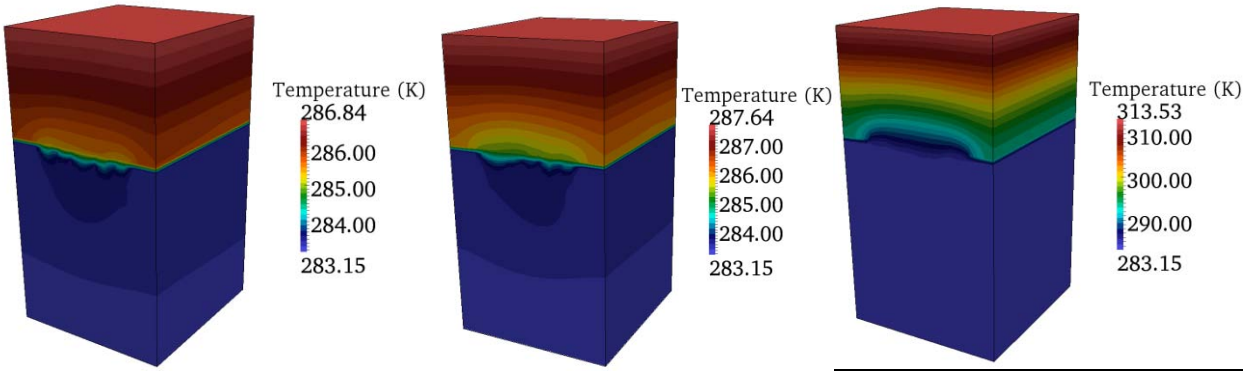

(a) **(b)** **(c)**

Figure IV.27 – Temperature distribution in the evaporator unit cell (a) with a copper casing (simulation #2); (b) with an aluminium casing (simulation #5) and (c) with a stainless steel casing (simulation #11) at 43.5W/cm². The wick is made of copper (ε=0.5 and d_{th}=10±5µm).

In summary, the thermal conductivity of the evaporator wall has a significant influence on the maximal casing temperature. An insulating casing (stainless steel for example) induces a relatively high overheating of the wall and by consequence gives lower values of the conductance. According to our simulations, the evaporator thermal performances are better with a conductive casing. However, this phenomenon is slightly marked if the wick is insulating.

IV.2.2.3 Influence of throat size distribution

Regarding the results reported in Table IV-4, it appears that the rise in the mean throat size causes the decrease in the nucleation flux (see simulations #4, #5 and #6 for example). The porosity is computed from the considered pore network. Hence, simulations don't have exactly the same porosity and as already discussed in section IV.2.2.1, the nucleation flux is expected to be slightly different. Nevertheless, this is not the only explanation. Indeed, the vapour is initiated when the temperature under the casing is 3K higher than the saturation temperature computed from the pressure corresponding to the formation of a bubble (see section III.3.3). The corresponding equations are recalled by equation (IV-3) and equation (IV-4).

$$T_{nucl} = T_{sat}(P_v) + \Delta T_{nucl} \quad \textbf{(IV-3)}$$

$$P_v = P_l + \frac{2\sigma}{r_p} \quad \textbf{(IV-4)}$$

The permeability is computed numerically. As reported in Table IV-4, the permeability increases when the throat size increases. Due to the change in the permeability, the liquid pressure drop within the wick decreases with the rise in the throat diameter (see Figure IV.28b). Indeed, the pressure drop is equal to 1629Pa for simulation #4 (mean throat diameter equal to 5µm), while the pressure drop is equal to 12.1Pa for simulation #6 (mean throat diameter equal to 20µm). The combined effect of the decrease in the pressure drop within the wick and the increase in the throat size causes the decrease in the pressure corresponding to the formation of a bubble (equation (IV-3)) and in consequence to the decrease in the

nucleation temperature (equation (IV-4)) as shown in Figure IV.28a. The slight difference of temperature along the wick/casing interface observed in Figure IV.28a is due to the porosity which is slightly different in simulations #4, #5 and #6. However, it's clear that according to the rules adopted in this model, the nucleation flux decreases with the rise in the throat diameter.

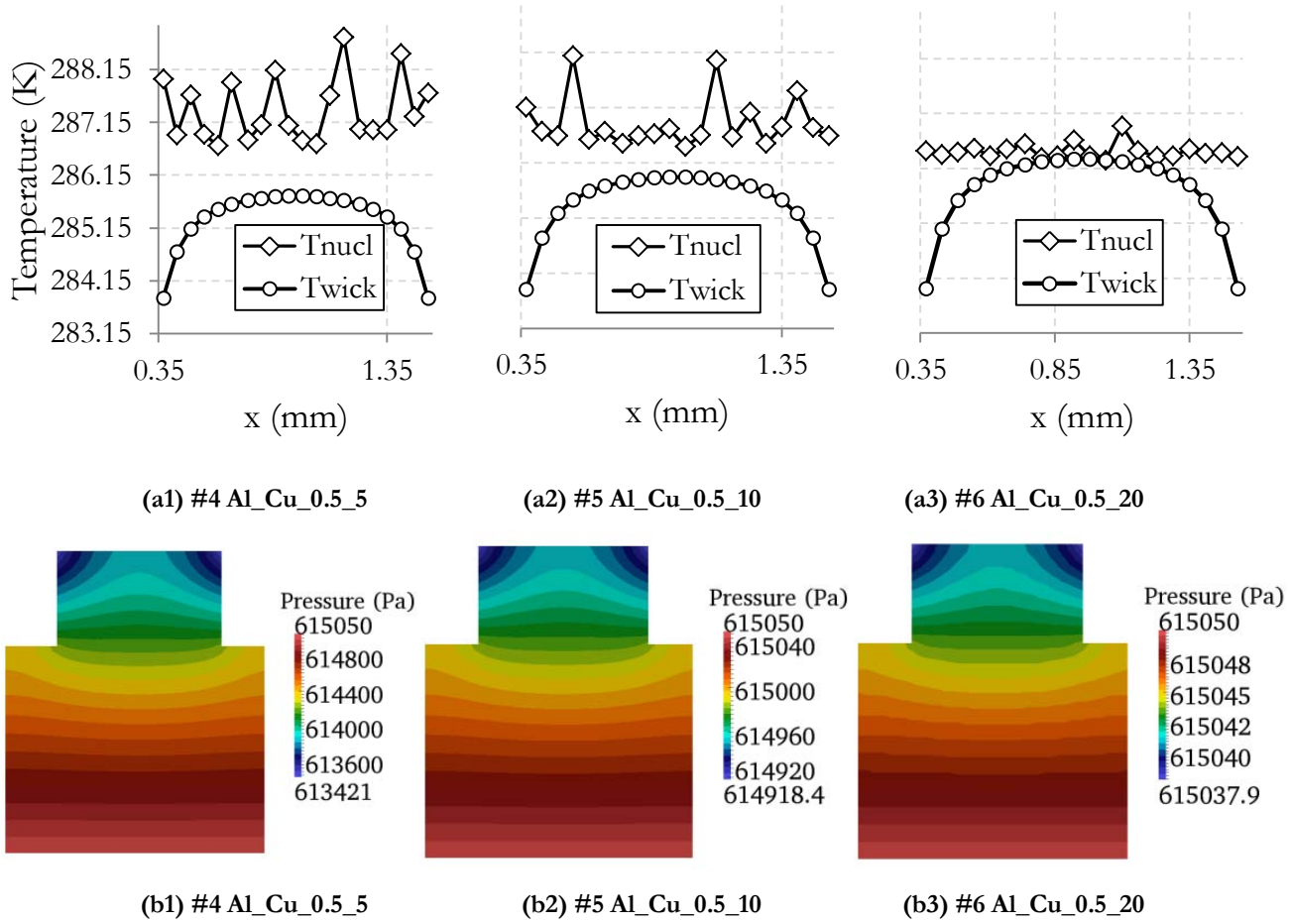

(a1) #4 Al_Cu_0.5_5 **(a2) #5 Al_Cu_0.5_10** **(a3) #6 Al_Cu_0.5_20**

(b1) #4 Al_Cu_0.5_5 **(b2) #5 Al_Cu_0.5_10** **(b3) #6 Al_Cu_0.5_20**

Figure IV.28 – (a) Temperature at the wick/casing interface and (b) Liquid pressure field within the wick at 31.3W/cm² for simulations #4 (figures a1 and b1), #5 (figures a2 and b2) and #6 (figures a3 and b3). T_{nucl} is the nucleation temperature and T_{wick} is the temperature along the wick/casing interface.

The conductance as a function of the heat load is shown in Figure IV.29 for simulations #4, #5 and #6 and in Figure IV.30 for simulations #13, #14 and #15. Considering a copper wick, whatever the porosity and the casing material, it appears that the best thermal performances of the evaporator are reached for a mean throat diameter equal to 10µm (see simulation #5 in Figure IV.29 and simulation #14 in Figure IV.30). Even though all results are not shown here, this trend was found to be the same for simulations #1, #2 and #3; simulations #4, #5 and #6; simulations #7, #8 and #9; simulations #10, #11 and #12; and simulations #13, #14 and #15.

The conductance is the worst whatever the configurations for a mean throat diameter equal to 5µm. Indeed, the range of heat loads where the evaporator operates in regime II is considerably reduced compared to the mean throat diameter equal to 10µm (see simulation #4 in Figure IV.29 and simulation #13 in Figure IV.30). Nevertheless, when the size of the mean throat diameter becomes too high, the thermal performances decrease: see simulation #6 in Figure IV.29, and simulation #15 in Figure IV.30.

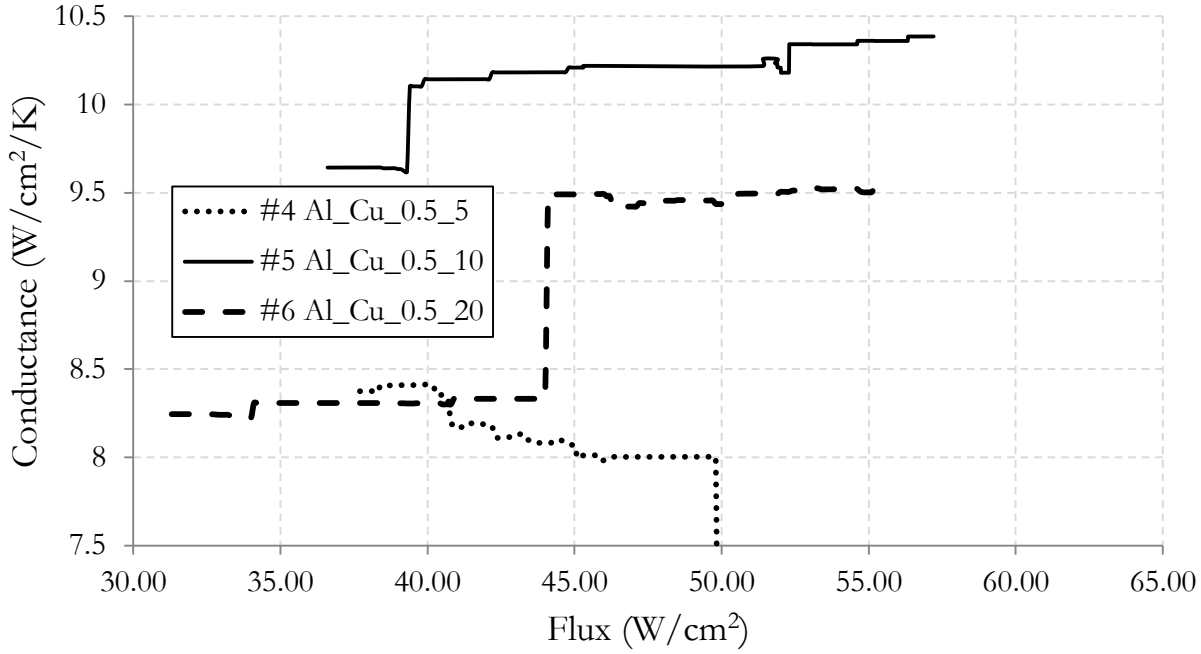

Figure IV.29 – Variation of the conductance as a function of the heat load applied to the casing for different throat size distributions. Results correspond to simulation #4, simulation #5 and simulation #6 for a copper wick and an aluminium casing. The average porosity of the porous medium is 0.5.

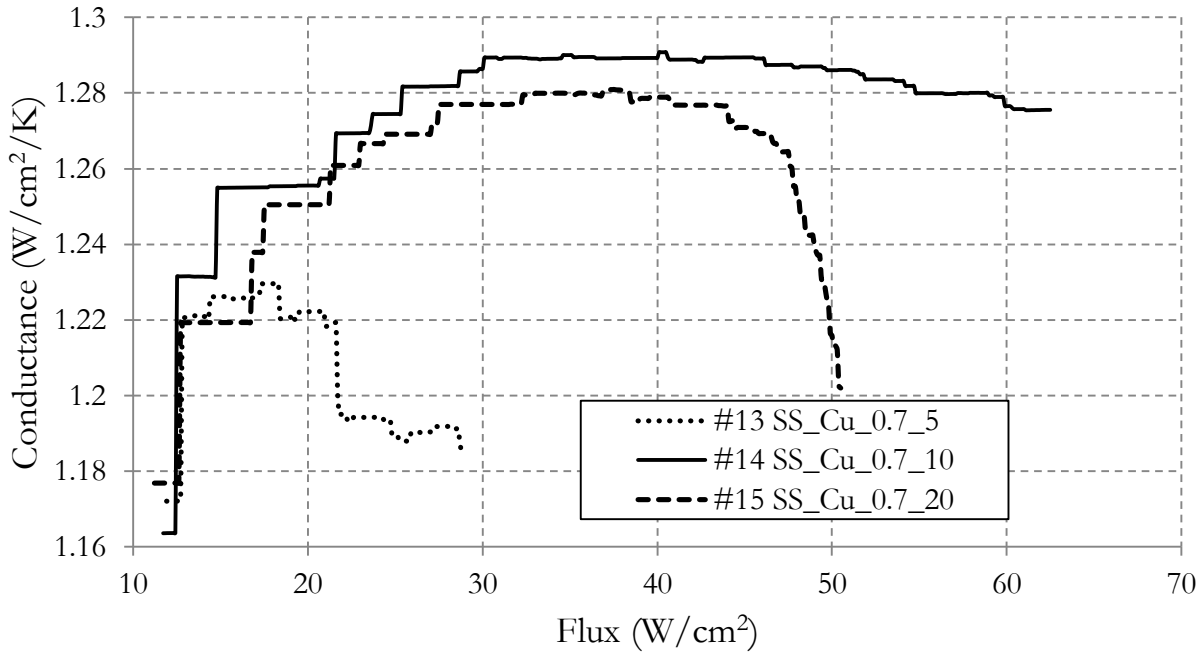

Figure IV.30 – Variation of the conductance as a function of the heat load applied to the casing for different throat size distributions. Results correspond to simulation #13, simulation #14 and simulation #15 for a copper wick and a stainless steel casing. The average porosity of the porous medium is 0.7.

The vapour saturation and the fraction of pores occupied by vapour under the casing are shown in Figure IV.31. Figure IV.32 shows the length average liquid saturation. The permeability increases with the throat size. Therefore, as for the liquid pressure field, the pressure drop in the vapour phase decreases with the rise in the throat diameter. Hence, the pressure drop along the liquid-vapour interface within the wick is expected to be potentially much lower than the capillary threshold. This explains why the vapour saturation is the lowest for a mean throat diameter equal to 20µm (see Figure IV.31a). The fraction of pores occupied by vapour under the casing is then higher for a mean throat size equal to 5µm (see Figure IV.31b) and the two-phase zone in the wick is relatively uniform in the depth of the wick (Figure IV.32a and Figure IV.32d). The shape of the two-phase zone is more tortuous with the increase in the throat dimeters (see Figure IV.32b, c, e and f). Comparing Figure IV.32b and Figure IV.32c (or Figure IV.32e and Figure IV.32f), the two-phase zone is deeper and covers a larger range of liquid saturation when the throats are equal to 10µm. This better mixing between the liquid and the vapour within the wick improves the heat exchange and thus permits to decrease the casing temperature explaining why the conductance is better for d_{th}=10µm±5µm.

Note that simulation #3 has reached the vapour breakthrough at the inlet of the wick due to a too high throat diameter and the recession of the menisci at the wick/groove interface (see Figure IV.33). This scenario is expected to occur more frequently with the increase in the throat size and is unacceptable during operating condition of a capillary evaporator because it induces the defusing of the whole loop. Actually, the recession of the meniscus has been also observed for several simulations (simulations #12 and #15 for examples).

In summary, it exists an optimum value of the throat size leading to both the best conductance values and the largest range of heat flux where the evaporator operates in regime II.

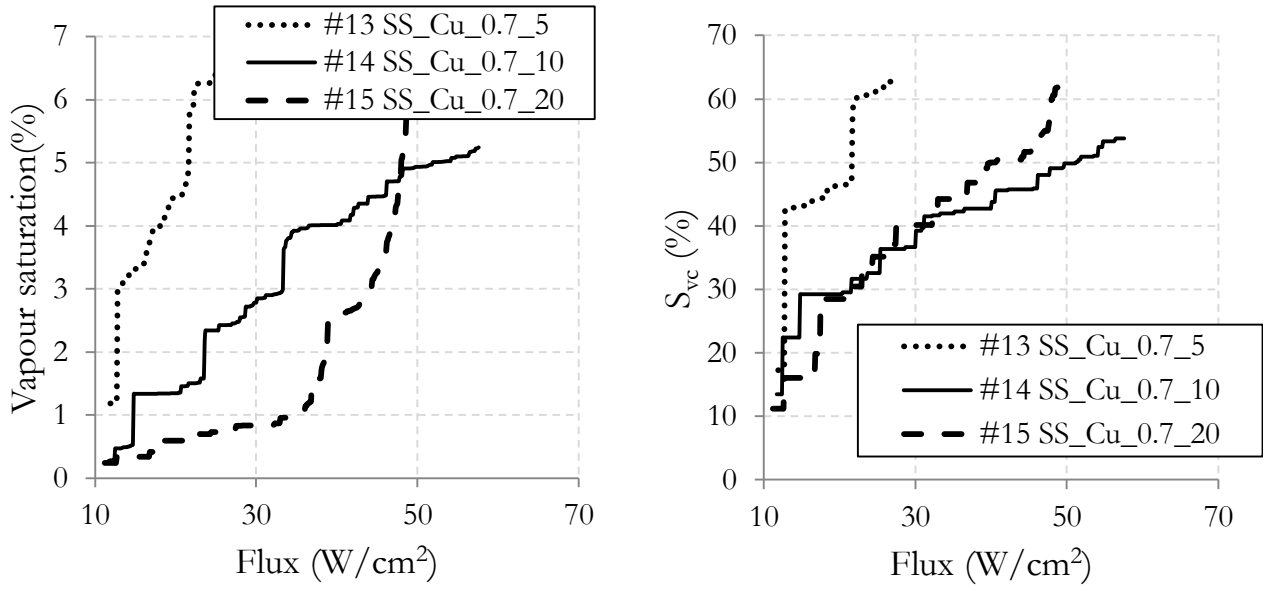

(a) **(b)**

Figure IV.31 – (a) Variation of the vapour saturation as a function of the heat load for different throat size distributions. (b) Variation of the fraction of pores occupied by vapour right under the casing (S_{vc}). The wick is made of copper ($\varepsilon = 0.7$) and the casing is made of stainless steel. The mean throat dimeter is equal to 5µm (simulation #13), 10µm (simulation #14) and 20µm (simulation #15).

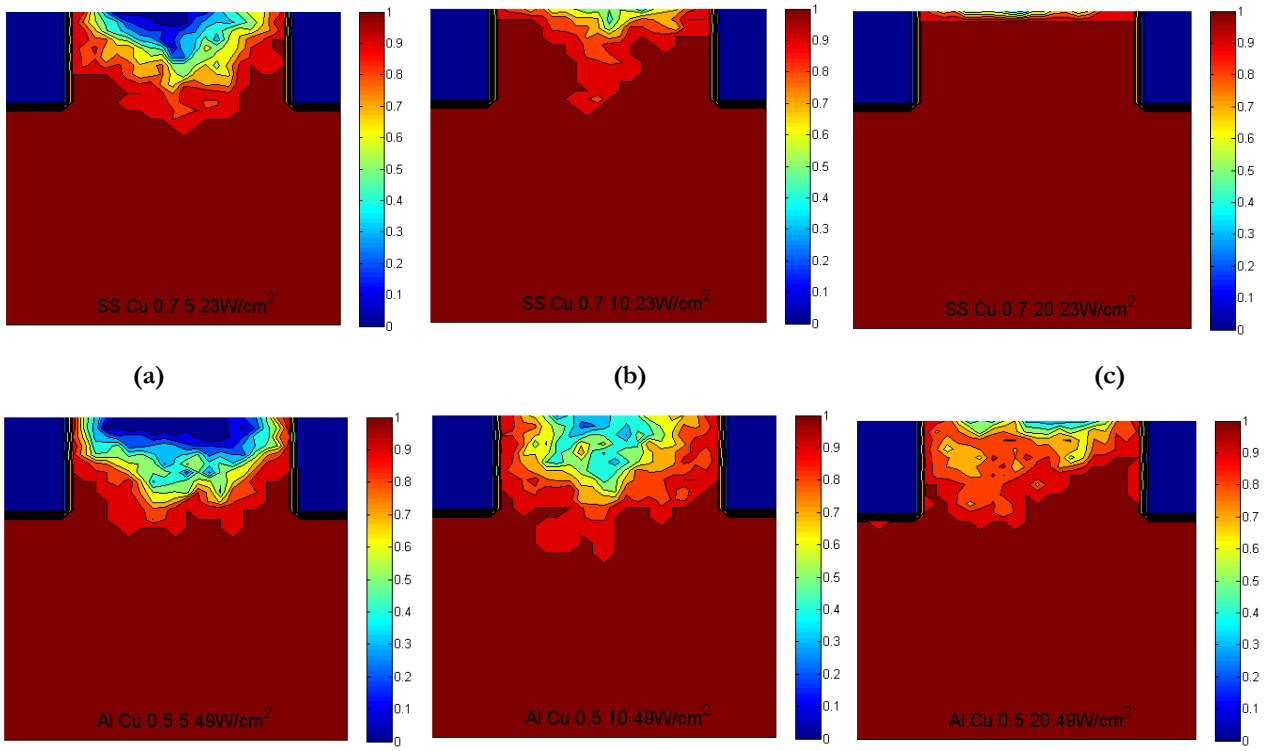

Figure IV.32 – Length average liquid saturation. Figures (a) to (c) are results for an SS-Cu evaporator with ε=0.7 at 23W/cm². Figures (d) to (f) are results for an Al-Cu evaporator with ε=0.5 at 49W/cm². The throat size diameter is equal to 5µm (figures (a) and (d)), 10µm (figures (b) and (e)) and 20µm (figures (c) and (f)).

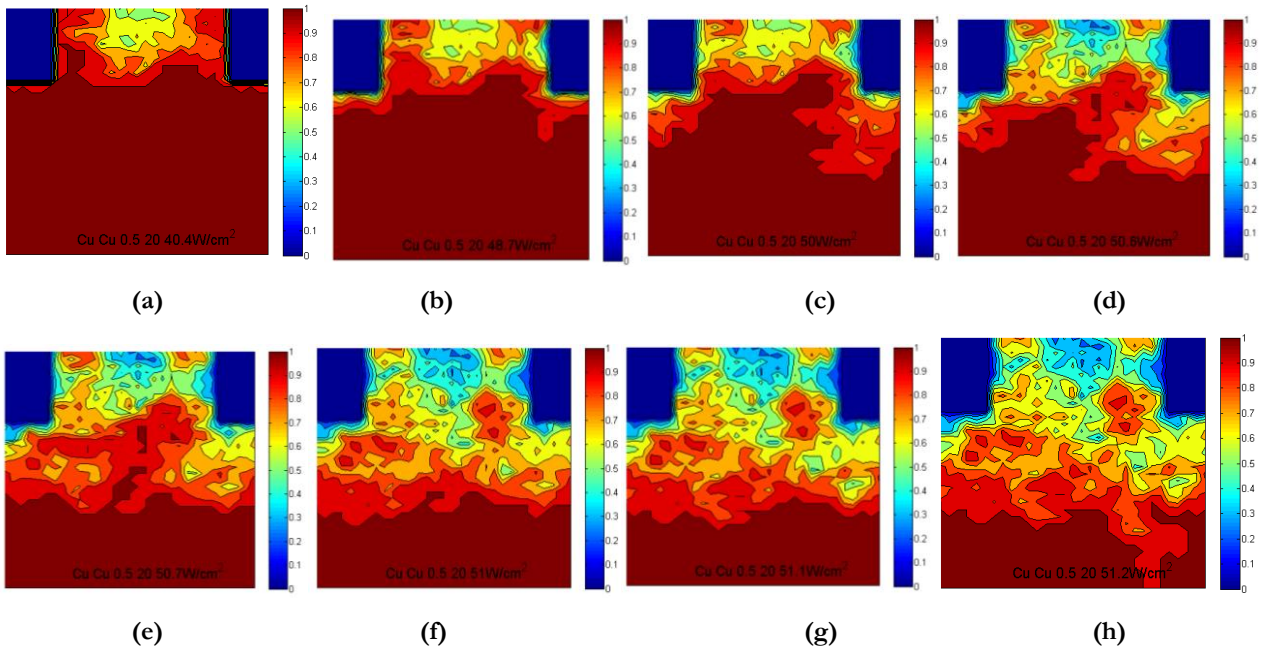

Figure IV.33 – Length average liquid saturation. The wick and the casing are made of copper. The porosity is equal to 0.5 and the mean throat diameter is 20µm. The heat loads applied at the external surface of the casing are (a) 40.4W/cm², (b) 48.7W/cm², (c) 50W/cm², (d) 50.6W/cm², (e) 50.7W/cm², (f) 51W/cm², (g) 51.1W/cm² and (h) 51.2W/cm².

IV.2.3 Summary

Since the best thermal performances of an evaporator are directly related to the occurrence of vapour within the wick, the designer should take into account the mean throat diameter, the wick material, the casing material and the porosity to design an evaporator which will favour the occurrence of vapour over the range of heat load that it is to be evacuated.

In summary to increase the conductance and the range of fluxes corresponding to regime II, the evaporator should have a wick and a casing that are both conductive, as well as a low porosity. Moreover, it exists an optimal throat size distribution that correlates with the best thermal performances.

IV.3 Synthesis and conclusions of the chapter

The mixed pore network model presented in Chapter III was used to perform a study of sensitivity. All simulations presented in this chapter have the same geometry dimensions and the wick is monoporous. Firstly, the location of grooves was investigated and three different positions were studied: at the inner surface of the casing (geometry A), at the outer surface of the wick (geometry B) and within the wick (geometry C). When the grooves are manufactured in the casing, the range of fluxes where the evaporator operates in regime II is relatively narrow compared to other geometries. The evaporator thermal performances are better when the grooves are manufactured within the wick or at the external surface of the wick. Geometry C is a promising groove configuration to enhance the evaporator thermal performances if a solution is found to keep a two-phase zone under the casing over a larger range of fluxes. Nevertheless, geometry B stays the most favourable configuration in terms of heat flux range where the evaporator operates with the best thermal performances. Moreover, these two configurations prevent the breakthrough of the vapour at the wick inlet.

In a second part, a parametric study was presented. Various casing materials, wick materials, porosities and throat size distributions were tested through 23 simulations. It was highlighted that the operator should take into account all these parameters to design an evaporator which will favour the occurrence of vapour over the range of heat load that it is necessary to evacuate. If the objective is to evacuate relatively low or moderate heat fluxes (lower than $20W/cm^2$), a high porosity and/or a wick with a low thermal conductivity are recommended. The casing material has a low influence on thermal performances if the wick is insulating or has a high porosity. Moreover, the parasitic heat flux is limited in this configuration. Nevertheless, note that both parameters induce a higher evaporator wall temperature. For a wick with a too low thermal conductivity, the evaporator can rapidly reach the maximum admissible temperature.

If the objective is to evacuate relatively high heat fluxes (higher than $20W/cm^2$), conductive material for both the wick and the casing is recommended as well as a low porosity. However, a trade-off needs to be found between these parameters to limit the undesired flux lost by conduction towards the wick inlet. These recommendations are based on thermal analyses. It is important to recall that copper and aluminium have relatively poor mechanical properties (see Table I-1) explaining why stainless steel is often encountered in the literature. Moreover, the chemical compatibility between copper and ammonia remains a challenge. Ammonia needs to be absolutely pure to avoid the creation of non-condensable gas. In practice, water is used instead of ammonia if the wick and/or the casing are made of copper.

Chapter V Bimodal capillary structure

Chapter V Bimodal capillary structure 147
V.1 Method of manufacturing the bimodal wick structure 148
V.2 Literature review 149
V.3 Bidispersed structure two-scale pore network model 151
V.4 Mathematical model 152
V.5 Model validation 154
V.6 Monoporous vs. bidispersed wick 160
V.7 Synthesis and conclusions of the chapter 167

In this chapter, two different kinds of wick are investigated: a monoporous capillary structure characterized by a monomodal pore size distribution and a bidispersed capillary structure characterized by a bimodal pore size distribution. Firstly, the model is validated by comparing the mixed pore network results experimental results found in literature. The evaporator thermal performance, i.e. the conductance, and the overheating of the casing are compared at different heat loads with experimental results. A good agreement is obtained. In a second part, the influence of the groove location is investigated when the wick is bidispersed. The results are compared to the monoporous case.

This chapter is adapted from "Numerical simulation of heat and mass transfer in bidispersed capillary structures: application to the evaporator of a loop heat pipe", L. Mottet and M. Prat submitted to Applied Thermal Engineering (Oct 23,2015).

V.1 Method of manufacturing the bimodal wick structure

Bimodal structures are characterized by the existence of two distinct pore size distributions It exists essentially two methods to manufacture them inducing a structural difference (Rasor and Desplat (1989) [102]). The first method collects together small pore particles into clusters, leading to a so-called "bidispersed" structure. Large pores are located between clusters of small pores (Figure V.1a). This process of fabrication was thoroughly used by the group of Catton ([103], [104], [105], [106], [107] and [108]) and used later by Singh et al. (2009) [38] and Lin et al. (2011) [109]. The second method consists in sintering a mix of powder and pore formers. The pore formers are then removed through a dissolution or evaporation process. In that case, large pores are located at the places of the pore formers (Figure V.1b), creating a so-called "biporous" structure. This method was mainly used by Yeh et al. ([46], [110]) (dissolving process) and by Wu et al. ([39], [40], [111], [112] and [113]) (evaporation process).

Scanning electron microscopy (SEM) images of a bidispersed structure and a biporous one are shown in Figure V.2. The large pores create preferential paths for the vapour while the small pores permit to increase the evaporation surface area and the number of menisci, which improve the transport of the liquid ([114]). It is therefore expected that the bimodal structure improves the performances through more appropriate liquid and vapour phase distributions within the wick when vaporisation occurs inside the capillary structure.

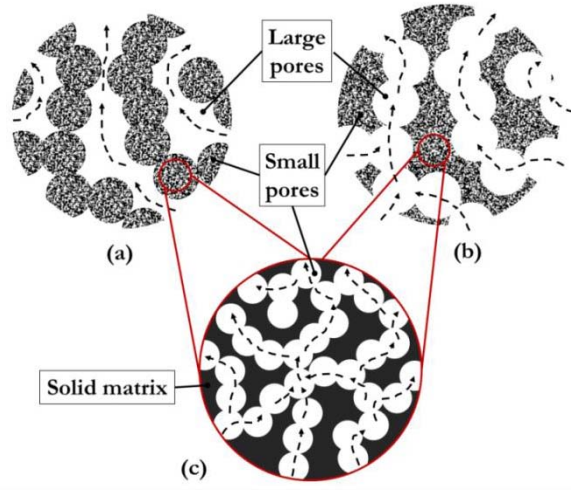

Figure V.1 – Schematic structure of a bimodal porous medium for (a) a bidispersed wick and (b) a biporous wick. The arrow indicates the flow paths. Adapted from Rasor and Desplat (1989) [102].

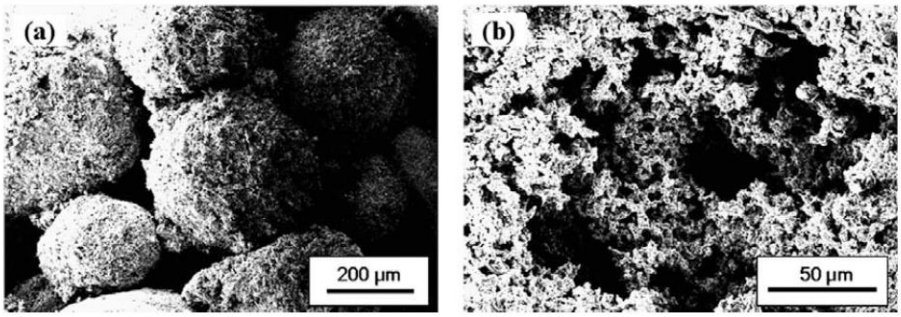

Figure V.2 – SEM pictures of wick structures with bimodal pore size distributions: (a) bidispersed wick and (b) biporous wick. Reprinted from [110].

V.2 Literature review

V.2.1 Experimental literature review

Several experimental studies were devoted to bidispersed wicks applied to LHP evaporators and several important parameters impacting the performance have been analysed. The optimal ratio between small pores and large pores was investigated by Cao et al. (2002) [101]. The influence of wick thickness, small pore size and cluster size on dryout values, on the evaporator wall overheating and on the heat transfer coefficient was studied in several papers published by the group of Catton ([103–107]). The 63µm-455µm-3mm (small pore diameter – cluster diameter – thickness of the wick) wick structure [107] was the most appropriate to evacuate high heat flux (around 990W/cm^2). However, their analysis of the heat transfer coefficient showed that the 40µm-300µm-1mm structure [105] led to the highest value. Indeed, the evaporative performance is duly enhanced by decreasing the size of clusters, as it was also shown by Lin et al. (2011) [109].

More recently, studies have turned to the use of biporous wick structures for LHP as their manufacturing method permits to achieve a greater control of the final porosity compared to the fabrication process for bidispersed structures. According to [46], [110] [113], a high content of pore formers of a small size leads to an enhancement of LHP performances compared to a classical wick. The evaporator temperature, the evaporator thermal resistance and the evaporator heat transfer performance were analysed by Wu et al. (2015) [112]. The heat transfer performance for the evaporator with a biporous wick is enhanced by nearly 80% compared to the evaporator with a monoporous wick. Another biporous process fabrication was proposed in [43] where it was shown that the tested LHP could start up and ran correctly under different heat loads.

For a given wick thickness, the critical heat flux is not necessarily as high as expected due to preferential vapour paths leading to the breakthrough of the vapour into the compensation chamber (see for example the 1mm thick wick in [105]). To prevent this issue, a bilayer wick composed by a monoporous layer at the inlet (near the compensation chamber) and a bidispersed [38] or biporous [39] layer next to the solid wall have been proposed an interesting solution. This configuration led to a decrease in the vapour temperature [38] and in the total thermal resistance of the evaporator [39] compared to a monolayer wick (monoporous or biporous/bidispersed wicks).

V.2.2 Numerical literature review

Only a few numerical studies complement these experimental works. An analytical model for predicting the operating conditions of a bidispersed wick was developed by Wang and Catton (2001) [115] and Vadnjal and Catton (2005) [116]. They assumed that three successive stages occur in the capillary structure. The first one corresponds to a liquid-saturated wick. The second stage begins with the occurrence of vapour within the large pores. Finally, when the capillary limit is reached, the menisci in the small pore are destroyed corresponding to the third stage. Later, the authors improved their model concerning the second stage (Reilly and Catton (2014) [108]) and obtained better agreement with experiments. For low heat flux, the heat transfer coefficient of the bidispersed wick is worse than the

one of the monoporous wick. This phenomenon is explained by the low effective thermal conductivity and the high porosity of the bidispersed structure. They also pointed out that the spacing between large pores is an important criterion to correctly evaluate the maximum admissible heat flux.

Chernysheva and Maydanik (2008) [30] and Chernysheva and Maydanik (2009) [31] have developed a continuum heat and mass transfer model for a flat evaporator unit cell. The model is two-dimensional and for steady-state operating condition. The original groove location considered in these papers has been discussed in section I.2.5.3.1. The model takes into account the phase change within the capillary structure considering three vaporisation modes (summarized in Figure V.3a): the evaporation occurs at the wick/groove interface and the wick is fully saturated with liquid (1st mode); then the wick is divided into two zones (a two-phase zone and a liquid-saturated zone) and the vaporisation occurs in the two-phase zone (2nd mode); and finally the wick is divided into three zones (a dry vapour zone located under the casing, a two-phase zone and a liquid-saturated zone) and the vaporisation occurs in the two-phase zone (3rd mode). The treatment of the two-phase zone is based on a radius R^* which defines the threshold meniscus radius from which the pores becomes vapour. The flow within the wick is computed using Darcy's law, while only conduction is considered for the heat transfer. A heat sink term appears in the energy equation to account for evaporation in the two-phase regions. Using this model, the prediction of the casing overheating is in accordance with experimental results (Figure V.3b). An interesting aspect of this method lies in the fact that structural characteristics (pore size distribution, porosity, permeability…) of the wick are taken into account. However, the convective term in the heat transfer equation is neglected and the studied geometry is original but not usual.

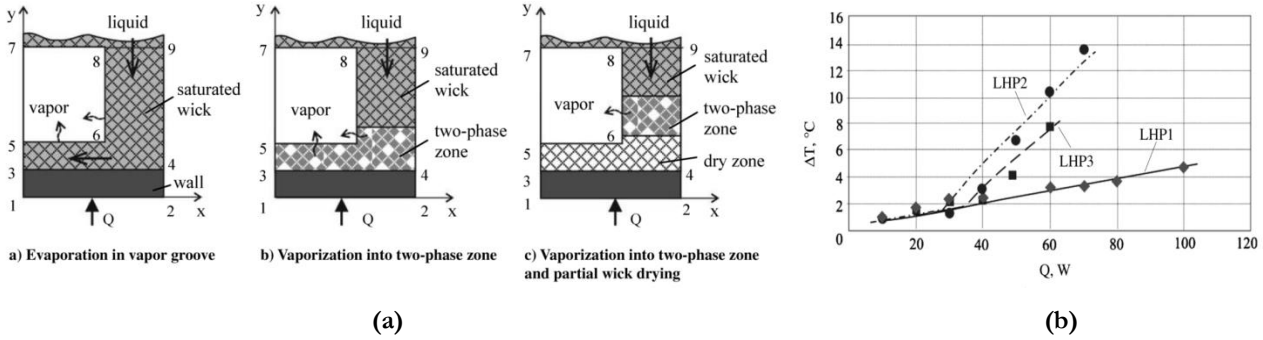

Figure V.3 – (a) Scheme of vaporisation modes and (b) Overheating of the casing as a function of the heat load. Experimental data: diamonds circles and squares; calculated data: solid, dashed and dot-dashed lines. From Chernysheva and Maydanik (2008) [30] and (2009) [31].

A 1D mathematical model of evaporative heat transfer in a loop heat pipe (with mono and bidispersed wick structures) was developed and compared with experiments by Lin et al. (2011) [49]. They assumed that the wick could be spontaneously separated into three regions when the heat flux is applied. The first one is a vapour blanket, the second one is a two-phase zone and the third one is a liquid-saturated zone. The liquid and vapour-saturated regions were assumed to be isothermal. The liquid flow and the heat transfer were only in the radial direction, while the vapour flow was only in the axial direction. The treatment of the two-phase zone was the same as in [31]. Their results were in a general accordance with the experiment. However, the mean absolute error of the evaporator wall temperature for the

monoporous wick (for the bidispersed wick respectively), for low heat flux, was about 40% (14% respectively). These deviations can be explained by the assumptions on the three regions which are not in agreement with the results reported in the section III.5.

V.3 Bidispersed structure two-scale pore network model

Our model is based on the representation of the porous medium in term of a two-scale cubic network of pores and throats as sketched in Figure V.4. In a one-scale cubic PNM (see Figure V.4a) such as the one used in [13], the distance a between two pores, referred to as the lattice spacing, also corresponds to the discretization step used to solve the governing equation and is constant, which is quite acceptable for a sintered wick. As illustrated in Figure V.1, the bidispersed capillary structure can be viewed as a network of small pores embedded in a network of larger pores, while the biporous medium can be viewed as a network of large pores embedded in a network of smaller pores. The purpose of this paper is to focus on the bidispersed wick. Two lattice spacings, denoted by a for the fine network and by b for the large pore network are therefore introduced for describing a bidispersed capillary structure.

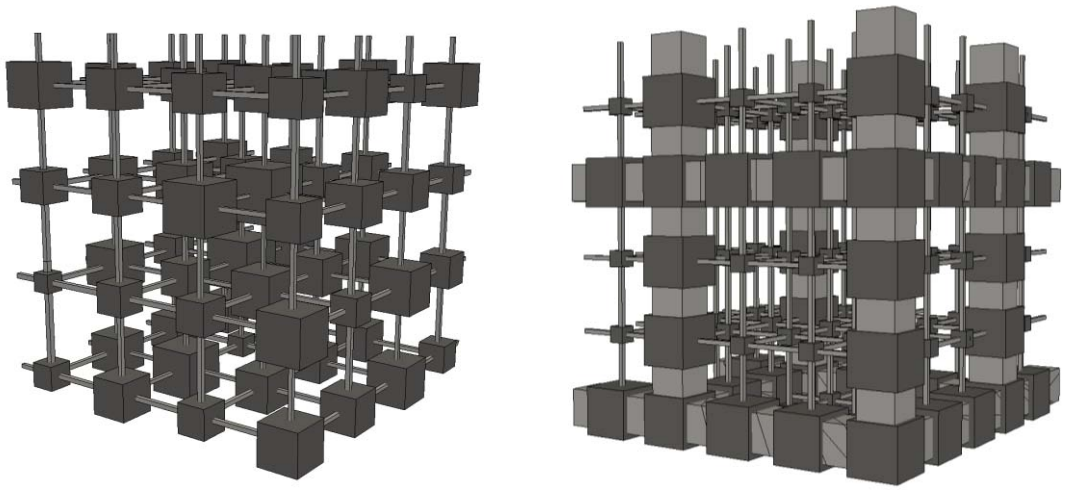

(a) **(b)**

Figure V.4 – Pore network model: (a) Monoporous wick and (b) bidispersed wick. Note that for simplicity only the pores are randomly distributed in Figure V.4a; whereas the network is depicted with a constant size of pores and throats in Figure V.4b. It should be clear however that both throats and pores are randomly distributed in the model presented in this section.

As illustrated in Figure V.4b, the distance b corresponds to the distance between two large channel intersections of the large pore network. A key aspect of the model is to interconnect properly the large pores and the fine pores. As a result, the distance between two large pores along the three main directions of the large pore network is not b but the finer spacing a (this is clearly illustrated in Figure V.4b). This allows connecting easily the pores of the fine network those of the large network. As the result, the discretization step of the transport equation in the two-scale PNM is actually the fine pore lattice spacing a since all the pores are in fact distributed over a Cartesian grid of step a. The large pore network simply corresponds to the introduction of a spatial correlation in the pore and throat size

distribution along the grid of spacing a so as to form the large pore network. In this respect, the discretization step is the same as in the one scale network.

In pore network models, the capillary pressure is expressed as a function of the throat size using the Laplace-Young equation. Generally, the pore size distribution (PSD) is given in literature. However, the PSD, obtained for example by mercury porosimetry, actually corresponds to throat size distributions (TSD). Thus, the throat diameters in the PNM must correspond to the "pore size distribution" obtained experimentally. In addition to the actual TSD, we want our network to have the same porosity as the real wick we are interested in. How to achieve this goal, i.e. how to specify the porosity and the PSD and TSD of the PNM from available experimental data for a given wick, is described in Appendix A for a one-scale PNM (monoporous wick) and in Appendix B for the two-scale PNM (bidispersed wick).

As explained in Appendix B, the main unknowns for the construction of the bidispersed network are the lattice spacing b of the large network, the porosity ε_L of the large network, the distribution of the large pore diameter $d_{p,L}$ and the one of the small pore diameter $d_{p,S}$, noting that the size of large pores, small pores and the size of the small pore clusters are generally available from the experimental works. These experimental data permit to determine an approximate number of large pores for the PNM to be representative of the real sample. In this respect, it is important to note that the large pore network controls the vapour preferential paths within the wick allowing the vapour to escape from beneath the casing. Thus, based on the geometrical consideration explained in Appendix B, b, ε_L, $d_{p,L}$ and $d_{p,S}$ are determined and used for the construction of the two-scale pore network.

V.4 Mathematical model

The mixed pore network model is the same as the one presented in section III.2. Here, only the adaptations of the model for the bidispersed structure are presented. All governing equations and boundary conditions not discussed here remain exactly the same as in section III.2. Subscript i denotes the liquid l or the vapour v phase, while subscript j corresponds to the large network L or the small network S.

V.4.1 Governing equations

Heat transfer occurs by convection and conduction within the wick,

$$\left(\rho c_p\right)_i \mathbf{u}_i . \nabla T = \nabla . \left(k_{i,j}^* \nabla T\right) \quad \textbf{(V-1)}$$

where $\mathbf{u}_i$ is the velocity of phase i and $k_{i,j}^*$ is the effective thermal conductivity of network j when the pores are occupied by phase i.

The effective thermal conductivity of the wick depends on the solid matrix conductivity, the fluid thermal conductivity and the porosity. The arithmetic average between the classical arrangement of the phases in parallel and in series is used:

$$k_{i,j}^{*} = \frac{1}{2}\left(\varepsilon_j k_i + (1-\varepsilon_j)k_w + \frac{k_i k_w}{\varepsilon_j k_w + (1-\varepsilon_j)k_i}\right) \quad \textbf{(V-2)}$$

where k_w is the thermal conductivity of the solid matrix.

Darcy's law (equation (V-3)) is combined with the mass conservation equation (equation (V-4)) for determining the pressure field within the wick.

$$\mathbf{u}_i = -\frac{K_j}{\mu_i}\nabla P \quad \textbf{(V-3)}$$

$$\nabla.(\rho_i \mathbf{u}_i) = 0 \quad \textbf{(V-4)}$$

V.4.2 Boundary conditions

Energy conservation (equation (V-5)) is imposed at the casing/wick interface.

$$\left(-k_{i,j}^{*}\nabla T\right).\mathbf{n} = (-k_c \nabla T).\mathbf{n} \quad \textbf{(V-5)}$$

$\mathbf{n}$ is the interface normal unit vector.

The liquid-vapour interface is located within the wick and/or at the wick/groove interface. Energy conservation (equation (V-6)) and temperature continuity (equations (V-6) and (V-8)) are imposed at the menisci located within the wick. Energy conservation (equation (V-9)) is imposed at the wick/groove interface if the considered wick point is in liquid state; otherwise a convective boundary condition is used (equation (V-10)).

Liquid-vapour interface within the wick: $\left(-k_{l,j}^{*}\,\nabla T\right).\mathbf{n} - \left(-k_{v,j}^{*}\,\nabla T\right).\mathbf{n} = \rho_l\, h_{lv}\mathbf{u}_l.\mathbf{n}$ **(V-6)**

$$\rho_v\,\mathbf{u}_v.\mathbf{n} = \rho_l\,\mathbf{u}_l.\mathbf{n} \quad \textbf{(V-7)}$$

$$T_l = T_v = T_{sat}\,(P_v) \quad \textbf{(V-8)}$$

Liquid-vapour interface at the wick/groove boundary: $\left(-k_{l,j}^{*}\,\nabla T\right).\mathbf{n} = \rho_l\, h_{lv}\mathbf{u}_l.\mathbf{n}$ **(V-9)**

Vapour-vapour interface at the wick/groove boundary: $\left(k_{v,j}^{*}\,\nabla T\right).\mathbf{n} = h_g\left(T - T_g\right)$ **(V-10)**

For the bidispersed case, permeabilities K_L and K_S and porosities ε_L and ε_S are defined for the large pore network and the small pore network respectively. Permeability and porosity of a link connecting a small pore and a large pore are taken as compound values between the two considered nodes (using harmonic means).

V.5 Model validation

V.5.1 Input properties

In this section, simulations are compared to experimental results available in Lin et al. (2011) [109]. These authors studied one monoporous wick (called sample A in [109]) and three bidispersed wicks (called sample B, C and D in [109]). Sample A and sample D are numerically studied in this section. The geometry dimensions, as well as the porous medium properties, the loop dimensions and the working fluid are the same as the ones used in the experiment of Lin et al. (2011) [109]. Unknown parameters not specified in [31] are deduced or taken to be as much as possible close to realistic values based on other studies by the same group ([39], [42], [46], [49], [110]). Note that the grooves are manufactured within the wick. All the properties used in the simulations are summarized in Table V-1.

Wick properties (Nickel)	**Sample A Monoporous wick**		**Sample D Bidispersed wick**	
Thermal conductivity (W/m/K)	91		91	
Throat diameter range (µm)	6±4		1.2 ± 1.1 and 13 ± 6	
Cluster diameter (µm)			20-62	
Throat diameter p.d.f	Normal		Normal	
Lattice spacing (mm)	a=0.0847		a=0.0847 and b=0.3388	
	Experiment	Numerical	Experiment	Numerical
Porosity	0.743	0.747	0.768	0.764
Permeability (m²)	2.3×10^{-12}	1×10^{-12}	7.7×10^{-12}	6.8×10^{-12}
Casing property (Aluminium)				
Thermal conductivity (W/m/K)	205			
Fluid property (Ammonia)	Liquid		Vapour	
Thermal conductivity (W/m/K)	0.52912		0.024365	
Dynamic viscosity (Pa.s)	156×10^{-6}		9.63×10^{-6}	
Specific heat capacity (J/kg/K)	4678.7		2841.3	
Latent heat of vaporisation (J/kg)	1225580			
Interfacial tension (N/m)	0.029589			
Liquid density (kg/m³)	624.46			
Inlet temperature/pressure				
P_{cc} (Pa)	615050			
$T_{sat}(P_{cc})$ (K)	283.15			
Geometrical dimensions (mm) (see Figure III.3 for definitions)				
L_x	5			
L_y	3.25			
L_z	3			
L_{xv}	0.5			
L_{yw}	0.75			
L_{yg}	1			
Loop dimension				
Number of grooves/length of grooves (mm)	8/40			
Length (mm)/inner diameter (mm) of the vapour line	470/5			
Length (mm)/inner diameter (mm) of the liquid line	580/4			
Length (mm)/inner diameter (mm) of the condenser	800/5			

Table V-1 – Porous material properties, fluid properties, geometrical dimensions and loop dimensions used in simulations.

V.5.2 Numerical results vs. experimental results

Of primary interest is the quantification of the evaporator thermal performance, i.e. the conductance h_{ev} (also called heat transfer coefficient),

$$h_{ev} = \frac{Q}{T_{c,max} - T_g} \quad \textbf{(V-11)}$$

where Q is the applied heat load in W/cm^2, $T_{c,max}$ is the maximal temperature of the casing and T_g is the vapour temperature within the removal channels, i.e. the vapour grooves.

The overheating of the casing ΔT_c, defined as the casing excess temperature, is the difference between the casing temperature $T_{c,max}$ and the saturation temperature within the groove T_g,

$$\Delta T_c = T_{c,max} - T_g \quad \textbf{(V-12)}$$

The variations of the evaporator conductance and the overheating of the casing as a function of the heat flux are shown in Figure V.5 and Figure V.6. The numerical conductance is greater than the one measured experimentally, whereas the overheating of the casing is underestimated. Note however that several unknown parameters were estimated, such as the compensation chamber temperature, the fin and groove dimensions as well as the wick thickness, and thus could explain the observed differences. Nevertheless, the trend is respected and a general good agreement is found. Our conclusion is that the agreement between the present model and the experimental results of Lin et al. (2011) [109] can be considered as sufficiently good to use with confidence our pore network model for studying bimodal capillary structures within a capillary evaporator. Moreover, this kind of model allows quantifying several parameters, such as the liquid-vapour phase distribution, the vapour saturation as well as the vapour flow rate, which are not easily obtained experimentally, while they are often key elements to explain the behaviour of the evaporator performance.

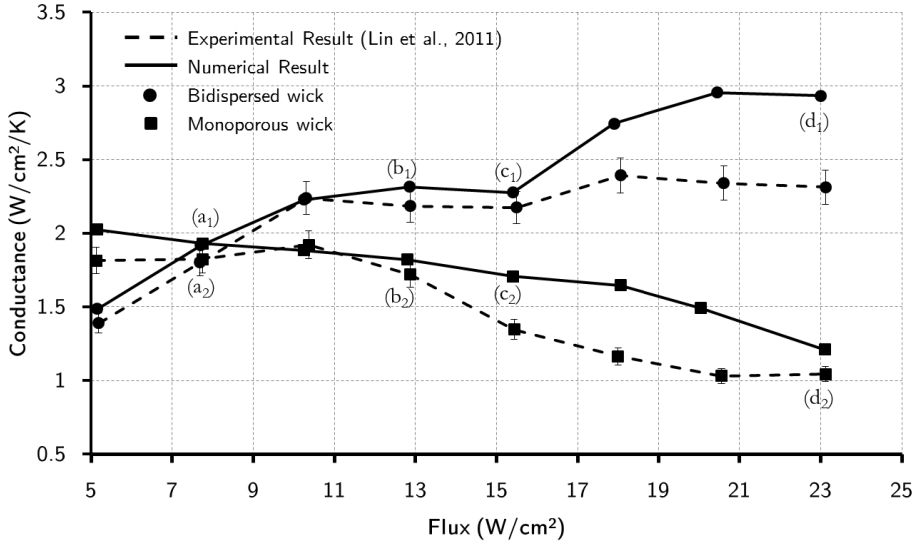

Figure V.5 – Variation of evaporator conductance as a function of the heat load applied to the casing. The labels (a_1- d_1, a_2-d_2) correspond to the phase distributions illustrated in Figure V.7.

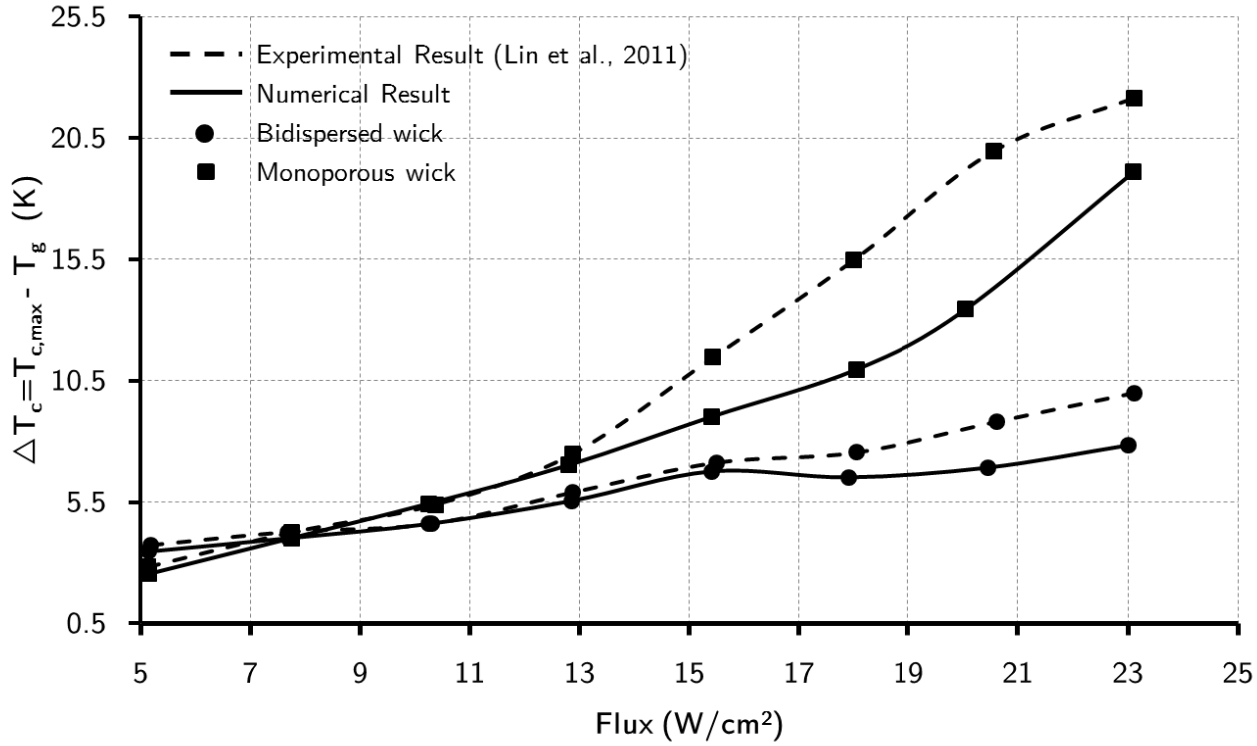

Figure V.6 – Variation of vapour ΔT_c as a function of the heat load applied to the casing.

V.5.3 Evaporator heat transfer coefficient and vapour saturation

The evaporator heat transfer coefficient as a function of the applied heat load is shown in Figure V.5. At low heat flux, the monoporous evaporator has better thermal performance than the bidispersed one. However, the evaporator heat transfer coefficient of the monoporous sample decreased rapidly after 10W/cm^2. The trend of the conductance for the bidispersed sample is different compared to the monoporous wick. From 5W/cm^2 to 25W/cm^2, the heat transfer increases from about 1.5W/cm^2/K to 3W/cm^2/K. The difference between these trends can be explained by considering the liquid-vapour phase distribution within the wick similarly as in [76]. For this purpose, the liquid-vapour phase distributions for different heat fluxes are depicted in Figure V.7 for both the bidispersed and the monoporous structures.

The fraction of pores right under the casing occupied by vapour in the plane located right under the casing and the vapour saturation within the wick are investigated to explain the conductance behaviour (Figure V.8). As can be seen from Figure V.7 and Figure V.8, the monoporous wick is rapidly invaded by vapour. At low heat flux, 60% of the wick are already invaded by vapour and 70% of the wick/casing interface are occupied by vapour pores. By contrast, the bidispersed wick vapour saturation is less than 5% and the fraction of pores occupied by vapour at the wick/casing interface is less than 30%.

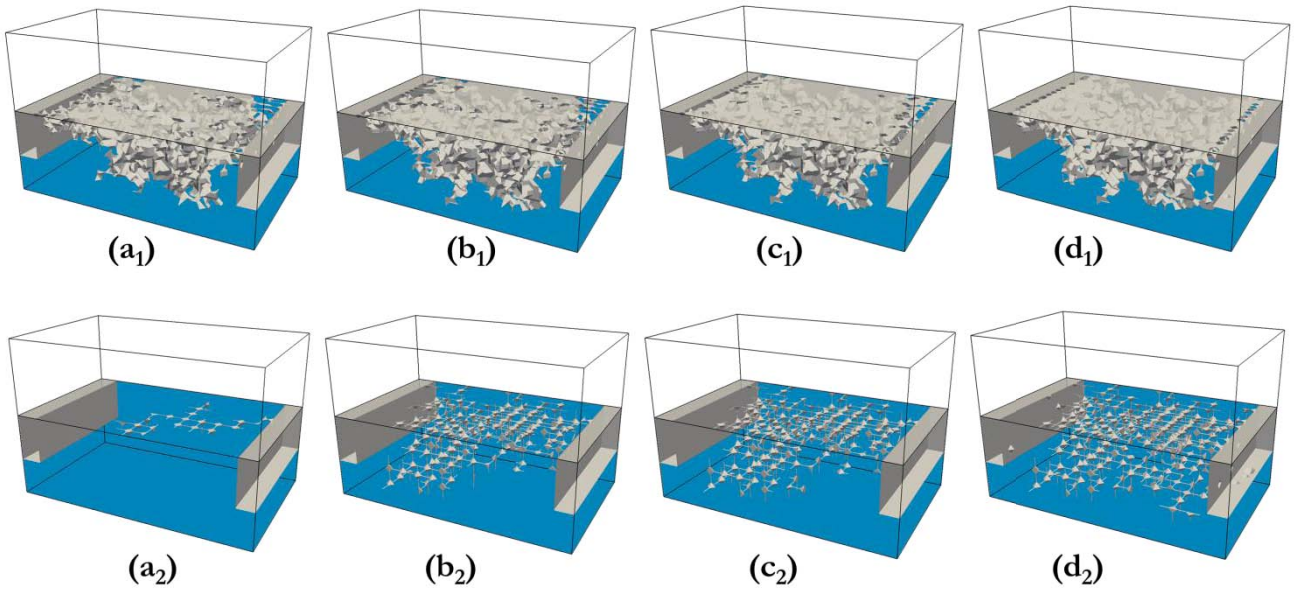

Figure V.7 – Pore network numerical visualisations of vapour and liquid phase distribution in the evaporator unit cell for the same fluxes in the monoporous and bidispersed wick. Vapour phase is in grey and liquid phase is in blue. Figures (a1) from (d1) correspond to the bidispersed wick structure and Figures (a2) from (d2) refer to the monoporous wick structure. (a_1) and (a_2) are results at 7.7W/cm²; (b_1) and (b_2) are results at 12.8W/cm²; (c_1) and (c_2) are results at 15.35W/cm² and (d_1) and (d_2) are results at 23W/cm².

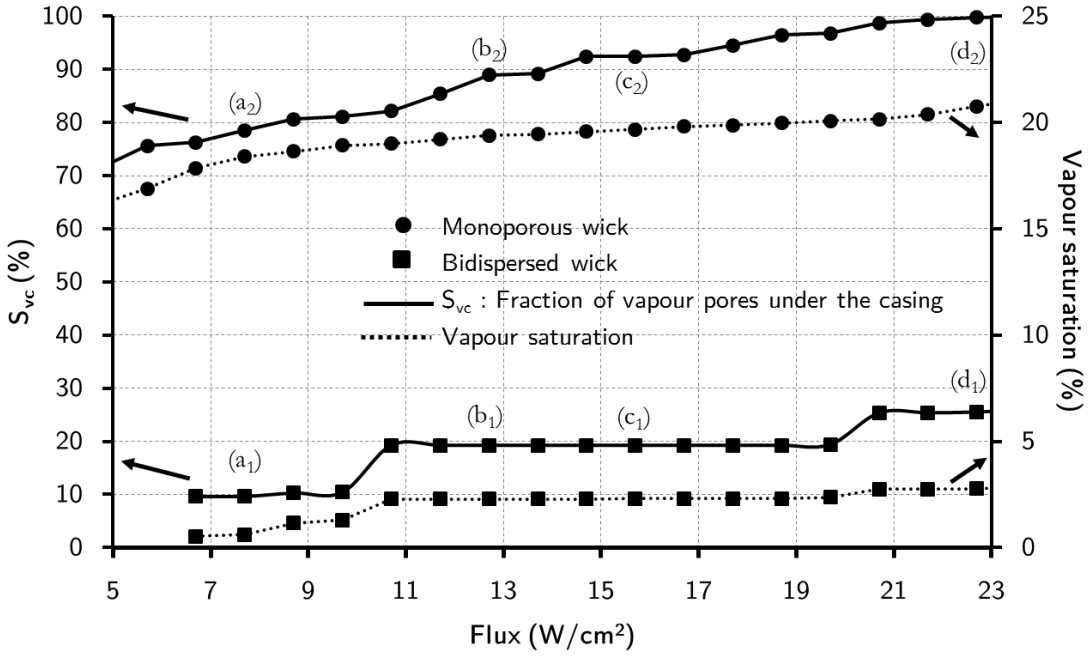

Figure V.8 – Variation of the vapour saturation and the occupancy state of pores under the casing as a function of the heat flux applied to the casing. S_{vc} is the fraction of pores occupied by vapour right under the casing. The labels (a_1- d_1, a_2-d_2) correspond to the phase distributions illustrated in Figure V.7.

Contrary to the monoporous wick, the liquid phase is predominant under the casing for the bidispersed wick, thus ensuring a better thermal performance in accordance with the results and discussion presented in [76]. Indeed, as discussed in [13] three evaporator regimes can be distinguished with the increase in the heat load. The first regime corresponds to the low heat loads where the wick is saturated, i.e. there is no meniscus recession within the wick and the conductance is constant. During this regime, the evaporator has relatively poor thermal performances. The second regime occurs when vapour begins to invade the wick. During this regime, a two-phase zone exists under the casing, i.e. the liquid and the vapour phases are both in contact with the casing. This second regime thus corresponds to the occurrence of a two-phase zone under the casing and can be itself divided into three parts qualitatively described as follows: the first one corresponds to the increase in the conductance; the second part corresponds to the best performance of the evaporator (the conductance reaches a plateau); the last part corresponds to the beginning of the decrease in the thermal performance when the vapour at the wick/casing interface exceeds a certain fraction of the wick/casing surface, i.e. the vapour becomes predominant in this zone. Finally, the last and third regime corresponds to a rapid fall in the conductance and begins when the layer of pores under the casing is fully occupied by vapour. Note that the upper and lower bonds of the fraction of pores occupied by vapour under the casing which delimit each regime depend on the geometry and properties of the wick and the casing.

As already mentioned, the monoporous evaporator has better thermal performance than the bidispersed one at low heat fluxes. Under 6.7W/cm^2, the bidispersed wick is still full of liquid (regime I) (Figure V.8), which as recalled above corresponds to relatively poor evaporator performances whereas the monoporous wick is already invaded by vapour, and thus in the best regime (regime II). Consistently, the heat transfer performance of the bidisperse wick is less good than the monoporous wick one. Beyond 6.7W/cm^2, the bidispersed wick operates in the second regime according to the conductance behaviour. The variation of the fraction of vapour pores under the casing is in good agreement with this observation. Indeed, the conductance increases with the heat load until 10W/cm^2 and seems to stabilize (according to experimental data) corresponding respectively to the first and second parts of the second regime described in [76]. The conductance of the monoporous wick is almost constant until 10W/cm^2, corresponding to a fraction of pores under the casing lower than 80%, i.e. the wick operates in the second regime. When more than 80% of the wick/casing interface is invaded by vapour, the conductance decreases, meaning that the evaporator operates in the third regime. The vapour becomes largely predominant under the casing thus adding a thermal resistance which induces the decrease in evaporator performance.

The best performance of evaporator is thus well correlated with the occurrence of a two-phase zone under the casing as expected. In brief, the bimodal capillary structure creates preferential paths for the vapour, thus keeping a two-phase zone in contact with the casing for a larger range of heat flux.

V.5.4 Evaporator wall temperature

The compensation chamber temperature is an input in our model which conditions the overall evaporator temperature field. Unfortunately, this value is not reported in Lin et al. (2011) [109]. The compensation chamber (CC) temperature was fixed at 283K in our simulations. With this temperature for the CC, the maximal temperature of the evaporator, located at the casing external surface, obtained numerically, was lower than the one obtained experimentally. Instead of fitting this temperature so as to obtain comparable values with the experiment as regards the maximal temperature, we simply consider the overheating of the casing ΔT_c. It is expected that the computed ΔT_c should be comparable to the experimental one. As can be seen in Figure V.6, this is indeed the case, especially for the bidispersed wick.

For low heat load, i.e. under 6.7W/cm^2, the overheating of the casing for the bidispersed wick is greater than the one of the monoporous wick as in the experiments. This trend is in accordance with the conductance behaviour. Indeed, the monoporous wick operates in the second regime (invasion of vapour) and has better thermal performance than the bidispersed one which is saturated with liquid and operates in the first regime.

Once the vapour has invaded the wick, the overheating of the bidispersed wick increases slowly; whereas the overheating of the monoporous one rises rapidly. This trend is well reproduced by the simulations. With the increase in the heat load, the fraction of vapour pores under the casing is greater than 80% for the monoporous sample (Figure V.8). The vapour induces a higher thermal resistance and thus the marked increase in the casing overheating. The large network of the bidispersed wick ensures paths for the vapour, thus facilitating the vapour escape. As a result, the vapour does not invade the layer of pores right under the casing and this prevents the overheating of the casing. Moreover, as pointed out by others author ([20,46]), the overheating of the casing rises quickly for a low k_v^*, whereas the overheating of the casing is not the operating limit for a more conductive wick, i.e. for high k_v^*. The effective thermal conductivity depends on the porosity and k_v^* is higher for a lower porosity. Indeed, the porosity of the bidispersed wick is greater than the one of the monoporous wick. The calculated vapour effective thermal conductivities are equal to 26.2W/m/K and 14.2W/m/K respectively. As explained at the beginning of the paragraph, this difference in the value of k_v^* induces a slower rising of the overheating for the bidispersed wick.

V.5.5 Vaporisation partition

The mass flow rate of vapour feeding the vapour groove is shown as a function of the heat flux applied to the casing in Figure V.9. This mass flow rate is divided into the mass flow rate which results from the liquid vaporisation at the wick/groove interface and the mass flow rate which results from the vaporisation within the wick. For a given heat flux, the mass flow rate of vapour is the same for the monoporous and the bidispersed wick. Hence, the two curves are exactly superimposed. For low heat flux, i.e. below than 7.7W/cm^2, the vapour essentially comes from the vaporisation process at the wick/groove interface for the bidispersed wick, whereas already 70% to 80% of the mass flow rate come from the vaporisation within the wick for the monoporous wick. Beyond 7.7W/cm^2, the vapour which feeds the groove of the bidispersed evaporator mostly comes from the vaporisation process within the capillary structure. Actually, the trend shown around 7.7W/cm^2 is correlated with the beginning of

regime II as defined in [76]. From 10W/cm^2, the mass flow rate distribution is almost similar for both wicks: around 80% to 100% of the vapour feeding the grooves come from the vaporisation within the wick.

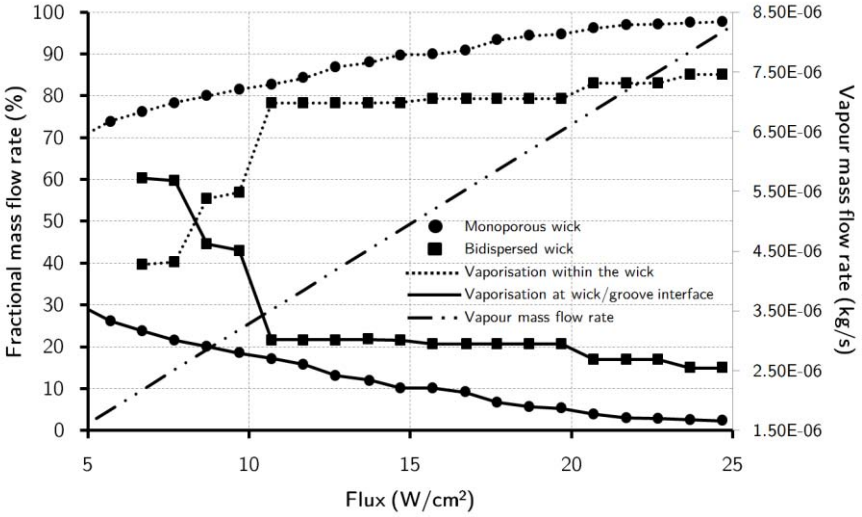

Figure V.9 – Variation of vapour mass flow rate partition and vapour mass flow rate as a function of the heat flux applied to the casing.

V.5.6 Summary

The presence of a two-phase zone, i.e. the coexistence of liquid and vapour in the same zone under the casing is positively correlated with the best evaporator thermal performance and prevents the overheating of the casing. At low heat flux, the vaporisation of the bidispersed wick takes place at the wick-groove interface only and the thermal performance is lower than for the monoporous wick which is already invaded by vapour, i.e. the vaporisation also takes place within the wick. For a higher heat load, the bidispersed wick reaches better thermal performance than the monodispersed wick. The first row of pores under the casing is almost full of vapour for the monoporous capillary structure, inducing an additional thermal resistance and a significant increase in the casing overheating. On the contrary, the large pores network in the bidispersed wick creates preferential paths for the vapour and keeps a two-phase zone under the casing for a large range of heat load. This phase distribution induces a slow rise in the casing overheating.

V.6 Monoporous vs. bidispersed wick

V.6.1 Input properties

A comparison of the thermal performances and the liquid-vapour phase distribution is performed using geometry A and geometry B presented in section IV.1 for a monoporous and a bidispersed wick. Geometry A corresponds to grooves within the inner surface of the casing and geometry B corresponds to grooves manufactured within the outer surface of the wick. All the properties used in the simulations are summarized in Table V-2. All the simulations presented in this section have been performed using

the Alexander's model to compute the effective thermal conductivity of the wick and ΔT_{nucl} is equal to 3K. The choice was made to use a large throat mean diameter one order of magnitude greater than the small throat mean size. This lead to a permeability for bidispersed wicks three orders of magnitude greater than the one computed for monoporous wicks.

Wick properties (Nickel)				
Throat diameter p.d.f	Normal			
Thermal conductivity (W/m/K)	90			
	Monoporous		Bidispersed	
	Geometry A	Geometry B	Geometry A	Geometry B
d_{throat} (µm)	2.3±2		2.3±2 and 23±5	
Lattice spacing (mm)	a =0.0613		a =0.0613 and b =0.245	
Porosity	0.805	0.806	0.806	0.802
Permeability (m^2)	4.4×10^{-14}	4.6×10^{-14}	5.2×10^{-11}	5.3×10^{-11}
Casing property (Stainless steel)				
Thermal conductivity (W/m/K)	20			
Fluid properties (Ammonia)				
	Liquid	Vapour		
Thermal conductivity (W/m/K)	0.52912	0.024365		
Viscosity (Pa.s)	1.56×10^{-4}	0.963×10^{-5}		
Specific heat capacity (J/kg/K)	4675.7	2841.3		
Heat latent of vaporisation (kJ/kg)	1225.58			
Liquid density (kg/m^3)	624.46			
Molar mass (kg/mol)	0.017			
Surface tension (N/m)	29.589×10^{-3}			
Inlet temperature/pressure				
P_{cc} (Pa)	615050			
$T_{sat}(P_{cc})$ (K)	283.15			
Geometry dimensions (mm) (see Figure III.3 for definitions)				
L_x	1.9			
L_y	3.4			
L_z	2			
L_{xv}	0.35			
L_{yw}	1.5			
L_{yt}	0.35			
L_{yg}	0.7			
Loop dimensions				
Number of grooves / Length of grooves (mm)	6/25			
Length (mm)/ inner diameter (mm) of the vapour line	200/2			
Length (mm)/ inner diameter (mm) of the liquid line	200/2			
Length (mm)/ inner diameter (mm) of the condenser	200/2			

Table V-2 – Porous materials properties, fluid properties and geometrical dimensions.

V.6.2 Nucleation flux

The nucleation fluxes for geometry A and geometry B with a monoporous or a bidispersed wick are given in Table V-3.

	Monoporous wick	Bidispersed wick
Geometry A	1.74W/cm²	5.81W/cm²
Geometry B	3W/cm²	8.475W/cm²

Table V-3 – Nucleation fluxes for geometry A and geometry B with a monoporous or a bidispersed wick.

As already pointed out and explained in section IV.1, the nucleation flux is higher for geometry B whatever the throat size distribution of the capillary structure. For both geometries, the occurrence of vapour is delayed when the wick is bidispersed and this can be explained as follows. The effective thermal conductivity decreases with the rise in porosity and as explained in section IV.2.2.1, the nucleation flux becomes higher if the effective thermal conductivity increases. The porosity of the bidispersed wick is divided into two different porosities: porosity of the network constituted by large throats and porosity of the network constituted by small throats. These two porosities are thus lower than the porosity of the monoporous wick. Hence, the global effective thermal conductivity of the bidispersed wick is higher than the one of the monoporous wick and by consequence the nucleation flux also.

V.6.3 Liquid-vapour phase distribution

Figure V.10a shows the variation of the fraction of pores occupied by vapour under the casing whereas Figure V.10b shows the variation of the vapour region depth. The liquid-vapour phase distributions for different heat fluxes are shown in Figure V.11. For a monoporous wick, a dry region exists under the casing for heat fluxes higher than 20W/cm² (see Figure V.10a and Figure V.11(d,h,i)). This is in contrast with the bidispersed wick for which a two-phase zone exists under the casing (Figure V.10a and Figure V.11(m,n,r,s)). Indeed, for bimodal wicks, the vapour occupancy under the casing is always lower than 60%, even when the vapour breakthrough towards the wick inlet is reached (at 57.415W/cm² for geometry A and 59.09W/cm² for geometry B). If the wick is bidispersed, the vapour preferentially invades large void spaces (pores and throats) due to low flow resistance, while there is no preferential path in the monoporous structure as it is clearly shown in Figure V.11.

If the wick is monoporous, the first layer of pores under the casing is more invaded by vapour with geometry A. On the contrary, if the wick is bidispersed, the first layer of pores under the casing is more invaded by vapour in geometry B configuration. This is due to the rule adopted in this model. The pore network is structured and the invasion percolation rules are adopted to create the vapour path from the pore where the nucleation temperature is reached and the grooves or the principal vapour cluster. For geometry A, the last layer of pores under the casing is constituted by a percolating network of large and small throats. Hence, when the nucleation temperature under the casing is reached, the vapour path follows the preferential paths created by large throats (see Figure V.11k). For geometry B, only the small throats form a connected network up to the grooves in the plane in contact with the casing. Hence, when the nucleation temperature under the casing is reached, no preferential path for the vapour exists

leading to the invasion of more throats (see Figure V.11p). This explains why the vapour saturation under the casing is slightly higher for geometry B when the wick is bidispersed.

For both geometries, the bimodal capillary structure influences the spatial liquid-vapour phase distribution and thus permits to keep a two-phase zone under the casing for a larger range of fluxes.

Intuitively, we could think that the preferential paths created by the large throats could induce a premature breakthrough of the vapour towards the wick inlet and those especially because the network is structured in this approach. However, as shown in Figure V.10b, the length of the vapour region has almost the same trend for a given geometry, whatever the capillary structure. On the other hand, the vapour breakthrough is the limiting parameter when the wick is bidispersed as it occurs when the evaporator operates in regime II, i.e. when a two-phase zone is present under the casing.

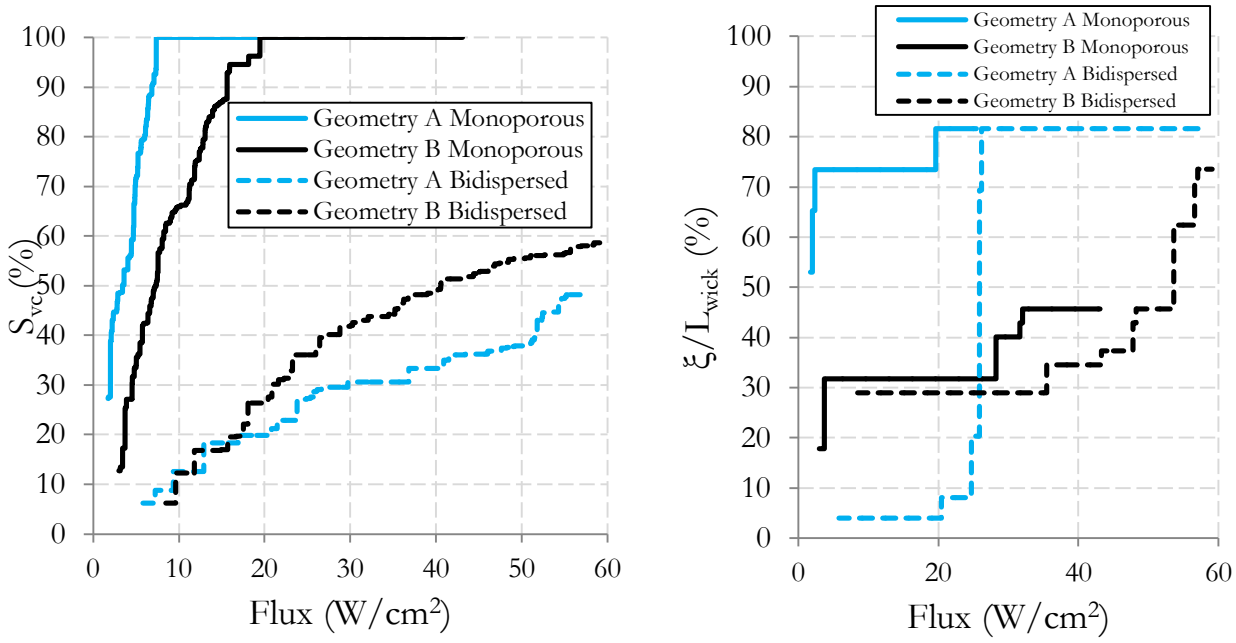

(a) **(b)**

Figure V.10 – (a) Variation of the occupancy state of pores under the casing as a function of the heat flux applied to the casing. S_{vc} is the fraction of pores occupied by vapour right under the casing. (b) Variation of the vapour region depth divided by the wick thickness (ξ/L_{wick}) (L_{wick} is equal to L_{yw} for geometry A and $L_{yw}+L_{yg}$ for geometry B).

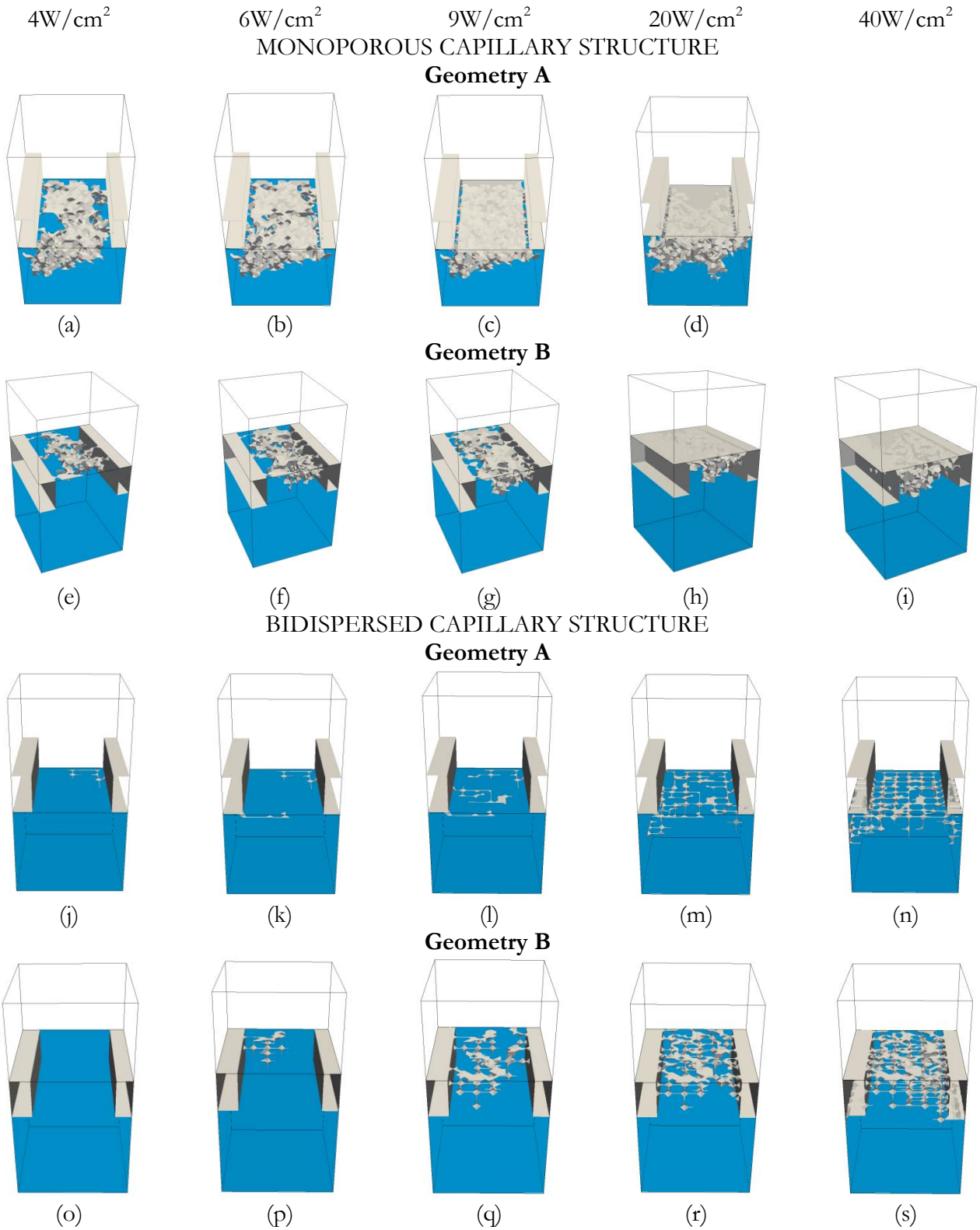

Figure V.11 – Pore network numerical visualisations of vapour and liquid phase distribution in the evaporator unit cell for the fluxes 4W/cm² (figures (a), (e), (j) and (o)), 6W/cm² (figures (b), (f) (k) and (p)), 9W/cm² (figures (c), (g), (l) and (q)), 20W/cm² (figures (d), (h), (m) and (r)) and 40W/cm² (figures (i), (n) and (s)) for geometry A (figures (a-d) and (j-n)) and for geometry B (figures (e-i) and (o-s)) with a monoporous wick (figures (a-i)) or a bidispersed wick (figures (j-s)). Vapour phase is in grey and liquid phase is in blue.

V.6.4 Evaporator thermal performances

The variation of the conductance as a function of the heat load for both geometries and for a monoporous and a bidispersed wick is shown in Figure V.12. The evaporator thermal performances are better for grooves located in the wick (geometry B) whatever the capillary structure of the wick, as already discussed in section IV.1.2.1. For geometry A, the conductance reaches a maximum of 0.49W/cm^2/K and 0.79W/cm^2/K with a monoporous wick and a bidispersed wick, respectively. For geometry B, the conductance reaches a maximum of 0.74W/cm^2/K and 1.22W/cm^2/K with a monoporous wick and a bidispersed wick, respectively. As already pointed out in section V.5.3, the conductance is improved when the wick is bimodal. However, the behaviour of the conductance is slightly different when the wick is bidispersed. Indeed, the conductance increases when the evaporator begins to operate in regime II and reaches a "plateau" corresponding to the best thermal performances. The range of fluxes where the evaporator operates with the best conductance is increased and it is possible to reach relatively high fluxes equal to 55W/cm^2. The vapour breakthrough, i.e. defusing of the evaporator, is reached before that the evaporator operates in regime III (dry region under the casing).

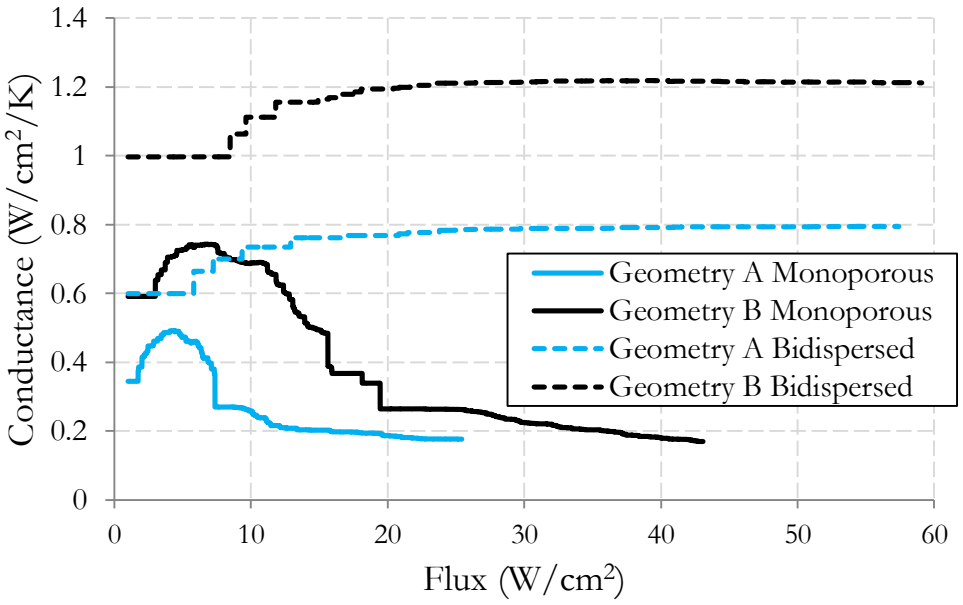

Figure V.12 – Variation of the conductance as a function of the heat load for geometry A and geometry B with a monoporous or a bidispersed wick structure.

V.6.5 Evaporator wall temperature

As the groove temperature is almost equivalent for both geometries and capillary structures, the conductance is mainly influenced by the maximum temperature of the casing which is shown in Figure V.13. For both capillary structures, the overheating of the casing is higher when the grooves are within the casing. As this difference is discussed in section IV.1, the reader can refer to this section for more explanations.

For a monoporous wick, the evaporator wall temperature reaches 383.15K for the heat loads equal to 19.33W/cm² and 25.86W/cm² in geometry A configuration and geometry B configuration, respectively. Beyond this temperature, we could assume that casing material and/or electronic devices suffer from serious damages as discussed in section I.1.5.3. Hence, the limiting parameter is the overheating of the casing when the wick is monoporous. Note that a dry region exists under the casing for the two previous cited fluxes. The use of a bidispersed wick eliminates this limitation as shown in Figure V.13. Indeed, the evaporator wall temperature is equal to 355.7K and 332.2K at 57.415W/cm² for geometry A and 59.09W/cm² for geometry B, respectively, at the moment of the vapour breakthrough towards the wick inlet. A two-phase zone persists under the casing and thus prevents the overheating of the casing.

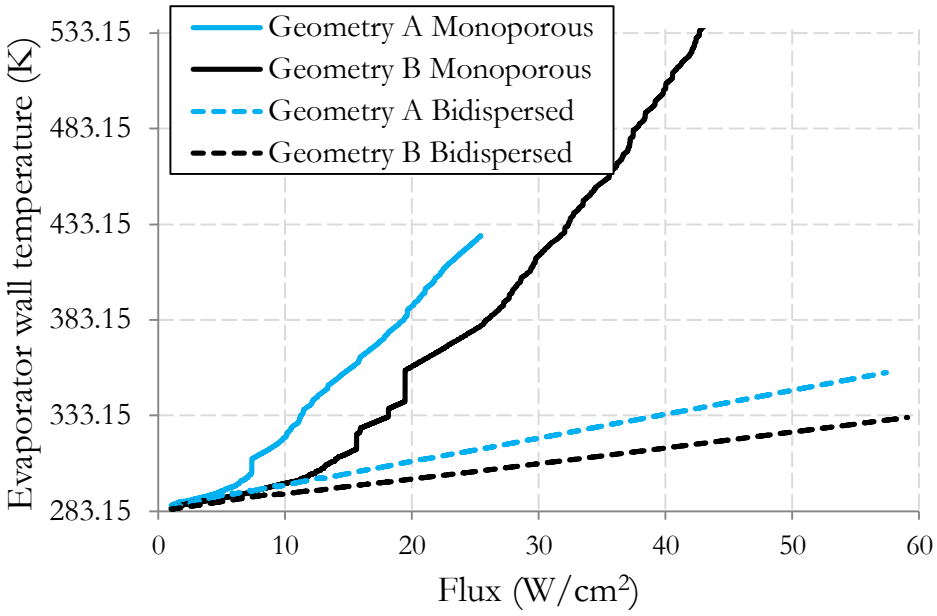

Figure V.13 – Variation of the evaporator wall temperature as a function of the heat load for geometry A and geometry B with a monoporous or a bidispersed capillary structure.

V.6.6 Summary

The evaporator reaches better thermal performances when the wick is bidispersed and whatever the grooves location. The evaporator can evacuate fluxes up to 57W/cm². Moreover, the range of fluxes where the evaporator operates in regime II is duly enhanced. For high heat fluxes, the first layer of pores under the casing is invaded by vapour if the wick is monoporous, while a two-phase zone remains if the wick is bidispersed. Indeed, the invasion scenario is slightly different for bimodal wick: the large throats create preferential paths for the vapour due to the low flow resistance. Hence, the coexistence of the liquid and the vapour under the casing is favoured. In consequence, the overheating of the casing is the limiting parameter when the wick is monoporous, while this is the breakthrough of the vapour towards the wick inlet when the wick is bidispersed.

V.7 Synthesis and conclusions of the chapter

Pore network models of a LHP/CPL evaporator were presented for a bidispersed and a monoporous wick structures. Simulations were compared with experimental data. The model was validated from the consideration of the steady-state evaporator thermal performance, i.e. its conductance, and the overheating of the evaporator. Comparisons with experimental results show a good agreement for both the monoporous and the bimodal capillary structures. The observed difference can be attributed to the unknown parameters (compensation chamber temperature, grooves dimensions…) which were deduced from other experimental studies. However, the trend of h_{ev} and ΔT_c are respected, and the mixed pore network model permits to explain their behaviour based on the liquid-vapour phase distribution within the wick.

The influence of the groove location was investigated for a monoporous and a bidispersed wick. The conclusions are the same whatever the capillary structure: grooves located at the outer surface of the wick improve the evaporator thermal performances. It was found that the main limiting parameter of the evaporator is the overheating of the wall if the wick is monoporous due to the occurrence of a dry region under the casing. By contrast, the main limiting parameter of the evaporator is the breakthrough of the vapour towards the wick inlet if the wick is bidispersed due to the preferential paths created by large throats.

We conclude that the mixed pore network model developed in this work is a useful tool to investigate the evaporator thermal performance and the casing temperature of an LHP/CPL for different bidispersed and monodispersed wick structures. It opens up the route towards the numerical optimization of bidispersed capillary structures.

Chapter VI Continuum modelling

Chapter VI Continuum modelling 169
VI.1 Motivations 170
VI.2 Problem formulation 170
VI.3 Method of solution 175
VI.4 Results and discussions 177
VI.5 Synthesis and conclusions of the chapter 197

In this chapter, a continuum model based on macroscopic equations is presented. The two-phase flow within the wick as well as the heat transfer with phase change in the whole evaporator unit cell is simulated. The method of solution is based on the well-known IMPES (IMplicit Pressure Explicit Saturation) algorithm. This chapter presents comparisons between results obtained from the pore network model and those obtained from the continuum model. Geometry A and geometry B are used to compare the results.

VI.1 Motivations

The average computation time for a given heat load with two-phase zone formation using the mixed pore network model presented in the previous chapters is about 1 or 2h. To obtain the results discussed in the previous chapters, the imposed heat flux was varied by increment of 0.05W/cm² to avoid divergence of the calculation. This leads to about 60 to 90 days of computational time. Therefore, simulations of the whole evaporator will lead to unacceptable computational time. This was the first motivation to develop a continuum model based on macroscopic equations. Indeed, this kind of approach is expected to be less computational time consuming. The method adopted here is based on the IMPES (IMplicit Pressure Explicit Saturation) algorithm mainly used in petroleum engineering (Aziz and Settari (1979) [117]) and the aim is to develop a continuum model to solve the two-phase flow with phase change in the capillary evaporator unit cell.

VI.2 Problem formulation

VI.2.1 Assumptions

The model is developed under unsteady condition. We assume local thermal equilibrium at the REV scale between the liquid, the vapour and the solid porous matrix. Vapour is supposed to be slightly compressible and we neglected the gravity field.

VI.2.2 Governing equations

VI.2.2.1 Two-phase flow

VI.2.2.1.1 Fluid mass conservation

The macroscopic fluid mass conservation of the liquid and the vapour are expressed as follows:

$$\frac{\partial}{\partial t}(\rho_l S_l \varepsilon) = -\nabla.(\rho_l \mathbf{u}_l) - \dot{m} \quad \textbf{(VI-1)}$$

$$\frac{\partial}{\partial t}(\rho_v (1 - S_l)\varepsilon) = -\nabla.(\rho_v \mathbf{u}_v) + \dot{m} \quad \textbf{(VI-2)}$$

$\mathbf{u}_i$ is the velocity of the phase i and ρ_i is the density of the phase i, where i corresponds to the liquid phase l or the vapour phase v. The other terms are defined below.

The vapour is supposed to be slightly compressible and the vapour density is expressed by the ideal gas law.

$$\rho_v = \frac{P_v M}{RT} \quad \textbf{(VI-3)}$$

ε is the porosity of the porous medium defined as the ratio between the void space and the total volume of the considered sample. The volume of void space can be expressed as the sum of the volume occupied by the liquid and the volume occupied by the vapour.

$$\varepsilon = \frac{V_{void}}{V_T} = \frac{(V_l + V_v)}{V_T} \quad \textbf{(VI-4)}$$

S_l is the saturation of the liquid phase within the porous medium and is defined as the ratio between the volume of void occupied by liquid and the total volume of void.

$$S_l = \frac{V_l}{V_{void}} \quad \textbf{(VI-5)}$$

For two-phase flows, the void space is only occupied by the two phases. Therefore,

$$S_l + S_v = 1 \quad \textbf{(VI-6)}$$

$\dot{m}$ is the mass rate of generation of vapour due to evaporation or liquid due to condensation per unit volume and is expressed as follows using the phase change model proposed by Lee (1980) [118]:

$$\dot{m} = \begin{cases} \beta S_l \rho_l \dfrac{T_{cell} - T_{sat}}{T_{sat}} & ; T_{cell} \geq T_{sat} \\ \beta (1 - S_l) \rho_v \dfrac{T_{cell} - T_{sat}}{T_{sat}} & ; T_{cell} < T_{sat} \end{cases} \quad \textbf{(VI-7)}$$

where T_{sat} is the saturation temperature of the fluid and T_{cell} is the temperature of the cell considered in the calculation grid. β is an empirical parameter.

VI.2.2.1.2 Darcy's law

The Darcy's law at the macroscopic level for the liquid phase and the vapour phase is given by

$$\mathbf{u}_l = -M_l \nabla P_l \quad \textbf{(VI-8)}$$

$$\mathbf{u}_v = -M_v \nabla P_v \quad \textbf{(VI-9)}$$

where P_i is the pressure of the liquid phase l or the vapour phase v.

M_l and M_v are the relative mobilities of the liquid and vapour phase defined by:

$$M_l = \frac{K k_{rl}}{\mu_l} \quad \textbf{(VI-10)}$$

$$M_v = \frac{K k_{rv}}{\mu_v} \quad \textbf{(VI-11)}$$

where K is the permeability of the porous medium and μ_i is the dynamic viscosity of the fluid phase i (liquid l or vapour v) considered as constant in the current model.

k_{ri} is the phase i relative permeability determined by the Van Genuchten model.

$$k_{rl}(S_l^*) = (S_l^*)^{\gamma_l}\left(1 - \left(1 - (S_l^*)^{1/m_l}\right)^{m_l}\right)^2 \quad \textbf{(VI-12)}$$

$$k_{rv}(S_l^*) = (1 - S_l^*)^{\gamma_v}\left(1 - (S_l^*)^{1/m_v}\right)^{2m_v} \quad \textbf{(VI-13)}$$

where m_l, m_v, γ_l and γ_v are parameters determined in our case from the pore network simulations (see Appendix D).

S_l^* is the effective liquid saturation.

$$S_l^* = \frac{S_l - S_{lr}}{1 - S_{lr} - S_{vr}} \quad \textbf{(VI-14)}$$

S_{lr} is the liquid phase residual saturation and S_{vr} is the vapour phase residual saturation. In the present model S_{lr} and S_{vr} are equal to zero assuming no trapping in the porous medium as explained in Appendix D.

VI.2.2.1.3 Final formulation

The problem is expressed in terms of liquid saturation S_l and vapour pressure P_v. Therefore we need two equations.

The liquid saturation equation is the fluid mass conservation equation (equation (VI-15)).

$$\frac{\partial}{\partial t}(\rho_l S_l \varepsilon) = -\nabla.(\rho_l \mathbf{u}_l) - \dot{m} \quad \textbf{(VI-15)}$$

The sum of equation (VI-1) and equation (VI-2), where the velocities are replaced by their expressions given in equation (VI-8) and equation (VI-9), corresponds to the second needed equation for the pressure (equation (VI-16)).

$$\frac{\partial}{\partial t}(\rho_l S_l \varepsilon + \rho_v (1 - S_l)\varepsilon) = \nabla.(K(\rho_l M_l + \rho_v M_v)\nabla P_v) - \nabla.\left(K\rho_l M_l \frac{\mathrm{d}P_{cap}}{\mathrm{d}S_l}\nabla S_l\right) \quad \textbf{(VI-16)}$$

The capillary pressure P_{cap} is the difference between the vapour and the liquid pressure (equation (VI-17)) and can be expressed by the Van Genuchten model (equation (VI-18)).

$$P_{cap} = P_v - P_l \quad \textbf{(VI-17)}$$

$$P_{cap} = \frac{1}{\alpha}\left((S_l^*)^{-1/m} - 1\right)^{1/n} \quad \textbf{(VI-18)}$$

where $m = 1 - 1/n$ and α are parameters determined from the pore network simulation as explained in Appendix D.

The derivative of the capillary pressure as a function of the liquid saturation is given by:

$$\frac{\mathrm{d}P_{cap}}{\mathrm{d}S_l} = -\frac{1}{\alpha}\frac{1}{nm}(S_l^*)^{-\frac{1}{m}-1}\left((S_l^*)^{-\frac{1}{m}} - 1\right)^{-m} \quad \textbf{(VI-19)}$$

VI.2.2.2 Energy equation

Heat transfer occurs by conduction and convection within the wick under local thermal equilibrium assumption.

$$\frac{\partial}{\partial t}\left(\left((1-\varepsilon)(\rho c_p)_w + \varepsilon(\rho c_p)_l S_l + \varepsilon(\rho c_p)_v (1 - S_l)\right) T\right) + \left((\rho c_p)_l \mathbf{u}_l + (\rho c_p)_v \mathbf{u}_v\right)\nabla T = \nabla.(k^*\nabla T) - \dot{m}h_{lv} \quad \textbf{(VI-20)}$$

where $(\rho c_p)_i$, is the heat capacity of the phase i, with i corresponding to the wick material w, the liquid phase l or the vapour phase v. T is the temperature and h_{lv} is the latent heat of vaporisation. k^* is the effective thermal conductivity determined by the arithmetic average (equation (VI-21)) between the parallel (equation (VI-22)) and the series (equation (VI-23)) model.

$$k^* = \frac{k_{//}^* + k_{\perp}^*}{2} \quad \textbf{(VI-21)}$$

$$k_{//}^* = (1-\varepsilon)k_w + \varepsilon S_l k_l + \varepsilon(1 - S_l)k_v \quad \textbf{(VI-22)}$$

$$k_{\perp}^* = \frac{1}{\frac{1-\varepsilon}{k_w} + \frac{\varepsilon S_l}{k_l} + \frac{\varepsilon(1-S_l)}{k_v}} \quad \textbf{(VI-23)}$$

Heat transfer through the metallic casing occurs by conduction:

$$\frac{\partial}{\partial t}\left(\left(\rho c_p\right)_c T\right) = \nabla.\left(k_c \nabla T\right) \quad \textbf{(VI-24)}$$

where $\left(\rho c_p\right)_c$ is the heat capacity of the casing and k_c is the thermal conductivity of the casing material.

VI.2.3 Boundary condition

The heat load q is applied at the external surface of the metallic casing.

$$\left(k_c \nabla T\right).\mathbf{n} = q \quad \textbf{(VI-25)}$$

where $\mathbf{n}$ is the interface normal unit vector.

Spatially periodic boundary conditions are imposed on the lateral sides of computational domain. The wick inlet is linked to the compensation chamber. The liquid pressure $P_{l,cc}$ and the temperature T_{cc} are imposed at the inlet of the wick to be equal at the compensation chamber condition (equation (VI-26) and equation (VI-27)). Note that the problem is expressed in terms of vapour pressure. Therefore, the inlet vapour pressure $P_{v,cc}$ is related to the liquid pressure by the capillary pressure from equation (VI-28). Moreover, the wick inlet is supposed to stay liquid saturated (equation (VI-29)).

$$T_{cc} = T_{sat} - \Delta T_{sub} \quad \textbf{(VI-26)}$$

$$P_{l,cc} = P_{sat}(T_{cc}) \quad \textbf{(VI-27)}$$

$$P_{v,cc} = P_{cap}\left(S_{l,wi}\right) \quad \textbf{(VI-28)}$$

$$S_{l,wi} = 0.9999 \quad \textbf{(VI-29)}$$

ΔT_{sub} is a possible subcooling of the liquid at the inlet of the wick and subscript wi means "wick inlet".

Grooves are supposed to be full of vapour. The groove pressure P_g (equation (VI-30)) is computed using the loop model presented in section III.2.6 (Chapter III). The groove temperature T_g is taken as the saturation temperature corresponding to the groove pressure P_g (equation (VI-31)) using the Clausius-Clapeyron relationship.

$$P_g = P_{l,cc} + \Delta P_{loop} \quad \textbf{(VI-30)}$$

$$T_g = T_{sat}\left(P_g\right) \quad \textbf{(VI-31)}$$

ΔP_{loop} is the pressure drop in the other components of the loop determined using the same method as the one presented in section III.2.6 (Chapter III).

No flow condition and energy conservation are imposed at the wick/casing interface.

$$(-k^{*}\nabla T).\mathbf{n} = (-k_c\nabla T).\mathbf{n} \quad \textbf{(VI-32)}$$

$$\nabla P_v.\mathbf{n} = 0 \quad \textbf{(VI-33)}$$

At the casing/groove interface, a convective boundary condition is imposed.

$$(k_c\nabla T).\mathbf{n} = h_g\left(T - T_g\right) \quad \textbf{(VI-34)}$$

The heat transfer coefficient is computed using relation presented in section III.2.5.5 (Chapter III).

The pressure is set at the groove pressure along the wick/groove interface and the temperature is taken at the saturation temperature.

$$P_{w/g} = P_g \quad \textbf{(VI-35)}$$

$$T_{w/g} = T_g = T_{sat}\left(P_g\right) \quad \textbf{(VI-36)}$$

Moreover, energy conservation is expressed as follows:

$$-k^{*}\frac{\partial T}{\partial y} = h_{lv}q_{ev} \quad \textbf{(VI-37)}$$

where q_{ev} is the interface mass flow rate calculated using equation (VI-38).

$$q_{ev} = \rho_l u_{l,y} = -\rho_l M_l\left(\frac{\partial P_l}{\partial y} - \frac{\mathrm{d}P_c}{\mathrm{d}S_l}\frac{\partial S_l}{\partial y}\right) \quad \textbf{(VI-38)}$$

where $u_{l,y}$ is the liquid velocity in the y-direction at the wick/groove interface.

VI.2.4 Initial condition

Before start-up, pressure and temperature are homogeneous in the fully liquid-saturated porous medium and the working fluid is saturated. At $t = 0$, the temperature and the pressure are set at the wick inlet saturation temperature T_{cc} and pressure $P_{l,cc}$. The wick is supposed to be saturated with the liquid: $S_l(t = 0) = 0.9999$.

VI.3 Method of solution

The above equations are solved using an home-made code written in Fortran90. The spatial discretization of equations is performed using a two-dimensional standard finite volume method. The pressure is solved using an implicit scheme and the liquid saturation is discretized using an explicit scheme. This method is well known as the IMPES method. The temperature is discretized using an implicit scheme. The iterative method leading to the steady-state solution is summarised in Figure VI.1.

The saturation has a great influence on the mobility and the capillary pressure. Therefore, it is necessary to use numerical schemes suitable to ensure the stability of the method. In the current model, we use:

- First order upwind scheme for relative permeabilities k_{ri} (equation (VI-12) and (VI-13)), vapour density ρ_v (equation (VI-3)) and convective term in the energy equation (equation (VI-20)).

- Harmonic average for the derivative of the capillary pressure $\mathrm{d}P_c/\mathrm{d}S_l$ (equation (VI-16)), and the effective thermal conductivity k^* (equation (VI-21)).

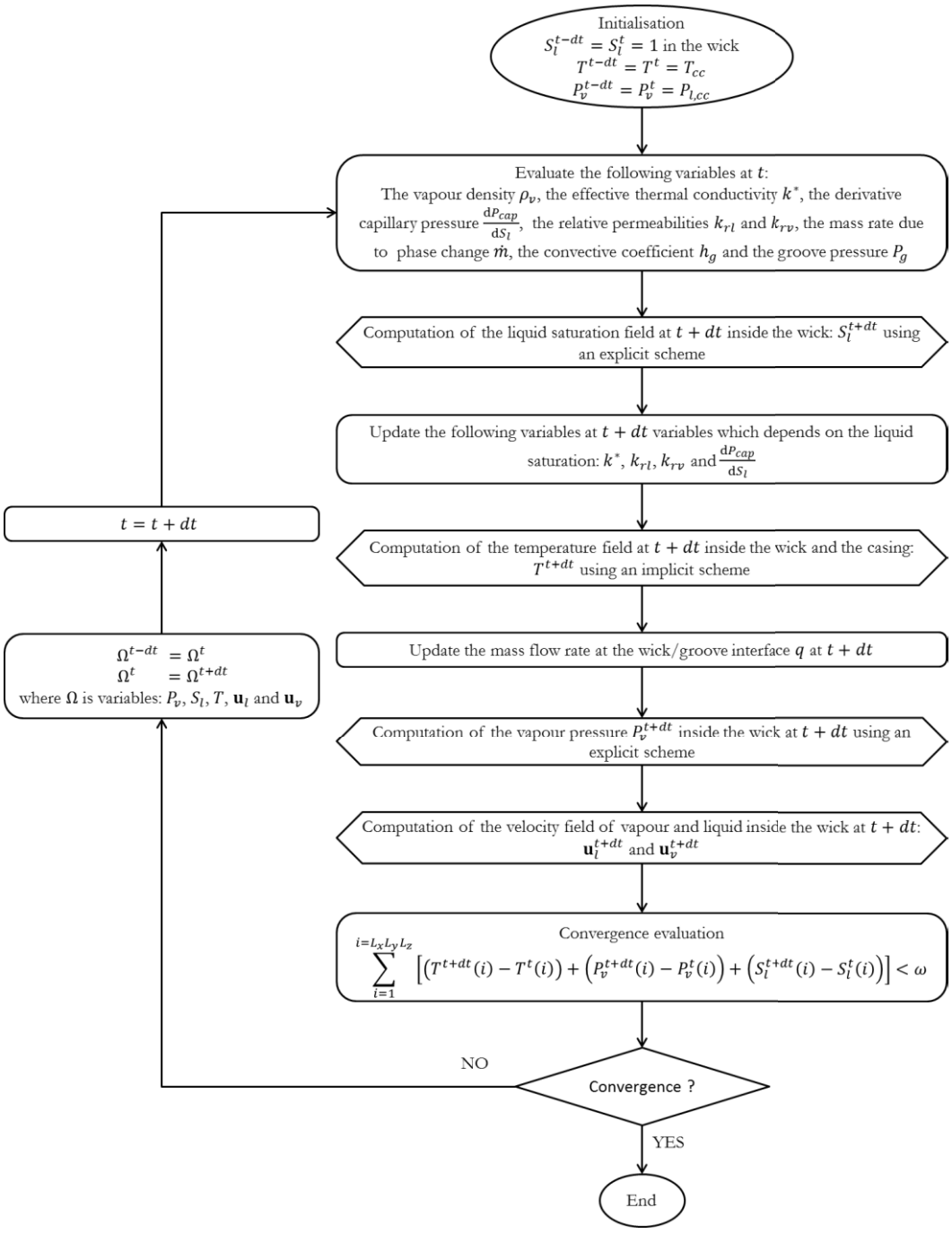

Figure VI.1 – Computational chart for the continuum model.

VI.4 Results and discussions

VI.4.1 Input parameters

For simplification PNS refers to Pore Network Simulation and CMS refers to Continuum Model Simulation in this section. The aim of this section is to compare results from PNS and CMS at steady-state. That's why, even if the transient regime is obtained with the continuum model, transient behaviour will not be discussed. Simulations have been performed with grooves manufactured at the inner surface of the casing (geometry A) and with grooves located at the outer surface of the wick (geometry B). Table VI-1 summarizes the different parameters used in both simulations (PNS and CMS). The effective thermal conductivity is computed using the average model. ΔT_{sup} is equal to 3K in pore network simulations.

Wick properties (Nickel)		
Thermal conductivity (W/m/K)	91	
Density (kg/m^3)	8000	
Specific heat capacity (J/kg/K)	444	
Throat diameter range (µm)	2.3±2	
Throat diameter p.d.f	Normal	
Porosity	0.77	
Permeability (m^2)	2.14×10^{-14}	
Casing property (Aluminium)		
Thermal conductivity (W/m/K)	20	
Density (kg/m^3)	7000	
Specific heat capacity (J/kg/K)	460	
Fluid property (Ammonia)	**Liquid**	**Vapour**
Thermal conductivity (W/m/K)	0.52912	0.024365
Dynamic viscosity (Pa.s)	156×10^{-6}	9.63×10^{-6}
Specific heat capacity (J/kg/K)	4678.7	2841.3
Latent heat of vaporisation (J/kg)	1225580	
Interfacial tension (N/m)	0.029589	
Liquid density (kg/m^3)	624.46	
Geometrical dimensions (mm) (see Figure III.3 for definitions)		
L_x	1.9	
L_y	3.4	
L_z	2	
L_{xv}	0.35	
L_{yw}	1.5	
L_{yg}	0.35	
Loop dimension		
Number of grooves/length of grooves (mm)	6/25	
Length (mm)/inner diameter (mm) of the vapour line	200/2	
Length (mm)/inner diameter (mm) of the liquid line	200/2	
Length (mm)/inner diameter (mm) of the condenser	200/2	

Table VI-1 – Porous materials properties, fluid properties and geometrical dimensions.

Figure VI.2 shows the variation of the capillary pressure as a function of the liquid saturation. The variation of the liquid and vapour relative permeabilities as a function of the liquid saturation is shown in Figure VI.3. These curves have been computed from pore network simulations as explained in Appendix D. Coefficients m_v, m_l, m, γ_v, γ_l and α are chosen to fit the curves obtained with PNS and are summarized in Table VI-2

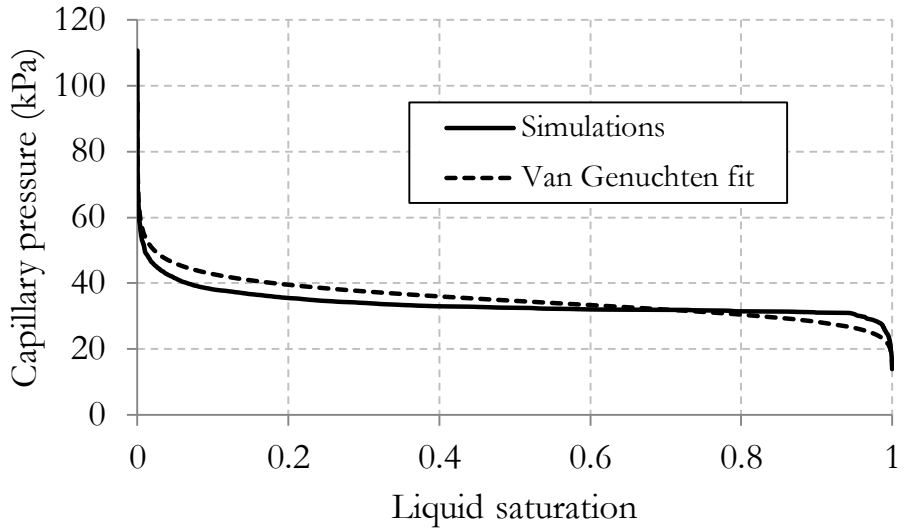

Figure VI.2 – Variation of the capillary pressure as a function of the liquid saturation.

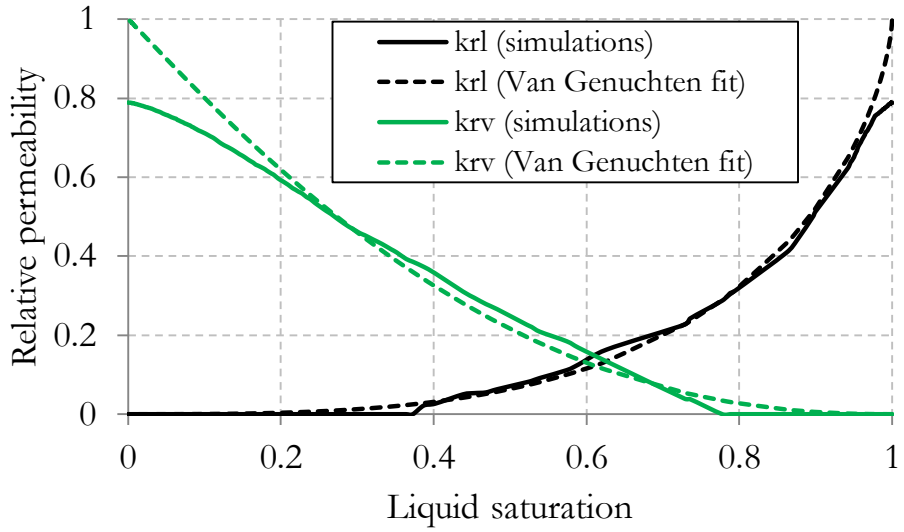

Figure VI.3- Variation of the liquid and vapour relative permeabilities as a function of the liquid saturation.

α	m	γ_l	m_l	γ_v	m_v
2.92×10^{-5}	1-(1/17)=0.94	1×10^{-3}	1-(1/3)=0.67	0.361	1-(1/26)=0.96

Table VI-2 – Van Genuchten coefficients used in continuum simulations.

The variables which permit to keep the interface temperature in the wick at the saturation temperature is β. Value for β was suggested by Yang et al. (2008) [119] and was justified by a good agreement between the model prediction and the experiment. The authors explained that in order to numerically maintain the interface temperature within T_{sat}±1K, β should be equal to $100s^{-1}$. This value was adopted in our simulations. A posteriori, this value is found to lead to a good agreement with the results from pore network model as discussed in section VI.4.3.

VI.4.2 Continuum model simulation (CMS) vs. pore network simulation (PNS)

VI.4.2.1 Liquid saturation

VI.4.2.1.1 General description of the liquid saturation field

The liquid saturation field computed from CMS and the length average liquid saturation (as defined in section IV.2.2) for geometry A and geometry B computed from PNS are shown for different heat fluxes in Figure VI.4 and Figure VI.5, respectively. The following discussion is a general description of the liquid saturation in the aim to compare CMS and PNS results. More quantitative details are discussed in next sections.

First of all, it is interesting to note that for both geometries, a two-phase zone under the casing is predicted by the continuum simulations. This is in accordance with the results found with the pore network approach. The shape of the two-phase zone obtained from PNS is sharp due to the random distribution of the pore and throat diameters. This differs from the smooth iso-saturations obtained from CMS.

For geometry A, the thickness of the two-phase zone computed from PNS is relatively narrow, while it occupies all the wick thickness in the CMS. However, the growth of the two-phase zone is almost similar whatever the model. Firstly, vapour invades the wick and the liquid saturation at the wick/groove interface stays relatively high (Figure VI.4a1 to a3 and Figure VI.4b1 to b3). In a second time, the liquid saturation at the wick/groove interface decreases (Figure VI.4a4 to a6 and Figure VI.4b4 to b6) and the shape of the two-phase zone over the wick thickness stays almost the same.

For geometry B, the two-phase zone predicted from PNS is mainly located in the upper part of the wick (Figure VI.5b). This is also observed from CMS in Figure VI.5a. The thickness of the two-phase zone is also in better agreement between PNS and CMS. Indeed, in contrast with the results for geometry A, the two-phase zone is less spread. However, the growth of the two phase zone is almost similar to geometry A. The wick is preferentially firstly invaded, i.e. the liquid saturation decreases in the capillary structure (Figure VI.5a1 to a3 and Figure VI.5b1 to b3). Then the liquid saturation at the wick/groove interface decreases (Figure VI.5a4 to a6 and Figure VI.5b4 to b6).

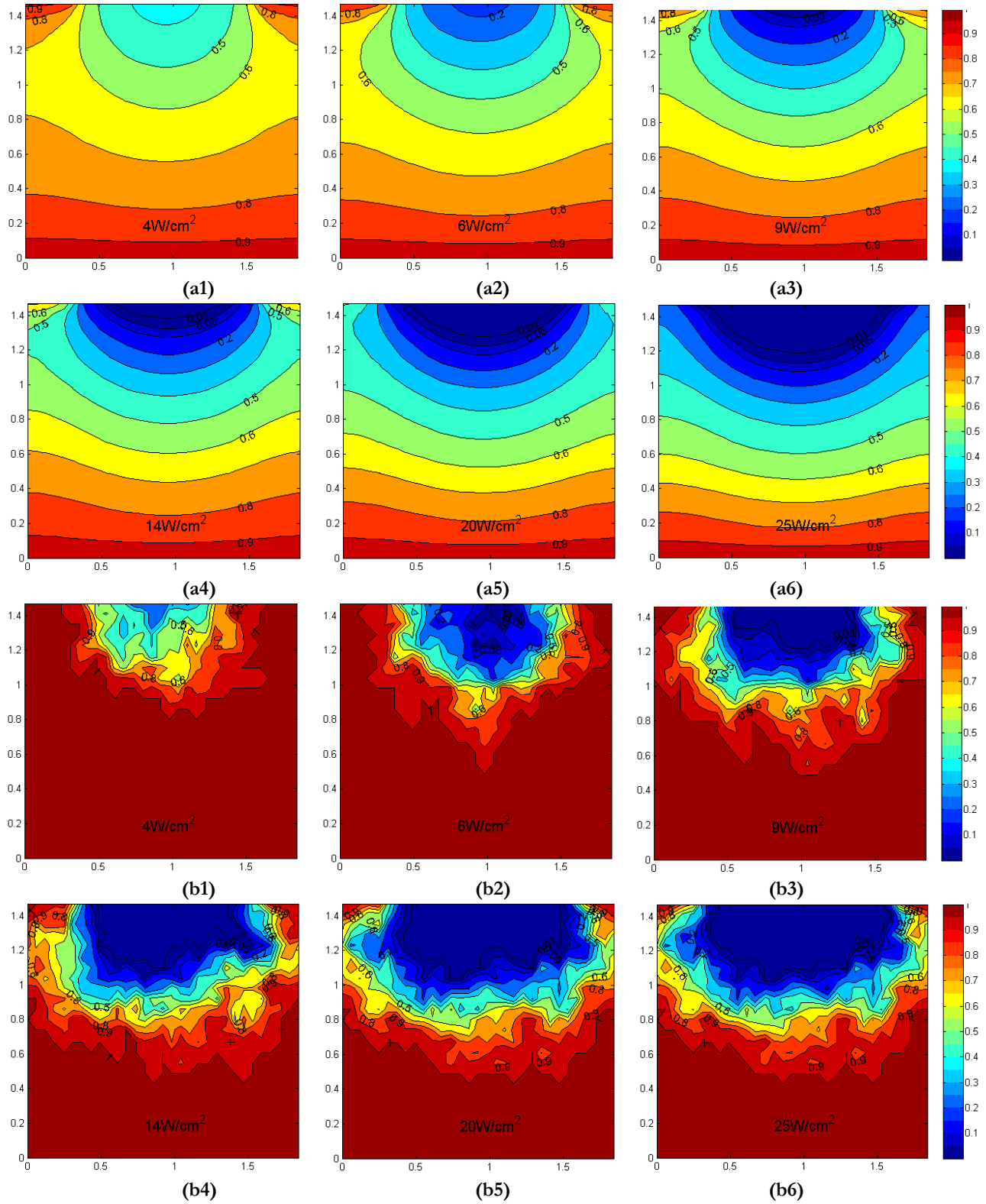

Figure VI.4 – (a) Liquid saturation field computed from continuum model simulations. (b) Length average liquid saturation computed from pore network simulations. Simulations are performed for geometry A, i.e. grooves are located at the inner surface of the casing. From (a1), and (b1), to (a6), and (b6), respectively, fluxes are equal to 4W/cm², 6W/cm², 9W/cm², 14W/cm², 20W/cm² and 25W/cm². Red colour corresponds to $S_l = 1$, i.e. liquid saturated zone and blue colour corresponds to $S_l = 0$, i.e. vapour saturated zone.

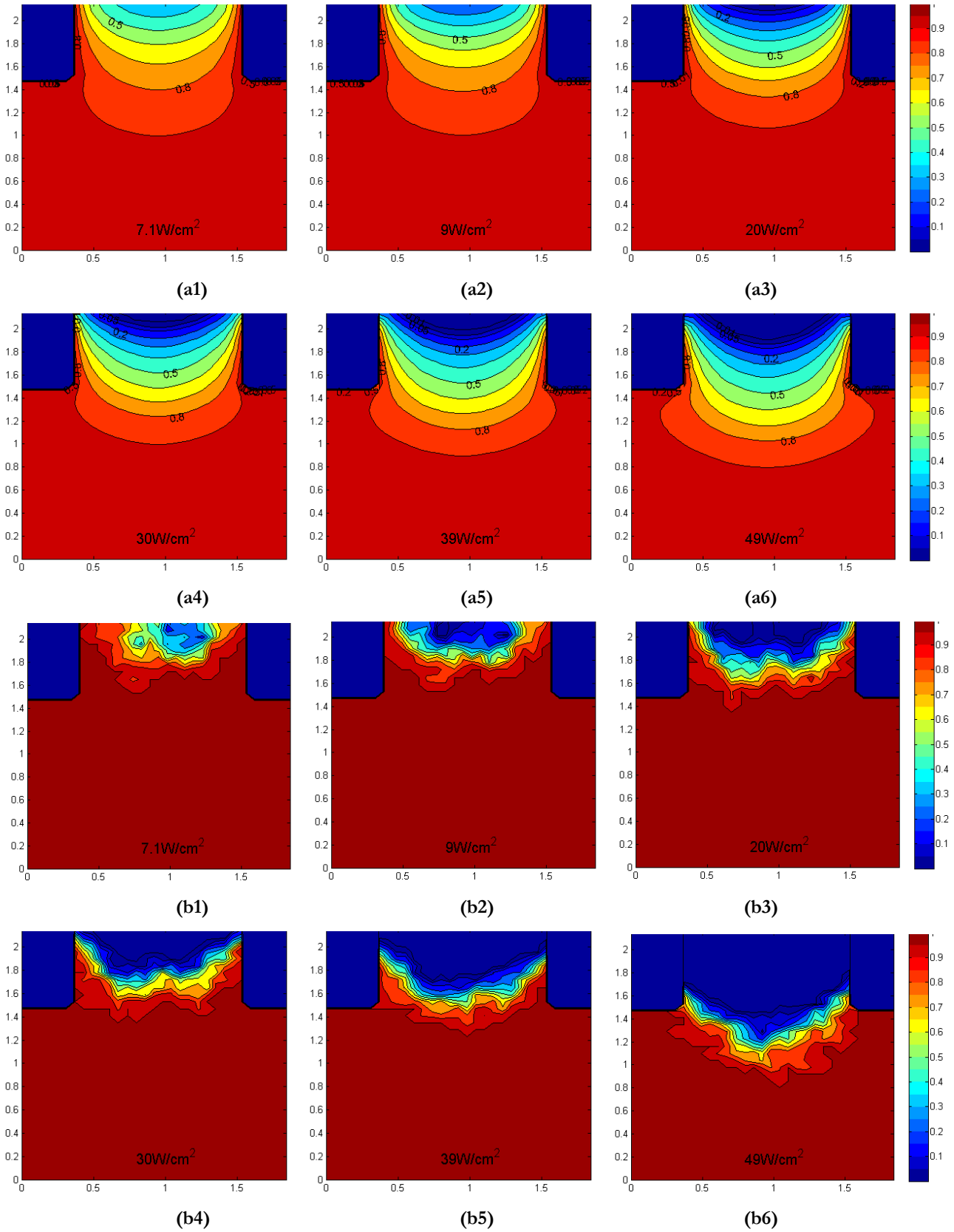

Figure VI.5 – (a) Liquid saturation field computed from continuum model simulations. (b) Length average liquid saturation computed from pore network simulations. Simulations are performed for geometry B, i.e. grooves are located at the outer surface of the wick. From (a1), and (b1), to (a9), and (b9), respectively, fluxes are equal to 7.1W/cm², 9W/cm², 20W/cm², 30W/cm², 39W/cm² and 49W/cm². Red colour corresponds to $S_l = 1$, i.e. liquid saturated zone and blue colour corresponds to $S_l = 0$, i.e. vapour saturated zone.

VI.4.2.1.2 Nucleation flux

For geometry A, PNS results predict vapour occurrence in the wick for heat flux higher than 40W/cm²; while, the liquid saturation begins to decrease from 1.1W/cm² with the CMS. Likewise, the nucleation flux determined form PNS for geometry B is equal to 7.1W/cm², while results from CMS shows that the liquid saturation begins to decrease from 2.6W/cm². The liquid saturation field for geometry A between 1.1W/cm² and 4W/cm² and for geometry B between 2.6W/cm² and 7.1W/cm² are shown in Figure VI.6 and Figure VI.7, respectively. Even though the liquid saturation begins to decrease before the nucleation flux predicted from PNS, the liquid saturation field stays relatively high. Indeed, S_l is always higher than 0.5.

The difference between the nucleation fluxes from which vapour begins to occur in the wick is directly due to the formulation of each model. Indeed, a nucleation superheat value ΔT_{sup} is used in the pore network approach. This value is taken equal to 3K and this choice is arbitrary. In the continuum model, the liquid saturation is explicitly calculated from equation (VI-15). Indeed, it was found that for ΔT_{sup} equal to 1K in PNS, the nucleation flux is equal to 1.35W/cm², which is in accordance with value found from CMS. This is in agreement with the explanation of Yang et al. (2008) [119]: the phase-change model adopted in the continuum model permits to keep the interface temperature at T_{sat}±1K. It was also found that the change in β does not impact the flux from which the liquid saturation begins to decrease. Moreover, even if results are not shown here, PNS with $\Delta T_{sup} = 1K$ shows that vapour invasion occurs mainly due to the presence of boiling points between 1.35W/cm² and 4W/cm² without growth of the two-phase region except in the first row of pores right under the casing.

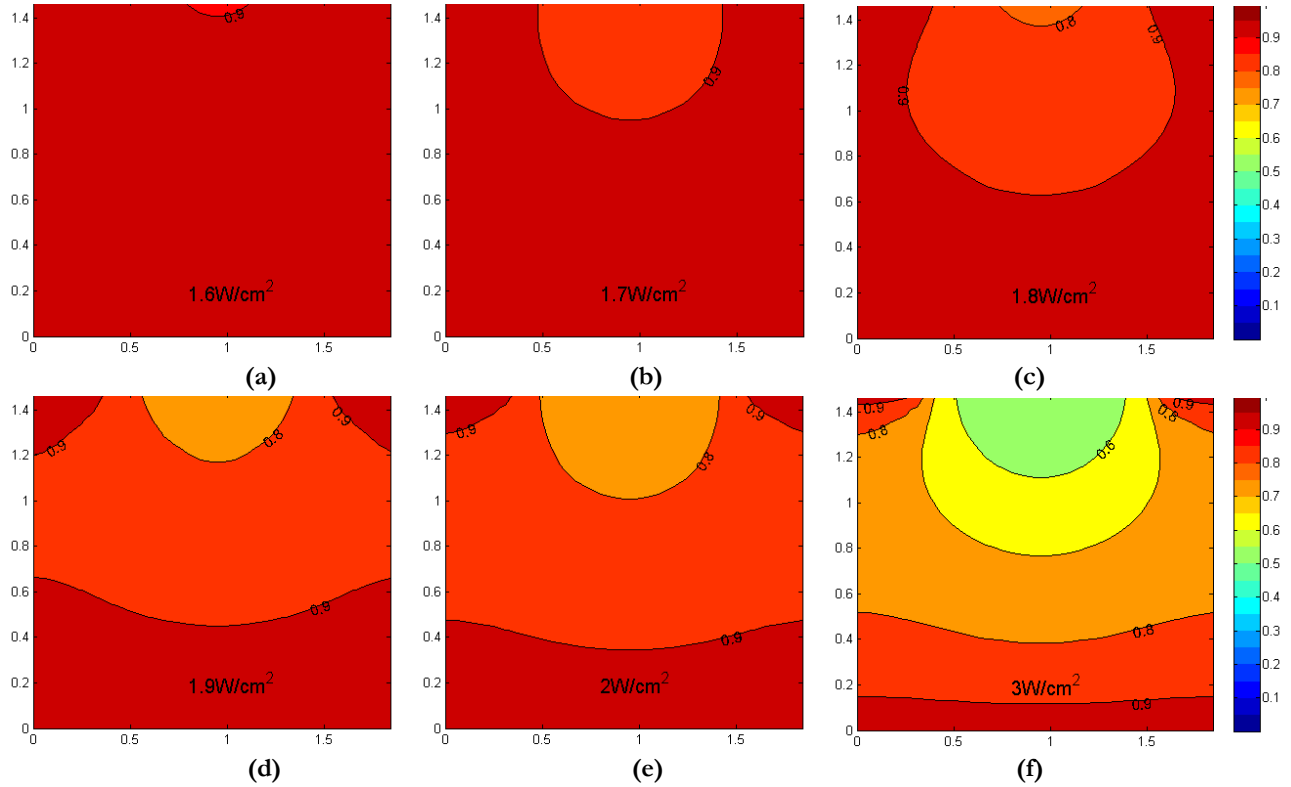

Figure VI.6 – Liquid saturation field computed from continuum model for geometry A for fluxes lower than the nucleation fluxes predicted by pore network simulations.

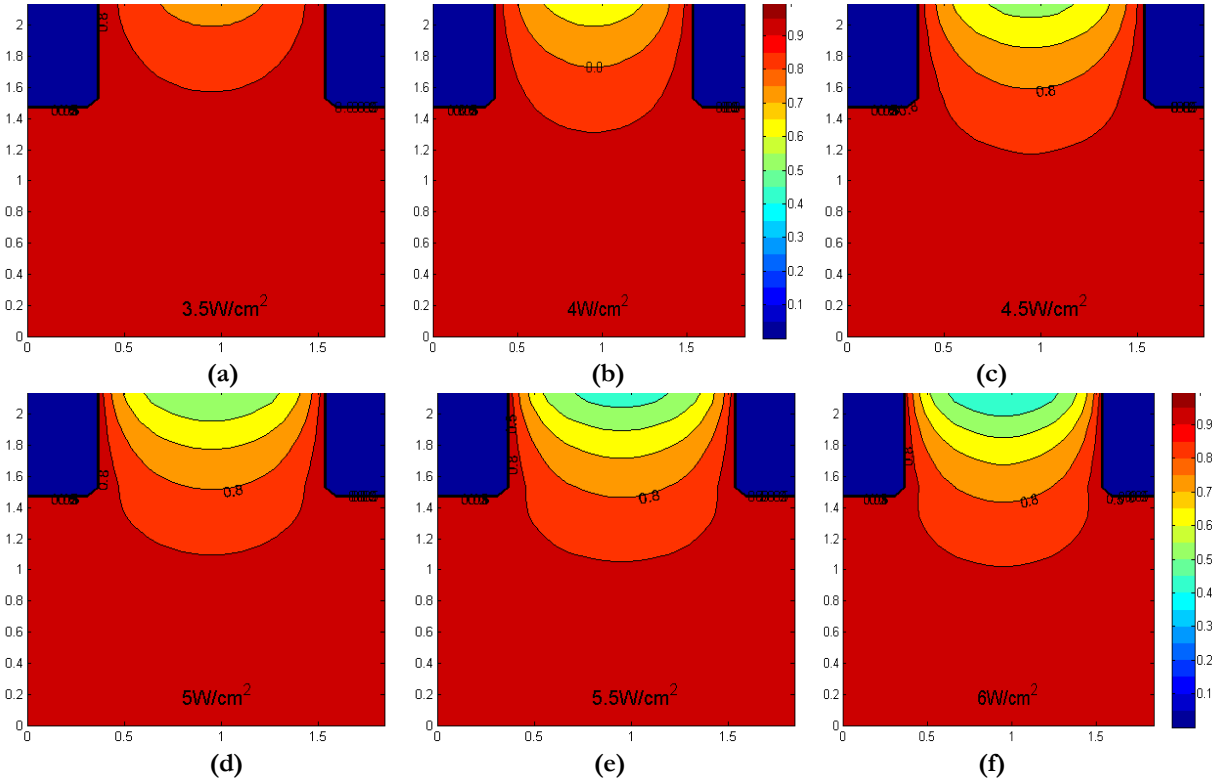

Figure VI.7 – Liquid saturation field computed from continuum model for geometry B for fluxes lower than the nucleation fluxes predicted by pore network simulations.

VI.4.2.1.3 Liquid saturation under the casing and at the wick groove interface and depth of the vapour region

Figure VI.8 shows the variation of the average and the minimum liquid saturation under the casing computed from CMS and the average liquid saturation under the casing obtained from PNS for geometry A and geometry B. The average liquid saturation under the casing, obtained from PNS, is the ratio of the volume of void occupied by the liquid to the total volume of void space considering the first row of pores right under the casing.

The variation of the average liquid saturation under the casing as a function of the heat load computed from PNS and CMS are in good agreement as shown in Figure VI.8. For geometry A, for low to moderate heat fluxes, i.e. until 9.6W/cm², the average liquid saturation under the casing decreases rapidly for reaching 0.1. For high heat fluxes, i.e. between 9.6W/cm² and 24.9W/cm², the average liquid saturation decreases slowly. A little amount of liquid persists under the casing. Finally, a totally dry region is then observed from 24.9W/cm² from CMS and 26W/cm² from PNS. For geometry B, the variation of the average liquid saturation under the casing from CMS differs a little bit more from PNS. Indeed, from CMS the decrease in S_{lc} is less abrupt than from PNS. Average liquid saturation is lower than 0.1 for heat fluxes beyond 29.6W/cm² and 22.5W/cm² according to CMS and PNS, respectively. In the same manner, a dry zone under the casing is expected to occur at 50W/cm² and 34.7W/cm² according to CMS and PNS, respectively. However, the general trend of the decreasing of the average liquid saturation under the casing is respected.

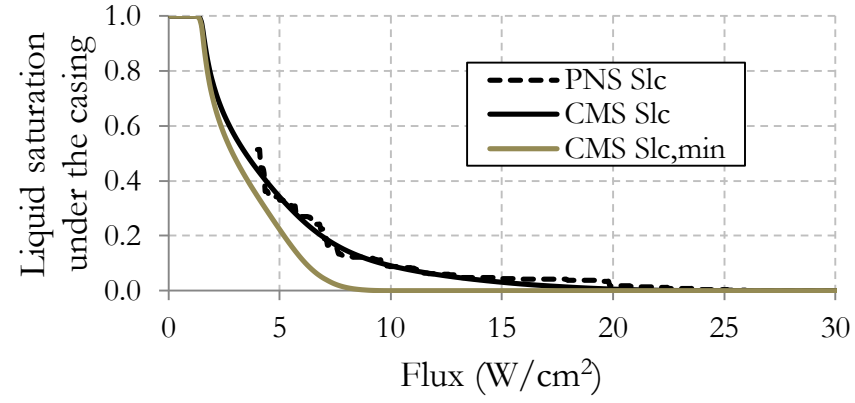

(a)

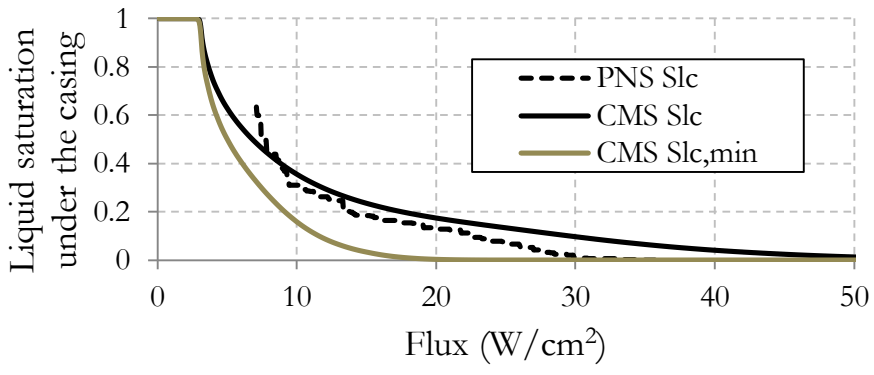

(b)

Figure VI.8 – Variation of average and minimum liquid saturation reached under the casing for (a) geometry A and (b) geometry B as a function of heat load. Solid lines are results from continuum model simulations and dashed line are results from pore network simulations.

The depth of the vapour region computed from PNS and the position of three liquid isosaturations (0.95, 0.75 and 0.5) computed from CMS are shown in Figure VI.9. For both geometries, the depth of the vapour region predicted from PNS is always between isosaturations 0.5 and 0.75. When liquid saturation is greater than 0.5, it means that the fluid is mainly under liquid state. Even if the two-phase zone is more spread in continuum model simulations, the location of the isosaturation 0.5 is in accordance with the vapour region depth computed from PNS for both geometries. From this point of view, results from CMS and PNS are thus in good agreement.

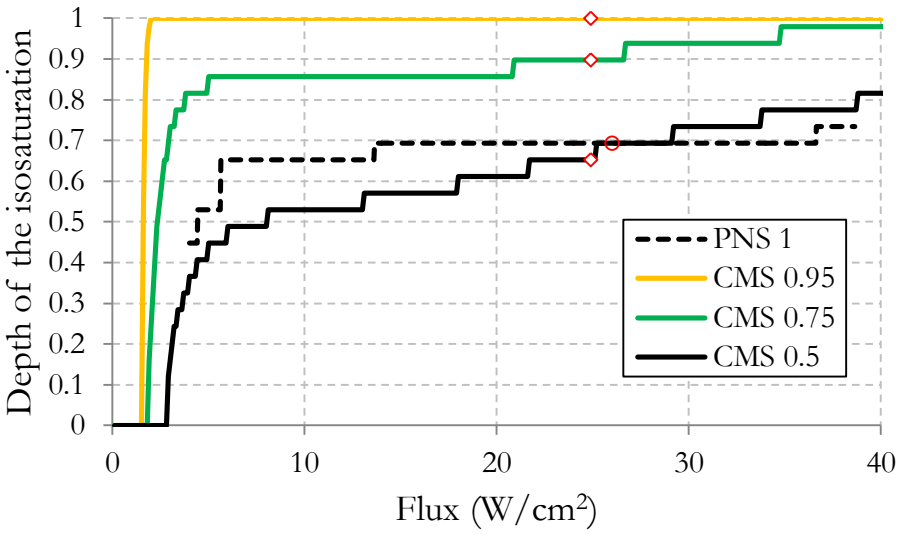

(a)

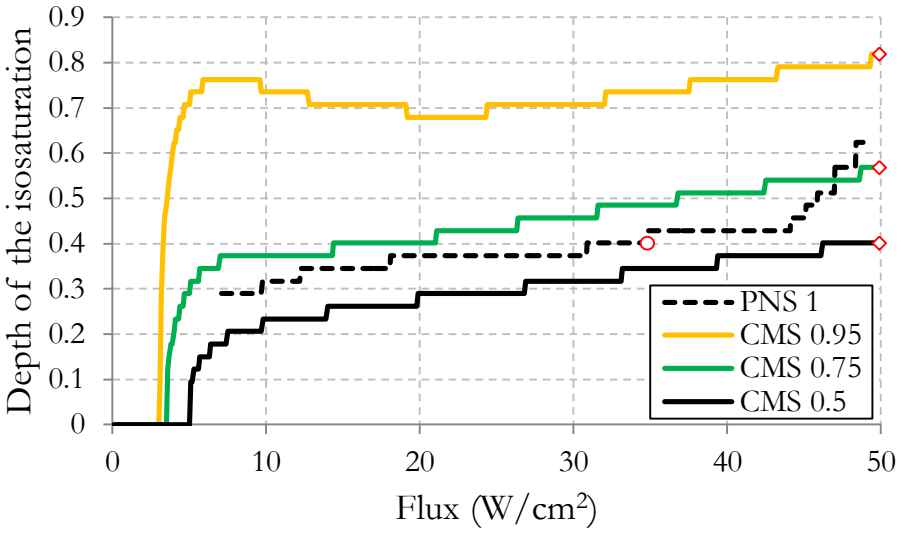

(b)

Figure VI.9 – Variation of depth of the vapour region divided by the wick thickness from pore network simulations (dashed lines) and variation of the position of three liquid isosaturations (0.95, 0.75 and 0.5) divided by the wick thickness from continuum model simulations for (a) geometry A and (b) geometry B. Red symbols indicate that a dry region exists under the casing ($S_{lc} = 0$).

Figure VI.10 shows the variation of the average and the minimum liquid saturation from CMS and the average liquid saturation obtained from PNS at the wick/groove interface for geometry A and geometry B. The average liquid saturation, obtained from PNS, is the ratio of the volume of void space occupied by liquid to the total volume of void space considering pores/throats located at the wick/groove interface. For both geometries, the decrease in the liquid saturation at the wick/groove interface is slower than the decrease in the liquid saturation under the casing (see Figure VI.8 and Figure VI.10).

For geometry A, the average liquid saturation at the wick/groove interface is underestimated from CMS compared to results from PNS. Indeed, at 9.6W/cm², S_{lg} is equal to 0.81 and 0.96 from CMS and PNS, respectively. For high heat load, i.e. at 24.9W/cm², this trend is more pronounced with S_{lg} equal to 0.77 and 0.15 for PNS and CMS, respectively. From PNS, the average liquid saturation at the wick/groove interface decreases slowly as long as a two-phase zone exists under the casing, i.e. until 26W/cm². S_{lg} at the wick/groove interface ranges between 0.99 and 0.74 when a two-phase zone exists, i.e. between 4W/cm² and 26W/cm². Between 26W/cm² and 39.25W/cm², S_{lg} ranges between 0.74 and 0.052. This phenomenon is not reproduced with the continuum model. Indeed, the decreasing of average liquid saturation at the wick/groove interface is more monotonic with the increase in the heat load.

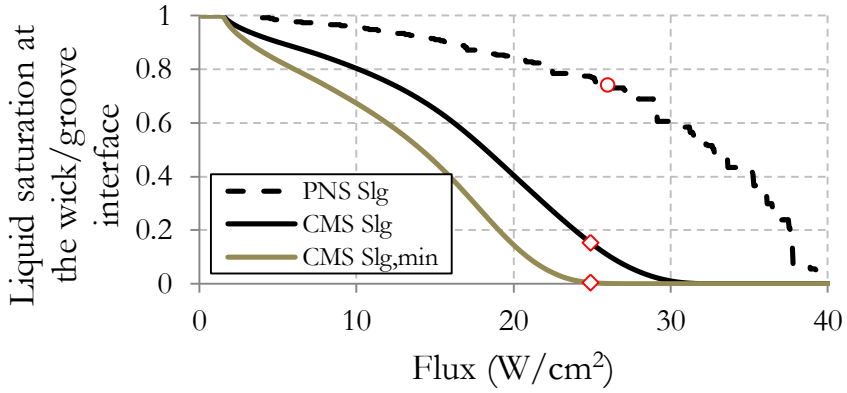

(a)

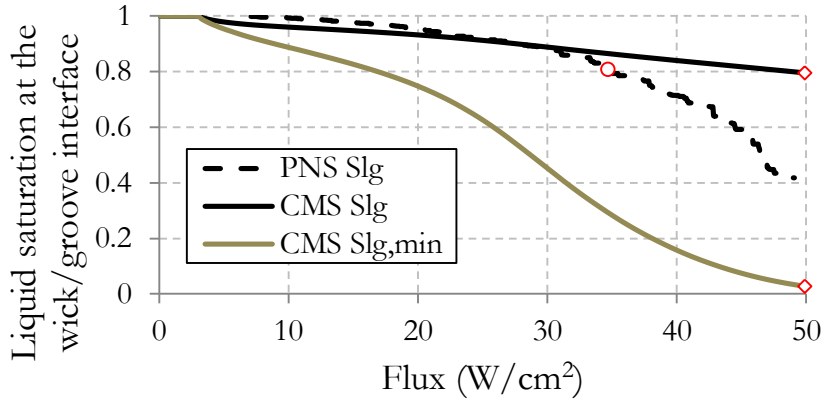

(b)

Figure VI.10 – Variation of the average and minimum liquid saturation reached at the wick/groove interface for (a) geometry A and (b) geometry B as a function of heat load. Solid lines are results from continuum model simulations and dashed line are results from pore network simulations. Red symbols indicate that a dry region exists under the casing ($S_{lc} = 0$).

For geometry B, the variation of average liquid saturation at the wick/groove interface obtained from PNS is almost the same as for geometry A. The wick/groove interface remains saturated with liquid as long as a two-phase zone exists under the casing. S_{lg} at the wick/groove interface ranges between 0.99 and 0.81 when a two-phase zone exists, i.e. between 7.1W/cm² and 34.7W/cm². Between 34.7W/cm² and 49.1W/cm², S_{lg} ranges between 0.81 and 0.41. Variation of the average liquid saturation at the wick/groove interface from CMS is relatively different than the one of geometry A. Indeed, the grooves remain relatively saturated with liquid over the whole range of heat load, i.e. S_{lg} is higher than 0.8.

VI.4.2.2 Temperature field

Temperature fields at 9W/cm² and 20W/cm² for geometry A and geometry B obtained from PNS and CMS are shown in Figure VI.11 and Figure VI.12.

A general good agreement is found between the CMS and the PNS whatever grooves location as long as a two-phase zone exists under the casing. The deviation of the maximum temperature is about 1.6K at 9W/cm² and 3K at 20W/cm² for geometry A and about 0.8K at 9W/cm² and 2K at 20W/cm² for geometry B. As already pointed out in pervious section, Figure VI.11 and Figure VI.12 show that the liquid isosaturation equal to 0.5 from CMS is almost located at the same position as the liquid-vapour interface obtained from PNS.

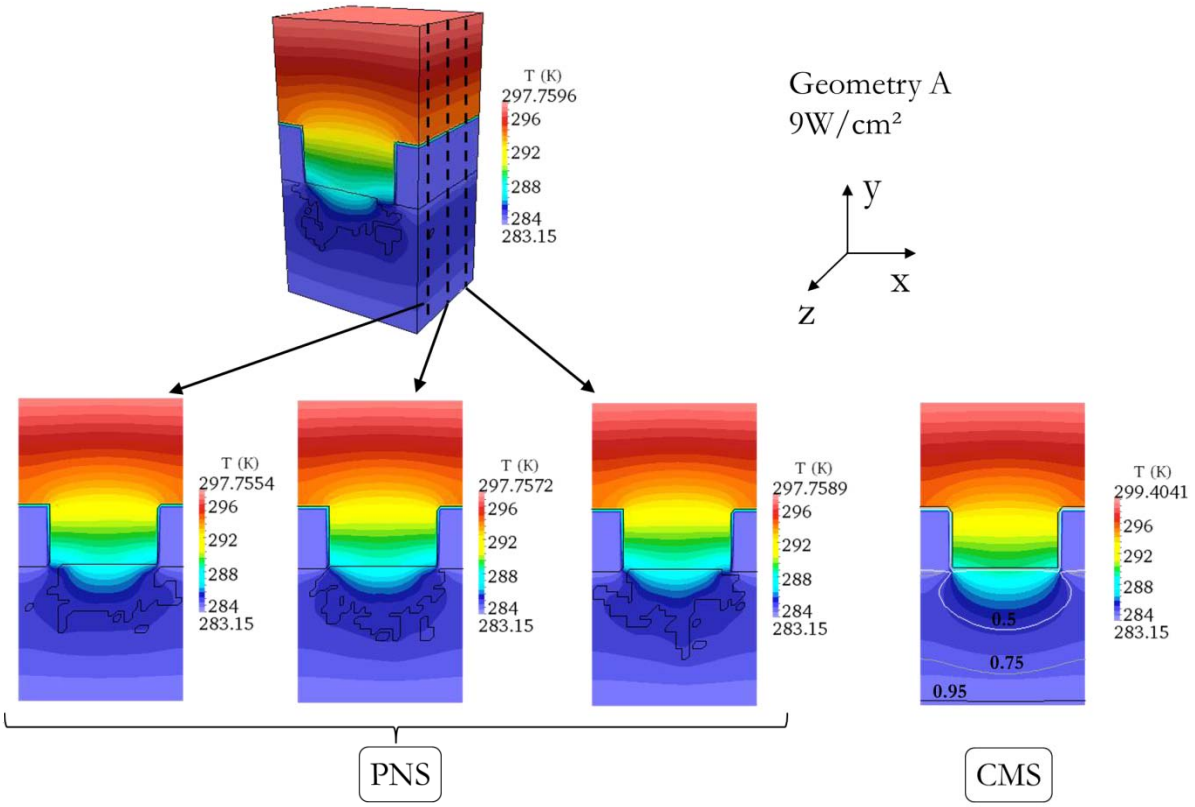

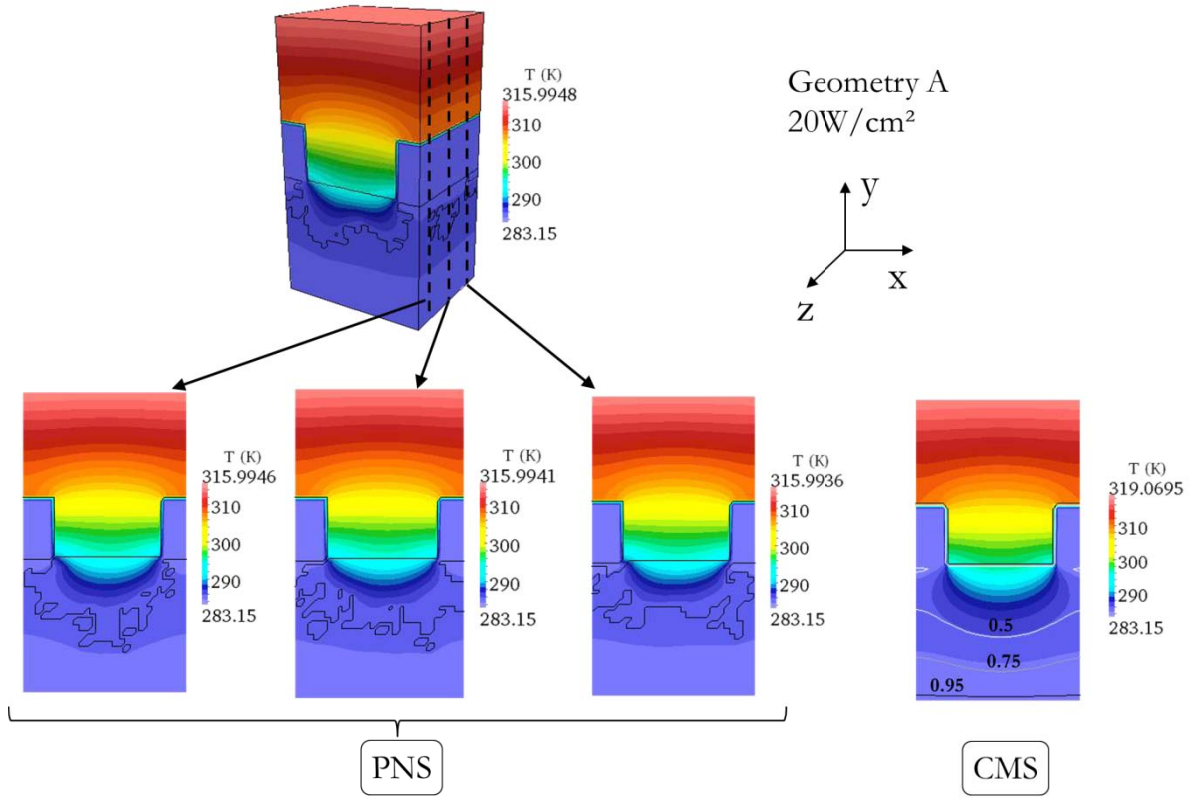

Figure VI.11 – Temperature fields for geometry A at 9W/cm² and 20W/cm² from pore network simulations and continuum model simulations. For PNS results, blacklines delimit the shape of the vapour phase within the wick. For CMS results, three liquid isosaturations are reported: 0.95 in dark, 0.75 in grey and 0.5 in white.

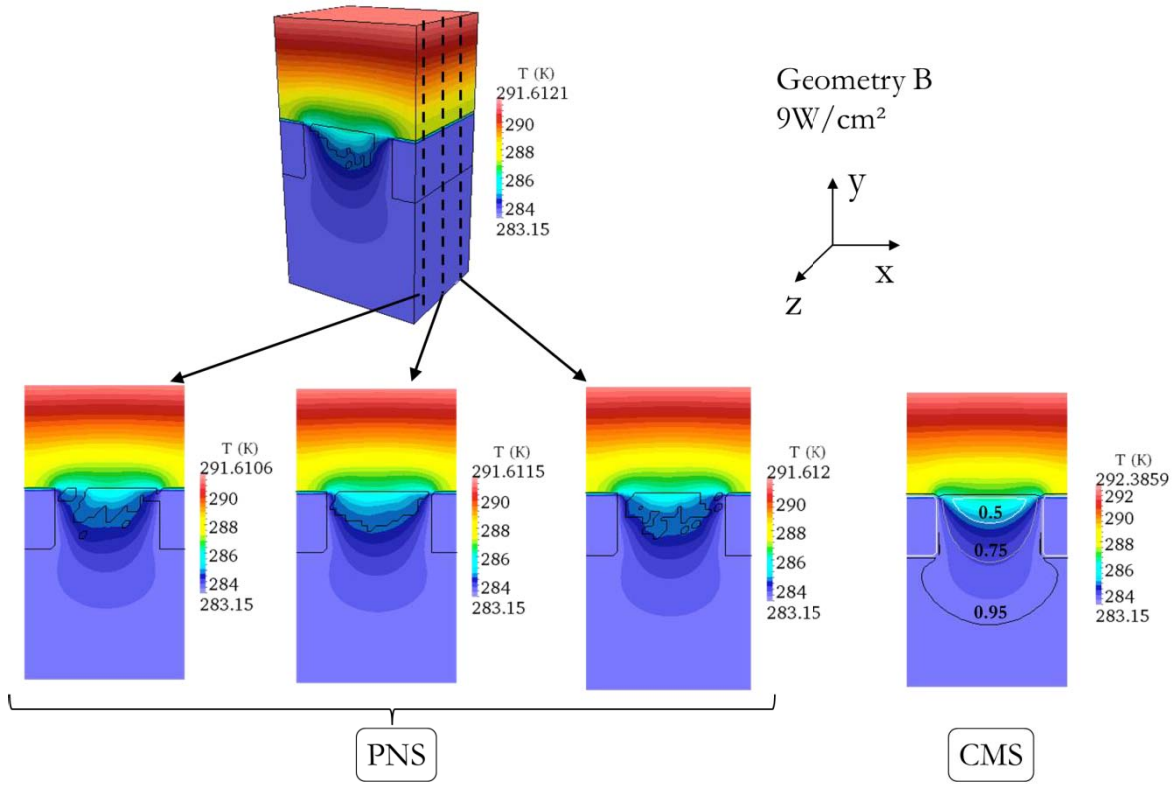

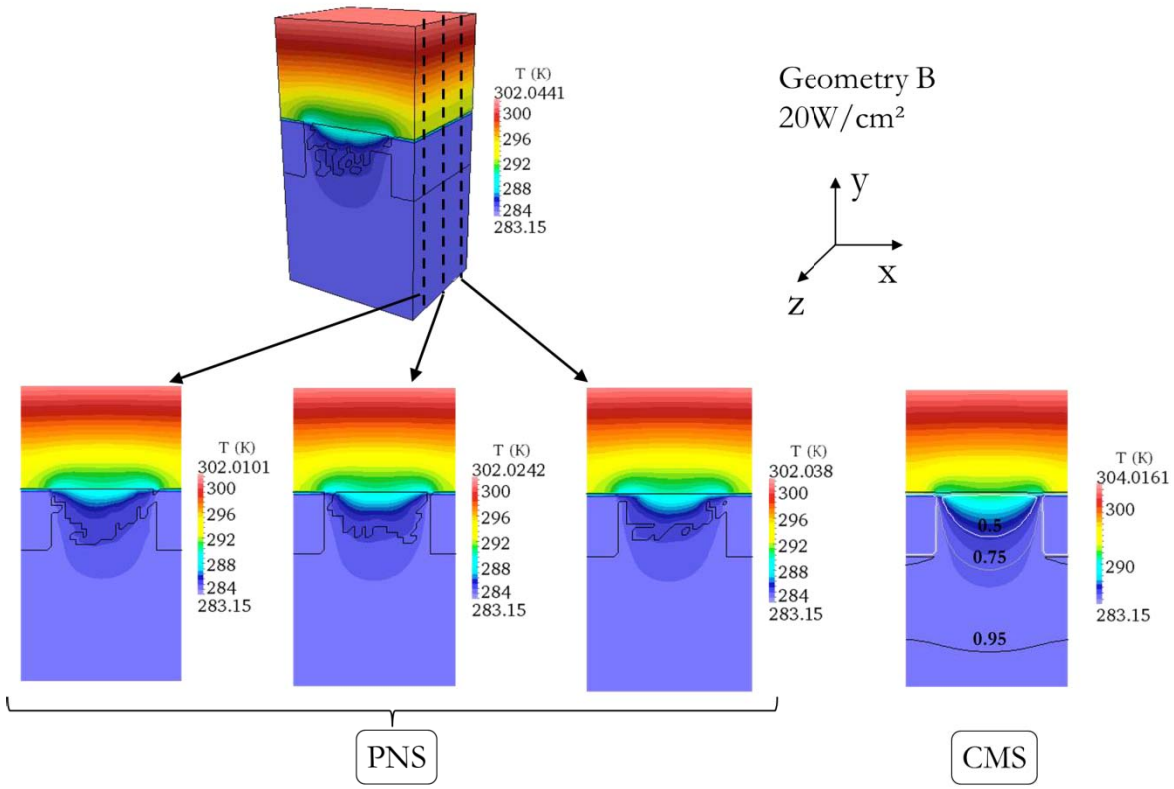

Figure VI.12 – Temperature fields for geometry B at 9W/cm² and 20W/cm² from pore network simulations and continuum model simulations. For PNS results, blacklines delimit the shape of the vapour phase within the wick. For CMS results, three liquid isosaturations are reported: 0.95 in dark, 0.75 in grey and 0.5 in white.

The variation of the evaporator wall temperature as a function of the heat load for geometry A and geometry B is shown in Figure VI.13. For geometry A, comparison of evaporator wall temperature between PNS and CMS is satisfactory with a maximal temperature deviation of 3.6K at 28.9W/cm² and a temperature standard deviation equal to 1.16K. For geometry B, results are comparable as long as a two-phase zone exists under the casing in PNS, i.e. until 34.7W/cm². From PNS, the dry region under the casing induces a fast increase in the evaporator wall temperature. From CMS, the average liquid saturation under the casing is equal to 0.07 at 37.4W/cm². Therefore, the increase in the casing temperature is not reproduced. However, results are comparable before this flux. Between 0.1W/cm² and 34.7W/cm², the maximal temperature deviation is equal to 3.37K at 34.7W/cm² and the standard deviation is equal to 0.84K.

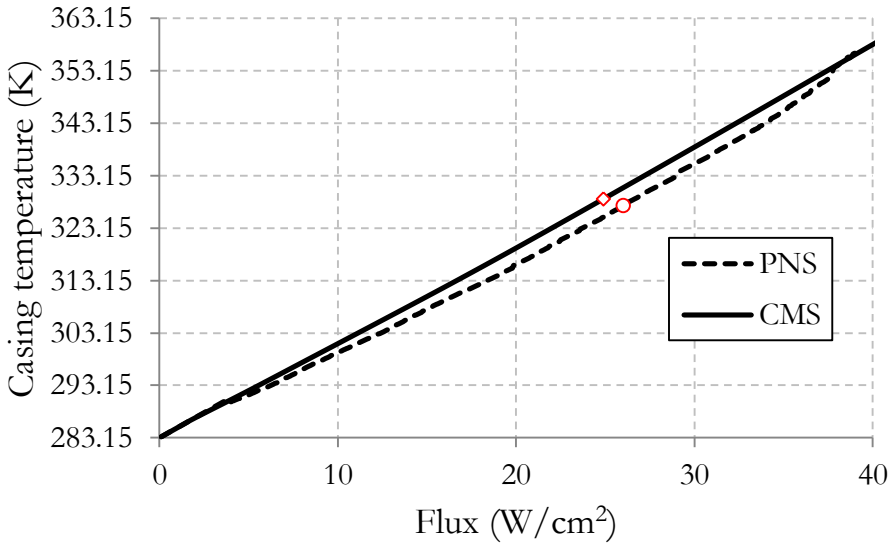

(a)

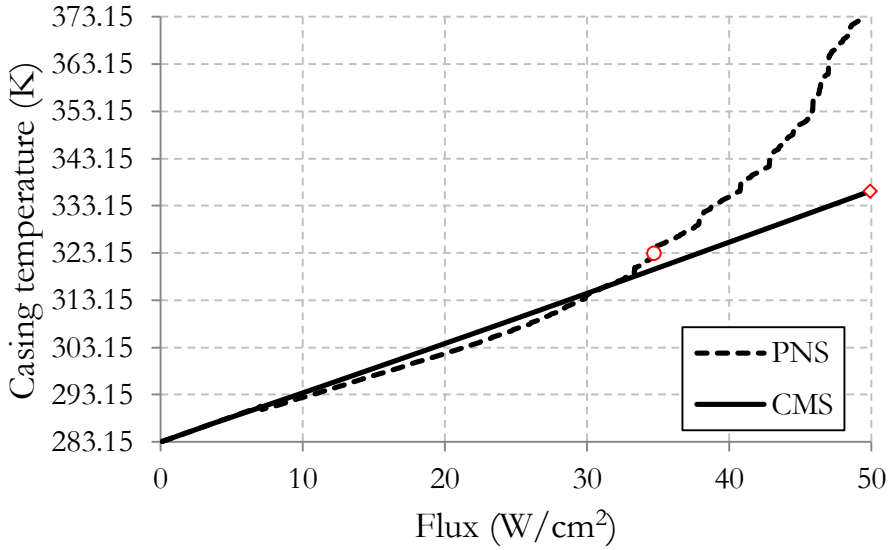

(b)

Figure VI.13 – Variation of the evaporator wall temperature as a function of the heat load for (a) geometry A and (b) geometry B. Red symbols indicate that a dry region exists under the casing ($S_{lc} = 0$).

VI.4.2.3 Evaporator thermal performance

The variation of the conductance as a function of the heat load is shown in Figure VI.14 for geometry A and geometry B. Note that the values of the conductance are not found to be the same for PNS and CMS. Indeed, a small deviation of casing or groove temperature induces a high change in the value of h_{ev}. Therefore, in the aim to compare the qualitative behaviour of the conductance more than the quantitative one, results from PNS are linked to the left axis and results from CMS are linked to the right axis. Moreover, note that for more visibility, the values of the conductance from PNS when the wick is fully saturated with liquid are not shown in Figure VI.14. PNS results are thus presented for the range of fluxes where the evaporator operates with the best thermal performance.

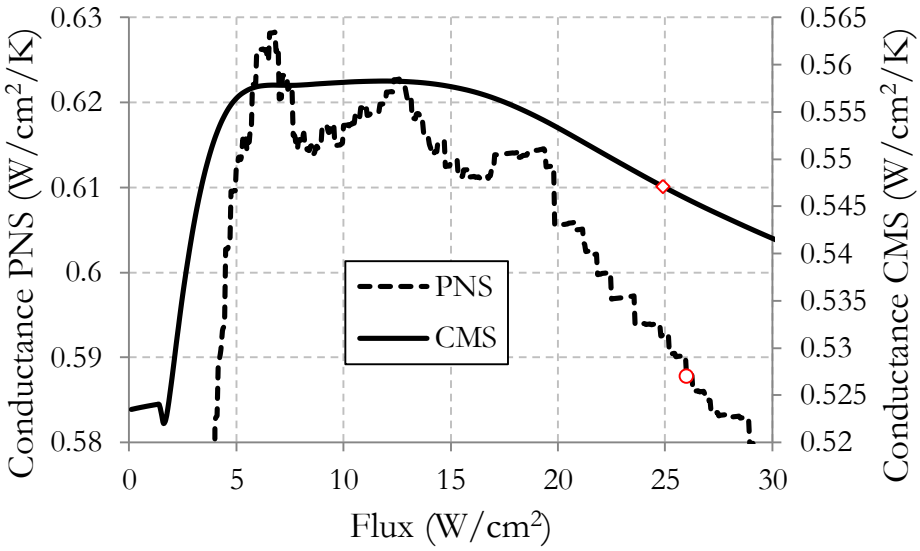

(a)

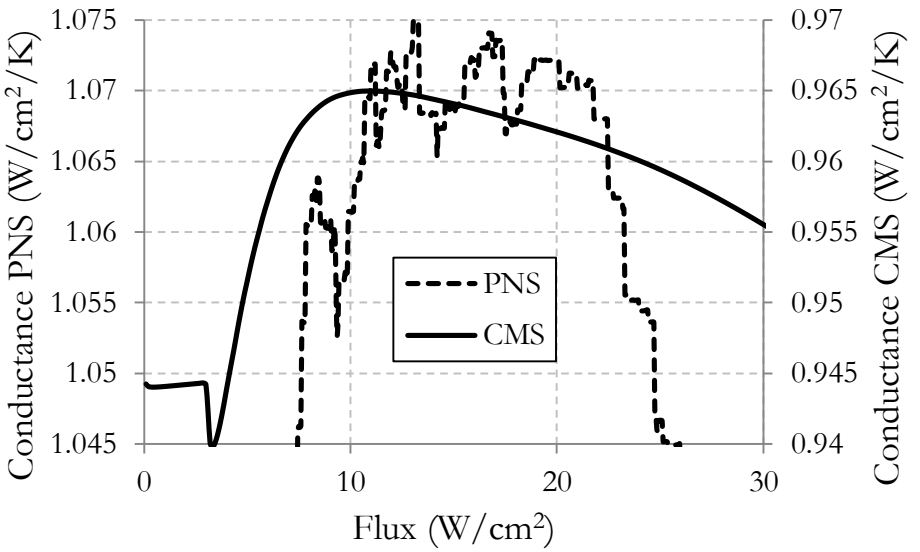

(b)

Figure VI.14 – Variation of the conductance as a function of the heat load for (a) geometry A and (b) geometry B. Left axis corresponds to the conductance calculated from PNS and right axis corresponds to the conductance calculated from CMS. Red symbols indicate that a dry region exists under the casing ($S_{lc} = 0$).

First of all, for both geometries, the three regimes observed with PNS are well reproduced with the continuum model and are discussed below.

- **Regime I:** For a fully liquid saturated wick, i.e. the evaporator operates in regime I, the conductance is constant. h_{ev} is equal to 0.52W/cm²/K between 0.1W/cm² and 1W/cm² for geometry A and equal to 0.94W/cm²/K between 0.1W/cm² and 2.6W/cm² for geometry B.
- **Regime II:** Vapour invades the wick and the evaporator operates in regime II. This regime can be divided into three parts: the value of the conductance increases rapidly, reaches a plateau, then decreases slowly. For geometry A, the evaporator reaches the best thermal performance for fluxes between 5W/cm² and 15W/cm² corresponding to an average liquid saturation under the casing between 0.35 and 0.03. For geometry B, the evaporator reaches the best thermal performance for fluxes between 7.5W/cm² and 17.5W/cm² corresponding to an average liquid saturation under the casing between 0.46 and 0.2.
- **Regime III:** For both geometries, a dry region exists under the casing and the conductance continues to decrease.

For both geometries, the range of fluxes where the evaporator operates with the best thermal performance are found to be almost the same whatever the model, i.e. pore network model or continuum model. Moreover even if the value of h_{ev} is not exactly the same from PNS and CMS, it is interesting to note that the Δh_{ev}, i.e. the increase in the conductance, predicted from the beginning of regime II is almost equivalent (same order of magnitude) for both models. Indeed, Δh_{ev} is equal to 0.046W/cm²/K from PNS and 0.036W/cm²/K from CMS for geometry A and Δh_{ev} is equal to 0.029W/cm²/K from PNS 0.025W/cm²/K from CMS for geometry B.

As can be seen, a small decrease in the conductance is observed between regime I and regime II in the CMS. Note that the PNS do not lead to this conductance behaviour since the transition between regime I and regime II is more abrupt, due to the consideration of a discrete liquid-vapour interface. A zoom on this singularity is shown for geometry A in Figure VI.15. The liquid saturation under the casing begins to decrease at 1.1W/cm² and S_{lc} is equal to 0.999845. Therefore, the wick can be considered as saturated with liquid. This explains why h_{ev} continues to be almost constant. At 1.5W/cm², the occurrence of vapour (S_{lc}=0.972) induces an increase in the thermal resistance within the wick whereas the two-phase zone is not sufficiently developed to ensure a good heat exchange. In consequence, the conductance decreases. Finally, beyond 1.6W/cm², the two-phase zone is slightly more developed promoting the heat exchange within the wick. Therefore, the conductance rises and the classical behaviour of regime II is observed.

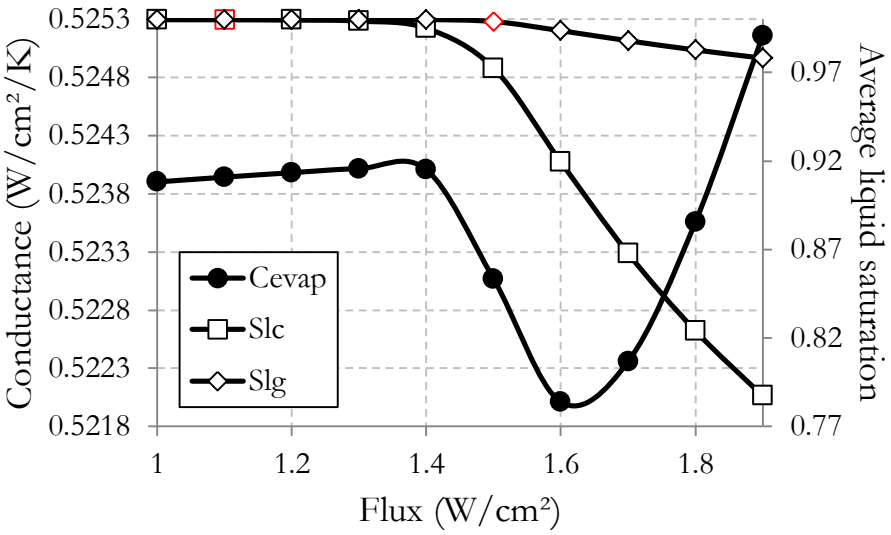

Figure VI.15 – Zoom on the variation of the CMS conductance, the average liquid saturation under the casing and the average liquid saturation at the wick/groove interface as a function of heat load for regime I (saturated wick) and the beginning of regime II. This figure is a zoom between 1W/cm² and 1.9W/cm² of results for geometry A shown in Figure VI.14a. Red symbols indicate the beginning of the decreasing of the average liquid saturation.

VI.4.3 Influence of β

The only parameter which can be adjusted in the continuum model is β. This parameter is used in the phase change model (equation (VI-7)). In accordance with Yang et al. (2008) [119], the value of $100s^{-1}$ was adopted in the simulations presented in the previous sections. However, it is interesting to discuss the influence of this parameter on results and more precisely on the liquid saturation and the evaporator wall temperature. Therefore, the average liquid saturation under the casing, the liquid saturation field and the evaporator wall temperature for various β are shown in Figure VI.16, Figure VI.17 and Figure VI.18, respectively. Note that a too high value of β induces numerical oscillations. Indeed, for $\beta = 1000s^{-1}$, calculations crash even for very low heat load.

From Figure VI.16 and Figure VI.17, it appears that the choice of β has a great impact on the liquid saturation field. The change is even more pronounced that β decreases. Indeed, at 10W/cm² for example, the average liquid saturation under the casing is equal to 0.71, 0.45, 0.18, 0.09 and 0.04 for $\beta = 1s^{-1}$, $\beta = 10s^{-1}$, $\beta = 50s^{-1}$, $\beta = 100s^{-1}$ and $\beta = 500s^{-1}$, respectively. Moreover, the whole wick can be considered as saturated with $\beta = 1s^{-1}$ at 10W/cm², while the two-phase zone is widely developed for β greater than $50s^{-1}$. This can be easily explained by the fact that the phase change model is directly proportional to the choice of β. If β is increased, the amount of liquid which becomes vapour necessarily increases and thus induces a wider two-phase zone within the wick.

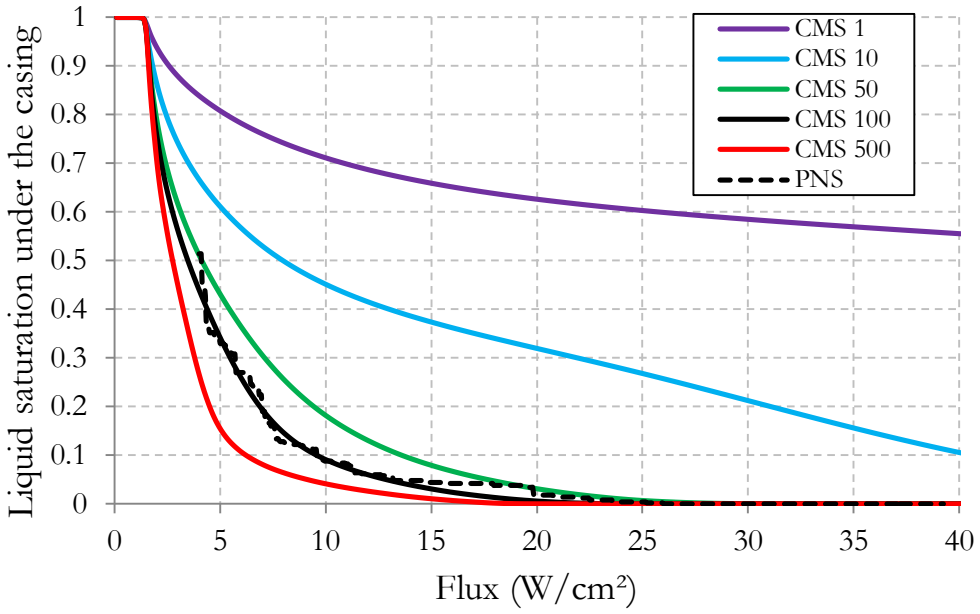

Figure VI.16 – Variation of the average liquid saturation under the casing for β equal to 1, 10, 50, 100 and 500 for geometry A.

Variations of the casing temperature and the conductance for the different β values are shown in Figure VI.18 and Figure VI.19, respectively. The general slope of the evaporator wall temperature is not significantly impacted by the choice of β. A zoom on 15W/cm² shows that the maximum temperature is equal to 311.77K and 309.63K for $\beta = 1s^{-1}$ and $\beta = 500s^{-1}$, respectively. Nevertheless, this difference of about 2K has a great impact on the conductance value and behaviour as shown in Figure VI.19. As already mentioned, a small change in casing and/or groove temperature induces a high change in conductance value. Moreover, the three regime are not well reproduced if β is too small, see $\beta = 1s^{-1}$ and $\beta = 10s^{-1}$ in Figure VI.19. Finally, β plays a role in the rise in the conductance at the beginning of regime II. ΔC_{evap} is equal to 0.031W/cm²/K, 0.036W/cm²/K and 0.053W/cm²/K for $\beta = 50s^{-1}$, $\beta = 100s^{-1}$ and $\beta = 200s^{-1}$, respectively. The increase in β induces an increase in the best thermal performance value theoretically reached by the evaporator.

From this point of view, the choice of β is crucial. Yang et al. (2008) [119] suggested to use $100s^{-1}$ to fit their experimental results. Interestingly, it appears that this value is also the best to fit our pore network simulation results.

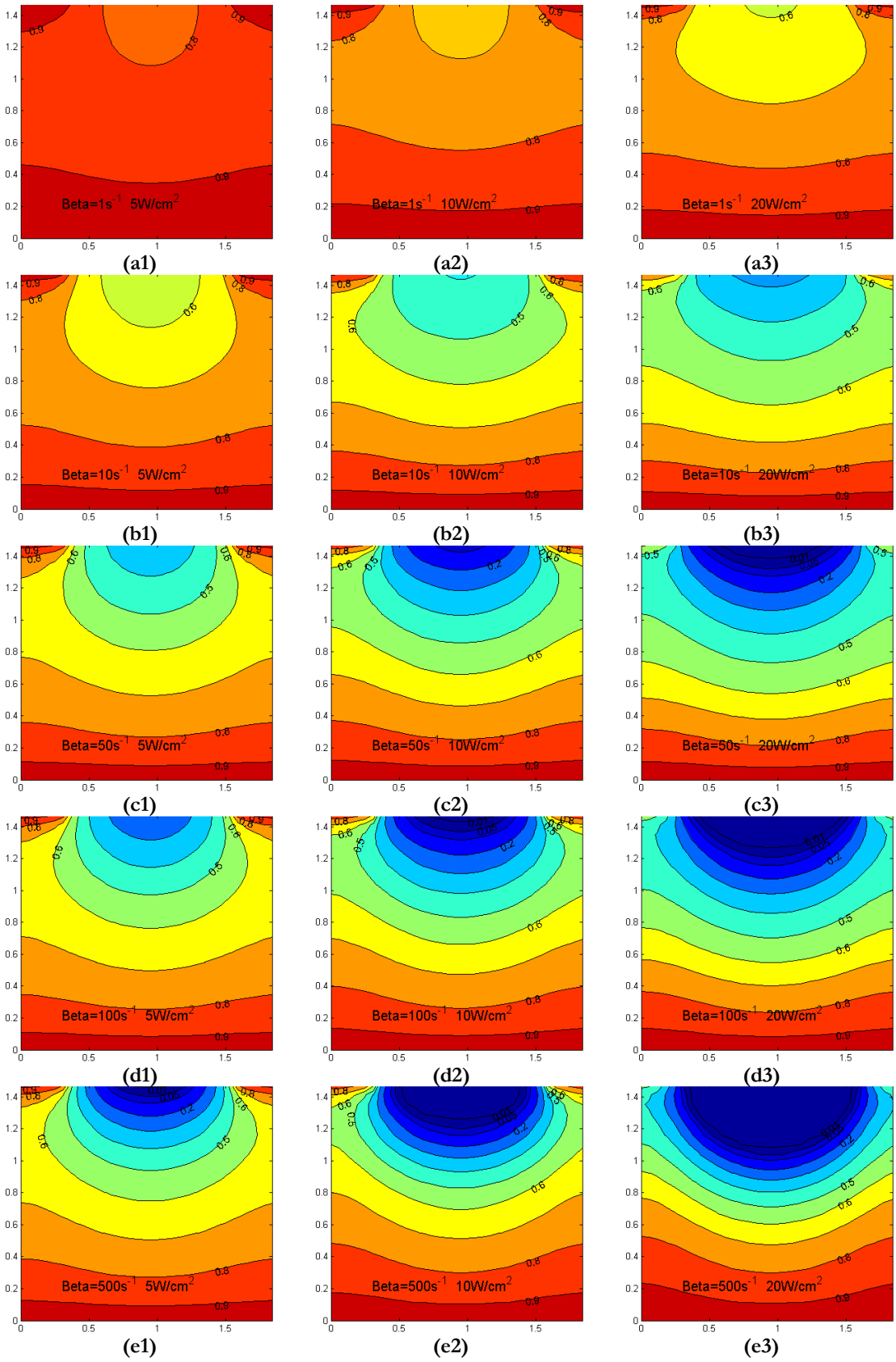

Figure VI.17 – Liquid saturation fields for geometry A with (a) $\beta = 1$, (b) $\beta = 10$, (c) $\beta = 50$, (d) $\beta = 100$ and (e) $\beta = 500$ for fluxes equal to 5W/cm², 10W/cm² and 20W/cm².

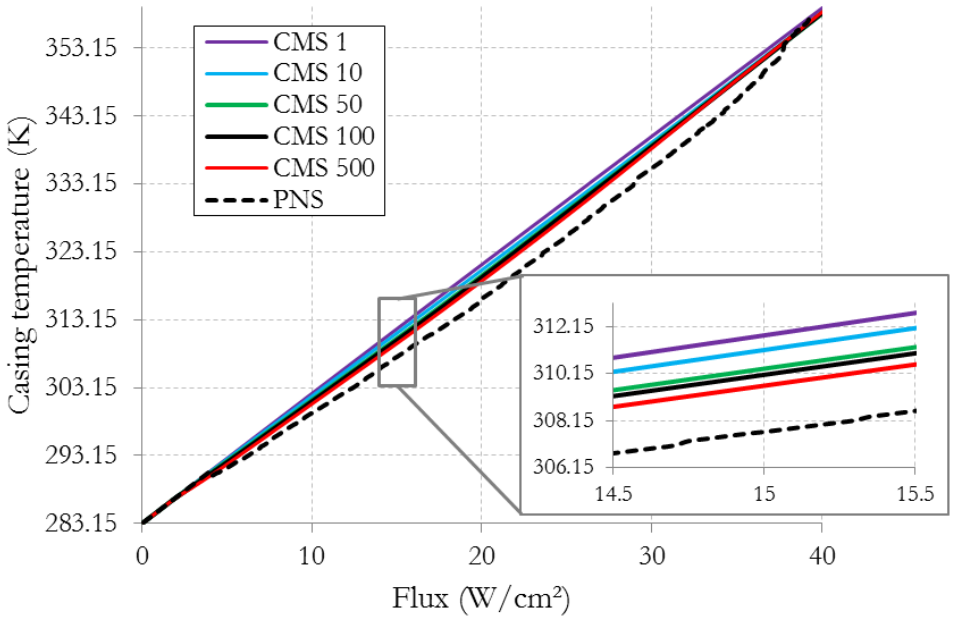

Figure VI.18 – **Variation of the evaporator wall temperature as a function of the heat load for different β values.**

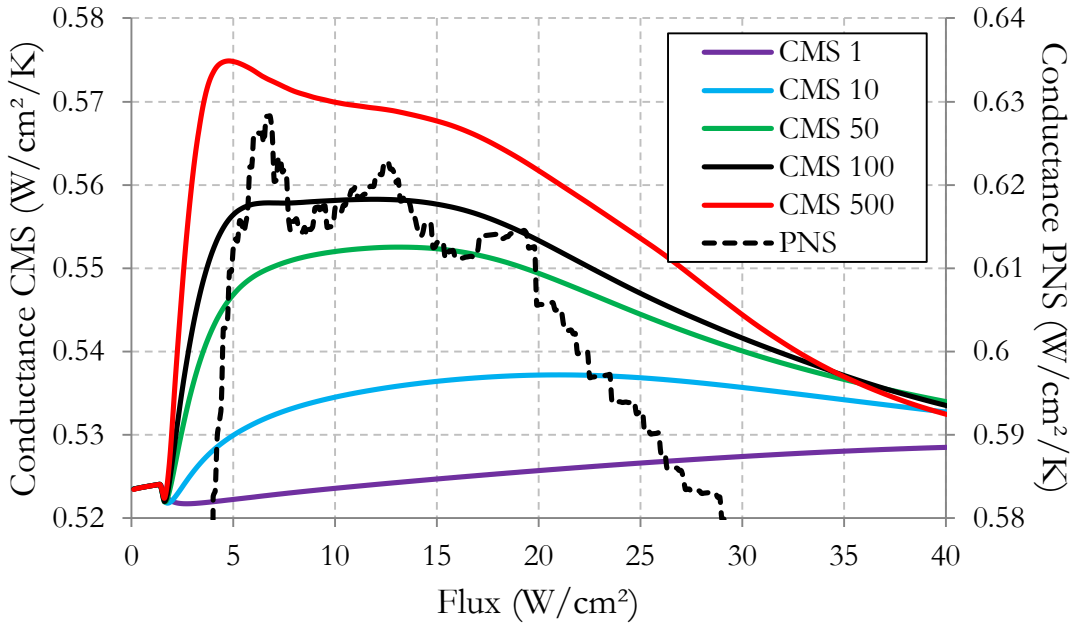

Figure VI.19 – Variation of the conductance as a function of the heat load for different β values.

VI.5 Synthesis and conclusions of the chapter

A continuum model based on macroscopic equation and the notion of saturation to study heat and mass transfer in a capillary unit cell was presented in this chapter in order to study the heat and mass transfer in the capillary evaporator unit cell. The model described the two-phase flow within the wick coupled with the energy equation and a phase change model. The method of solution is based on the IMPES algorithm. Comparisons between results obtained from the continuum model and the pore network model were performed in this chapter. The two common geometries were tested: when the grooves are manufactured at the inner surface of the casing (geometry A) and when the grooves are manufactured at the outer surface of the wick (geometry B). The capillary pressure curve and relative permeability curves were directly computed from pore network simulations.

It was shown that the results from PNS and CMS are comparable as long as a two-phase zone exists under the casing. Like the pore network model, the continuum model predicted the occurrence of a two-phase zone under the casing. The spreading of this zone is, however, widely larger in the CMS compared to the PNS. Nevertheless, the liquid isosaturation 0.5 matches with the depth of the vapour region determined from PNS. The results obtained from PNS and CMS for the overheating of the evaporator wall and the behaviour of the conductance are in good agreement. Moreover, the three regimes found from PNS are well reproduced with the continuum model.

Finally, the impact of the parameter β which controls the phase change was discussed. This parameter is the main key of the continuum model for reproducing the results found with the pore network model with a good agreement. The value of $100s^{-1}$, suggested and used by other authors, led to the best results in the comparison with the PNS.

As expected the computational time is significantly less with the CMS. It takes approximately 1h to construct the curve of the conductance as a function of the heat flux in regime II with the CM against 60 to 90 days with the PNM on the same machine.

Naturally, the appropriateness of the comparison performed in this chapter can be questioned since the PNS were performed on a relatively small network. In other terms, the length scale separation between the representative elementary volume size and the porous domain size was poor. Ideally, the comparison should be performed over domains containing much more pores than considered in the PNS of this chapter. Nevertheless, we believe that the comparison was instructive.

Although more work would be desirable to fully evaluate the capabilities of the continuum model, we conclude that the continuum model is a valuable tool in the prospect of studying the transient regimes and/or to study the transfers over domains greater than the evaporator unit cell considered in the present work.

Conclusions and prospects

The extensive review of Chapter I and Chapter II has highlighted that the mechanisms involved in capillary evaporator are complex and multiple. Works on the whole loop system systematically supposed a fully liquid-saturated wick as well as unidirectional transfers in the evaporator. These assumptions are not very realistic and have conducted several authors to study only the evaporator. Then, three kinds of works are found: the ones assuming a liquid-saturated wick, the ones assuming a vapour pocket within the capillary structure and the last and rare ones assuming a two-phase zone in the wick. In front of these different assumptions, one of the challenges of this thesis was to find a consensus on this subject and then to propose some keys to improve the evaporator thermal performances.

In Chapter III, a mixed pore network was presented under steady-state operating condition to study the heat and mass transfer with phase change in a three-dimensional evaporator unit cell. In this model, temperature and pressure fields are computed using a mean field approach while the capillary is managed using a classical pore network approach.

The model was validated by a comparison with experimental data available in literature. The satisfactory agreement between the simulations and this experiment is an indicator that this mesoscale model can be used with some confidence to study thermal and fluidic mechanisms involved in a capillary evaporator. A discussion on the choice of the effective thermal conductivity correlation was conducted permitting to highlight several points. First of all, if the wick is saturated with liquid or has a low thermal conductivity (insulating wick: PTFE for example), the choice of the effective thermal conductivity correlation has a relatively low impact on the predicted evaporator wall temperature. On the other hand, for conductive wick and when vapour occurs within the capillary structure, this choice has a greater impact. Hence, based on comparisons with the experiment, it is recommended to use Alexander's model. Nevertheless, the average model is sufficient if the wick is saturated with liquid or insulating.

The analysis of three-dimensional simulations has permitted to distinguish three operating regimes as regards the liquid-vapour phase distribution within the wick when the applied heat load is varied. The first regime is characterized by a fully liquid-saturated wick for low heat load. In this regime, called regime I, the evaporator heat transfer coefficient is constant. Regime II corresponds to the occurrence of vapour within the wick. During this regime, a two-phase zone exists under the casing within the wick, i.e. liquid and vapour coexist in a same region, over a relatively large range of heat loads. It was shown that this regime is positively correlated with the best evaporator thermal performances. The last regime, i.e. regime III, begins when a dry region occurs under the casing, i.e. the first layer of pores under the casing is in vapour state. This regime leads to a significant degradation of performances. Therefore, the three-dimensional simulations suggest that the evaporator should be designed so as to favour the occurrence of regime II, i.e. a two-phase zone under the casing, over a large range of heat loads.

The mixed pore network was then exploited to test the impact of the grooves location in Chapter IV. Three different geometries were studied: grooves manufactured at the external surface of the wick (geometry A), grooves manufactured at the inner surface of the casing (geometry B) and grooves manufactured within the wick (geometry C). It was shown that geometry A is the worst design in terms

of thermal performances and fluxes loss. Moreover, geometry A induces a liquid-vapour phase distribution which is close to the vapour breakthrough at the wick inlet, while geometries B and C prevent this undesirable situation. Geometry C is a promising groove configuration regarding evaporator thermal performances. Indeed, the evaporator heat transfer coefficient reaches the highest value in this configuration but for a relatively narrow range of fluxes due to a premature transition between regime II and regime III. Finally, geometry B is the most favourable design in terms of heat flux range where the evaporator operates in regime II, i.e. with the best evaporator heat transfer value.

In the second part of Chapter IV, a parametric study was performed with three different casing materials, three different wick materials, two different porosities and four different throat size distributions. The increase in the wick thermal conductivity and/or the decrease in the porosity induce a decrease in the evaporator wall temperature but an increase in the flux lost by conduction towards the wick inlet. A conductive casing material permits to considerably reduce the overheating of the casing if the wick is conductive, while this effect is almost inexistent if the wick is insulating. Finally, results have shown that it exists an optimum value of the throat size leading to both the best conductance and the largest range of heat flux where the evaporator operates in regime II. Therefore, a trade-off needs to be found between all these parameters to have the best evaporator thermal performances, the lowest evaporator wall temperature and the lowest parasitic flux.

Chapter V was dedicated to the study of the influence of a bidispersed wick on evaporator thermal performances, casing overheating and liquid-vapour phase distribution. Bidispersed wicks are porous media characterized by two throat size distributions. Results obtained with the mixed pore network model were firstly confronted to experimental results available in literature. A general good agreement was found for both monoporous and bidispersed wick structures. Therefore, the mixed pore network model presented in this thesis is also suitable to study bimodal wick structures. Large throats create preferential paths for the vapour and permit to keep a two-phase zone under the casing over a large range of fluxes. Consequently, the evaporator wall temperature is considerably reduced and the evaporator heat transfer coefficient is significantly increased.

Then, the impact of groove location was studied for a monoporous and a bidispersed wick. Conclusions are the same as in Chapter IV: when the grooves are manufactured at the inner surface of the wick (geometry B) the evaporator thermal performances are better than for the grooves manufactured at the outer surface of the casing (geometry A). Simulations have highlighted that the operating limit of the evaporator is the vapour breakthrough towards the wick inlet if the wick is bidispersed. Indeed, preferential paths created by large throats could induce a premature deprime of the loop. However, this phenomenon occurs for very high heat load in our simulations. On the other hand, if the wick is monoporous, the operating limit of the evaporator is the overheating of the casing when a dry region under the casing exists, i.e. when the evaporator operates in regime III.

In Chapter VI, a second model based on a continuum approach was presented. The aim of this chapter was to propose a model which needs less computing time. Results, obtained from the continuum model and the mixed pore network model, were compared for two grooves positions (at the outer surface of the wick and at the inner surface of the casing). Capillary pressure curves and relative permeability curves were directly computed from the pore network model.

It was shown that the continuum model is able to predict the occurrence of a two-phase zone under the casing for both geometries. The average liquid saturation under the casing computed from the continuum simulations and from the pore network simulations are almost equivalent. However, it was found that the spreading of the two-phase zone with geometry A is larger with the continuum simulations than with the pore network simulations. It appears that the isosaturation equal to 0.5 (from continuum simulations) matches with the depth of the vapour region determined in pore network simulations. Finally, in terms of liquid-vapour phase distribution and evaporator heat transfer coefficient, the three regimes observed with the pore network model are well reproduced with the continuum approach.

In a last part, the influence of parameter β which is present in the phase change model was studied. It was shown that a too high value of β induces numerical problems or the quick growth of the vapour zone in the wick. On the contrary, a too low β underestimates the value of the liquid saturation within the wick. The value of $\beta = 100s^{-1}$ was found to lead to a good agreement with the results from pore network simulations.

In conclusion, the mixed pore network model and the continuum model developed during this thesis and associate results presented in this manuscript are valuable tools to understand the complex and multiple mechanisms in capillary evaporators. These models are tools opening up the route towards the numerical optimization of the thermal performances at the evaporator scale.

Specific areas that should be considered as a priority for future works in the continuity of this thesis are suggested below.

- **Need clarification**
  - As pointed out in the literature review, some authors use the kinetic evaporation theory to determine the mass flow rate of vapour or the convective coefficient at the wick/groove interface. Note that such a coefficient was not used in models presented in this thesis. Investigation to clarify the legitimacy of using the kinetic evaporation theory in the modelling of transfers in capillary evaporators needs to be performed.
- **Improvement of the mixed pore network model**
  - A three-dimensional model for vapour flow and heat transfer in grooves will permit to improve the understanding of transfers in capillary evaporator.
  - In addition to a better groove model, an improvement of the loop model will be necessary. Indeed, in our model, the inlet temperature and pressure are supposed to be constant whatever the heat load applied at the external surface of the casing. This hypothesis is questionable since several experimental studies highlight that the vapour mass flow rate at the exit of the evaporator influences the temperature inlet.
  - The incipient liquid-vapour phase distribution within the wick is determined using percolation rules. It will be interesting to develop a three-dimensional transient model which takes into account the pressurization step of the vapour before vapour reaches the grooves. This will be very interesting especially to study in more details the behaviour of the promising geometry C presented in this thesis (grooves within the wick).

- The choice of the effective thermal conductivity correlation can have a great impact on the predicted results. Therefore, it will be interesting to have experimental measurements of the effective thermal conductivity for a sintered porous medium and use them as an input in the mixed pore network model presented in the thesis. Indeed, the prediction of the effective thermal conductivity remains an issue to be addressed.
- Finally, the parallelization of the pore network model should be considered to decrease the computation time and to obtain results on network with a larger number of pores. This step will be all the more inevitable that the network is unstructured.

- **Improvement of the continuum model**
  - The phase-change model should be reconsidered since results are highly dependent on the choice of β.
  - Finally, the continuum model should be extended to the third dimension in order to simulate the heat and mass transfer at the scale of an evaporator.
- **Exploitation of codes**
  - It will be interesting to do more simulations using the pore network model for studying the impact of the throat size. An optimal value was found but it will be good to investigate a larger range of throat size to confirm this trend.
  - A parametric study with a bidispersed wick using pore network model is suggested to investigate the impact of the large and small throat size.
  - A parametric study of the capillary strip thickness of geometry C using pore network and/or continuum model will be interesting for finding solutions permitting to keep a two-phase zone under the casing over a larger range of fluxes. The numerical development of the transient growth of the vapour will also help to study this geometry.
  - Transient results from the continuum model have not been treated in this thesis and should be done in further works.
- **Toward the consideration of realistic microstructures**
  - Improvements in the simulations of heat and mass transfers in capillary evaporator can be expected from the consideration of 3D digital images of realistic microstructures. These images can be either obtained from experimental imagery techniques such as X-ray tomography or generated numerically (so as to generate microstructures resembling sintered wick microstructures for example). Then instead of using a structured cubic network, the next step will be to construct the network directly from the 3D digital images. Several algorithms are available to perform this task. In contrast with our cubic network, this leads to the consideration of unstructured pore networks based of the skeleton of the pore space determined from the images. From this, the unstructured pore network can be used to determine the macroscopic parameters needed for the continuum model or to simulate directly the heat and mass transfer with phase change in the evaporator using algorithms similar to the ones used on the cubic network but adapted to the unstructured nature of the network.

Appendix A. Determination of properties for the monoporous pore network

In the pore network model, the capillary pressure is expressed as a function of throat size. The throat (bond) diameters correspond to the "pore" diameters given in the experimental data (using mercury porosimetry for example). The number of pores in the PNM is limited in order to perform the simulations for a reasonable computational time. This often results in a lower numerical porosity than the real one. The following method was adopted to obtain a porosity comparable with the real porosity of the considered sample. The method is based on the adjustment of the pore radius. The aim is to determine the appropriate pore size diameter d_p so as to have a good agreement between the given porosity and the calculated one. The wick geometrical dimension and the total number of pores are inputs of the model, as well as the throat radius distribution and the porosity ε. The process to determine d_p is presented here for cube/cuboid representation of pores/throats, in three dimensions. In the following equations the subscripts p and t refer to "pore" and "throat", respectively.

The porosity ε of the material is given and is used as an input parameter for the model.

$$\varepsilon = \frac{V_{void}}{V_T} \quad \textbf{(A-1)}$$

where V_{void} is the volume of void space and V_T is the total volume of the wick. The total volume corresponds to the total volume of the wick for the considered evaporator unit cell and is simply deduced from the geometrical dimension of the wick.

The void space volume can be approximated by equation (A-2).

$$V_{void} = V_p N_p + 3V_t N_t \quad \textbf{(A-2)}$$

where V_p is the volume of one pore, V_t is the volume of one throat, N_p is the total number of pores and N_t is the total number of throats in the considered geometry. Note that the pore network can be viewed as the repetition in space of the pattern represented by one pore and three throats. Therefore, for a monoporous network: $N_t = 3N_p$.

Let's now express the volume of pores and throats. Pores are cubic and their volumes can be therefore expressed using equation (A-3).

$$V_p = d_p^3 \quad \textbf{(A-3)}$$

Throats are considered as cuboid and their volumes are given by equation (A-4).

$$V_t = d_t^2 l_t \quad \textbf{(A-4)}$$

where d_t is the throat diameter and l_t the length of the throat.

The distance between two pores, i.e. nodes, is the lattice spacing, noted a and is constant in each direction. Hence, the length of the throat can be expressed as the distance between two pores minus twice the pore radius.

$$l_t = a - d_p \quad \textbf{(A-5)}$$

Combining and rearranging equations (A-1) to (A-5), a third-degree polynomial equation is obtained with the pore diameter d_p as an unknown.

$$d_p^3 - \left(d_t^2 \frac{N_t}{N_p}\right) d_p + \left(d_t^2 a \frac{N_t}{N_p} - \frac{V_T \varepsilon}{N_p}\right) = 0 \quad \textbf{(A-6)}$$

The classical Cardano's method is used to solve equation (A-6). Defining two coefficients A and B by equations (A-7) and (A-8), the discriminant Δ is calculated with equation (A-9).

$$A = -\left(d_t^2 \frac{N_t}{N_p}\right) \quad \textbf{(A-7)}$$

$$B = \left(d_t^2 a \frac{N_t}{N_p} - \frac{V_T \varepsilon}{N_p}\right) \quad \textbf{(A-8)}$$

$$\Delta = -(4A^3 + 27B^2) \quad \textbf{(A-9)}$$

Once, the discriminant is calculated, three cases have to be considered.

1st case: $\Delta < 0$

Equation (A-6) has two complex roots and one real root. The real solution is given by equation (A-10).

$$d_p = \sqrt[3]{\frac{1}{2}\left(-B + \sqrt{-\frac{\Delta}{27}}\right)} + \sqrt[3]{\frac{1}{2}\left(-B - \sqrt{-\frac{\Delta}{27}}\right)} \quad \textbf{(A-10)}$$

2nd case: $\Delta = 0$

Equation (A-6) has two real solutions given by equation (A-11) and equation (A-12).

$$d_p = \frac{3B}{A} \quad \textbf{(A-11)}$$

$$d_p = -\frac{3B}{2A} \quad \textbf{(A-12)}$$

The suitable solution is the one which satisfies the following condition: $0 < d_p < a$.

3rd case: $\Delta > 0$

Equation (A-6) has three real solutions (equation(A-13)).

$$d_p = 2\sqrt{-\frac{A}{2}}\cos\left(\frac{1}{3}arccos\left(-\frac{B}{2}\sqrt{\frac{27}{-A^3}}\right)+\frac{2k\pi}{3}\right) \quad \textbf{(A-13)}$$

with $k = 1{,}2\ ou\ 3$.

The suitable solution is the one which satisfies the following condition: $0 < d_p < a$.

At this stage, the mean pore diameter d_p is determined so as to obtain the desired porosity. However, the pore size has to be distributed randomly. Moreover, if the pore diameter is constant, this implies a constant length of throat in the network. Therefore, in order to have a random distribution of the throat's length, a standard deviation σ_{d_p} of the pore size has to be determined.

As the pore diameter cannot exceed the size of a grid's mesh, i.e. $a \times a$, the standard deviation is defined by equation (A-14) .

$$\delta_{d_p} = 0.99a - d_p \quad \textbf{(A-14)}$$

Once pore and throat sizes are randomly distributed, the numerical porosity can be computed. This leads to a porosity very close to the desired value while keeping the disordered nature of the porous structure.

Appendix B. Determination of properties for the bidispersed pore network

The known inputs of the model are:

- From experimental data (Lin et al. (2011) [109]):
  - the mean diameter of large pores $d_{Lp,\mathbb{R}}$;
  - the mean diameter of small pores $d_{Sp,\mathbb{R}}$;
  - the mean diameter of clusters $d_{c,\mathbb{R}}$;
  - and the total porosity $\varepsilon_{\mathbb{R}}$.

- From the pore network construction:
  - the volume of the wick V_T for the considered evaporator unit cell;
  - the step of the network a;
  - and the total number of computational nodes within the wick for the considered evaporator unit cell.

The unknowns that must be specified for the construction of the pore network are:

- the porosity of the large network $\varepsilon_{L,PN}$;
- the lattice spacing of the large network b;
- the mean diameter of large pores $d_{Lp,PN}$;
- and the mean diameter of small pores $d_{Sp,PN}$.

As for the monoporous PNM, the throat diameters correspond to the pore diameters of the experimental data. Note that the clusters and pores are supposed to be circular in the real sample, while they are modelled as cubic in the pore network.

B.1 Determination of large network porosity ε_L

Each cluster is assumed to be spherical with a single contact point with its neighbours and embedded in a grid fitted on the spheres as depicted in Figure B.1. At the scale of one cluster, the cluster's volume $V_{c,\mathbb{R}}$ and the volume of one grid's cell V_{cell} are:

$$V_{c,\mathbb{R}} = \frac{4}{3}\pi\left(\frac{d_{c,\mathbb{R}}}{2}\right)^3 \quad \textbf{(B-1)}$$

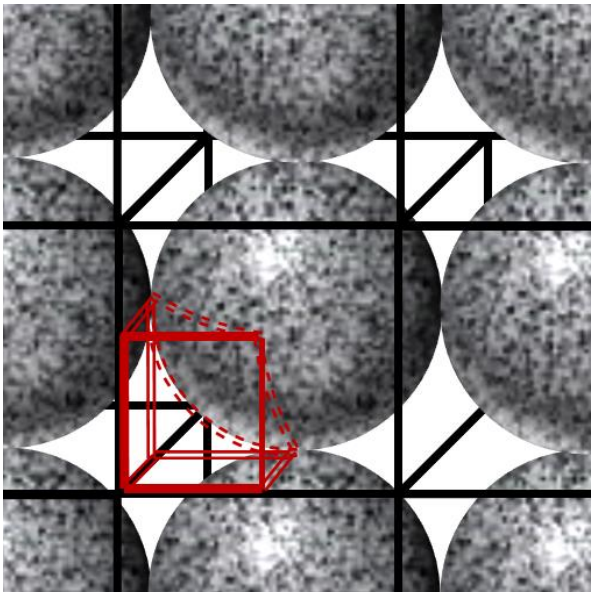

Figure B.1 – Sketch of an ideal arrangement of spherical clusters (in grey), assuming a constant diameter, with a single contact point between clusters. Clusters are embedded in a grid fitted on the spheres. White space represents the location of large pores. Red lines delimited 1/8 of the void space within one grid cell, i.e. 1/8 of one large pore volume.

$$V_{cell} = d_{c,\mathbb{R}}^3 \quad \textbf{(B-2)}$$

Therefore, the volume of void space not occupied by the cluster in one cell is:

$$V_{void,L} = V_{cell} - V_{c,\mathbb{R}} \quad \textbf{(B-3)}$$

Note that this volume corresponds to the volume occupied by large pores. Thus, whatever, the cluster size, the theoretical porosity of the large network $\varepsilon_{L,\mathbb{t}}$ is:

$$\varepsilon_{L,\mathbb{t}} = \frac{V_{void,L}}{V_{cell}} = 1 - \frac{\pi}{6} \quad \textbf{(B-4)}$$

In the three-dimensional cell, the corner delimited by the red lines in Figure B.1 represents 1/8 of the total volume of one large pore. Thus, the volume of the large network void space inside one cell is equal to the volume of one large pore and is calculated as follows:

$$V_{Lp,\mathbb{t}} = \varepsilon_{L,\mathbb{t}} V_{cell} \quad \textbf{(B-5)}$$

Considering a spherical pore, the volume of a large pore based on experimental data is:

$$V_{Lp,\mathbb{R}} = \frac{4}{3}\pi\left(\frac{d_{Lp,\mathbb{R}}}{2}\right)^2 \quad \textbf{(B-6)}$$

Finally, the porosity of the large pore network is scaled as follows:

$$\varepsilon_{L,\mathbb{R}} = \varepsilon_{L,\mathbb{t}}\frac{V_{Lp,\mathbb{R}}}{V_{Lp,\mathbb{t}}} \quad \textbf{(B-7)}$$

Note that, by deduction, the porosity of the small network is:

$$\varepsilon_{S,\mathbb{R}} = \varepsilon_{\mathbb{R}} - \varepsilon_{L,\mathbb{R}} \quad \textbf{(B-8)}$$

where $\varepsilon_{\mathbb{R}}$ is the porosity of the sample as given by the experiment.

In the PNM, the inputs for the porosities are thus:

$$\varepsilon_{L,PN} = \varepsilon_{L,\mathbb{R}} \quad \textbf{(B-9)}$$

$$\varepsilon_{S,PN} = \varepsilon_{S,\mathbb{R}} \quad \textbf{(B-10)}$$

B.2 Determination of large network step b

Step b is determined from the comparison of the two ratios:

- Cluster number ratio: $N_{c,\mathbb{R}}/N_{c,PN}$

- Large pore number ratio: $N_{Lp,\mathbb{R}}/N_{Lp,PN}$

The ratios are the quantities calculated from experimental data divided by the quantities corresponding to the pore network model. Note that the number of clusters in the PNM is actually lower than in the real sample. Therefore, the number of large pores in the PNM is scaled such that:

$$N_{Lp,\mathbb{R}} = \frac{N_{c,PN}}{N_{c,\mathbb{R}}}N_{Lp,\mathbb{R}} \quad \textbf{(B-11)}$$

Step b is then determined to satisfy condition (B-11) as close as possible. The following section describes how to determine each ratio.

B.2.1 Number of clusters

From experimental data, the approximate number of clusters within the evaporator unit cell is simply defined by:

$$N_{c,\mathbb{R}} = \frac{V_T}{V_{cell}} \quad \textbf{(B-12)}$$

In the PNM, clusters are cubic and the volume of one cluster is:

$$V_{c,PN} = b^3 \quad \textbf{(B-13)}$$

Therefore, the number of clusters in the PNM is defined as follows:

$$N_{c,PN} = \frac{V_T}{V_{c,PN}} \quad \textbf{(B-14)}$$

B.2.2 Number of large pores

From the experimental data and based on the porosity definition, the average large pore number is determined as follows:

$$N_{Lp,\mathbb{R}} = \varepsilon_{L,PN} \frac{V_T}{V_{Lp,\mathbb{R}}} \quad \textbf{(B-15)}$$

Considering that the grooves are manufactured within the casing, the following procedure is applied to determine the number of large pores within the wick. If the grooves are machined within the wick, the procedure is done twice: once for the lower part of the wick, i.e. the part close to the compensation chamber, and once for the upper part, i.e. the porous fin close to the casing; then the numbers of large pores are added. The following three values are defined:

$$i = \mathrm{int}\left(\frac{n_i - 1}{b/a} + 1\right) \quad \textbf{(B-16)}$$

$$j = \mathrm{int}\left(\frac{n_{jw} - 1}{b/a} + 1\right) \quad \textbf{(B-17)}$$

$$k = \mathrm{int}\left(\frac{n_k - 1}{b/a} + 1\right) \quad \textbf{(B-18)}$$

where n_i is the number of pores in the x direction, n_{jw} is the number of pores in the y direction, n_k is the number of pores in the z direction; int is a function which returns the integer part of the number obtained inside brackets. Actually, i returns the number of planes (yOz) defining the junction between two clusters in the x direction, j returns the number of planes (xOz) defining the junction between two clusters in the y direction and k returns the number of planes (xOy) defining the junction between two clusters in the z direction.

Finally, the total number of large pores in the network is:

$$N_{Lp,PN} = n_i \times j \times k + \left(n_{jw} - j\right) \times i \times k + \left(n_k - k\right) \times i \times j \quad \textbf{(B-19)}$$

Note that the total number of large throats in the network is:

$$N_{Lt,PN} = N_{Lp,PN} + 2 \times i \times j \times k \quad \textbf{(B-20)}$$

B.2.3 Ratio comparison

Combining equations (B-12) to (B-19), the step b is determined such that the number of clusters ratio $N_{c,\mathbb{R}}/N_{c,PN}$ and the number of large pores ratio $N_{Lp,\mathbb{R}}/N_{Lp,PN}$ are as close as possible.

B.3 Determination of the pore size $d_{Lp,PN}$ and $d_{Sp,PN}$

Finally, the mean diameters of pores and throats are determined. The two third-degree polynomial equations to be solved for the large network and for the small network are given by equation (B-21) and equation (B-22), respectively.

$$d_{Lp,PN}^3 - \left(d_{Lt,PN}^2 \frac{N_{Lt,PN}}{N_{Lp,PN}}\right) d_{Lp,PN} + \left(d_{Lt,PN}^2 a \frac{N_{Lt,PN}}{N_{Lp,PN}} - \frac{V_T \varepsilon_{L,PN}}{N_{Lp,PN}}\right) = 0 \quad \textbf{(B-21)}$$

$$d_{Sp,PN}^3 - \left(d_{St,PN}^2 \frac{N_{St,PN}}{N_{Sp,PN}}\right) d_{Sp,PN} + \left(d_{St,PN}^2 a \frac{N_{St,PN}}{N_{Sp,PN}} - \frac{V_T \varepsilon_{S,PN}}{N_{Sp,PN}}\right) = 0 \quad \textbf{(B-22)}$$

The classical Cardano's method is used to solve equations (B-21) and (B-22) similarly as in Appendix A.

Appendix C. Computation of permeability

C.1 General method

The computation of the permeability is based on the traditional pore network model and is described, for example, in Prat (2010) [120]. The principle of the method is to impose a pressure gradient ΔP across a network. Hence, the pressure field in the porous structure is computed, and finally, the macroscopic permeability is deduced form Darcy's law. The considered network size is $L_x \times L_y \times L_z$ and is composed by $n_i \times n_j \times n_k$ pores.

The flow resistance is taken into account only in throats, i.e. the flow resistance is neglected in pores. Pore and throat sizes are randomly distributed according to given probability distribution functions.

The local hydraulic conductance g_{ij} of a cylindrical throat is defined assuming a Poiseuille flow (equation (C-1))

$$g_{ij} = \frac{\pi d_{ij}^4}{128 l_{ij}} \quad \textbf{(C-1)}$$

where d_{ij} is the diameter of the throat and l_{ij} its length.

The flow rate between two adjacent pores i and j is expressed as:

$$q_{ij} = \frac{g_{ij}}{\mu}(P_i - P_j) \quad \textbf{(C-2)}$$

where μ is the dynamic viscosity and P_i and P_j are the pressures in pores i and j, respectively.

By imposing a pressure difference ΔP across the network, the mass balance is expressed at each node (equation (C-3)).

$$\sum_j q_{ij} = 0 \quad \textbf{(C-3)}$$

where i is the considered nodes and j denotes the six neighbour nodes.

This gives a linear system of equations which is solved numerically and which gives the pressure field within the pore network. As the local pressure in the pores is now known, the local flow rate q_{ij} is then calculated for each throat using equation (C-2)

Considering that the pressure difference is imposed in y-direction, the flow rate Q through the network can be computed by summing up the flow rate q_{ij} in any row of throats located in a x-z plane (equation(C-4)).

$$Q = \sum_i q_{ij} \quad \textbf{(C-4)}$$

Finally, the permeability of the network is deduced from Darcy's law and is expressed by equation(C-5).

$$K = \frac{Q\mu L_y}{\Delta P L_x L_z} \quad \textbf{(C-5)}$$

The above procedure is quite simple to implement and permit to ensure a good agreement between the permeability given experimentally and the one of the computed porous structure.

C.2 Determination of the permeability: case of a bidispersed structure

Assuming a bimodal, network, two different permeabilities have to be considered: the one of the network constituted by the small pores and the one of the network constituted by the large pores. The procedure described above is done firstly for the small pore network and in a second time for the large pore network. Thus, the two permeabilities K_s and K_l are obtained. The procedure is applied a last time on the whole network to ensure a good agreement of the total permeability of the porous structure with experimental data.

Appendix D. Pore network model computation of capillary-pressure and relative permeability curves

D.1 General presentation

The relative permeability (liquid and vapour) and the capillary pressure as a function of the liquid saturation are inputs of the continuum model presented in Chapter VI. Indeed, the Darcy's law for the liquid and the vapour phase (equation (VI-8) and equation (VI-9)) is a function of the relative permeability. Moreover, the capillary pressure as a function of the liquid saturation is also necessary (see equation (VI-18)). Usually, these parameters (relative permeabilities and capillary pressure curve) are determined experimentally. Moreover, these properties are material and fluid dependant. Since these data elements are not necessarily available in literature for the case of sintered wicks, the aim is to find simple, but nevertheless realistic, relations between these parameters and the liquid saturation. The found relation between the capillary pressure and the liquid saturation has to be easily differentiable.

The traditional pore network model is a suitable tool to determine these porous wick properties. Procedures are described in details in the following.

D.2 Capillary pressure curve

The method to determine the capillary pressure curve as a function of the liquid saturation is based on successive pressure increments across the network. The pressure is uniform in the liquid and vapour phases but different between the two phases.

Firstly, the considered network is full of liquid at the pressure P_l. An additional fictive row of pores is implemented at the inlet of the network. This row is in vapour state and at the pressure P_v. At the liquid-vapour interface, the capillary invasion pressure threshold ΔP_{cap} for each throat is calculated according to the Young-Laplace equation (equation (D-1)):

$$\Delta P_{cap} = \frac{2\sigma}{r_t} cos\theta \quad \textbf{(D-1)}$$

where r_t is the throat radius and θ is the contact angle.

If the difference between the vapour and the liquid pressure is greater than the capillary pressure threshold, the meniscus is moved into the adjacent pore, otherwise not (equation (D-2)).

$$\begin{cases} if\ \Delta P_{cap} < P_v - P_l, invasion\ of\ the\ adjacent\ pore \\ if\ \Delta P_{cap} \geq P_v - P_l, stable\ meniscus \end{cases} \quad \textbf{(D-2)}$$

This condition is verified along the whole liquid-vapour interface, and all non-stable meniscuses are moved. At this stage, the liquid saturation is calculated and the pressure jump at the interface $\Delta P = P_v - P_l$ is noted. This corresponds to the first point of the capillary pressure curve.

The next step consists in increasing the vapour pressure. The new vapour pressure is then $P_v = P_v + \Delta P_v$. The procedure of invasion is repeated again from the liquid-vapour phase distribution obtained previously. Note that such procedure induces the trapping of some liquid clusters within the porous structure. The liquid clusters are removed as we consider no trapping of liquid. The procedure is performed until the whole porous medium is in vapour state, i.e. full of vapour.

The capillary pressure curve as the function of the liquid saturation is finally obtained (Figure D.1) and can be fitted using Van Genuchten model (eq. (D-3)).

$$P_{cap} = \frac{1}{\alpha}\left((S_l^*)^{-1/m} - 1\right)^{1/n} \quad \textbf{(D-3)}$$

where $m = 1 - 1/n$ and α are the fitted parameters.

S_l^* is the effective liquid saturation (equation (D-4)).

$$S_l^* = \frac{S_l - S_{lr}}{1 - S_{lr} - S_{vr}} \quad \textbf{(D-4)}$$

S_{lr} is the liquid phase residual saturation and S_{vr} is the vapour phase residual saturation. In the present model S_{lr} and S_{vr} are equal to zero assuming no trapping in the porous medium, i.e. trapped liquid clusters are removed during the invasion process.

In the example of the capillary pressure curve presented in Figure D.1, α and n are equal to 2.92×10^{-5} and 17, respectively.

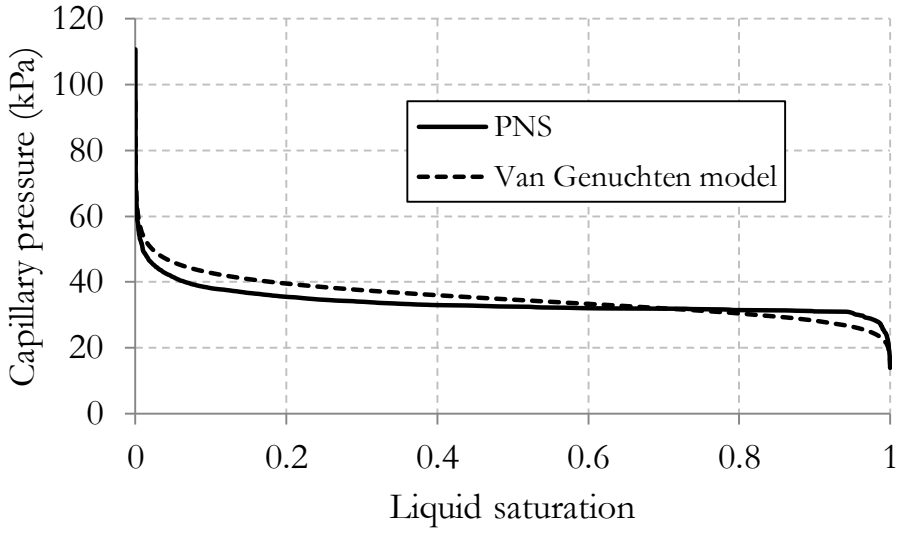

Figure D.1 – Capillary pressure curve as a function of the liquid saturation.

D.3 Relative permeability

The method to determine the relative permeabilities as a function of liquid saturation is as follows. The first liquid-vapour distribution is determined from the capillary pressure procedure (section D.2). For this liquid-vapour phase distribution, the vapour phase is set at constant pressure P_v. A pressure P_l, with $P_v \neq P_l$, is imposed at the inlet of the network. The pressure field in the liquid phase is then computed following the same procedure as presented in Appendix C. Finally, the liquid relative permeability is deduced from equation(D-5):

$$k_{rl} = \frac{Q\mu_l L_y}{K\Delta P L_x L_z} \quad \textbf{(D-5)}$$

where $\Delta P = P_v - P_l$ and K is the macroscopic permeability computed as described in Appendix C.

The next step consists in displacing the liquid-vapour interface following the procedure presented for the computation of the capillary pressure curve (section D.2). The liquid relative permeability can then be determined for this new liquid saturation according to the procedure explained previously. k_{rl} is then computed as long as the main liquid cluster is connected to the inlet of the network.

Once the vapour is connected to the outlet of the network, the vapour relative permeability can be computed as follows. The liquid phase is set at a constant pressure P_l. A pressure P_v, with $P_v \neq P_l$, is imposed at the outlet of the network. The pressure field in the vapour phase is then computed following a procedure similar to the one presented in Appendix C. Finally, the vapour relative permeability is deduced from equation (D-6):

$$k_{rv} = \frac{Q\mu_v L_y}{K\Delta P L_x L_z} \quad \textbf{(D-6)}$$

where $\Delta P = P_v - P_l$ and K is the macroscopic permeability computed as described in Appendix C.

k_{rv} is then computed for each new liquid-vapour phase distribution until all pores are in vapour state. The relative permeability curves as a function of the liquid saturation are finally obtained (Figure D.2) and can be fitted using Van Genuchten model (equations (D-7) and (D-8)).

$$k_{rl}(S_l^*) = (S_l^*)^{\gamma_l}\left(1 - \left(1 - (S_l^*)^{1/m_l}\right)^{m_l}\right)^2 \quad \textbf{(D-7)}$$

$$k_{rv}(S_l^*) = (1 - S_l^*)^{\gamma_v}\left(1 - (S_l^*)^{1/m_v}\right)^{2m_v} \quad \textbf{(D-8)}$$

where m_l, m_v, γ_l and γ_v are the fitted parameters.

In the example presented in Figure D.2, γ_l, γ_v, n_l and n_v are equal to 1×10^{-3}, 0.361, 3 and 26, respectively.

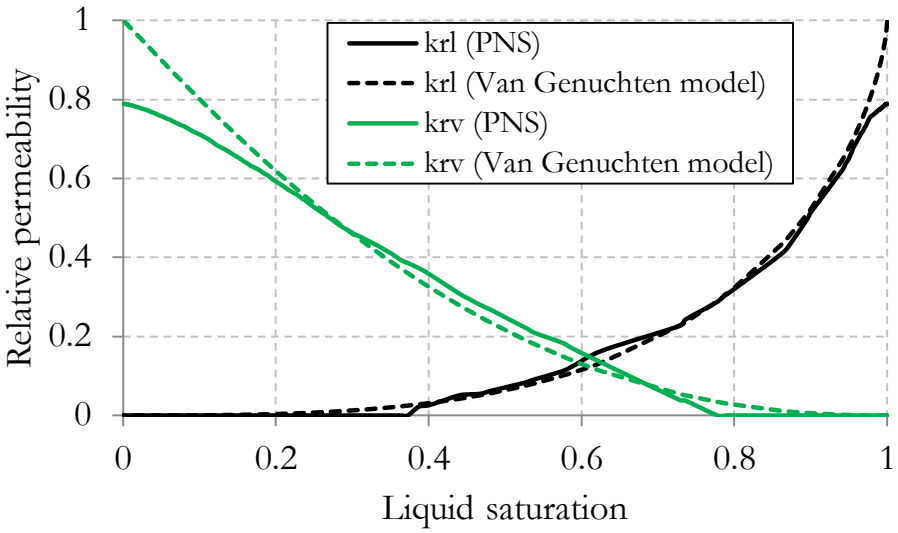

Figure D.2 – Variation of the liquid and vapour relative permeabilities as a function of the liquid saturation.

References

[1] T. Coquard, "Transferts couplés de masse et de chaleur dans un élément d'évaporateur capillaire," PhD Thesis (in French), Institut National Polytechnique de Toulouse, 2006.

[2] C. Figus, "Changement de phase en milieu poreux: Application à l'étude d'un évaporateur capillaire," PhD Thesis (in French), Institut National Polytechnique de Toulouse, 1996.

[3] C. Louriou, "Modélisation instationnaire des transferts de masse et de chaleur au sein des évaporateurs capillaires," PhD Thesis (in French), Institut National Polytechnique de Toulouse, 2010.

[4] J. Ku, "Operating Characteristics of Loop Heat Pipes," presented at the 29th International Conference on Environmental System, 1999.

[5] Y. F. Maydanik, "Loop heat pipes," *Applied Thermal Engineering,* vol. 25, pp. 635-657, 2005.

[6] S. Launay, V. Sartre, and J. Bonjour, "Parametric analysis of loop heat pipe operation: a literature review," *International Journal of Thermal Sciences,* vol. 46, pp. 621-636, 2007.

[7] S. Launay and M. Vallée, "State-of-the-Art Experimental Studies on Loop Heat Pipes," *Frontiers in Heat Pipes,* vol. 2, 2011.

[8] A. Ambirajan, A. Adoni, J. S. Vaidya, A. A. Rajendran, D. Kumar, and P. Dutta, "Loop Heat Pipes: A Review of Fundamentals, Operation,and Design," *Heat Transfer Engineering,* vol. 33, pp. 387-405, 2012.

[9] Y. F. Maydanik, M. A. Chernysheva, and V. G. Pastukhov, "Review: Loop heat pipes with flat evaporators," *Applied Thermal Engineering,* vol. 67, pp. 294-307, 2014.

[10] B. Siedel, V. Sartre, and F. Lefèvre, "Literature review: Steady-state modelling of loop heat pipes," *Applied Thermal Engineering,* vol. 75, pp. 709-723, 2015.

[11] B. Siedel, "Analysis of heat transfer and flow patterns in a loop heat pipe: Modelling by analytical and numerical approaches andexperimental observations," PhD Thesis, Institut National des Science Appliquées de Lyon, 2014.

[12] M. A. Chernysheva, S. V. Vershinin, and Y. F. Maydanik, "Operating temperature and distribution of a working fluid in LHP," *International Journal of Heat and Mass Transfer,* vol. 50, pp. 2704-2713, 2007.

[13] S. Launay, V. Sartre, and J. Bonjour, "Analytical Model for Characterization of Loop Heat Pipes," *Journal of Thermophysics and Heat Transfer,* vol. 22, pp. 623-631, 2008.

[14] P.-Y. A. Chuang, "An improved steady-state model of loop heat pipe based on experimental and theorical analyses," PhD Thesis, Pennsylvania State University, 2003.

[15] P.-Y. A. Chuang, J. M. Cimbala, and J. S. Brenizer, "Experimental and analytical study of a loop heat pipe at a positive elevation using neutron radiography," *International Journal of Thermal Sciences,* vol. 77, pp. 84-95, 2014.

[16] Y. F. Maydanik, S. V. Vershinin, M. A. Korukov, and J. M. Ochterbeck, "Miniature Loop Heat Pipes — A Promising Means for Cooling Electronics," *IEEE Transactions on Components and Packaging Technologies,* vol. 28, pp. 290-296, 2005.

[17] A. Faghri, *Heat pipe science and technology*: Taylor & Francis, 1995.

[18] M. Hamdan, "Loop Heat Pipe (LHP) Modeling and Development by Utilizing Coherent Porous Silicion (CPS) Wicks," PhD Thesis, University of Cincinnati, 2003.

[19] H.-Y. Kwak and R. L. Panton, "Tensile strength of simple liquids predicted by a model of molecular interactions," *Journal of Physics D: Applied Physics,* vol. 18, pp. 647-659, 1985.

[20] D. Mishkinis and J. M. Ochterbeck, "Homogeneous Nucleation and the Heat Pipe Boiling Limitation," *Journal of Engineering Physics and Thermophysics,* vol. 76, pp. 61-64, 2003.

[21] T. Kaya and J. Goldak, "Numerical analysis of heat and mass transfer in the capillary structure of a loop heat pipe," *International Journal of Heat and Mass Transfer,* vol. 49, pp. 3211-3220, 2006.

[22] D. Mishkinis, P. Prado, R. Sanz, A. Torres, A. S. S. Merino, and T. Tjiptahardja, "Development of LHP for Intermediate Temperature Range," in *15th International Heat Pipe Conference*, Clemson, USA, 2010.

[23] A. Adoni, J. S. Vaidya, A. Ambirajan, D. Kumar, B. Krishnaswamy, and P. Dutta, "Evaporation Heat Transfer Coefficient in a Capillary Pumped Loop and Loop Heat Pipe for Different Working Fluids," *Heat Transfer Engineering,* vol. 33, pp. 765-774, 2012.

[24] J. Choi, B. Sung, C. Kim, and D.-A. Borca-Tasciuc, "Interface engineering to enhance thermal contact conductance of evaporators in miniature loop heat pipe systems," *Applied Thermal Engineering,* vol. 60, pp. 371-378, 2013.

[25] T. Fang, T. Ming, C. P. P. Tso, X. Huang, and W. Liu, "Analysis of non-uniform heat loads on evaporators with loop heat pipes," *International Journal of Heat and Mass Transfer,* vol. 75, pp. 313-326, 2014.

[26] Z. Wang and J. M. Ochterbeck, "Steady state operation of cylindrical loop heat pipe evaporators," presented at the 13th International Heat Transfer Conference, 2006.

[27] X. Zhang, X. Li, and S. Wang, "Three-dimensional simulation on heat transfer in the flat evaporator of miniature loop heat pipe," *International Journal of Thermal Sciences,* vol. 54, pp. 188-198, 2012.

[28] R. Boubaker, "Modélisation thermodynamique instationnaire d'une boucle fluide diphasique à pompage capillaire pour la traction ferroviaire: étude du phénomène de changement de phase dans l 'évaporateur," PhD Thesis (in French), Université de Pau et des peys de l'Adour, 2014.

[29] V. V. Maziuk, A. L. Rak, and A. V. Balashchanke, "Heat flow distribution in evaporators of loop heat pipes," presented at the IV Minsk International seminar "Heat Pipes, Heat Pumps, Refrigerators", 2000.

[30] M. A. Chernysheva and Y. F. Maydanik, "Heat and mass investigation in the evaporation zone of a loop heat pipe," presented at the 7th Minsk International Conference "Heat Pipes, Heat Pumps, Refrigerators, Power Sources", 2008.

[31] M. A. Chernysheva and Y. F. Maydanik, "Heat and Mass Transfer in Evaporator of Loop Heat Pipe," *Journal of Thermophysics and Heat Transfer,* vol. 23, pp. 725-731, 2009.

[32] D. Khrustalev and A. Faghri, "Heat transfer in the inverted meniscus type evaporator at high heat fluxes," *International Journal of Heat and Mass Transfer,* vol. 38, pp. 3091-3101, 1995.

[33] R. R. Riehl and N. dos Santos, "Loop heat pipe performance enhancement using primary wick with circumferential grooves," *Applied Thermal Engineering,* vol. 28, pp. 1745-1755, 2008.

[34] P. Santos, E. Bazzo, and A. Oliveira, "Thermal performance and capillary limit of a ceramic wick applied to LHP and CPL," *Applied Thermal Engineering,* vol. 41, pp. 92-103, 2012.

[35] V. M. Kiseev, V. V. Vlassov, and I. Muraoka, "Experimental optimization of capillary structures for loop heat pipes and heat switches," *Applied Thermal Engineering,* vol. 30, pp. 1312-1319, 2010.

[36] L. Bai, G. Lin, H. Zhang, and D. Wen, "Mathematical modeling of steady-state operation of a loop heat pipe," *Applied Thermal Engineering,* vol. 29, pp. 2643-2654, 2009.

[37] L. Mottet, T. Coquard, and M. Prat, "Heat and mass transfer in the porous wick of a capillary evaporator," presented at the 5th International Conference on Porous Media and its Applications in Science and Engineering, 2014.

[38] R. Singh, A. Akbarzadeh, and M. Mochizuki, "Effect of Wick Characteristics on the Thermal Performance of the Miniature Loop Heat Pipe," *Journal of Heat Transfer,* vol. 131, p. 082601, 2009.

[39] S.-C. Wu, F.-C. Lin, S.-H. Chen, C.-C. Yeh, S. K. Wang, and Y.-M. Chen, "Manufacturing of the Complex Wick with Double-Layer Bi-Porous Structure and Applying to a Loop Heat," presented at the 10th International Heat Pipe Symposium, 2011.

[40] S.-C. Wu, C.-J. Huang, S.-H. Chen, and Y.-M. Chen, "Manufacturing and testing of the double-layer wick structure in a loop heat pipe," *International Journal of Heat and Mass Transfer,* vol. 56, pp. 709-714, 2013.

[41] M. Nishikawara and H. Nagano, "Heat Transfer of LHP Evaporators with Micro Gaps," presented at the International Symposium on space technology and science, 2013.

[42] S.-C. Wu, T.-W. Gu, D. Wang, and Y.-M. Chen, "Study of PTFE wick structure applied to loop heat pipe," *Applied Thermal Engineering,* vol. 81, pp. 51-57, 2015.

[43] H. Li, Z. Liu, B. Chen, W. Liu, C. Li, and J. Yang, "Development of biporous wicks for flat-plate loop heat pipe," *Experimental Thermal and Fluid Science,* vol. 37, pp. 91-97, 2012.

[44] J. Li and G. P. Peterson, "3D heat transfer analysis in a loop heat pipe evaporator with a fully saturated wick," *International Journal of Heat and Mass Transfer,* vol. 54, pp. 564-574, 2011.

[45] B. Siedel, V. Sartre, and F. Lefèvre, "Numerical investigation of the thermohydraulic behaviour of a complete loop heat pipe," *Applied Thermal Engineering,* vol. 61, pp. 541-553, 2013.

[46] C.-C. Yeh, B.-H. Liu, and Y.-M. Chen, "A study of loop heat pipe with biporous wicks," *Heat and Mass Transfer,* vol. 44, pp. 1537-1547, 2008.

[47] S. Mo, P. Hu, J. Cao, Z. Chen, H. Fan, and F. Yu, "Effective Thermal Conductivity of Moist Porous Sintered Nickel Material," *International Journal of Thermophysics,* vol. 27, pp. 304-313, 2006.

[48] M. A. Chernysheva and Y. F. Maydanik, "3D-model for heat and mass transfer simulation in flat evaporator of copper-water loop heat pipe," *Applied Thermal Engineering,* vol. 33-34, pp. 124-134, 2012.

[49] F.-C. Lin, B.-H. Liu, C.-T. Huang, and Y.-M. Chen, "Evaporative heat transfer model of a loop heat pipe with bidisperse wick structure," *International Journal of Heat and Mass Transfer,* vol. 54, pp. 4621-4629, 2011.

[50] C. Figus, Y. Le Bray, S. Bories, and M. Prat, "Heat and mass transfer with phase change in a porous structure partially heated: continuum model and pore network simulations," *International Journal of Heat and Mass Transfer,* vol. 42, pp. 2557-2569, 1999.

[51] X. Huang, W. Liu, A. Nakayama, and S. W. Peng, "Modeling for heat and mass transfer with phase change in porous wick of CPL evaporator," *Heat and Mass Transfer,* vol. 41, pp. 667-673, 2005.

[52] Z. Liu, W. Liu, and A. Nakayama, "Flow and heat transfer analysis in porous wick of CPL evaporator based on field synergy principle," *Heat and Mass Transfer,* vol. 43, pp. 1273-1281, 2007.

[53] M. Nishikawara, H. Nagano, and M. Prat, "Evaporator heat transfer analysis of a loop heat pipe with low thermal conductivity wicks," presented at the 17th International heat pipe conference, 2013.

[54] R. Boubaker, V. Platel, A. Berges, M. Bancelin, and E. Hannezo, "Dynamic model of heat and mass transfer in an unsaturated porous wick of capillary pumped loop," *Applied Thermal Engineering,* vol. 76, pp. 1-8, 2015.

[55] A. S. Demidov and E. S. Yatsenko, "Investigation of heat and mass transfer in the evaporation zone of a heat pipe operating by the ‘ inverted meniscus ’ principle," *International Journal of Heat and Mass Transfer,* vol. 37, pp. 2155-2163, 1994.

[56] Y. H. Yan and J. M. Ochterbeck, "Numerical Investigation of the Steady-State Operation of a Cylindrical Capillary Pumped Loop Evaporator," *Journal of Electronic Packaging,* vol. 125, p. 251, 2003.

[57] C. Ren, Q.-S. Wu, and M.-B. Hu, "Heat transfer with flow and evaporation in loop heat pipe's wick at low or moderate heat fluxes," *International Journal of Heat and Mass Transfer,* vol. 50, pp. 2296-2308, 2007.

[58] J. Li, D. Wang, and G. P. Peterson, "A Compact Loop Heat Pipe With Flat Square Evaporator for High Power Chip Cooling," *IEEE Transactions on Components, Packaging and Manufacturing Technology,* vol. 1, pp. 519-527, 2011.

[59] B. Siedel, V. Sartre, and F. Lefèvre, "Complete analytical model of a loop heat pipe with a flat evaporator," *International Journal of Thermal Sciences,* vol. 89, pp. 372-386, 2015.

[60] Y. Cao and A. Faghri, "Analytical solutions of flow and heat transfer in a porous structure with partial heating and evaporation on the upper surface," *International Journal of Heat and Mass Transfer,* vol. 37, pp. 1525-1533, 1994.

[61] T. Kaya and T. T. Hoang, "Mathematical modeling of loop heat pipes and experimental validation," *Journal of Thermophysics and Heat Transfer,* vol. 13, pp. 314-320, 1999.

[62] M. Hamdan and E. Elnajjar, "Thermodynamic analytical model of a loop heat pipe," *Heat and Mass Transfer,* vol. 46, pp. 167-173, 2009.

[63] A. V. Alexseev, "Micro loop heat pipe evaporator coherent pore structures," MSc Thesis, Texas A&M University, 2003.

[64] N. Atabaki, "Experimental and computational studies of loop heat pipes," PhD Thesis, McGill University, 2006.

[65] N. Jesuthasan, "Modeling of Thermofluid Phenomena in Segmented Network Simulations of Loop Heat Pipes," PhD Thesis, McGill University, 2011.

[66] A. Adoni, A. Ambirajan, V. S. Jasvanth, D. Kumar, and P. Dutta, "Theoretical and experimental studies on an ammonia-based loop heat pipe with a flat evaporator," *Ieee Transactions on Components and Packaging Technologies,* vol. 33, pp. 478-487, 2010.

[67] L. Lachassagne, "Développement expérimental et modélisation numérique d'une boucle diphasique à pompage capillaire en environnement gravitaire: application au refroidissement de composants d'électronique de puissance en contexte automobile," PhD Thesis (in French), Ecole Nationale Supérieure de Mécanique et d'Aérotechnique de Poitiers, 2010.

[68] L. Lachassagne, Y. Bertin, V. Ayel, and C. Romestant, "Steady-state modeling of Capillary Pumped Loop in gravity field," *International Journal of Thermal Sciences,* vol. 64, pp. 62-80, 2013.

[69] N. Blet, "Analyse expérimentale et par voie de modélisation d'une boucle gravitaire à pompage capillaire multi-évaporateurs," PhD Thesis (in French), Ecole National Supérieure de Mécanique et d'Aérotechnique de Poitiers, 2014.

[70] S. Launay, V. Platel, S. Dutour, and J.-L. Joly, "Transient Modeling of Loop Heat Pipes for the Oscillating Behavior Study," *Journal of Thermophysics and Heat Transfer,* vol. 21, pp. 487-495, 2007.

[71] T. Kaya, R. Pérez, C. Gregori, and A. Torres, "Numerical simulation of transient operation of loop heat pipes," *Applied Thermal Engineering,* vol. 28, pp. 967-974, 2008.

[72] V. V. Vlassov and R. R. Riehl, "Mathematical model of a loop heat pipe with cylindrical evaporator and integrated reservoir," *Applied Thermal Engineering,* vol. 28, pp. 942-954, 2008.

[73] M. Nishikawara, H. Nagano, and T. Kaya, "Transient Thermo-Fluid Modeling of Loop Heat Pipes and Experimental Validation," *Journal of Thermophysics and Heat Transfer,* vol. 27, pp. 641-647, 2013.

[74] Q. Liao and T. Zhao, "Evaporative heat transfer in a capillary structure heated by a grooved block," *Journal of Thermophysics and Heat Transfer,* vol. 13, pp. 126-133, 1999.

[75] Q. Liao and T. Zhao, "A visual study of phase-change heat transfer in a two-dimensional porous structure with a partial heating boundary," *International Journal of Heat and Mass Transfer,* vol. 43, pp. 1089-1102, 2000.

[76] L. Mottet, T. Coquard, and M. Prat, "Three dimensional liquid and vapour distribution in the wick of capillary evaporators," *International Journal of Heat and Mass Transfer,* vol. 83, pp. 636-651, 2015.

[77] Y. Cao and A. Faghri, "Conjugate analysis of a flat-plate type evaporator for capillary pumped loops with three-dimensional vapor flow in the groove," *International Journal of Heat and Mass Transfer,* vol. 37, pp. 401-409, 1994.

[78] M. A. Chernysheva and Y. F. Maydanik, "Numerical simulation of transient heat and mass transfer in a cylindrical evaporator of a loop heat pipe," *International Journal of Heat and Mass Transfer,* vol. 51, pp. 4204-4215, 2008.

[79] J. Li, D. Wang, and G. P. Peterson, "Experimental studies on a high performance compact loop heat pipe with a square flat evaporator," *Applied Thermal Engineering,* vol. 30, pp. 741-752, 2010.

[80] Y. Xuan, K. Zhao, and Q. Li, "Investigation on Heat and Mass Transfer in a Evaporator of a Capillary-Pumped Loop with the Lattice Boltzmann Method: Pore Scale Simulation," *Transport in Porous Media,* vol. 89, pp. 337-355, 2011.

[81] Q. Li, K. Zhao, and Y. Xuan, "Simulation of flow and heat transfer with evaporation in a porous wick of a CPL evaporator on pore scale by lattice Boltzmann method," *International Journal of Heat and Mass Transfer,* vol. 54, pp. 2890-2901, 2011.

[82] M. A. Chernysheva and Y. F. Maydanik, "Peculiarities of heat transfer in a flat disk-shaped evaporator of a loop heat pipe," *International Journal of Heat and Mass Transfer,* vol. 92, pp. 1026-1033, 2016.

[83] Z. Wan, W. Liu, Y. L. L. Liu, and A. Nakayama, "Conjugate Numerical Investigation of a Miniature Flat Plate Evaporator of Capillary Pumped Loop," presented at the 2007 International Conference on Mechatronics and Automation, 2007.

[84] Z. Wan, W. E. I. Liu, Z. Tu, and A. Nakayama, "Conjugate numerical investigation of a miniature flat-plate evaporator of a capillary pumped loop for electronics cooling," *TASK QUARTERLY,* vol. 12, pp. 5-19, 2008.

[85] Z. Wan, J. Liu, J. H. Wan, Z. Tu, and W. Liu, "An overall numerical investigation on heat and mass transfer for miniature flat plate capillary pumped loop evaporator," *Thermochimica Acta,* vol. 518, pp. 82-88, 2011.

[86] M. A. Chernysheva and Y. F. Maydanik, "Investigation of heat and mass transfer in a flat evaporator of a copper–water loop heat pipe under uniform and concentrated heating," presented at the 8th Minsk International Conference "Heat Pipes, Heat Pumps, Refrigerators, Power Sources", 2011.

[87] M. A. Chernysheva and Y. F. Maydanik, "Simulation of thermal processes in a flat evaporator of a copper–water loop heat pipe under uniform and concentrated heating," *International Journal of Heat and Mass Transfer,* vol. 55, pp. 7385-7397, 2012.

[88] M. A. Chernysheva, V. G. Pastukhov, and Y. F. Maydanik, "Analysis of heat exchange in the compensation chamber of a loop heat pipe," *Energy,* vol. 55, pp. 253-262, 2013.

[89] R. Boubaker and V. Platel, "Vapor pocket behavior inside the porous wick of a capillary pumped loop for terrestrial application," *Applied Thermal Engineering,* vol. 84, pp. 420-428, 2015.

[90] T. Zhao and Q. Liao, "On capillary-driven flow and phase-change heat transfer in a porous structure heated by a finned surface: measurements and modeling," *International Journal of Heat and Mass Transfer,* vol. 43, pp. 1141-1155, 2000.

[91] X. Huang and W. Liu, "A mathematical model to analyze heat and mass transfer characteristics of a CPL evaporator porous wick," *Heat Transfer - Asian Research,* vol. 34, pp. 209-218, 2005.

[92] J. T. Gostick, M. a. Ioannidis, M. W. Fowler, and M. D. Pritzker, "Pore network modeling of fibrous gas diffusion layers for polymer electrolyte membrane fuel cells," *Journal of Power Sources,* vol. 173, pp. 277-290, 2007.

[93] C. Sleicher and M. Rouse, "A convenient correlation for heat transfer to constant and variable property fluids in turbulent pipe flow," *International Journal of Heat and Mass Transfer,* vol. 18, pp. 677-683, 1975.

[94] S. Patankar, *Numerical heat transfer and fluid flow*, 1980.

[95] M. Adams, S. Balay, J. Brown, P. Brune, L. Dalcin, S. Farley*, et al.*, "Portable, Extensible Toolkit for Scientific Computation," ed, 2015.

[96] T. Coquard, M. Prat, A. Larue de Tournemine, and C. Figus, "Pore-network models as a tool for the analysis of heat and mass transfer with phase change in the capillary structure of loop heat pipe.," presented at the 14th International Heat Pipe Conference, Florianopolis, Brazil, 2007.

[97] D. Wilkinson and J. F. Willemsen, "Invasion percolation: a new form of percolation theory," *Journal of Physics A: Mathematical and general,* vol. 16, pp. 3365-3376, 1983.

[98] J. Hoshen and R. Kopelman, "Percolation and cluster distribution. I. Cluster multiple labeling technique and critical concentration algorithm," *Physical Review B,* vol. 14, pp. 3438-3445, 1976.

[99] M. Prat, S. Veran-Tissoires, N. Vorhauer, T. Metzger, and E. Tsotsas, "Fractal Phase Distribution and Drying: Impact on Two-Phase Zone Scaling and Drying Time Scale Dependence," *Drying Technology,* vol. 30, pp. 1129-1135, 2012.

[100] M. Nishikawara, H. Nagano, L. Mottet, and M. Prat, "Formation of unsaturated regions in the porous wick of a capillary evaporator," *International Journal of Heat and Mass Transfer,* vol. 89, pp. 588-595, 2015.

[101] X. L. Cao, P. Cheng, and T. Zhao, "Experimental study of evaporative heat transfer in sintered copper bidispersed wick structures," *Journal of Thermophysics and Heat Transfer,* vol. 16, pp. 547-552, 2002.

[102] N. S. Rasor and J. L. Desplat, "K-max: a material with exceptional heat transfer properties," 1989.

[103] T. Semenic, Y. Y. Lin, and I. Catton, "Use of liquid film evaporation in biporous media to achieve high heat flux over large areas," presented at the VI Minsk International Seminar "Heat Pipes, Heat Pumps, Refrigerators", 2005.

[104] T. Semenic, Y. Y. Lin, and I. Catton, "Use of liquid film evaporation in biporous media to achieve high heat flux over large areas," presented at the ASME Summer Heat Transfer Conference, 2005.

[105] T. Semenic, Y. Y. Lin, I. Catton, and D. B. Sarraf, "Use of biporous wicks to remove high heat fluxes," *Applied Thermal Engineering,* vol. 28, pp. 278-283, 2008.

[106] T. Semenic, Y. Y. Lin, and I. Catton, "Thermophysical Properties of Biporous Heat Pipe Evaporators," *Journal of Heat Transfer,* vol. 130, p. 022602, 2008.

[107] T. Semenic and I. Catton, "Experimental study of biporous wicks for high heat flux applications," *International Journal of Heat and Mass Transfer,* vol. 52, pp. 5113-5121, 2009.

[108] S. W. Reilly and I. Catton, "Utilization of Pore-Size Distributions to Predict Thermophysical Properties and Performance of Biporous Wick Evaporators," *Journal of Heat Transfer,* vol. 136, p. 061501, 2014.

[109] F.-C. Lin, B.-H. Liu, C.-C. Juan, and Y.-M. Chen, "Effect of pore size distribution in bidisperse wick on heat transfer in a loop heat pipe," *Heat and Mass Transfer,* vol. 47, pp. 933-940, 2011.

[110] C.-C. Yeh, C.-N. Chen, and Y.-M. Chen, "Heat transfer analysis of a loop heat pipe with biporous wicks," *International Journal of Heat and Mass Transfer,* vol. 52, pp. 4426-4434, 2009.

[111] S.-C. Wu, D. Wang, and Y.-M. Chen, "Investigating the effect of double-layer wick thickness ratio on heat transfer performance of loop heat pipe," *International Journal of Thermal Sciences,* vol. 86, pp. 292-298, 2014.

[112] S.-C. Wu, B. H. Hsieh, D. Wang, and Y.-M. Chen, "Manufacture of a biporous nickel wick and its effect on LHP heat transfer performance enhancement," *Heat and Mass Transfer,* 2015.

[113] S.-C. Wu, D. Wang, W.-J. Lin, and Y.-M. Chen, "Investigating the effect of powder-mixing parameter in biporous wick manufacturing on enhancement of loop heat pipe performance," *International Journal of Heat and Mass Transfer,* vol. 89, pp. 460-467, 2015.

[114] M. T. North, D. B. Sarraf, J. H. Rosenfeld, Y. F. Maydanik, and S. V. V. Vershinin, "High heat flux loop heat pipes," presented at the 6th European Symposium on Space Environmental Control Systems, Noordwijk, The Netherlands, 1997.

[115] J. Wang and I. Catton, "Evaporation heat transfer in thin biporous media," *Heat and mass transfer,* vol. 37, pp. 275-281, 2001.

[116] A. Vadnjal and I. Catton, "Modelling Heat Transfer Performance of a Thin Bi-Porous Evaporator for a Heat Pipe," presented at the ASME Summer Heat Transfer Conference, 2005.

[117] K. Aziz and A. Settari, *Petroleum Reservoir Simulations*: Applied Science Publishers Ltd, 1979.

[118] W. Lee, "A pressure iteration scheme for two-phase flow modeling," *Multiphase transport fundamentals, reactor safety, applications,* vol. 1, pp. 407-431, 1980.

[119] Z. Yang, X. F. Peng, and P. Ye, "Numerical and experimental investigation of two phase flow during boiling in a coiled tube," *International Journal of Heat and Mass Transfer,* vol. 51, pp. 1003-1016, 2008.

[120] M. Prat, "Pore network models for the study of transfers in the porous wick of loop heat pipes," *Heat Pipe Science and Technology, An International Journal,* vol. 1, pp. 129-149, 2010.